A Unified Approach to Crack Fields and Crack Propagation

Xiao Su

St Anne's College

University of Oxford

A thesis submitted for the degree of

Doctor of Philosophy

Hilary 2025

This thesis is dedicated to

SU Zhen and WANG Yingli

For their love and support

Acknowledgements

Looking back, my DPhil journey at Oxford has been nothing short of remarkable and will remain an experience I will never forget.

I would like to extend my deepest gratitude to my supervisor, Professor James Marrow. Your thoughtful guidance has been invaluable throughout this academic adventure. Your constant encouragement to push the limits of my abilities has had a profound impact. I am truly grateful for your immense availability, your sharp academic insight, and your unwavering passion and rigor in research, all of which have greatly shaped my work and will continue to inspire me as both a role model and a source of motivation.

I would also like to extend my heartfelt thanks to all my colleagues in the TJM Group. The discussions we shared have been immensely beneficial, and I have received much precious assistance from all of you. Special thanks to Dr Abdalrhaman Koko, whose excellent research work and generous support helped me make significant progress in the early stages of my DPhil study. I am also grateful to Robin Scale and Dr Jicheng Gong for providing samples, and to Robin Scale for assisting with sample preparation and fatigue precracking, along with many enriching discussions. My thanks go to Zikang Zhang, Marcus Williamson, and Marin Vukšić for their help in the experiments. The time shared with Shivansh Nauriyal, Rory Whybrow, Georgy Grishchenko and Qingchuan Lu at the office and beamline is among my fondest memories.

I would like to thank DCCEM, LIMA Lab, and the Materials IT staff for their support throughout my research.

I am also grateful to the China Oxford Scholarship Fund (COSF) for providing financial support and for the opportunity to meet so many outstanding individuals.

A big thank you to my friends in the chinese society at Oxford. From the moment I arrived at Oxford, the friendships I built with you all have added beautiful colours to my life beyond research. The time spent with you has become an irreplaceable part of my Oxford memories.

I am forever thankful to my parents for their unconditional love.

Lastly, my deepest thanks to Jier Wang for accompanying alongside me in this beautiful journey.

Abstract

Title: A Unified Approach to Crack Fields and Crack Propagation

Author: Xiao Su, St Anne's College

Supervisor: Professor T James Marrow

Date of Submission: Hilary 2025

Understanding the mechanical behaviour of materials requires detailed characterisation of crack-tip fields and propagation mechanisms, particularly at small length scales. This thesis develops a generalised, field-based methodology for evaluating fracture parameters and propagation mechanisms using full-field techniques including optical DIC, SEM-DIC, and HR-EBSD. A literature review traces the development of fracture mechanics from global, geometry-based fracture toughness concepts to local, field-based approaches, highlighting the limitations of conventional methods for short fatigue cracks and microscale testing. The first study analyses short fatigue cracks in Zircaloy-4 using high-resolution optical DIC, confirming the feasibility of extracting fracture parameters from field data and showing that short fatigue cracks exhibit distinct crack-tip driving force characteristics. The method is then extended to single crystal nickel-alloy, where concurrent SEM-DIC and HR-EBSD capture both displacement and lattice strain fields of a short fatigue crack in situ for the first time, enabling direct evaluation of energy integrals from measured data. Finally, a microscale fracture toughness testing method based on indentation cracking in silicon integrates HR-EBSD strain mapping and energy-based analysis to extract mode-specific stress intensity factors, retaining the practicality of indentation testing while enhancing its interpretability. Overall, the work offers a robust alternative to classical approaches, grounded in full-field local measurements.

Table of Contents

Chapter 1

Literature Review

1.1 Introduction

Material failure is a critical consideration in designing structures under harsh conditions. Since the 1950s, fracture mechanics has introduced a range of valuable concepts and theories, leading to successful applications across various engineering disciplines. There is a constant need for the extreme design and utilisation of structural materials under challenging conditions, requiring a deep understanding of failure mechanisms linked to different material properties.

Research in this field has expanded to include detailed observations of material damage, supported by increasingly direct, rich and comprehensive mechanical data. As a result, the modelling of mechanical behaviour now better accounts for complex factors [1]. This enhanced knowledge

allows for precise tailoring of materials' microstructures, accurate predictions of material lifespan, and new development of testing frameworks to address existing theoretical gaps.

The majority of damage originates from cracks, with their development governed by the local conditions at the crack tip. Full-field techniques with high spatial resolution have emerged as powerful tools for accurately characterising local crack tip conditions. Various imaging modalities, including optical, electron, X-ray, coupled with digital image correlation, enable precise mapping of displacements. On the other hand, diffraction methods utilising neutrons, electrons, and X-rays can detect changes in lattice spacing and accurately map the strain fields. These techniques, whether used individually or in combination, enable the in-situ assessment of strain and displacement fields at the crack tip, delivering critical data that propels ongoing research.

With abundant data collected at the local crack tip, the direct evaluation of classic crack-controlling parameters such as the J-integral and stress intensity factors (SIFs) becomes straightforward, helping quantify the real crack driving force. Different methods are viable and finite element post-processing, in particular, has been recognised as an efficient and robust option. This approach will be applied and developed throughout the chapters of this thesis, with new insights being obtained through the analysis of the collected data. Additionally, other analytical tools, such as Geometrically Necessary Dislocation (GND) analysis and trace analysis to characterise plasticity, will also be employed as supplementary methods.

1.2 From ‘Global’ Conditions to ‘Local’ Measurements

Prior to the use of full-field techniques, crack analysis relied largely on theoretical continuum mechanics and 'global' conditions. Commonly considered were factors such as the overall load applied, sample geometry, crack geometry (including shape and length), and other secondary factors. This review will first cover fundamental concepts and standard fracture toughness testing methods, which typically assume idealised crack configurations and uniform loading conditions.

Notably, cracks - especially short cracks - are primarily governed by local conditions. The introduction of full-field characterisation techniques offers an indispensable opportunity to more accurately assess the conditions at the crack tip. This review will then progress to explore the advancements in full-field techniques related to crack studies.

1.2.1. Fundamental Concepts for Crack Analysis

1.2.1.1. Crack as a Stress Field Concentrator

Cracks are critical to structural failure, but their understanding was limited before the 20th century. The recognition of the gap between actual and theoretical strength of a perfect crystal initiated crack studies. Inglis [2] provided the first stress analysis of an elliptical hole in an infinite plate under remote stress in 1913, described by the following equation:

$$\sigma_A = \sigma_0 \left(1 + 2\sqrt{\frac{a}{\rho}} \right) \tag{1-1}$$

where σ_A is the local stress at the crack (hole) tip, σ_0 is the remote applied stress, $2a$ and 2b are the length and width of the elliptical hole, respectively, and ρ is the curvature radius at the tip.

As shown in Figure 1.1, Inglis demonstrated that local stress around a crack is concentrated and exceeds the applied stress, influenced by the crack length and tip radius of curvature.

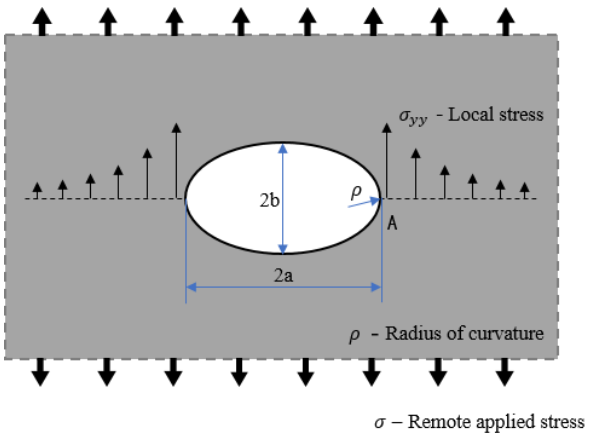

FIGURE 1.1
The Inglis elastic stress concentration at an elliptical hole. (adapted from Mechanical Engineering Design lecture notes: https://www.cdmunicas.it/med)

1.2.1.2. Early Theories of Crack Analysis: Energy and Stress Perspectives

From an energy perspective, Griffith [3] first approached the fracture strength in 1920 by invoking the law of thermodynamics, linking the new surface energy required with the release of elastic strain energy from crack growth. Consider a $2a$ long through-thickness crack in a wide plate under remote tensile stress σ_0 in plane stress conditions, Griffith's energy balance is given by the following equation:

$$\frac{\partial G}{\partial A} = \frac{\partial \Pi}{\partial A} + \frac{\partial W_s}{\partial A} = -\frac{\pi {\sigma_0}^2 a}{E'} + 2\gamma_s = 0 \tag{1-2}$$

where, G is the total energy, A is the crack area, Π is the potential energy supplied by the internal strain energy and external forces, W_s is the work required to create new surfaces, E' is the effective Young's modulus and γ_s is the surface energy of the material. This provides a fundamental criterion for solving the critical applied stress at fracture propagation.

The criterion proved effective for glass assuming perfect elasticity. Irwin and Orowan [4, 5] modified it in 1948 by considering plastic dissipation, assuming that energy dissipated by plastic flow doesn't affect energy release, regardless of crack geometry or loading conditions. Irwin [6] introduced the concept of 'strain energy release rate' G in 1956, a fundamental criteria in fracture mechanics. It is defined as the total energy released or dissipated per unit area as the crack propagates. The critical strain energy release rate, denoted as G_c, represents the material's fracture toughness. Notably, G_c is independent of loading conditions and crack geometry. Equation (1-3) shows the connections and differences among these energy-based methods for the example of a 'Griffith' 2D crack:

$$\sigma_f \approx \underbrace{\sqrt{\left(\frac{2E'\gamma_s}{\pi a}\right)}}_{\text{Griffith 1920}} \approx \underbrace{\sqrt{\left(\frac{2E'\left(\gamma_s+\gamma_p\right)}{\pi a_{eff}}\right)}}_{\text{Irwin \& Orowan 1948}} \approx \underbrace{\sqrt{\frac{E'G}{\pi a}}}_{\text{Irwin 1956}} \tag{1-3}$$

The comparison shows that γ_p accounts the additional plastic dissipation.

The stress approach for crack analysis began with Westergaard's 1938 paper which developed a semi-inverse method for stresses and displacements ahead of a sharp crack. In 1957, Irwin [7] solved the stress field near the crack tip for different loading modes, introducing the 'stress intensity factor' K. Williams' solution [8] incorporates higher-order terms. Both analyses assume isotropic linear elasticity, with the full form in Equation (1-4). Figure 1.2 depicts the three loading modes, while Figure 1.3 shows the coordinate system and stress normal to the crack plane. In Equation (1-4), σ_{ij} is the stress tensor, K denotes the stress intensity factor with a subscript to denote the loading mode. f_{ij} is the dimensionless function of θ. A and g represent the amplitude and the dimensionless function for higher-order terms, respectively. Sneddon [9] provided a similar analysis.

$$\sigma_{ij} = \frac{K_I}{\sqrt{2\pi r}} f_{ij}^{I}(\theta) + \frac{K_{II}}{\sqrt{2\pi r}} f_{ij}^{II}(\theta) + \frac{K_{III}}{\sqrt{2\pi r}} f_{ij}^{III}(\theta) + \sum_{m=0}^{\infty} A_m r^{\frac{m}{2}} g_{ij}^{(m)}(\theta) \qquad (1\text{-}4)$$

The solution is characterised by leading terms with a stress singularity of $1/\sqrt{r}$ at the crack tip. This single-parameter description defines a key concept in fracture mechanics. Numerous analytical solutions have been developed for various geometries and loading configurations [10, 11], and complex cases can be solved using finite element analysis. Table 1.1 presents a few examples, with details discussed in Section 1.2.2. Additionally, higher-order terms, referred to as "T-stress" [12, 13], quantify the effect of fracture constraint.

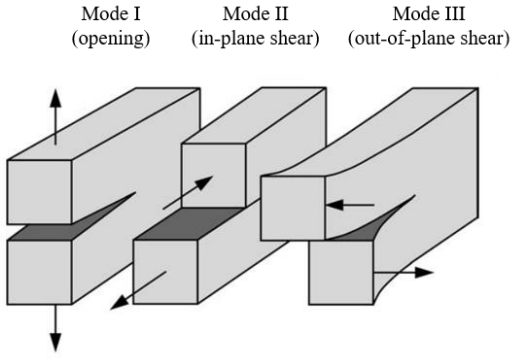

FIGURE 1.2
Three modes of loading. (from [14])

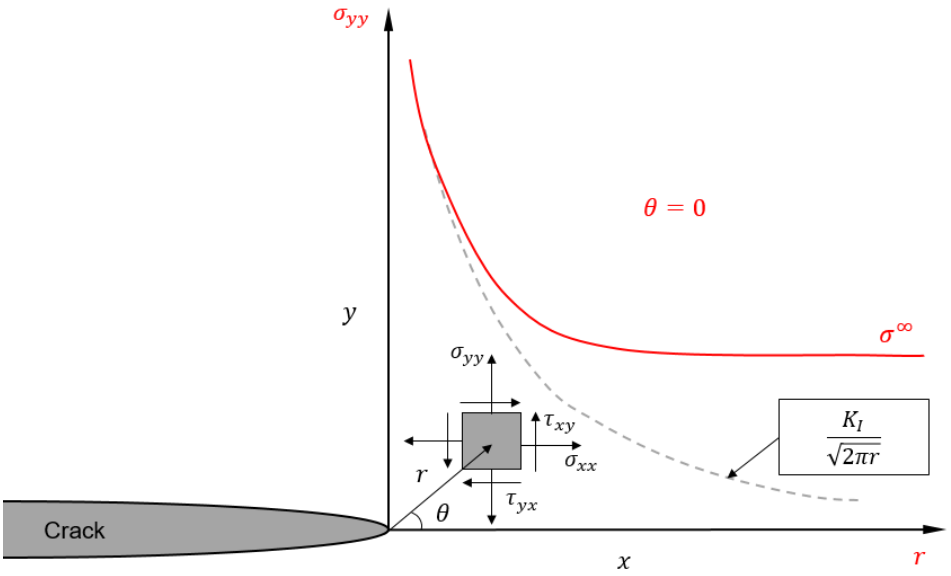

FIGURE 1.3

Definition of the coordinate system ahead of a crack tip and the singular stress field component normal to the crack plane in an isotropic linear elastic material under Mode I loading.

TABLE 1.1

Solutions of stress intensity factor for different configurations. [14]

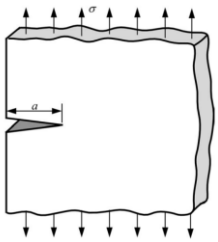 Edge crack in a semi-infinite plate $\boldsymbol{K_I = 1.12\sigma\sqrt{\pi a}}$	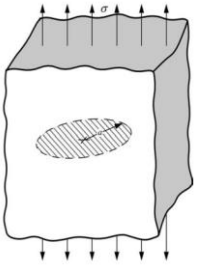 Penny-shaped crack in an infinite medium $K_I = \frac{2}{\pi}\sigma\sqrt{\pi a}$
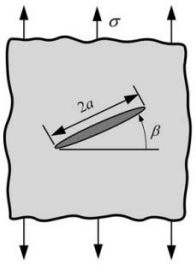 Through inclined crack in an infinite plate $\boldsymbol{K_I = \sigma\cos^2(\beta)\sqrt{\pi a}}$ $\boldsymbol{K_{II} = \sigma\sin(\beta)\cos(\beta)\sqrt{\pi a}}$	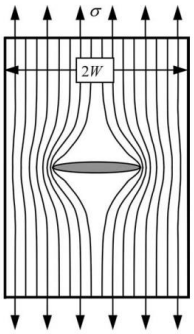 Through crack in a finite plate (lines schematise stress concentration) $K_I = \sigma\sqrt{\pi a}\left[\sec\left(\frac{\pi a}{2W}\right)^{1/2}\right]\left[1 - 0.025\left(\frac{a}{W}\right)^2 + 0.06\left(\frac{a}{W}\right)^4\right]$

The stress-based approach and the energy-based approach are uniquely related and both provide a single parameter description of the same linear elastic approximation at the crack tip. This relationship is given by Equation (1-5). The determination of critical K and G has since attracted great interest, with early applications by Wells [15, 16] and by Winne and Wundt [17].

$$G = \frac{K_I^2}{E'} + \frac{K_{II}^2}{E'} + \frac{K_{III}^2}{2\mu} \tag{1-5}$$

1.2.1.3. Development of the J-Integral Method

The existence of infinite local stress and an infinitely sharp crack is a recognised limitation in linear elastic crack theory. Irwin [18, 19] extended the use of stress analysis to estimate the size of the plastic zone. And the strip yield model, proposed by Dugdale [20] and Barenblatt [21], used superposition to effectively model the yielding by combining a crack under remote tension with one under closure stress.

Based on observations of crack blunting in relatively tough materials, Wells [22] proposed using crack tip opening displacement ($CTOD$) as a measure of fracture toughness. This work established a relationship between $CTOD$ and K for small-scale yielding, inherently implying a connection with G, as shown by the following equation.

$$\delta = \frac{K_I^2}{m\sigma_{YS}E'} = \frac{G}{m\sigma_{YS}} \tag{1-6}$$

where δ is the $CTOD$, σ_{YS} is the uniaxial yield strength of the material and m is a dimensionless constant that is approximately 1.0 for plane stress and 2.0 for plane strain. Irwin [19] postulated that the presence of crack tip plasticity can be regarded as the effect of a slightly longer actual crack. Figure 1.4 illustrates the plastic zone correction and its relationship with $CTOD$ and the crack tip field. Due to the straightforward nature of its measurement, standard $CTOD$ testing methods were developed and widely used [23-25].

Another single crack field characterising parameter, the J integral, developed by Rice [26] in 1968, marked a significant advancement in fracture mechanics. The integral is defined as

$$J = \int_{\Gamma} \left(W \mathrm{d}y - T_i \frac{\partial u_i}{\partial x} ds \right) \tag{1-7}$$

where W is the strain energy density, T_i are components of the traction vector, u_i are the displacement vector components, and ds is a length increment along an arbitrary contour around the tip of a crack, Γ, which is illustrated in Figure 1.5.

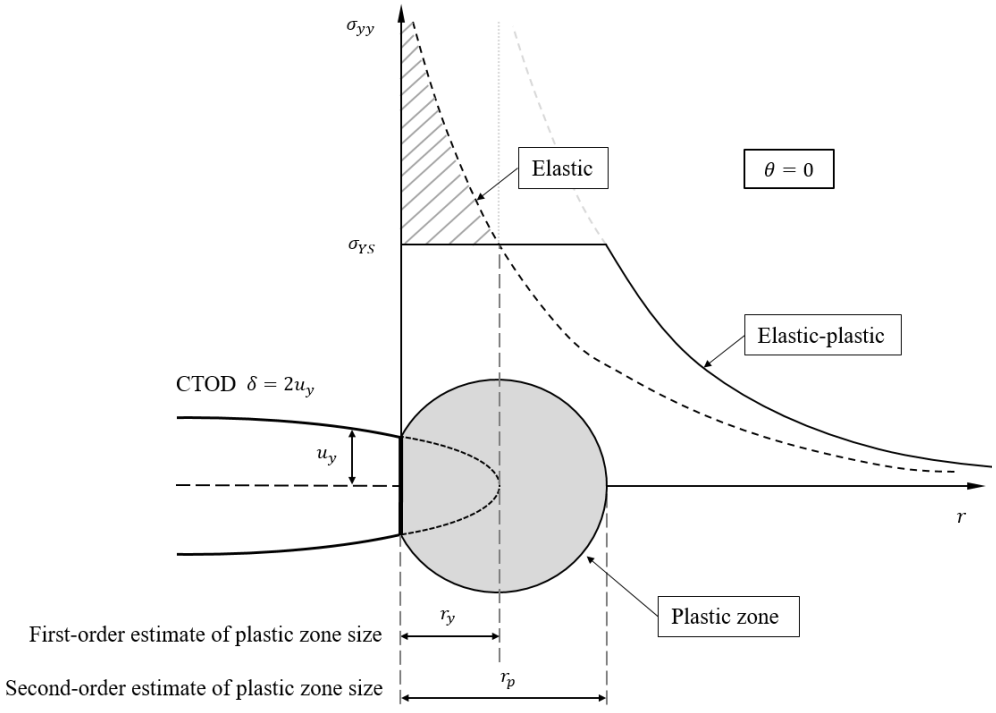

FIGURE 1.4
Plastic zone correction and its relationship with $CTOD$ and the crack-tip field.

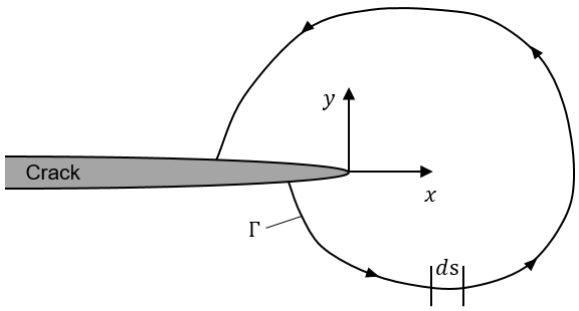

FIGURE 1.5
Arbitrary contour around the tip of a crack.

Designed to analyse cracks in nonlinear materials, this parameter overcomes the limitations of linear elasticity by conceptualising elastic-plastic deformation as nonlinear elastic. It can be evaluated through an arbitrary contour around the crack tip, effectively characterising the material's fracture toughness with its versatility. Rice demonstrated that the path-independent J contour integral is equivalent to the energy release rate in nonlinear materials. For the special case of a linear elastic material:

$$J = G = \frac{K_I^2}{E'} \tag{1-8}$$

Subsequent research by Hutchinson [27], Rice and Rosengren [28] confirmed that J also serves as a stress intensity parameter without the existence of very large strains (~0.10):

$$\sigma_{ij} = k\left(\frac{J}{r}\right)^{1/(n+1)} \tag{1-9}$$

where k is a proportionality constant. For a linear elastic material, $n = 1$, and Equation (1-9) predict a $1/\sqrt{r}$ singularity, which is consistent with the K description. More generally, the so-called 'HRR singularity' of the crack field is accurate in an annular region within the elastic-plastic deformation zone, which is confirmed by broad finite element analysis [29-33]. From a testing perspective, J can be estimated as a sum of an elastic part and a plastic part:

$$J = J_{el} + J_{pl} = \frac{K_I^2}{E'} + \frac{\eta_{pl} A_{pl}}{Bb} \tag{1-10}$$

where A_{pl} is the plastic area under the load–displacement curve, as shown in Figure 1.6, η_{pl} is the corresponding geometric factor, B is the thickness and b is the remaining ligament.

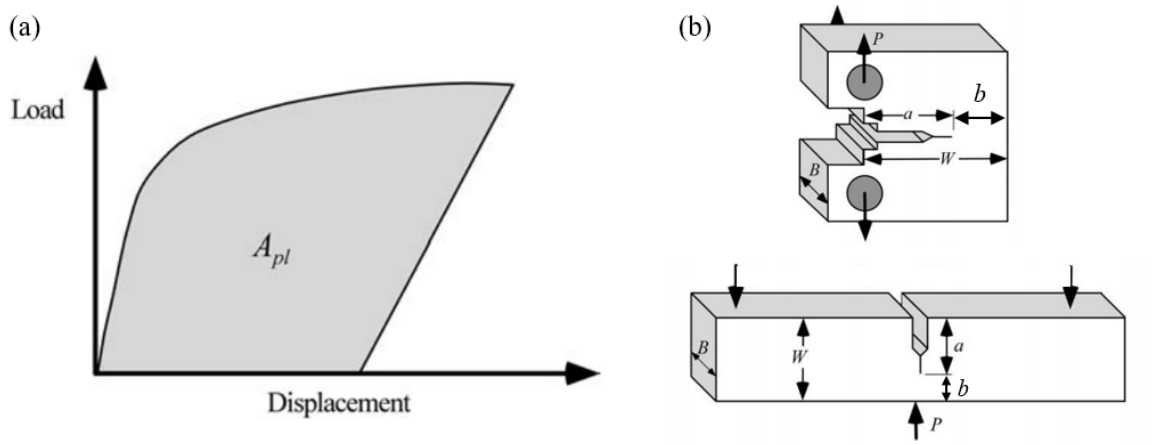

FIGURE 1.6
(a) Plastic energy absorbed by a test specimen during a J_{Ic} test. (b) Schematic of thickness B and ligament b for common specimen geometry. (from [14])

Further analysis by Shih [34] established a unique relationship between J and $CTOD$, proving that both are equally valid for assessing crack tip conditions in scenarios without excessive plasticity or significant crack growth. Experimental $CTOD$ estimates are similar in form to J tests,

$$\delta = \delta_{el} + \delta_{pl} = \frac{K^2}{m\sigma_{YS}E'} + \delta_{pl} \tag{1-11}$$

These analyses reveal the fundamental connections between the crack field and various controlling parameters at the crack tip.

1.2.2. Standard Tests and Fatigue Equations

Having established fundamental parameters for evaluating crack driving force, it is possible to assess a material's resistance to crack propagation as a benchmark for structural integrity design. This involves testing at critical state, when fracture initiates, commonly referred to as fracture toughness testing. This section reviews the development of standardised methods, starting with conventional approaches based on global conditions, and then covering models of fatigue cracks.

1.2.2.1. Fracture Toughness Testing

The process of material failure is a complex interplay of deformation behaviour and fracture mechanisms, constrained by geometry. Materials demonstrate deformation characteristics that vary from linear elastic, nonlinear elastic to elastic-plastic, influencing the necessary fracture parameters and testing methods to assess fracture toughness. Regarding fracture behaviour, materials can fracture with ductility, characterised by slow, stable crack extension and energy absorption, or in a brittle manner, marked by rapid, unstable propagation and a sudden load drop at initiation. These variations require distinct assessment methods; ductile fractures need a resistance curve (R curve) for comprehensive evaluation. Moreover, the geometric configurations of test specimens, such as thickness and size, significantly impact the fracture response. Constraints imposed by these factors affect stress distribution and fracture mode, with higher constraint favouring brittle fracture by increasing the tensile stress at the crack tip, and lower constraint promoting ductility, as evident in resistance curve toughness. Typically, discussions focus on conditions of plane stress or plane strain, with the higher constraint of plane strain providing a conservative estimate of fracture toughness.

For brittle fracture, the crack tip is predominantly governed by linear elastic deformation, making initiation toughness a critical indicator of a material's fracture resistance since any additional resistance post-initiation is minimal. The plane strain fracture toughness, K_{Ic}, serves as an effective point measure of this resistance. It is evaluated under conditions of plane strain in mode I, characterised by slow or quasi-static loading rates and mainly linear-elastic behaviour. Significant contributions to the standardisation of K_{Ic} testing were made by Srawley and Brown [35, 36]. They developed specifications for various aspects of the testing process, including specimen design, size requirements, fatigue precracking, fixturing, the use of load transducers, crack opening displacement gauges, and overall testing procedures. Following a decade of developmental work,

these efforts converged in the ASTM standard E399, which is continuously updated to reflect the latest methodologies and practices, with its most recent iteration being E399-24 [37].

As shown in Figure 1.7, compact tension (C(T)) specimens and single edge-notched bend (SE(B)) specimens in three-point bending are commonly used for K_{Ic} testing. ASTM E399 mandates fatigue precracking to generate a sharp crack with an initial size between $0.45W$ and $0.55W$. To determine the critical load P_Q near crack initiation, a 95% secant offset procedure is applied, along with strict specimen geometry constraints specified in Equation (1-12). The corresponding fracture toughness K_{Ic} is then calculated using Equation (1-13).

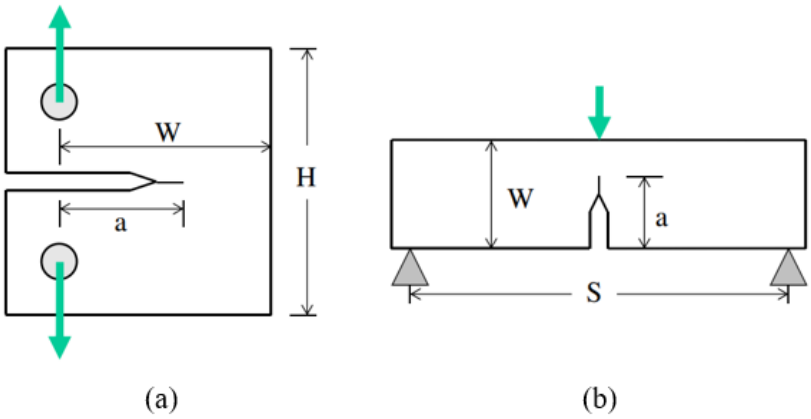

FIGURE 1.7
Geometry of fracture test specimens: (a) compact tension specimen, (b) single edge-notched bend specimen in three-point bending. (from [14])

(a) $$B, a \geq 2.5\left(\frac{K_Q}{\sigma_{YS}}\right)^2$$

(b) $$P_{max} \leq 1.1P_Q \tag{1-12}$$

$$K = \frac{P_Q}{B\sqrt{W}} f\left(\frac{a}{W}\right) \tag{1-13}$$

where a and W are defined in Figure 1.7, B denotes the specimen thickness, and $f(\frac{a}{W})$ is a geometric function dependent solely on the crack size-to-width ratio a/W. For C(T) specimens,

$$f(\frac{a}{W}) = \frac{(2+\frac{a}{W})}{\left(1-\frac{a}{W}\right)^{\frac{3}{2}}}\left[0.886 + 4.64\left(\frac{a}{W}\right) - 13.32\left(\frac{a}{W}\right)^{2} + 14.72\left(\frac{a}{W}\right)^{3} - 5.60(\frac{a}{W})^{4}\right] \quad (1\text{-}14)$$

and for SE(B) specimens,

$$f(\frac{a}{W}) = \frac{3\frac{S}{W}\sqrt{\frac{a}{W}}}{2\left(1+2\frac{a}{W}\right)\left(1-\frac{a}{W}\right)^{\frac{3}{2}}}\left[1.99 - \frac{a}{W}\left(1-\frac{a}{W}\right)\left\{2.15 - 3.93\left(\frac{a}{W}\right) + 2.7\left(\frac{a}{W}\right)^{2}\right\}\right] \quad (1\text{-}15)$$

For tougher materials, the tearing resistance to crack propagation over small increments can be significant, rendering point measurements inadequate. However, if plastic deformation is limited and elastic conditions predominantly govern the test piece, the stress intensity factor, K, can still effectively characterise the crack tip field, albeit with minor modifications. In such cases, a K-based R curve can be developed, offering solutions for both crack initiation and extension resistance. Focused research has been undertaken to establish a testing method for thin-section materials with small-scale plastic deformation. The ASTM standard E561 for the K-R curve test method was initially standardised and approved in 1974, and has since been tested and verified by researchers, with strict validity criteria that should be acknowledged.

In ASTM E561, the calculation of K relies on the same formula as Equation (1-13). However, a middle-cracked tension (M(T)) specimen is recommended, with the corresponding geometry function given by:

$$f(\frac{a}{W}) = \sqrt{\frac{\pi a}{W}\sec(\frac{\pi a}{W})} \quad (1\text{-}16)$$

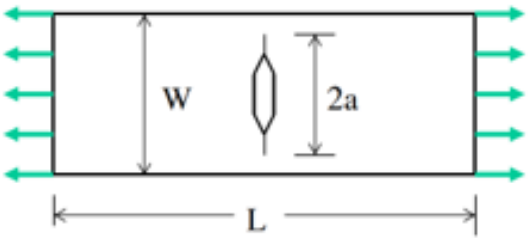

FIGURE 1.8
Geometry of middle-cracked tension specimen. (from [14])

Note that this standard employs an effective crack length, a_{eff}, incorporating Irwin's plastic zone correction. Similarly, for the measurement to be valid, the initial crack size must fall within the range of $0.35W$ to $0.55W$, and the following criterion is enforced:

(a) $$L \geq 3W$$

(b) $$(W - a) \geq 8r_y = \frac{4}{\pi}\left(\frac{K_{max}}{\sigma_{YS}}\right)^2 \quad (1\text{-}17)$$

where r_y is the plastic zone size estimation at the maximum expected toughness K_{max}.

For ductile fractures, plastic deformation at the crack tip predominates, leading to increased material resistance as the crack extends. Consequently, toughness is typically described using a resistance curve, utilising the J integral or $CTOD$. In contrast to elastic materials, much of the strain energy absorbed by an elastic–plastic material remains unrecoverable after crack growth or unloading. This led Rice to associate the J integral with the work done on a nonlinear elastic body rather than the energy released from the body, forming the basis for early experimental evaluations of the J integral [26].

Building on these principles, various J estimation equations were developed for those standard fracture specimens [38], such as those used in E813-81, the first ASTM standard for J testing. To evaluate the initiation toughness, J_{Ic}, near the onset of stable crack growth, ASTM E1152-82 standard initiated the estimation of the J integral as a combination of elastic and plastic components, as shown in Equation (1-10). This method includes approximations for determining

a plastic factor. Subsequently, incremental J integral equations, such as those developed by Ernst [39], were integrated into the first J–R curve standard, ASTM E1152-87, to assess the plastic components,

$$J_{pl(i)} = \left[J_{pl(i-1)} + \frac{\eta_{pl(i-1)}}{B b_{i-1}} A_{pl}^{i-1,i}\right]\left(1 - \frac{\gamma_{i-1}}{b_{i-1}}(a_i - a_{i-1})\right) \tag{1-18}$$

while the elastic part was derived from the stress intensity factor,

$$J_{el} = \frac{K^2}{E'} \tag{1-19}$$

in which $A_{pl}^{i-1,i}$ is the increment of plastic area from step $i-1$ to i, as shown in Figure 1.9; η and γ are geometry factors.

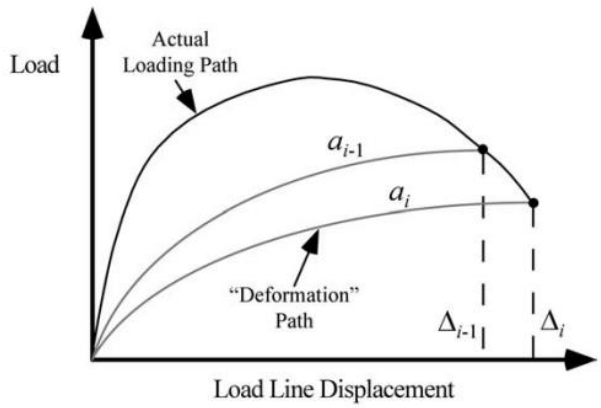

FIGURE 1.9
Schematic load-displacement curve for a J-R curve test. (from [14])

Essential to these tests are the K measurements and the monitoring of load, displacement, and crack length as 'global' inputs. To circumvent the need for multiple specimens, methods were developed to indirectly track the crack length, either by elastic unloading compliance or by electrical potential drop techniques. In 1996, the last versions of ASTM E813-89 and E1152-95 were merged into a single standard E1737-96 [40], which was short-lived, as the more comprehensive ASTM E1820-96 was introduced in 1997 [41] to replace all previous toughness test standards, including E399, E813, E1152, E1137, and E1290 ($CTOD$ testing). ASTM E1820

recommended the use of SE(B), C(T), and disc-shaped compact tension (DC(T)) specimens with deep cracks ranging from $0.45W$ to $0.70W$ for J and $CTOD$ determinations, while restricting the crack length to $0.45\,W$ to $0.55\,W$ for K determinations. Additionally, it has the following restrictions,

(a) $$\Delta a_{max} \leq 0.25 b_0$$

(b) $$B, b_0 \geq \frac{20 J_{max}}{\sigma_{YS}} \tag{1-20}$$

1.2.2.2. Fatigue Crack Propagation Laws

Beyond the analyses previously outlined in fracture mechanics, the concept of similitude also proves valuable for analysing fatigue cracks. It suggests that the crack tip conditions can be uniquely defined by the crack tip field. Provided that the plastic zone is small enough to remain within the elastic singularity zone, the rate of crack growth during fatigue cycles is predominantly governed by the stress intensity factors that define the fatigue loading, K_{min} and K_{max}. These factors may alternatively be represented by ΔK and stress ratio R, where $\Delta K = K_{max} - K_{min}$, and $R = K_{max}/K_{min}$. This analysis assumes the absence of historical effects on the crack and a constant stress intensity amplitude. Figure 1.10 presents a typical schematic log-log plot illustrating the relationship between crack growth rate and ΔK in metallic fatigue behaviour. The sigmoidal curve consists of three distinct regions, each representing different fatigue crack growth behaviours under varying stress intensity factor ranges. In Region I, the crack growth rate (da/dN) gradually decreases and eventually approaches zero at a threshold ΔK_{th}. In Region II, the crack growth rate follows the exponential 'Paris' relationship, indicating a stable and predictable propagation phase. However, at high ΔK values, the growth rate accelerates due to either microscopic fracture events as K_{max} approaches K_c or crack-tip plasticity effects that limit the applicability of linear elastic fracture mechanics (LEFM).

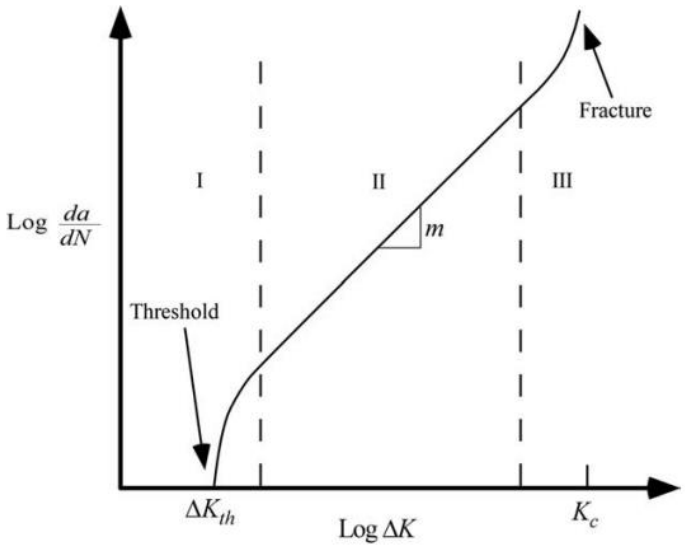

FIGURE 1.10
Typical fatigue crack growth behaviour in metals. (from [14])

Paris and Erdogan [42] introduced the first and most renowned empirical equation for stage II fatigue crack growth, now commonly referred to as the Paris law:

$$\frac{da}{dN} = C\Delta K^m \tag{1-21}$$

where da/dN represents the crack growth rate (length per cycle), C and m are material constants. Further research has indicated that the exponent m typically ranges from 2 to 4 for most metals when not exposed to corrosive conditions. Many researchers have formulated equations that capture either the entire or segments of the sigmoidal relationship between da/dN and ΔK [43-49]. For instance, Klesnil and Lukas [45] adjusted Equation (1-21) to include considerations for the threshold:

$$\frac{da}{dN} = C(\Delta K^m - \Delta K_{th}^m) \tag{1-22}$$

The most widely recognised model describing fatigue crack growth across all three regions was developed by NASA and initially introduced by Forman and Mettu [49], which is expressed as follows:

$$\frac{da}{dN} = C\Delta K^m \frac{1-\left(\frac{\Delta K_{th}}{\Delta K}\right)^p}{1-\left(\frac{K_{max}}{K_c}\right)^q} \tag{1-23}$$

It should be noted that although these equations reflect certain physical considerations, their quantitative relationship is primarily based on empirical evidence. Success in life prediction has been achieved through the integration of these equations. The calculation of the stress intensity factor is performed in the same manner as indicated by test standards, based on remote loading, involving approximations, and relying on the fitting of shape functions.

While crack growth predictions for long cracks, such as the above, are generally well established, the characterisation of short fatigue crack behaviour remains challenging due to its fundamental differences. Figure 1.11 from [50] shows the divergent rate behaviour of short fatigue cracks compared to long crack data. Since most fatigue cracks remain in the short crack regime for a significant portion of their lifetime, improving the understanding of their growth mechanisms is vital for refining predictive models.

Fatigue short cracks can be classified into two types: microstructurally short cracks and mechanically short cracks. Microstructurally short cracks are typically considered to have dimensions on the same order as the grain size of the material, generally within 100 μm. In this regime, the assumption of a homogeneous isotropic continuum no longer holds, and fatigue crack growth is significantly influenced by the microstructure. When the crystallographic features favours crack propagation, the growth rate increases, whereas barriers such as grain boundaries or second-phase particles can impede propagation, potentially leading to crack arrest.

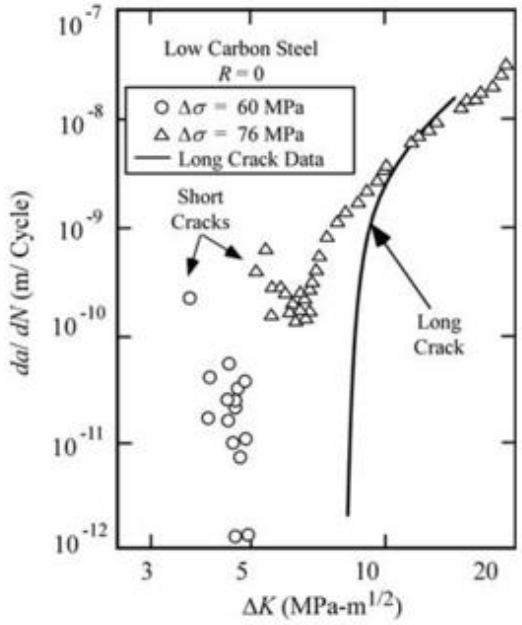

FIGURE 1.11
Rate behaviour of short cracks in a low-carbon steel. (from [50])

Longer short cracks, typically ranging from 100 μm to 1 mm in length, are classified as mechanically short cracks. While their characteristic dimensions satisfy the continuum assumption, they often exhibit higher growth rates than long cracks under the same ΔK, particularly near the threshold. One factor to explain this is that significant crack-tip plasticity alters the local stress field, leading to the breakdown of the elastic singularity at the crack tip [51]. As a result, the crack behaves as if it has a longer effective length [52]. This correction is referred to as the "intrinsic crack length," illustrated in Figure 1.4. Another factor is based on observations of crack closure. This perspective suggests that, at low ΔK values, the closure loads of long cracks are significantly higher [50]. By using an effective ΔK, denoted as ΔK_{eff}, it is possible to eliminate the deviation observed in short fatigue crack data.

In addition to short cracks, the impact of loading history is also an important factor in fatigue. Underloads and overloads, in particular, introduce substantial uncertainties into the calculation of K [53, 54] and affect the performance of those empirical laws, violating their underlying assumptions. These considerations collectively highlight the need for full-field techniques to

measure the actual conditions at the crack tip. Such measurements are essential for the precise and reliable assessment of K, which has long been a critical issue in the fields of fracture and fatigue.

1.2.3. Full-Field Techniques

Measurement is the initial step in evaluating crack-controlling parameters. In the early stages of fracture mechanics, global measurements were the primary data source for evaluating the state of a crack. These measurements typically included load and displacement values at the sample's holding end, as well as the sample geometry and crack length. From these data, local conditions at the crack tip were inferred. However, the introduction of full-field techniques has enabled researchers to directly measure local deformation at the crack tip, providing significantly richer and more direct data. This advancement has the potential to completely transform the methods used to assess the state of a crack.

In contrast to traditional contact methods such as hardness testing [55-57] and compliance techniques [58], early non-contact methods like photoelasticity [59, 60], Moiré interferometry [61-64], and thermoelastic stress analysis [65-67] have gained a certain degree of full-field capability. However, they may lack sufficient resolution for precise crack tip field measurements. This section reviews promising full-field techniques specifically for assessing the crack tip field.

1.2.3.1. Caustics Method

The shadow optical method of caustics was first proposed by Manogg [68, 69] and further developed by Kalthoff [70-72], Theocaris [73, 74], Rosakis [75, 76], and their colleagues. This method is sensitive to the strain gradients around geometrical discontinuities, making it particularly suitable for evaluating the elastic stress intensity factor of a specimen. When illuminated by a light source, the out-of-plane deformation of the specimen surface creates a bright ring, known as the caustic, in the reflected image. Figure 1.12 shows a typical example. The diameter, D, of the caustic is related to the mode I stress intensity factor, as described in [77]:

$$K_I \propto \frac{D^{\frac{5}{2}}}{z_0} \tag{1-24}$$

where z_0 represents the distance between the specimen and the image plane of the caustic.

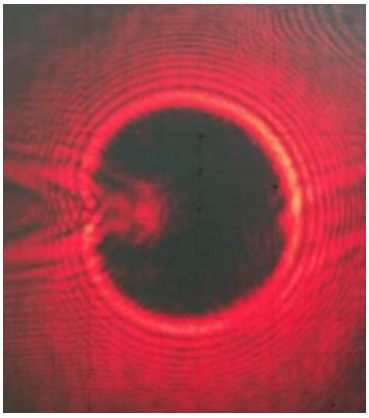

FIGURE 1.12
A typical example of caustic acquired during experiment. [78]

Rosakis and Freund [79] have argued that the J integral can be calculated based on a proportionality to the maximum diameter of the caustic raised to the third power. Bull and Hermann [80] investigated crack closure using the caustic method during a fatigue test. Subsequently, Tomlinson and Patterson [81] examined crack closure by measuring the residual caustic. The primary drawback of this optical caustics method is the challenge of characterising short cracks with relatively small plastic zone sizes.

1.2.3.2. Raman Spectroscopy

Introduced by Anastassakis et al. [82] in 1970, Raman spectroscopy is a non-destructive method extensively used for studying ceramics. Figure 1.13 provides a schematic illustration of Raman spectroscopy and presents an example of an obtained stress map. This technique operates based on inelastic interactions between a penetrating laser beam and the vibrations of the crystal lattice [83]. By measuring the Raman shift, the internal stress within the sample can be determined [84].

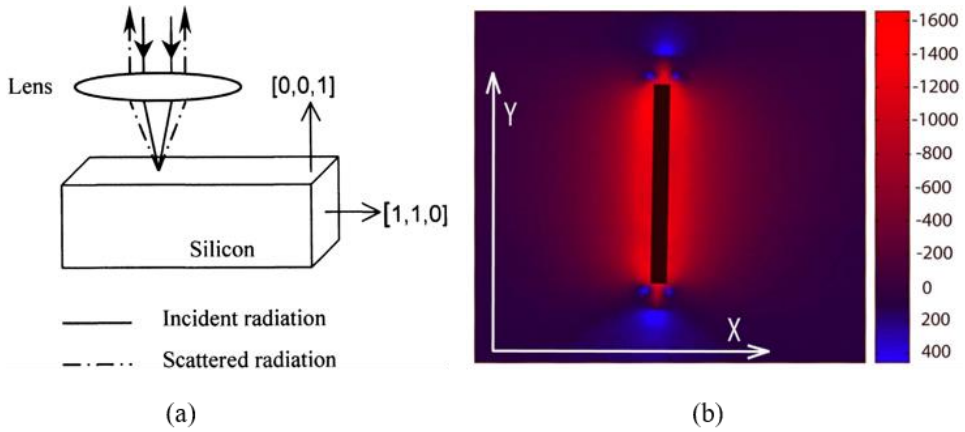

FIGURE 1.13
Stress mapping using Raman spectroscopy: (a) Schematic illustration of backscattering Raman spectroscopy [85]; (b) Stress map of 350 mN wedge indentation in Si obtained using 488 nm excitation wavelength (in MPa) [86].

Raman measurements have been compared with Electron Backscatter Diffraction (EBSD) [86], finite element analysis [87], and atomic force microscopy [88] in silicon-related materials to evaluate accuracy. Confocal Raman microscopy (CRM) is reported to match or trail EBSD by an order of magnitude, but can probe beneath surfaces in transparent materials by tuning wavelength and focus [89], and works in ambient conditions unlike EBSD [86]. Its primary limitation is the Raman activity of the target material. Most materials, particularly metals, are not Raman active, though it has been suggested that adding a silicon layer may enable such measurements, as demonstrated by Zhang et al. in crack tip stress studies on Inconel 617 at high temperatures [90-92].

Applications of Raman spectroscopy in analysing crack tip fields have been documented. Moon et al. [93] measured the localised stress field at the crack tip in a ceramic-metal composite using Raman spectroscopy, comparing the results with finite element modelling to explore crack propagation at the microscale. Pezzotti et al. [94] characterised the microscopic bridging stresses near the crack tip of highly anisotropic silicon nitride using Raman spectroscopy with micrometre spatial resolution.

1.2.3.3. Digital Image Correlation

Many scholars have contributed to the development of Digital Image Correlation (DIC) [95], with the 1983 work by Sutton et al. [96] being an important milestone in the field. They employed white light as an illumination source and used the Sum of Squared Differences (SSD) method to compute displacements, achieving sub-pixel accuracy through bilinear interpolation. Additionally, strain calculations from the displacement gradients were incorporated, contributing to the early establishment of the full-field measurement framework. The basic principle of DIC involves tracking subsets of a pair of images captured before and after deformation, as illustrated in Figure 1.14. The least-squares correlation [97] is an early method, commonly employed for comparing the deformed and undeformed images, which is expressed as:

$$C\left(U_i, \frac{\partial U_i}{\partial x_j}\right) = \sum_{\Delta M} [f^*(x_1^*, x_2^*) - f(x_1, x_2)]^2 \tag{1-25}$$

Here, C represents the correlation function used to compare displacement and strain between the deformed and undeformed images. Specifically, U_i is the displacement in the i-direction (e.g., horizontal or vertical) at a point in the image, while $\frac{\partial U_i}{\partial x_j}$ is the partial derivative of the displacement with respect to the j-direction, which represents the strain field. The summation $\sum \Delta M$ is taken over a small region of interest, known as a subset, which is used to track the local deformation in the image. In this formula, $f^*(x_1^*, x_2^*)$ and $f(x_1, x_2)$ represent the deformed and undeformed images, respectively, at the coordinates (x_1^*, x_2^*) and (x_1, x_2). The goal is to minimise the difference between these two images, thereby obtaining the values of displacement and strain that describe the local deformation of the object. More advanced correlation models extend this basic formulation by incorporating higher-order terms to account for shear and strain gradients across the subset, for example [98]. These improvements enhance the accuracy of the measured

displacement fields, especially in regions with high deformation gradients or nonlinear strain distributions.

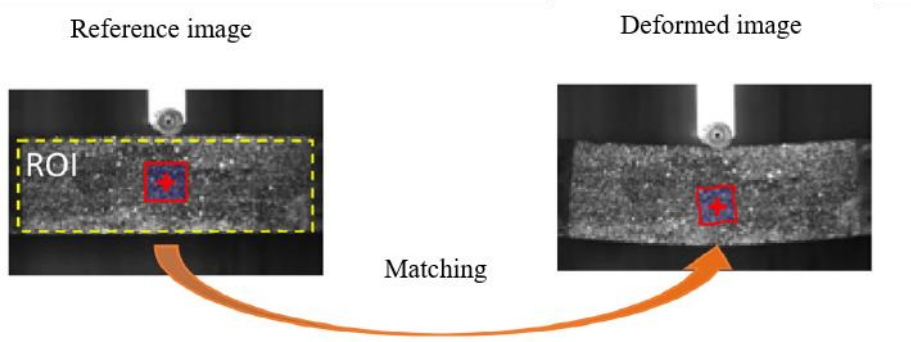

FIGURE 1.14
Tracking subsets between a pair of images. Adapted from [99].

The core of the DIC method lies in the selection of appropriate subsets. A subset is a small region in the image with distinct texture or features, which can be tracked through deformation. The size of the subset plays a critical role in ensuring accurate displacement tracking and strain calculation [99, 100]. By performing the correlation analysis over multiple subsets, DIC provides a full-field displacement and strain map, allowing for a comprehensive analysis of the deformation behaviour of the object.

For reliable and accurate matching, the selected subset must have sufficient intensity variations to be uniquely identified in the deformed image. This requires the test object's surface to be covered with a speckle pattern, either natural (e.g., surface texture) or artificial (e.g., spray-painted patterns). The speckle pattern deforms with the specimen surface during deformation and serves as a key feature for tracking surface deformation in the DIC matching process. It has been observed that DIC displacement accuracy is closely related to speckle pattern quality [101-103], as a well-designed pattern with sufficient contrast and random distribution allows reliable feature recognition and correlation between images. Poor speckle quality can lead to correlation errors, noise amplification, and inaccurate strain measurements, which ultimately compromise the reliability of experimental results.

Figure 1.15 illustrates the typical experimental setups for 2D-DIC and Stereo-DIC. In Stereo-DIC, two cameras are used to retrieve both in-plane and out-of-plane displacements. Figure 1.16 provides a schematic illustration of a subset before deformation (reference) and after deformation (target). A subsequent review underscored the practical applications of this method, evaluating its accuracy and effectiveness [104].

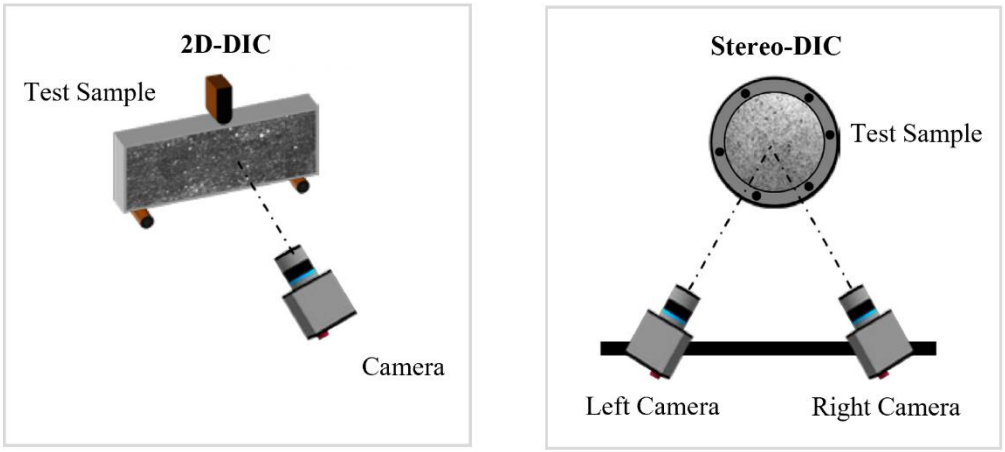

FIGURE 1.15
Typical experimental setups for 2D-DIC and Stereo-DIC. Adapted from [99].

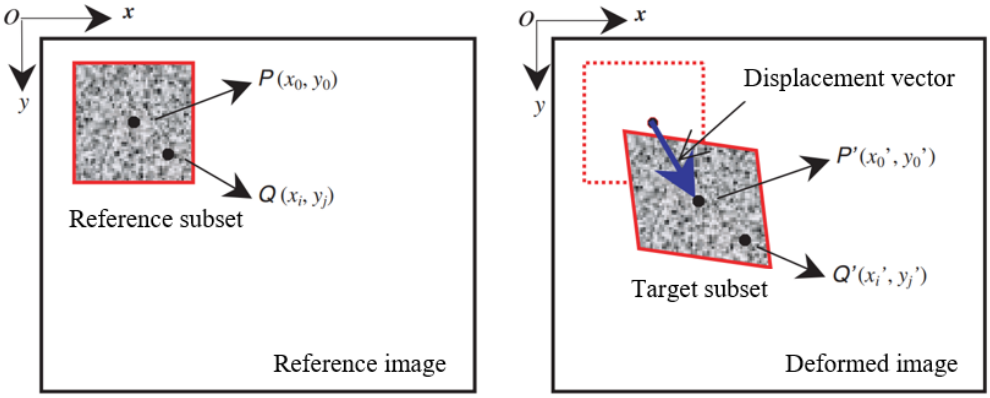

FIGURE 1.16
Reference subset and target subset in DIC. Adapted from [105].

Crack field studies drew early interest from DIC researchers. In 1987, McNeill, Peters, and Sutton [97] used DIC to capture full-field displacements and computed stress intensity factors by fitting them to elastic solutions via least squares. Their work, which compared results with ASTM

standards, introduced a full-field approach to fracture analysis but also noted sensitivity to crack tip positioning.

The method has experienced significant development since its establishment. In 1989, Bruck and Sutton [106] improved computational efficiency by introducing the Newton-Raphson method as an alternative to the Coarse-fine search. Luo et al. [107] later developed a 3D displacement measurement technique using stereo CCD cameras. By 1997, Sun, Lyons, and McNeill [108] integrated DIC with high-magnification optical microscopy. Vendroux and Knauss [109, 110] extended DIC to scanning tunnelling microscopy (STM) in 1998, enabling full-field submicron deformation measurement, advancing its use in micromechanics.

Since 2000, many scholars have made further improvements to the algorithms of DIC and have studied the systematic errors associated with these methods [98, 111-115]. In 2005, Sun et al. [116] introduced a Finite Element-based DIC method, followed by the Q4-DIC method proposed by Besnard, Hild, and Roux [117]. Both approaches later came to be recognised as Global DIC methods. Research by Lecompte, Pan, Sutton, and others [101] subsequently focused on how factors such as speckle quality can impact DIC measurement quality. Around 2009, several review articles [105, 118, 119] comprehensively summarised the principles, applications, and error assessments of DIC, marking the method's growing maturity and adoption.

The development of DIC has facilitated its further application in micromechanics research. Fonseca, Mummery, and Withers [120] have conducted full-field strain mapping based on material microstructures, highlighting the promising prospects of DIC in in situ microscopy. Sutton et al. [121, 122] addressed spatial and drift distortions and published a key report on SEM-DIC, including validations and precision assessments. Members of the same research group, including Li [123], extended this work to full-field thermal deformation measurements under temperature. Tschopp et al. [124] discussed the combined use of SEM-DIC and EBSD techniques in situ experiments. In 2011, Zhu et al. [125] introduced the stereovision SEM-DIC technique. Research

by Kammers and Daly analysed SEM-DIC patterning methods such as Focused Ion Beam (FIB), template, nanoparticle, and e-beam lithography [126], and related errors [127]. In 2013, Carroll et al. [128] applied high-resolution DIC to fatigue crack propagation, while Gioacchino and Fonseca [129, 130] demonstrated plastic strain mapping at sub-micron resolution using SEM-DIC. Figure 1.17 presents a selection of strain plots from these studies. These studies highlight SEM-DIC's value for stress and strain analysis in crystalline materials, especially when integrated with EBSD.

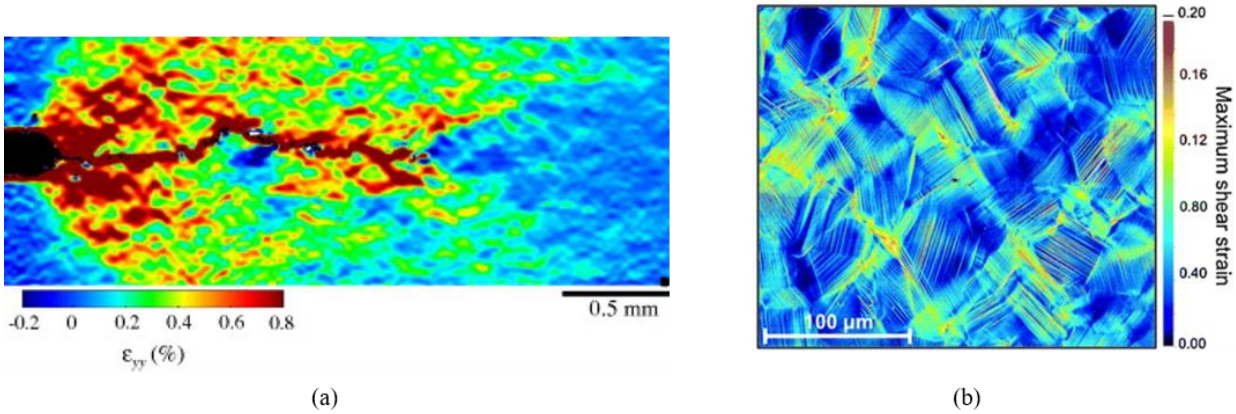

FIGURE 1.17
DIC in micromechanics: (a) An example of strain accumulation in the wake of a propagating fatigue crack using high resolution DIC. [128] (b) Sub-micron strain mapping at 7 % macroscopic elongation using SEM-DIC (subset size $216 \times 216nm^2$) [129].

Since its inception, DIC has been employed for investigating crack tip fields in fracture mechanics, which remains one of the most active areas of DIC application. Section 1.3 will provide a detailed review of crack field parameterisation using DIC, highlighting the critical role of post-processing in these analyses.

1.2.3.4. High Resolution Electron Backscatter Diffraction (HR-EBSD)

Although it emerged in 1973 [131], EBSD began attracting widespread attention since 1993 when it was implemented as an automated technique within a scanning electron microscope [132]. The conventional EBSD setup is shown in Figure 1.18. A polished crystalline specimen is typically tilted 70° to enhance backscattered electron contrast. A high-energy electron beam (typically 20 kV) is focused on a small region of the sample surface, achieving a spatial resolution of up to

approximately 20 nm. The backscattered electrons interact with the crystal's atomic planes and diffract according to Bragg's law, generating Kikuchi lines of varying intensity. These lines are recorded on an electron-sensitive screen to form Kikuchi bands, or EBSD patterns. These patterns are effectively used to measure strain due to their sensitivity, as detailed in references [133, 134].

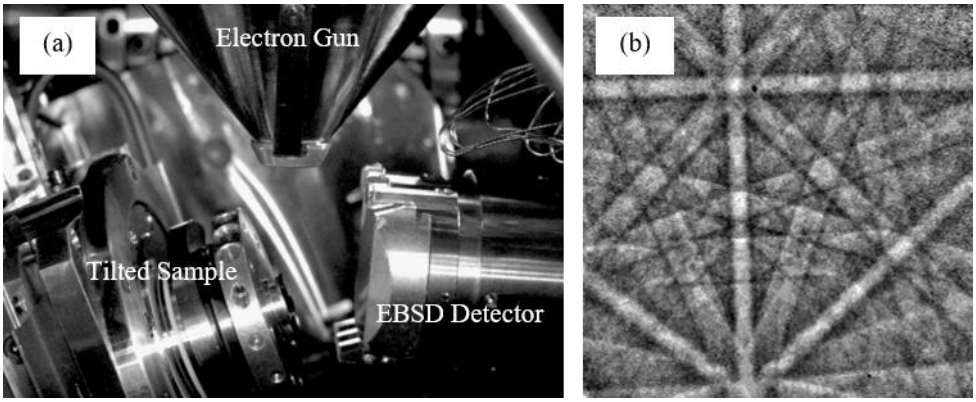

FIGURE 1.18
Capturing patterns: (a) EBSD setup: view inside the SEM chamber. (b) Raw EBSD Pattern.

Wilkinson [135] improved the angular resolution of EBSD detectors by using a larger specimen-to-screen distance. In 2006, Wilkinson, Meaden, and Dingley [136, 137] reported a method using cross-correlation to accurately detect shifts in zone axes within patterns, using wide-angle EBSD patterns to quantify both strain and lattice rotations with improved accuracy. The proposed procedure is outlined in Figure 1.19. Multiple regions of interest (ROIs) are extracted from the electron backscatter patterns, then normalised and filtered to eliminate long-range gradients and high-frequency noise. Cross-correlation functions (XCF) are calculated for each ROI to determine the image shifts relative to a reference pattern. Strain and rotation, derived from the deformation gradient tensor, are calculated based on the geometrical relationships shown in Figure 1.20, aggregating shifts from numerous ROIs.

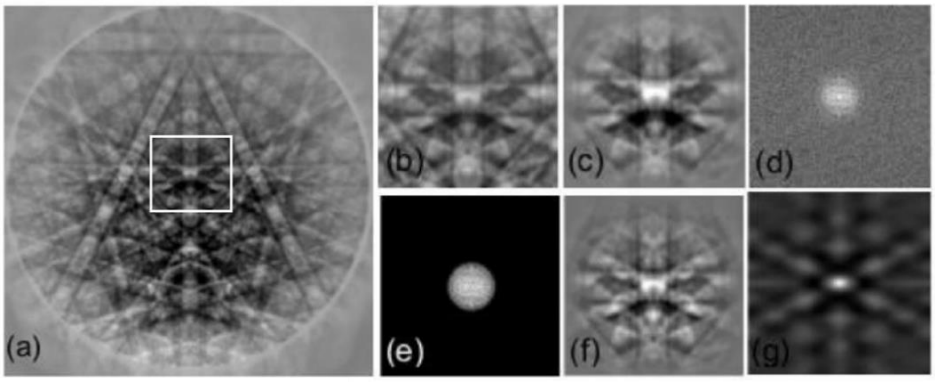

FIGURE 1.19
Pattern processing: (a) an EBSD pattern from GaN; (b) subtracting the ROI; (c) removing background intensity; (d) applying fast Fourier transform; (e) filtering low and high-frequency noise; (f) transforming the ROI back to the real domain; (g) correlation with the reference pattern. Adapted from [138].

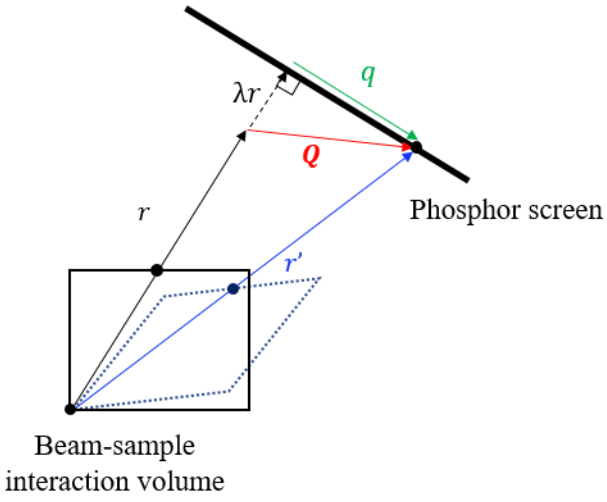

FIGURE 1.20
Shift in an EBSD pattern between the reference and deformed states.

Specifically, the deformation gradient tensor $\boldsymbol{\beta}$ is also the mapping function, which relates the zone axis vectors $\boldsymbol{r}$ and $\boldsymbol{r}'$ between the reference and test patterns:

$$\boldsymbol{r}' = \boldsymbol{\beta}\boldsymbol{r} = \boldsymbol{Q} + \boldsymbol{r} \tag{1-26}$$

$\boldsymbol{\beta}$ can also be considered as the sum of the displacement gradient tensor, $\boldsymbol{A}$, and the identity matrix $\boldsymbol{I}$:

$$\boldsymbol{\beta} = \boldsymbol{A} + \boldsymbol{I} = \begin{bmatrix} \frac{\partial u_x}{\partial x} & \frac{\partial u_x}{\partial y} & \frac{\partial u_x}{\partial z} \\ \frac{\partial u_y}{\partial x} & \frac{\partial u_y}{\partial y} & \frac{\partial u_y}{\partial z} \\ \frac{\partial u_z}{\partial x} & \frac{\partial u_z}{\partial y} & \frac{\partial u_z}{\partial z} \end{bmatrix} + \begin{bmatrix} 1 & 0 & 0 \\ 0 & 1 & 0 \\ 0 & 0 & 1 \end{bmatrix} \tag{1-27}$$

Equation (1-26) can be written as

$$\begin{bmatrix} x' \\ y' \\ z' \end{bmatrix} = \left(\begin{bmatrix} \frac{\partial u_x}{\partial x} & \frac{\partial u_x}{\partial y} & \frac{\partial u_x}{\partial z} \\ \frac{\partial u_y}{\partial x} & \frac{\partial u_y}{\partial y} & \frac{\partial u_y}{\partial z} \\ \frac{\partial u_z}{\partial x} & \frac{\partial u_z}{\partial y} & \frac{\partial u_z}{\partial z} \end{bmatrix} + \begin{bmatrix} 1 & 0 & 0 \\ 0 & 1 & 0 \\ 0 & 0 & 1 \end{bmatrix} \right) \begin{bmatrix} x \\ y \\ z \end{bmatrix} \tag{1-28}$$

where xyz are the coordinates of the end point of the vector r and x′y′z′ are the coordinates of the end point of the vector r'. Geometrically, $q = Q - \lambda r$ where λ is an unknown constant, thus

$$q_x = \frac{\partial u_x}{\partial x} x + \frac{\partial u_x}{\partial y} y + \frac{\partial u_x}{\partial z} z - \lambda \mathrm{x} \tag{1-29}$$

$$q_y = \frac{\partial u_y}{\partial x} x + \frac{\partial u_y}{\partial y} y + \frac{\partial u_y}{\partial z} z - \lambda \mathrm{y} \tag{1-30}$$

$$q_z = \frac{\partial u_z}{\partial x} x + \frac{\partial u_z}{\partial y} y + \frac{\partial u_z}{\partial z} z - \lambda \mathrm{z} \tag{1-31}$$

Combining pairs of these equations, the following can be obtained

$$xz\left(\frac{\partial u_x}{\partial x} - \frac{\partial u_z}{\partial z}\right) + yz\frac{\partial u_x}{\partial y} + z^2\frac{\partial u_x}{\partial z} - \mathrm{x}^2\frac{\partial u_z}{\partial x} - yx\frac{\partial u_z}{\partial y} = zq_x - xq_z \tag{1-32}$$

$$yz\left(\frac{\partial u_y}{\partial y} - \frac{\partial u_z}{\partial z}\right) + xz\frac{\partial u_y}{\partial x} + z^2\frac{\partial u_y}{\partial z} - \mathrm{xy}\frac{\partial u_z}{\partial x} - \mathrm{y}^2\frac{\partial u_z}{\partial y} = zq_y - yq_z \tag{1-33}$$

Shifts are only measured in the phosphor screen, thus $q_z = 0$, therefore

$$x\underline{\left(\frac{\partial u_x}{\partial x} - \frac{\partial u_z}{\partial z}\right)} + y\underline{\frac{\partial u_x}{\partial y}} + z\underline{\frac{\partial u_x}{\partial z}} - \frac{\mathrm{x}^2}{\mathrm{z}}\underline{\frac{\partial u_z}{\partial x}} - \frac{yx}{z}\underline{\frac{\partial u_z}{\partial y}} = q_x \tag{1-34}$$

$$y\underline{\left(\frac{\partial u_y}{\partial y} - \frac{\partial u_z}{\partial z}\right)} + x\underline{\frac{\partial u_y}{\partial x}} + z\underline{\frac{\partial u_y}{\partial z}} - \frac{\mathrm{xy}}{\mathrm{z}}\underline{\frac{\partial u_z}{\partial x}} - \frac{\mathrm{y}^2}{\mathrm{z}}\underline{\frac{\partial u_z}{\partial y}} = q_y \tag{1-35}$$

There are eight unknowns in these equations (underlined), requiring four independent q_x and q_y measurements from the diffraction pattern to solve them. Although this procedure extracts the full rotation matrix, one degree of freedom in the strain tensor remains undetermined. Since EBSP forms near the surface, the traction-free boundary condition provides an additional equation, i.e. $\sigma_{zz} = 0$. Combined with the computed values of $\left[\frac{\partial u_x}{\partial x} - \frac{\partial u_z}{\partial z}\right]$ and $\left[\frac{\partial u_y}{\partial y} - \frac{\partial u_z}{\partial z}\right]$, this equation allows the missing component to be resolved. Using infinitesimal strain theory, the deformation gradient is decomposed into elastic strain (ε_{ij}, symmetric part) and lattice rotations (ω_{ij}, asymmetric part)

$$\varepsilon_{ij} = \frac{1}{2}(A_{ij} + A_{ij}^T) \tag{1-36}$$

$$\omega_{ij} = \frac{1}{2}(A_{ij} - A_{ij}^T) \tag{1-37}$$

This cross-correlation based method has demonstrated the ability to measure shifts between similar features in EBSD patterns with a precision of ± 0.05 pixels, corresponding to a strain measurement sensitivity of 2×10^{-4}.

Similar algorithms have been explored by other groups [139-141]. In 2011, Britton et al. [142] observed that cross-correlation may fail in certain areas of EBSPs during significant rotational changes and introduced a robust iterative fitting routine. Around the same time, Maurice et al. [143] and Britton et al. [144] independently proposed pattern remapping to improve small strain measurements amidst larger lattice rotations in plastically deformed metals.

Conventional HR-EBSD, using a reference point within the field of view, only allow for the measurement of relative elastic strains, not absolute strains. Britton et al. [145, 146] explored using simulated patterns for absolute strain and rotation, highlighting challenges from simulation quality, pattern centre uncertainties, aberrations, and variability in sample location. To address these challenges, Karamched and Wilkinson [147] proposed offsetting HR-EBSD data with Finite Element Models (FEM)-derived average strains. Other methods include co-correlated strained

patterns [148], reference selection algorithms [149], and using annealed materials as references [150]. HR-EBSD data has also been correlated with Crystal Plasticity Finite Element (CPFE) model results [151, 152]. Recent in-situ studies measured elastic strains in micro-pillars of tungsten [153], FeMnSi [154] and single crystal silicon wafer [155], confirming the complementary strengths of HR-EBSD and in situ micromechanical testing for microscale strain analysis. Some of these cases will be discussed in more detail later.

Besides elastic strain measurement, quantifying plastic activity remains a key research focus. EBSD cannot directly measure plastic strain, but early attempts inferred it from pattern blurring. With automated mapping, efforts have been made to correlate plastic deformation with crystal misorientation. Adams et al. [156] utilised Nye's theory to estimate Geometrically Necessary Dislocation (GND) densities near grain boundaries in polycrystalline samples, while Field et al. [157] later applied this to single crystals. Pantleon [158] improved the method by calculating six components of the lattice curvature tensor from conventional EBSD data. Additionally, Demir et al. [159] used 3D-EBSD to reconstruct the full GND tensor by incorporating both in-plane and out-of-plane rotational gradients. HR-EBSD further improved precision; Wilkinson et al. [160] reported GND density estimates accurate to $\pm 10^{12} m^{-2}$ at $200nm$ step size, and later examined the effects of detector binning and step size on GND measurements [161].

Comparison studies have shown strong agreement between HR-EBSD and confocal Raman microscopy [86] through stress mapping near indentations, as well as with atomic force microscopy (AFM) [162], where EBSD-derived surface profiles matched AFM topography. These results highlight the high precision of HR-EBSD strain and displacement gradient measurements. The applications of HR-EBSD span various key areas: fatigue cracks in nickel [163], residual plastic strain from thermomechanical heat treatment of Ti–6Al–4V [164], indentation in iron [160] and titanium [165, 166] and thermal and mechanical loading of Ni containing hard inclusions [147, 167]. Jiang et al. [168] and Zhang et al. [169] used HR-EBSD to study fatigue crack nucleation

in Ni-based superalloys. Jiang et al. [168] linked crack initiation to localised residual stress and GND density evolution, while Zhang et al. [169] quantified pre-existing stress near non-metallic inclusions. Figure 1.21, from Zhang's work [169], shows HR-EBSD capturing stress and GND localisation within a single grain before and after cyclic loading, emphasizing damage development in relation to microscale features.

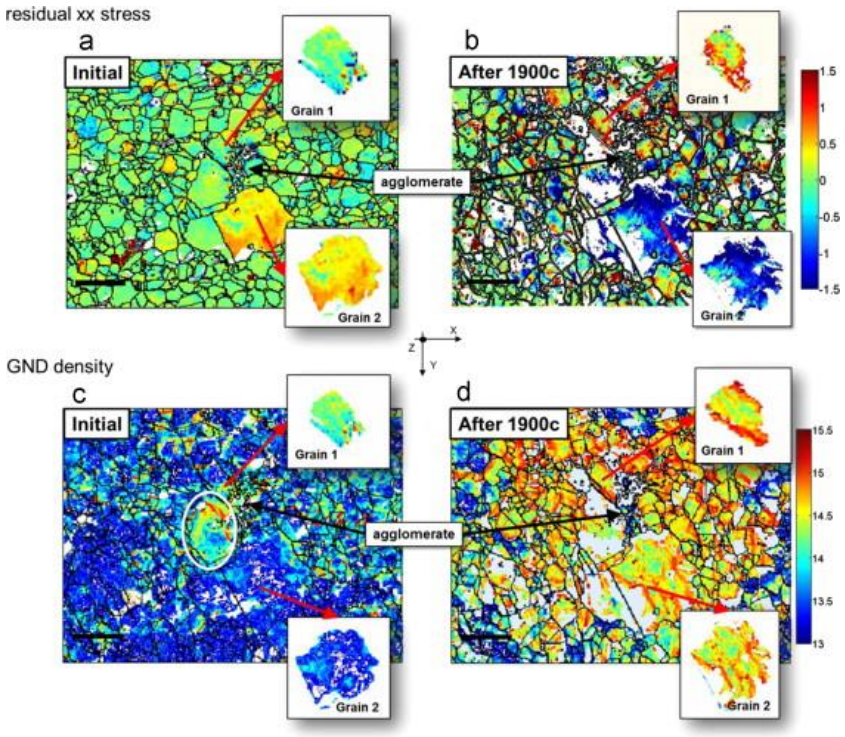

FIGURE 1.21
Field plots of HR-EBSD measured in-plane xx stress (GPa) (a) before and (b) after 1900 loading cycles, with grain boundaries marked in black. GND density maps ($\log_{10}$(GND density in m^2)) (c) before and (d) after fatigue. Two surrounding grains are selected for further analysis. Scale bar: 12.5 μm.

HR-EBSD has been used to investigate stress evolution and dislocation behaviour at crack tips in semi-brittle materials. In-situ microcantilever testing on tungsten single crystals [170] revealed that stress gradients and dislocation pile-ups influence local strengthening, while dislocation emission from the crack tip leads to finite crack tip blunting. As shown in Figure 1.22 from this study, HR-EBSD effectively resolves crack-tip stress and GND density evolution, highlighting its high-resolution capability for tracking stress localisation and dislocation activity.

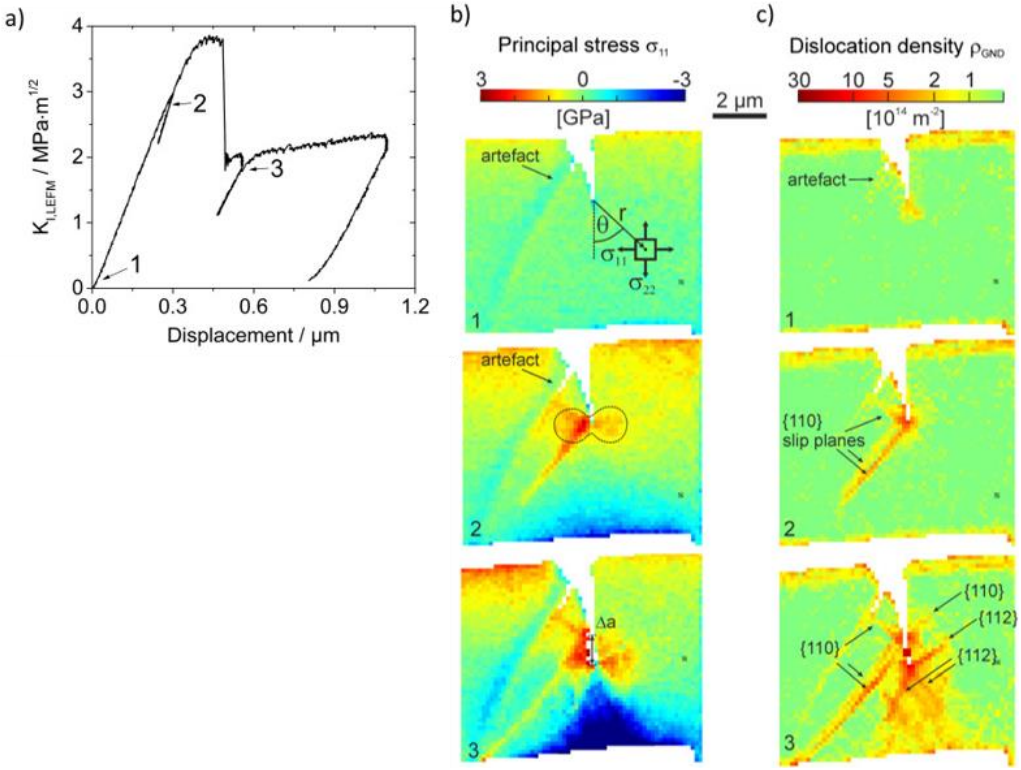

FIGURE 1.22
(a) Stress intensity factor as a function of the indenter displacement, with numbered points indicating EBSD analysis locations. (b) Principal stress and (c) GND density near the crack at three stages: (1) before testing, (2) end of elastic loading, and (3) after crack initiation. Taken from [170].

1.2.3.5. Tomography and Digital Volume Correlation (DVC)

Tomography is an imaging technique that employs a penetrating source (usually X-rays) to acquire 3D datasets by reconstruction of sections. While a detailed review of the advancement of imaging techniques is beyond the scope of this thesis, further information can be referenced in [171]. Advances in synchrotron X-ray sources now enable spatial resolutions below 100 nm. Imaging speed has also improved, allowing radiographs and 3D images within seconds. Techniques such as 3D X-ray Diffraction (3D-XRD), diffraction contrast tomography (DCT), and X-ray Absorption Near Edge Structure (XANES) enable simultaneous mapping of crystallographic orientation and chemical variations.

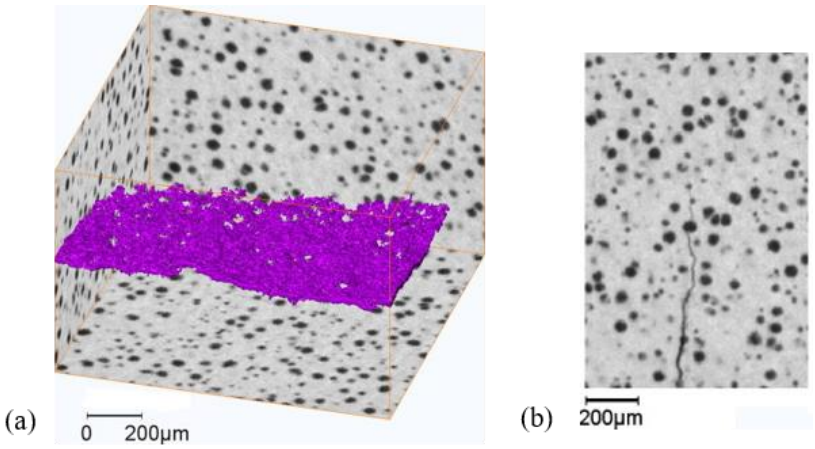

FIGURE 1.23
Tomography image: (a) 3D rendering of the crack surface in nodular graphite cast iron. (b) A section through the image. [172]

For this thesis, emphasis is placed on the evolution of damage and the acquisition of full-field data. Digital volume correlation (DVC) shares concepts with DIC but is specifically developed for measuring volumetric displacements. Bay et al. [173] first applied DVC in 1999 to study continuum-level strain fields in trabecular bone. Since then, improved correlation methods have been introduced [174-176], with the global approach receiving particular focus. DVC-based analysis has been extensively applied to study the deformation of various materials, including both laboratory and synchrotron tomography images of polymer foams [177-179], rock wool [180], wood [181], granular materials [182], and geomaterials [183, 184]. It is important to note that the implementation requires a distributed feature (usually a natural part of the microstructure) as the speckle pattern in the specimen.

Tomography is ideal for crack studies due to its 3D nature. Early fracture research used computed tomography (CT) to observe crack closure [185], though pre-DVC analyses relied on particle tracking, lacking full-field resolution. Toda et al. [186, 187], performed in situ observations of cracks using microstructural pores as displacement markers to estimate stress intensity factors (SIFs), as shown in Figure 1.24. Crack driving forces were estimated for pairs of micro-pores by fitting analytical solutions. Research by Marrow et al. [188] has explored the early stages of fatigue

crack nucleation and reported on crack arrest by microstructural barriers. Applications extend to composites [189], cast iron [190, 191], Aluminium Lithium Alloy [192], and Al-SiC [193].

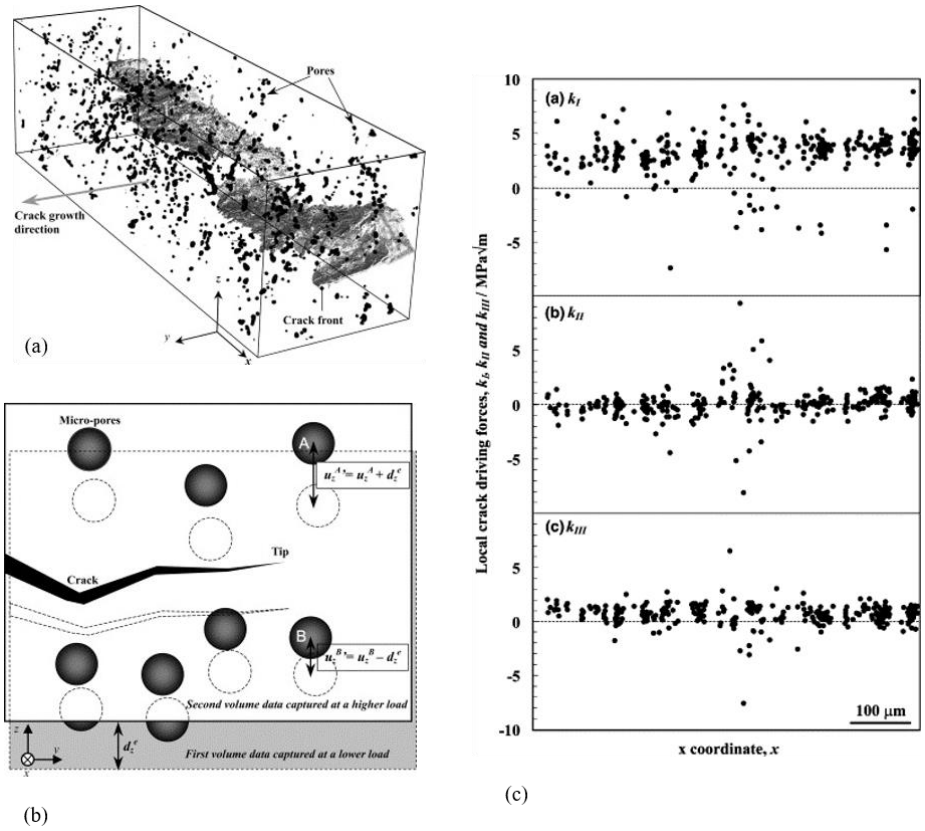

FIGURE 1.24
(a) 3D view of a crack and pore distribution in the analysed sample volume. (b) Schematic illustration of the bipolar separation of the mode I local stress intensity factor measured at each micro-pore. (c) Variations of modes I, II and III local crack driving forces along the crack front line. Reproduced from [186].

With DVC, full-field crack tip measurements became possible. Barranger et al. [194] validated DVC results against simulations. Limodin et al. [190] utilised DVC to study fatigue crack closure and evaluate SIFs by fitting theoretical solutions. This work was later extended to link DVC-derived SIFs with crack growth rates [191] and finite element results [172]. The 2010 study by Rannou et al. [172] covers aspects such as crack tip displacement fields, crack geometry analysis, crack modelling, and stress intensity factor estimation (see Figure 1.25). Withers et al. [195] combined synchrotron X-ray diffraction and imaging to evaluate crack tip fields, determining SIFs via crack opening displacement (COD).

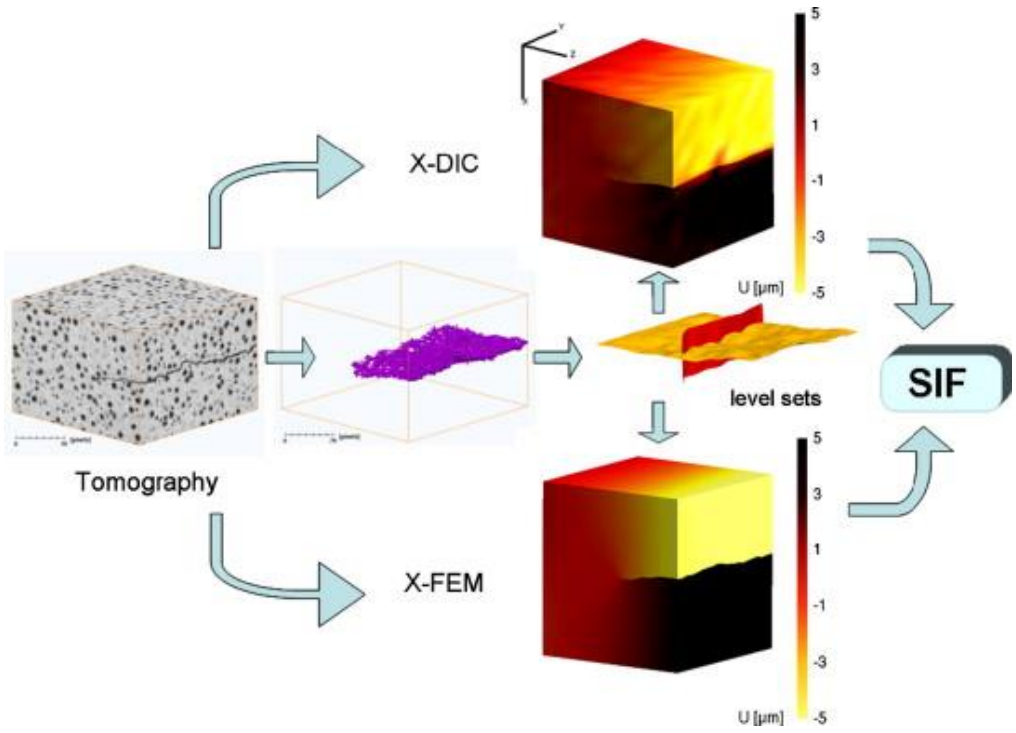

FIGURE 1.25
Schematic of the methods used in [172] for determining stress intensity factors by computed tomography.

The propagation of short fatigue cracks is influenced by microstructure. In 2011, King et al. [196] integrated Diffraction Contrast Tomography (DCT) and microtomography to study this in magnesium alloys. DCT is a non-destructive, 3D technique that maps grain shape and crystal orientation. It enables the study of fatigue crack growth by characterizing the undamaged microstructure. In contrast, FIB-based methods are restricted to small volumes and post-failure analysis.

Subsequently, in 2014, Marrow et al. [188] further utilised DVC to extract three-dimensional displacement fields from sequential X-ray tomography datasets, enabling quantification of local crack opening displacements and the corresponding opening modes. This provided the first full-field 3D measurement of mixed-mode crack opening in a short fatigue crack, enhancing the understanding of crack dynamics within these complex microstructures.

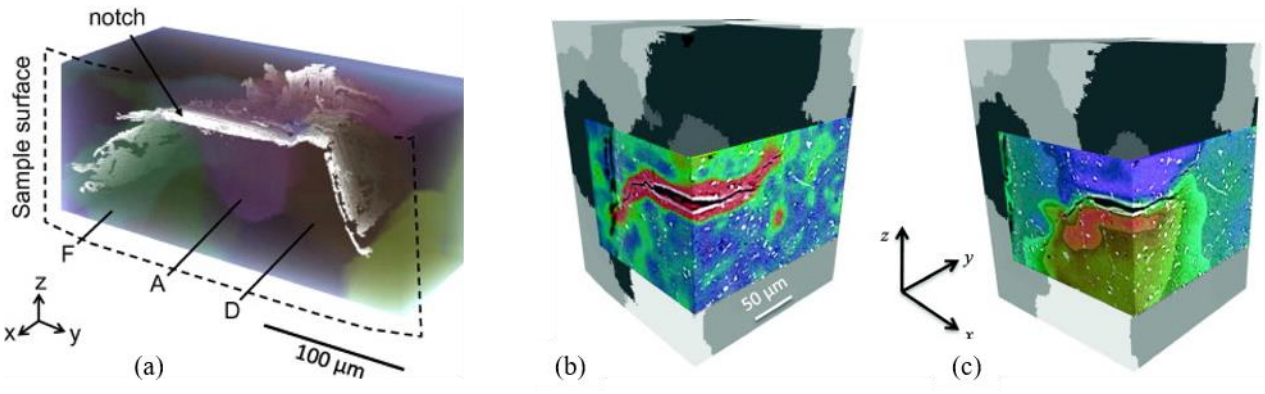

FIGURE 1.26
(a) 3D rendering showing the crack (white) and the grains (coloured). [196] (b) *z*-displacement and (c) maximum principal strain visualisations of DVC measurement of crack opening behaviour on the orthogonal planes. [188]

When combined with finite element analysis, DVC holds promising potential in the field of fracture mechanics. For example, in materials such as graphite that provide a good 3D speckle pattern, DVC has been utilised to investigate fracture behaviour under complex stress conditions and to assess performance degradation [197-199]. This approach enriches our understanding of material responses and aids in enhancing structural integrity assessments. It is important to note that the displacements obtained by DVC provide the total strain without directly distinguishing between elastic and plastic strain components. In 2015, Mostafavi et al. [200] demonstrated the potential of integrating DVC with inverse modelling methods in ductile metals to evaluate material yield strength and strain-hardening properties in a nano-tomography study of a nano-indentation in oxide dispersion strengthened (ODS) steel. This study underscores the capabilities of DVC in providing comprehensive insights into the mechanical behaviour of materials under varying conditions.

1.3 Determination of Crack-Controlling Parameters

As noted, image correlation has been used to study crack tip fields since its early development, with SIFs commonly calculated by fitting theoretical solutions. Most early work relied on 2D surface displacement fields. Chiang and Asundi [201] were among the first to propose determining

the SIFs by comparing measurements with known field function. Subsequently, Huntley and Field [202] employed least squares methods: both were based on speckle photography. Abanto-Bueno and Lambros evaluated SIFs in functionally graded materials [203] and compared them to far-field values. Roux and Hild [204] and Onekama et al. [205] independently introduced integrated DIC-based approaches in 2006. Lopez-Crespo et al. [206] extended this to mixed-mode fatigue using a Muskhelishvili-based method without speckle patterns. In 2009, Roux et al. [118] proposed using specific terms from theoretical solutions to infer the positions of crack tips. These studies have progressively enhanced the performance of fittings through better understanding of SIF solutions.

As a result, SIF analysis is becoming more widely applicable. Applications such as crack closure [207], mixed-mode loading [208] and fatigue cyclic loading [209, 210] have demonstrated the high local precision of this approach. The previous section also reviewed similar works in DVC research. However, the accuracy of this method depends on precise crack tip determination [206]. Both DIC and DVC can struggle to measure displacement fields near the crack tip when sharp discontinuities and crack-tip singularities are present [211].

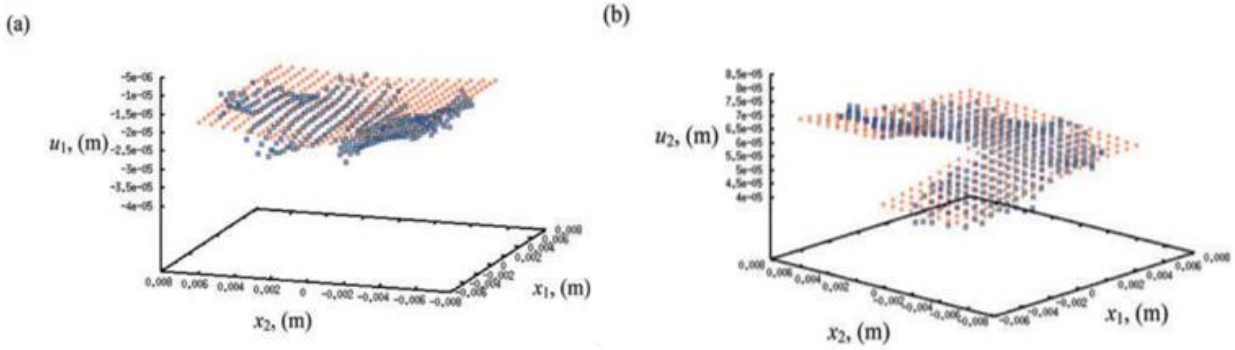

FIGURE 1.27
Field fitting approach: representative horizontal, u_1 (a) and vertical, u_2 (b) displacement vectors measured (blue) by DIC plotted alongside those (red) derived from the best fit to the whole displacement field. [209]

In addition to fitting strain or displacement fields, an alternative framework involves direct integration from full field data. In 2005, Réthoré et al. [212] applied an interaction integral to DIC data, showcasing an early method of leveraging comprehensive field data. Becker et al. [213, 214] introduced a novel Finite Element (FE)-based method that uses the DIC-obtained displacement

field as input for finite element calculations to assess the *J* integral and stress intensity factors, as shown in Figure 1.28. Unlike theoretical fitting methods, this approach applies to both elastic and elastic-plastic materials and is less sensitive to crack tip location. This is particularly advantageous for materials that are damaged by microcracking, where determining the exact crack tip position is challenging.

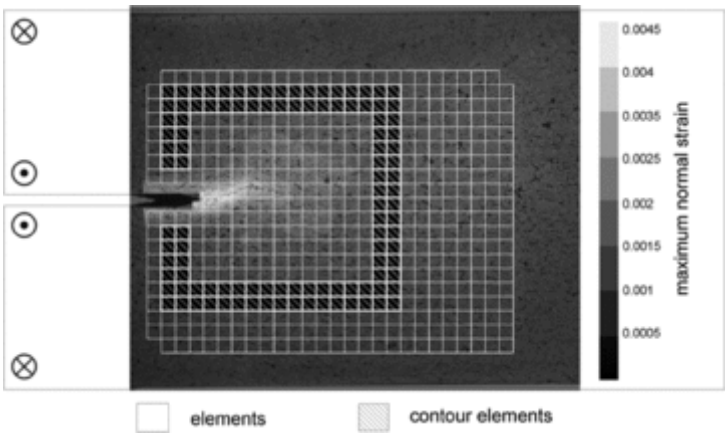

FIGURE 1.28
Double-Torsion (DT) specimen. Shown are the surface displacement field, FE elements and area contour elements used to calculate *J* (specimen is not to scale). Taken from [214].

In 2016, Barhli et al. [215] expanded the application of this method to strain-only data obtained from X-ray diffraction. In 2017, Barhli et al. [216] then utilised standardised finite element software to perform *J* integral calculations, which were easier to implement and capable of handling missing and noisy data. By 2020, Becker et al. [217] were using 3D data acquired through DVC to calculate the *J* integral. However, unlike DIC, displacements measured by DVC tend to have higher error levels, typically ranging from 0.05 to 0.1 voxels, due to its reliance on the natural feature distribution for correlation, which is often not optimal. To address this issue, Becker and Marrow [218] introduced a FE-based filter in 2021, effectively reducing the disturbance caused by imperfections in the displacement data. Koko et al. [219] conducted a comparative study of a long fatigue crack using deformation fields from strains obtained by EDXD (Energy-Dispersive X-ray Diffraction) and displacements by DIC.

Full-field measurements obtained through DIC and DVC in the literature have an additional limitation: they are unable to accurately capture sharp crack tip features. This poses a challenge for micro-scale, high-resolution investigations of crack tip fields. In this context, HR-EBSD presents a promising alternative for such analyses. More recently, Koko et al. utilised strain (i.e. displacement gradient) fields obtained from HR-EBSD as input to investigate the local boundary conditions of twins [220] and slip bands [155]. This method has also been applied to quantify the crack tip fields of cleavage cracks in silicon in 3D and to study quasi-static, mixed-mode conditions of critical cracks at the microscale [155], as shown in Figure 1.29. Depending on the application, HR-EBSD postprocessing can involve either integration of the strain field to reconstruct the full displacement field, which is subsequently used as boundary conditions in finite element (FE) models, or direct evaluation of the J-integral and stress intensity factors from the measured deformation gradients. Each approach has its own advantages and limitations: while displacement reconstruction enables flexible input to numerical models, direct evaluation offers a more immediate, though often noisier, route to fracture parameters.

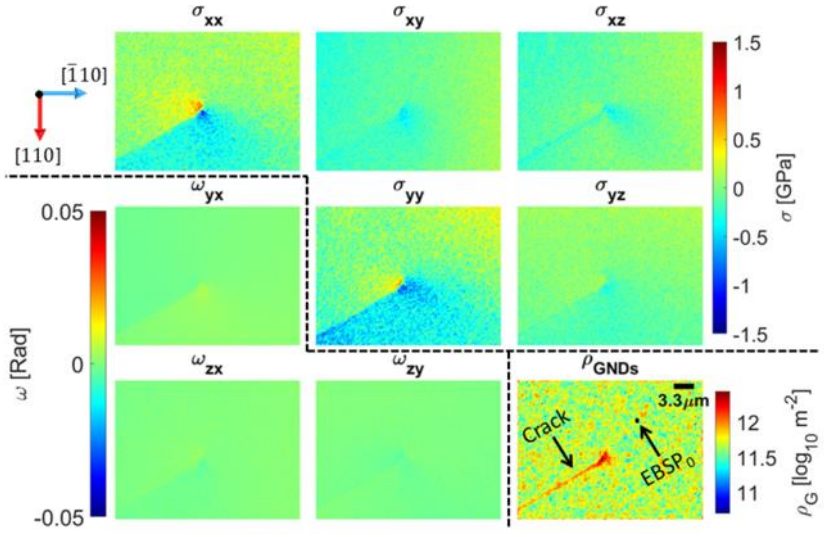

FIGURE 1.29
Example HR-EBSD data: elastic stress components (σ_{ij}), rotation (ω_{ij}) and geometrically necessary dislocation (GND) density (ρ_{GNDs}) calculated in the microscope reference frame, showing high normal stresses in the surface plane. Taken from [155].

These research efforts demonstrate that local full-field measurements not only overcome geometric constraints and directly capture actual conditions at the crack tip but also enable the characterisation of local crystallographic features, offering a comprehensive and detailed depiction of deformation and fracture behaviours. This provides a promising approach for analysing crack fields and crack propagation.

1.4 Short Fatigue Cracks

The study of short fatigue cracks is an active and important area of research, given that these cracks can account for a considerable portion of the total fatigue life of an engineering component. Short fatigue cracks exhibit significant variability in their growth rates, and their behaviour shows a situation where plastic activity and fracture mechanisms interact. The surrounding microstructure strongly influences the crack tip field. Short fatigue crack propagation is predominantly a localised phenomenon, making it challenging to determine the driving forces of the crack from remote boundary conditions. This complexity makes it an ideal topic for exploration in this thesis.

Pearson [221] first linked the unexpected growth rates of short cracks to microstructural effects. Tokaji [222] further classified short cracks as microstructurally or mechanically short, as discussed in Section 1.2.2.2. In the 1980s, research focused on how grain boundaries impede slip activity and how crack closure causes retardation. Ohr [223] reviewed Transmission Electron Microscopy (TEM) observations of dislocation formation and motion at the crack tip, providing valuable insights that significantly supplemented modelling efforts. The Navarro model [224] emphasised the resistance to slip at grain boundaries as the dominant factor, successfully predicting variations in short fatigue crack growth rates. Building on these works, Sadananda and Vasudevan [225] proposed a unified model for short and long cracks, assuming that equivalent crack tip driving forces yield similar propagation rates.

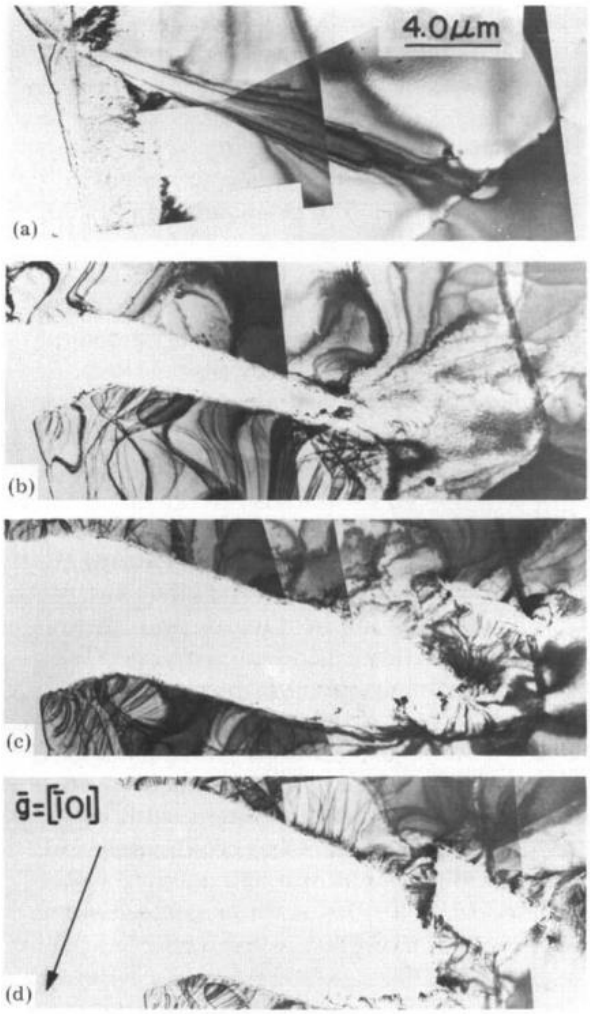

FIGURE 1.30
A series of early electron micrographs showing the interaction between a crack and a grain boundary in molybdenum. As the crack approached the boundary, a small crack was nucleated and eventually joined the main crack. [223]

Additional observations addressed the role of crystallographic features. In 1994, Boyd-Lee and King accomplished the 3D reconstruction of microstructures in the vicinity of cracks through SEM sectioning [226]. Zhai, Wilkinson, and Martin [227] utilised EBSD to determine grain orientations and slip plane traces, elucidating how the twist and tilt angles of the crystallographic crack plane at grain boundaries act as the major factors. Subsequent work of Zhai established a crystallographic model [228]. Sugeta et al. [229] utilised Atomic Force Microscopy (AFM) for microscopic observation of the growing fatigue crack in silicon iron. In their experiment, fatigue cracks were observed to propagate along primary slip planes and undergo deflection or kinking when slip was restricted. Meanwhile, physically meaningful dislocation models were gradually developed. A

1991 study by Pippan [230, 231] proposed a model where dislocation emission and crack growth thresholds are governed by dislocation dynamics, emphasizing dislocation interactions in crack propagation. Wilkinson and Roberts [232] described crack advance via dislocation motion during loading/unloading. Cleveringa et al. [233] demonstrated a discrete dislocation analysis. Bjerkén and Melin [234] employed the discrete dislocation method to model dislocation pile-ups at the grain boundary.

The use of synchrotron X-ray tomography and FIB tomography marked a new phase in short fatigue crack research. In 2003, Ludwig et al. [235] utilised synchrotron X-ray microtomography (μXCT) to study the interactions between short cracks and grain boundaries in cast aluminium alloys. In this study, EBSD was employed to determine the grain orientations on the sample surfaces. An interrupted fatigue test was conducted, and the crack growth was monitored at intervals ex situ. In 2007, Holzapfel [236] used FIB tomography to study the interactions of cracks with precipitates and grain boundaries. Schäf et al. [237] utilised FIB Tomography to analyse how crystallography at grain boundaries impedes short crack propagation.

Furthermore, in situ observations highlight the advantages of X-ray tomography. In 2004, Marrow et al. [238] used synchrotron X-ray tomography to observe the early stage nucleation of short fatigue cracks in an austempered ductile cast iron, and data on crack propagation rates were also obtained. Tomography images from this work are shown in Figure 1.31. In 2005, Ferrié et al. [239] achieved three-dimensional visualisation of short fatigue cracks in cast aluminium alloys using high-resolution X-ray tomography. The study utilised the Ga infiltration technique to enhance the visibility of grain boundaries. Buffière et al. [240] reviewed the use of high-resolution μXCT for the 3D characterisation of metal fatigue cracks. In 2009, Birosca [241] utilised X-ray microtomography combined with EBSD to achieve three-dimensional characterisation of fatigue cracks in Ti-6246, demonstrating the strong dependence of crack paths on the microstructure.

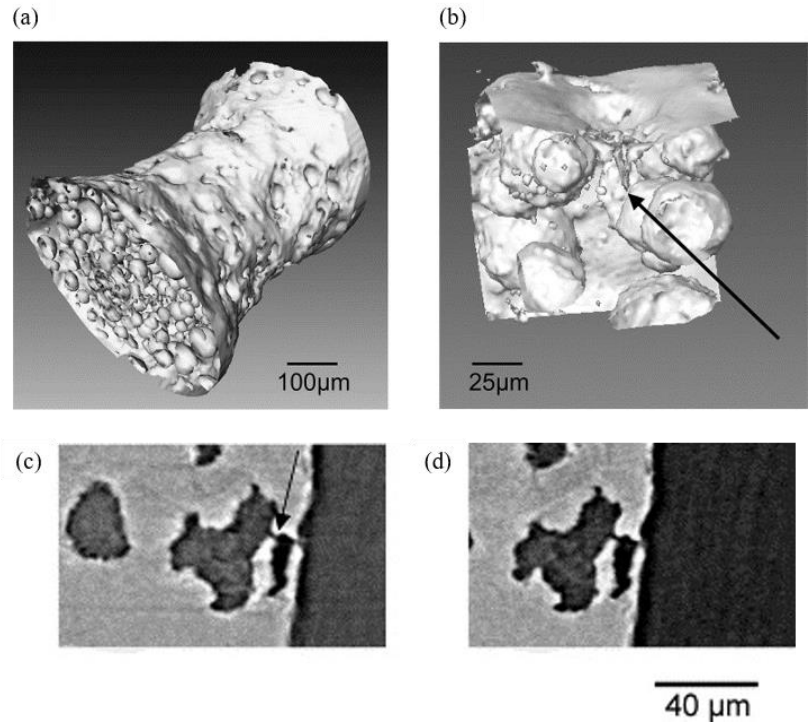

FIGURE 1.31
(a) (b) Three-dimensional images of the fatigue specimen after 500,000 cycles: (a) the gauge volume, (b) a magnified section showing a fatigue crack nucleated at a pore, with the crack tip marked by an arrow. Scale bars are approximate. The scale bars are approximate. (c) (d) The effect of tensile stress on tomographic imaging of a short fatigue crack nucleated at graphite nodule during 10^6 cycles at 200 MPa stress amplitude: (c) with a tensile stress of 100 MPa, (d) the same region with no applied stress. [238]

Advanced techniques have further refined the in situ analysis of short fatigue cracks. In 2010, Limodin [242] combined DVC with μXCT, showing that short cracks exhibit higher COD and SIFs. In 2011, Herbig et al. [243] used novel X-ray DCT and phase contrast tomography (PCT) to demonstrate that in certain grains, crack propagation follows an alternating slip mechanism. Chapman et al. [244] conducted the first three-dimensional analysis of naturally initiated surface-connected and internal fatigue cracks in air and vacuum environments at elevated temperatures. In 2014, Marrow et al. [188] utilised μXCT, DVC and DCT to investigate the influence of microstructural features on the local crack propagation rates. Serial Block Face Scanning Electron Microscopy (SBFSEM) also provided detailed three-dimensional fractographs. This work showed that short fatigue cracks in magnesium propagate with a mixed opening mode. It identified basal plane fracture as a primary fatigue mechanism, while emphasising the influence of microstructural barriers, such as grain boundaries and twin interfaces, on crack propagation rates. The study also

indicated that elastic deformation primarily governs crack-tip displacements, as plastic strain was minimal and localised. Furthermore, it assessed μXCT and DCT in characterising crack morphology and microstructure, noting their effectiveness in capturing coarse precipitates and grain structures while recognising limitations in resolving finer precipitates and visualising the interactions between twinning, grain orientation, and crack development.

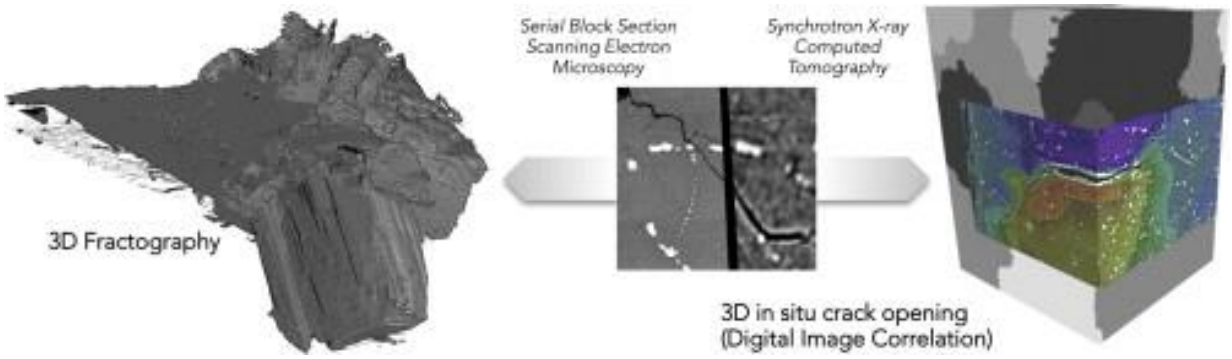

FIGURE 1.32
Three-dimensional in situ crack field quantification and post-test examination of crack topography. [188]

Continuous progress in modelling has significantly advanced the understanding of short fatigue crack behaviour, particularly regarding the local nature of the crack driving force. Early work by Gao et al. [245] applied grain boundary engineering to increase special boundary fractions, studied crack propagation in treated materials, and validated microstructural effects on crack driving forces using finite element (FE) analysis. Santus and Taylor [246] established a physical model for short crack propagation, where the short crack threshold can be calculated using the Chapetti model [247]. In 2010, McDowell and Dunne [248] developed a Crystal Plasticity model using EBSD input, while Hansson and Melin developed a discrete dislocation model [249]. Wan and Dunne [250] employed the Extended Finite Element Method (XFEM) with anisotropic properties and grain boundary modelling. These frameworks introduced the explicit consideration of slip anisotropy and grain boundary interaction, illustrating that crack advance depends on local stress and strain fields. Subsequently, in 2018, Wilson, Zheng and Dunne [1] introduced a stored energy-based method for crack driving force prediction. Other models include Rovinelli et al. [251], who incorporated non-Schmid effects and microstructural hardening in a fatigue damage indicator

framework, and Brockman et al. [252], who developed a parallelised, XFEM-enhanced platform coupling crystal plasticity, fatigue indicator parameters, and grain boundary resistance models across complex loading cycles. These studies indicate that, for the stress intensity factor to remain a valid descriptor of the crack driving force, it must be evaluated from locally resolved, microstructure-sensitive fields rather than inferred from global conditions.

In addition, Electron microscopy (EM) has played an important role in fatigue research, offering high-resolution, localised observations. As shown in Figure 1.33, Guo, Britton, and Wilkinson [253] conducted a detailed crystallographic analysis using HR-EBSD to explore the interactions between slip bands and grain boundaries. Guo et al. [138] further utilised Differential Aperture X-ray Laue Microdiffraction (DAXM) and HR-EBSD to quantitatively examine the stress field distributions at dislocation pile-ups near three-dimensional grain boundaries, providing a quantitative description of local stress concentrations. Carroll et al. [128] combined DIC with EBSD, achieving the first full-field measurements of the plastic strain field at the sub-grain scale during fatigue crack propagation. Jiang et al. [254] applied SEM-DIC to study crack nucleation and early propagation at sub-micron resolution, focusing on associated strain localisation. These local observations clearly demonstrate that the effective crack driving force arises from the actual near-tip stress and strain distributions shaped by the surrounding microstructure, and that local full-field measurements can now provide sufficient spatial resolution to quantify these fields accurately.

Accurate measurement of the local crack-tip field enables analysis of plastic strain accumulation, thereby correlating directly with the growth rate of short fatigue cracks. This fundamental relationship was initially highlighted by Chan and Lankford [255], who established a power-law connection between the crack-tip plastic strain range and the stress intensity factor range (ΔK), as shown in Equation (1-38). Their cumulative plastic strain criterion, described in Equation (1-39), proposed that crack advancement occurs incrementally whenever the accumulated local plastic

strain exceeds a critical threshold (ε_P^*), offering a physically motivated framework for modelling and predicting short fatigue crack propagation.

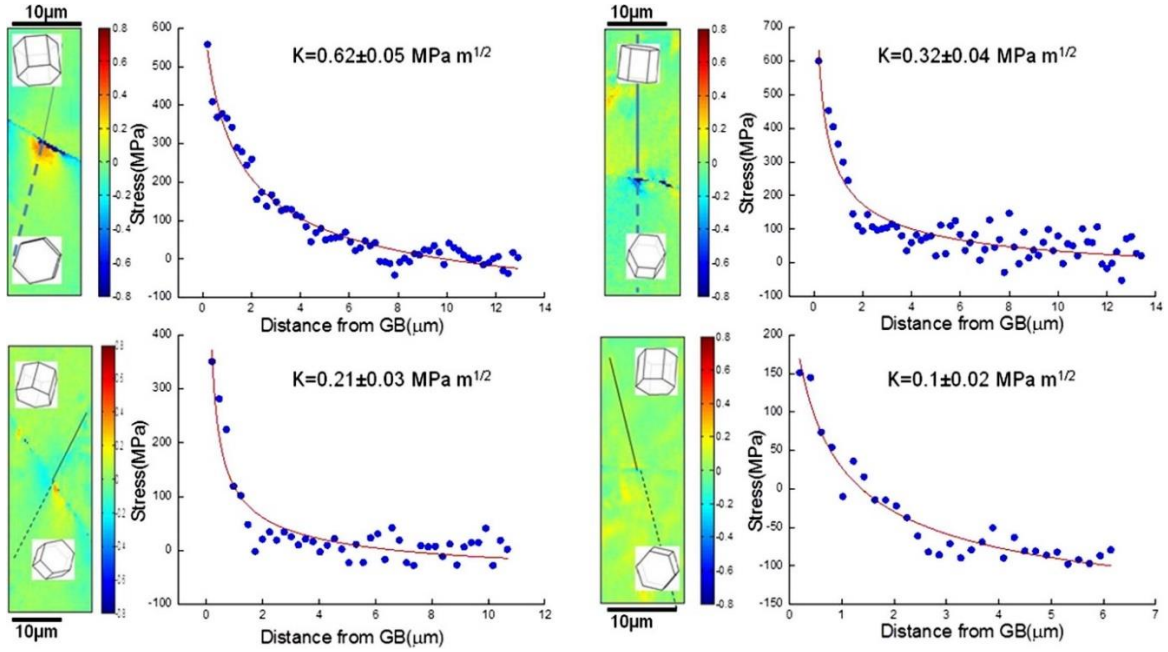

FIGURE 1.33
Stress profile in front of the blocked slip bands and fitted stress profiles. The solid line represents the position of the incoming slip band and the dashed line is the direction along which the stress profile was extracted. The value and standard error of K obtained from fitting are shown for each stress profile. [253]

$$\Delta\varepsilon_p = C\Delta K^n \tag{1-38}$$

$$\Delta N = \frac{\varepsilon_P^*}{\Delta\varepsilon_p} \tag{1-39}$$

Subsequent studies have expanded upon this foundational relationship. Musinski and McDowell [256] reviewed this connection alongside other strain-range-based models for short crack growth, including those proposed by Miller [257]. They further introduced Fatigue Indicator Parameters (FIPs) to account for microstructural effects, a concept now central to computational models for microstructure-sensitive fatigue crack growth.

Building on mixed-mode propagation analyses by Hoshide and Socie [258], McDowell and Berard [259] established a close relationship between the Fatigue Strain (FS) parameter and both the

elastic-plastic fracture mechanics (EPFM) ΔJ-integral and the cyclic crack-tip displacement range (ΔCTD). This relationship also aligns with strain-based critical plane fatigue criteria [260]. McDowell and Dunne [248] further emphasised the role of plastic strain accumulation at the crack tip. Numerous experimental and modelling studies have confirmed the effectiveness of $\Delta CTOD$ [261-264], particularly crack-tip opening and sliding displacements, as reliable correlators for crack advancement.

Collectively, these studies illustrate that precise characterisation of the crack-tip field and accurate evaluation of crack driving forces would substantially enhance the modelling and prediction of short crack behaviour. Such insights are essential for improving fatigue life predictions and facilitating the design of fatigue-resistant materials.

As noted previously, Koko et al. performed an in situ investigation of the local boundary conditions of twins [220] and slip bands [155] using strain fields obtained from HR-EBSD to calculate the J-integral and SIFs. Figure 1.34 illustrates the study of deformation twins, showing how the J integral and Mode-I/II SIFs vary with twin thickness. The figure reveals that as twin thickness increases, corresponding to higher applied loading in the in situ experiment, the locally derived J-integral and SIFs increase accordingly. This demonstrates that the local strain field mapping enables a direct quantification of the evolving crack-tip driving forces as deformation progresses. More importantly, the results exemplify how the SIF, when computed from locally measured microstructural fields rather than from global boundary conditions, reflects the true near-tip mechanical response. Thus, it provides experimental support for the view that short crack driving forces must be evaluated from locally resolved fields that capture the influence of microstructural features.

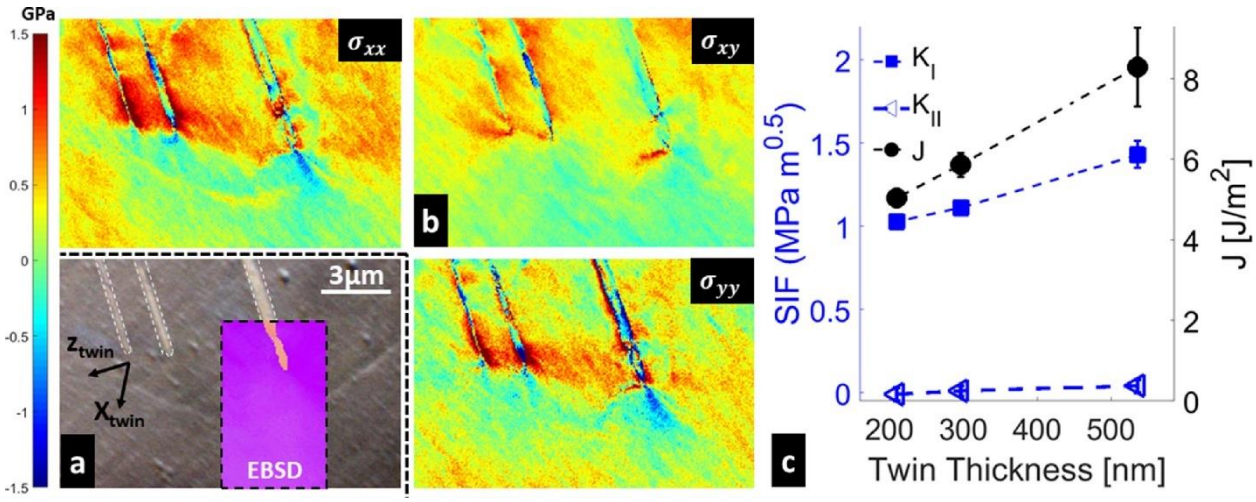

FIGURE 1.34

a) FSD image (with inset EBSD map of grain orientation) of three $\sum 3\,(\bar{1}2\bar{1})[\bar{1}\bar{1}\bar{1}]$ ferrite deformation twins in age hardened duplex stainless-steel. b) HR-EBSD calculated stress tensors. c) J integral, and Mode-I and II stress intensity factors (K_I and K_{II}) as a function of twin thickness. [220]

Through this review, it becomes evident that studies utilizing X-ray Computed have confirmed complex mixed-mode loading at crack tips, helped explain crack-crystallography interactions, and illustrated basal plane fracture as a key mechanism. They also revealed the effects of various crack-tip factors on the elastic field. However, resolution limitations inhibit the precise characterisation of the crack-tip elastic field and the complex plastic activities driving crack growth. This underscores the advantages of EM-based techniques, which have proven their strong potential in investigating the local fields around slip bands and twins.

1.5 Fracture Toughness Testing at the Microscale

The development of micro-scale fracture toughness testing methods is increasingly vital in modern materials science and engineering. With rapid advancements in microelectronics [265, 266], microelectromechanical systems (MEMS) [267], nanotechnology [268], and the emergence of ceramics in demanding environments such as protective coatings [269, 270], thin films[271], and energy storage materials [272, 273], understanding fracture behaviour at micro and nanoscales is essential. Materials at these scales often exhibit significantly different fracture characteristics

compared to their bulk counterparts, thus necessitating precise micro-scale fracture toughness assessments. This need is particularly acute in ceramics, where grain boundaries play a central role in determining fracture toughness and crack propagation. Accurate evaluation of micro-scale fracture properties, especially at grain boundaries and interfaces such as diffusion-bonded layers in coatings and lithium battery materials, enables informed interface design and targeted microstructural engineering. Such methods underpin the development of next-generation materials, offering insights that translate directly into enhanced reliability, manufacturability, and operational performance.

The previous sections have introduced standard fracture toughness testing methods. However, micro-scale fracture toughness testing differs significantly due to the inherent scale dependence of fracture toughness, which necessitates experimental investigations at the appropriate dimensional level. Fracture toughness is fundamentally a measure of energy dissipation required for crack propagation across a sample. The factors influencing energy dissipation vary across different scales, leading to distinct apparent fracture toughness characteristics at different length scales. Therefore, fracture toughness is not merely a function of measurement resolution but an intrinsically scale-dependent physical quantity. This necessitates micro-scale fracture toughness testing to adhere to three key principles:

First, testing must be performed using miniature specimens containing micro- to nano-scale cracks. Additionally, ultra-low load mechanical testing devices with high displacement resolution are essential to ensure accurate and reliable loadings. Second, high-resolution measurement techniques are indispensable for capturing full-field information at the microstructural level. Advanced methods enable direct visualisation of crack propagation, plastic zone evolution, residual stress distributions, and interactions between cracks and crystallographic features, including inclusions, dislocations, slip systems, twins, grain boundaries, and phase boundaries. This comprehensive characterisation is crucial for understanding the fundamental mechanisms

governing fracture behaviour at small scales. Lastly, appropriate computational models are required to accurately quantify fracture toughness at the micro-scale. These models must incorporate crack-controlling parameters such as the actual elastic field at the crack tip. They should be able to reflect all microstructural constraints to ensure that the toughness evaluation reflects the actual fracture resistance of the material. By integrating micro-scale experimental techniques with advanced measurement and modelling approaches, a rigorous and scale-appropriate assessment of fracture toughness can be achieved.

The method evolution history represents a progressive refinement toward better alignment with the fundamental principles outlined above. Nanoindentation, developed in the early 1970s [274, 275], has gradually become a widely adopted technique in micro-mechanical testing. Advances in technology have enabled the reduction of indenter size while improving the accuracy and resolution of both indentation depth and load measurements, making it an ideal choice for micro-mechanical analysis. As shown in Figure 1.35, an indent is created by pressing the tip into the sample surface until the specified load or displacement is reached.

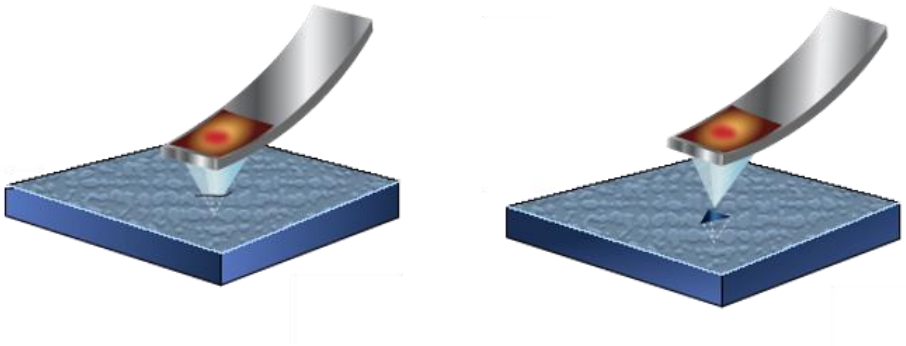

FIGURE 1.35
Schematic of nanoindentation.
Source: https://www.nanophys.kth.se/nanolab/afm/icon/brukerhelp/Content/NanoIndentation/NanoindentOverview

The Lawn–Evans–Marshall (LEM) method is a classical, idealised model for evaluating fracture toughness based on indentation [276-279]. According to the equation:

$$K_c = \alpha \cdot \sqrt{\frac{E}{H}} \cdot \frac{P_{max}}{c^{3/2}} \quad (1\text{-}40)$$

where E is the modulus of elasticity, H is the hardness, P_{max} is the maximum load during indentation and c is the average crack length, the fracture toughness can be directly calculated. The value of the coefficient α is related to the geometry of the indenter and the material properties, and it is typically determined through experimentation. It assumes that cracking arises from the interplay of elastic and plastic deformation beneath the indenter. During loading, the reversible elastic component promotes the growth of median cracks while suppressing radial ones (see Figure 1.36). This suppression is lifted upon unloading, allowing residual tensile stresses to drive radial crack extension. These residual stresses dominate the final stages of crack evolution and result in the characteristic half-penny crack geometry often observed in brittle materials.

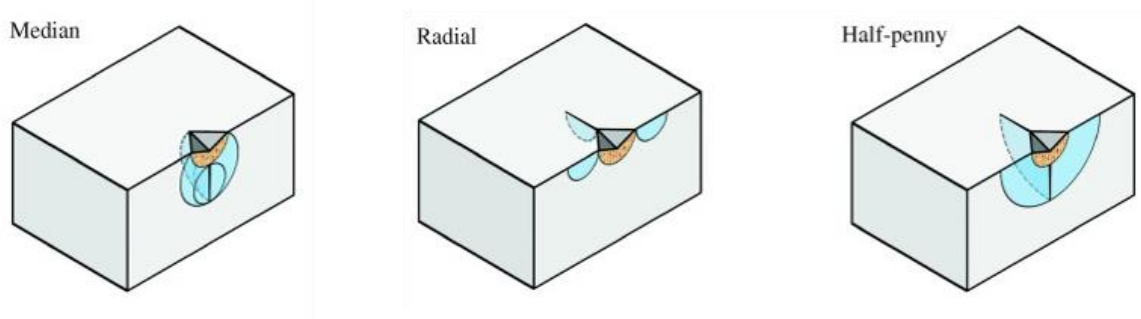

FIGURE 1.36
Example of possible crack geometries under sharp indentation loading. [280]

However, subsequent studies have questioned whether these idealised conditions are met in many practical cases [280-282]. The E/H ratio (or E/σ_y , where σ_y is the yield stress), Poisson's ratio, and indenter geometry can all introduce uncertainty in crack behaviour. For LEM to be applicable, cracks must be long and adopt a half-penny geometry, with a c/a ratio greater than 2, where c denotes the surface crack length and a the contact radius. Yet in practice, experimental observations [283] suggest that surface cracks are more commonly radial in nature, and in many materials, especially when the loading conditions do not strictly meet the required criteria, true half-penny cracks do not develop. In coarse-grained or crystallographically anisotropic materials,

the formation of symmetric crack geometries is further limited. Cracking may occur in a mixed-mode fashion, with median cracks sometimes not reaching the surface, and shallow lateral cracks may form.

The E/H ratio plays a significant role: in brittle materials ($E/\sigma_y \approx 10$), median cracks dominate, while in ductile materials ($E/\sigma_y \approx 100$), enhanced plasticity favours radial cracking. Higher E/H values tend to promote earlier radial crack initiation. Indenter geometry also matters, as sharper indenters more readily generate radial cracks. Additionally, residual stresses within the material can further influence cracking behaviour. Taken together, these factors significantly constrain the applicability of the LEM method and motivate the present study: how to use indentation to reliably generate cracks that reach a critical state, driven by residual stress and subsequently arrested, and to evaluate the complex crack tip driving force under such conditions.

To more directly measure the fracture toughness of materials at the microscale, micromechanical experimental methods based on nanoindentation and FIB fabrication have been developed. For different situations and needs, test specimens of various shapes have been designed, including micro-pillars, thin films [284-286], micro-tensile specimens [287], double-clamped beams [288, 289], and single and double cantilever beams [290, 291].

Sebastiani et al. [292] developed the micro-pillar splitting method, which utilises cohesive-zone finite element modelling (CZ-FEM) to calculate coefficients in Equation (1-40) for estimating K_c. Figure 1.37 shows an example of a pillar from this study after splitting. Some studies suggest that residual stress are completely released by the FIB milling process [292, 293]. However, this is not necessarily true, as FIB implantation can also induce residual stress, as noted in the work of Hofmann [294]. Subsequent research has discussed the influence of indenter geometry [295] and indentation position [296]. Bolelli et al. [297] applied this method to monitor the fracture toughness of thermal barrier coatings under thermal cycling fatigue.

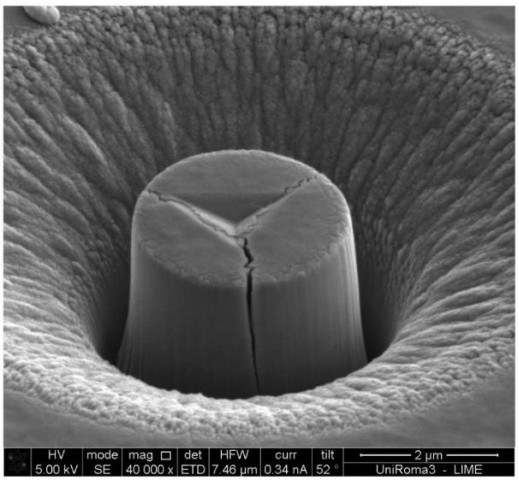

FIGURE 1.37
Example of one of the pillars after splitting (TiN sample). [292]

Another notable method is the micro-cantilever test. In 2005, Di Maio and Roberts [298] used this method to study the fracture toughness of coated materials, while Halford et al. [299] tested TiAl specimens. These studies are the pioneering work of this method, which uses classic fracture mechanics formulas to assess the mode I fracture toughness at the microscale:

$$K_{Ic} = \sigma_c \sqrt{\pi a} \cdot F(a/b) \tag{1-41}$$

where σ_c is the fracture stress, a is the crack length and $F(a/b)$ is a dimensionless shape factor dependent on sample geometry. In practice, σ can be calculated with indenter loading:

$$\sigma = \frac{PLy}{I} \tag{1-42}$$

where P is the applied bending force from the indenter, L is the distance between the crack and the point where the force is applied, I is the moment of inertia of the beam cross section, and y is the vertical distance between the upper surface and the neutral plane of the beam. Importantly, the value of the shape function F was estimated by FE analysis, using specimen and crack geometry as the input. For example, in [298] the equation derived is

$$F\left(\frac{a}{b}\right) = 1.85 - 3.38\left(\frac{a}{b}\right) + 13.24\left(\frac{a}{b}\right)^2 - 23.26\left(\frac{a}{b}\right)^3 + 16.8\left(\frac{a}{b}\right)^4 \tag{1-43}$$

where b is the height of the parallel vertical face and a is the crack length, as shown in Figure 1.38. It is required that $0.3 \leq (a/b) \leq 0.5$.

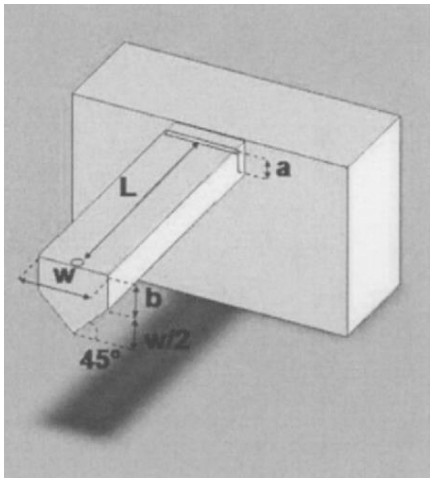

FIGURE 1.38
Sample geometry as a result of sample preparation in micro-cantilever test.

In fact, finite element (FE) modelling plays a crucial role in developing testing geometries, determining the associated geometry functions, and understanding the influence of aspect ratios, notch shapes, and material plasticity. In practical situations, due to fabrication limits, material anisotropy, and the complexity of notch geometries, the sample dimensions are difficult to control precisely. This requires extensive finite element simulations to investigate the impact of specimen geometry effects [300].

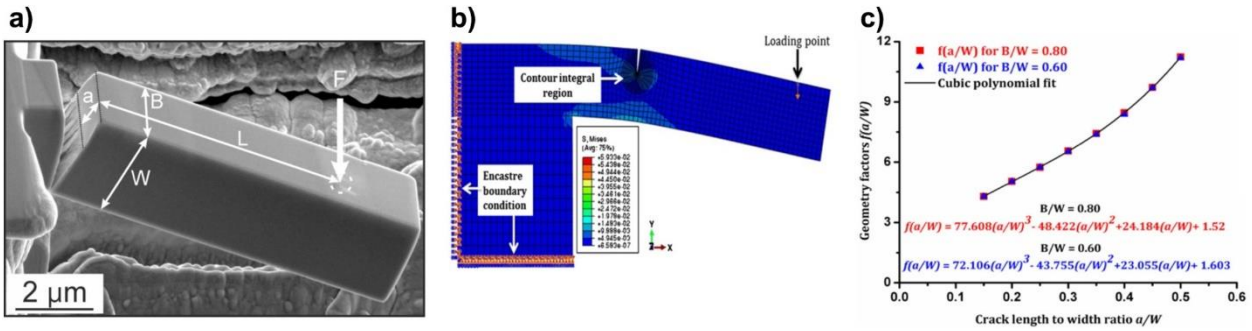

FIGURE 1.39
(a) SEM image of a fractured cantilever in a NiAl single crystal, (b) FE model for the determination of the geometry function, shown in (c) for different a/W aspect ratios. [300]

Another important factor to consider is the influence of the plastic zone at the crack tip. For brittle materials, the plastic zone can be neglected; however, for most metals, the size of the plastic zone

may be comparable to that of the specimen, which can significantly suppress the fracture process [301, 302]. Additionally, dislocation movement within the crystal complicates the situation further. For instance, when dislocation motion is hindered by dislocation pile-up or interfaces [303], the expansion of the plastic zone is suppressed, which may promote the occurrence of cleavage fracture. Figure 1.40 schematically illustrates some possible situations at the crack tip [304].

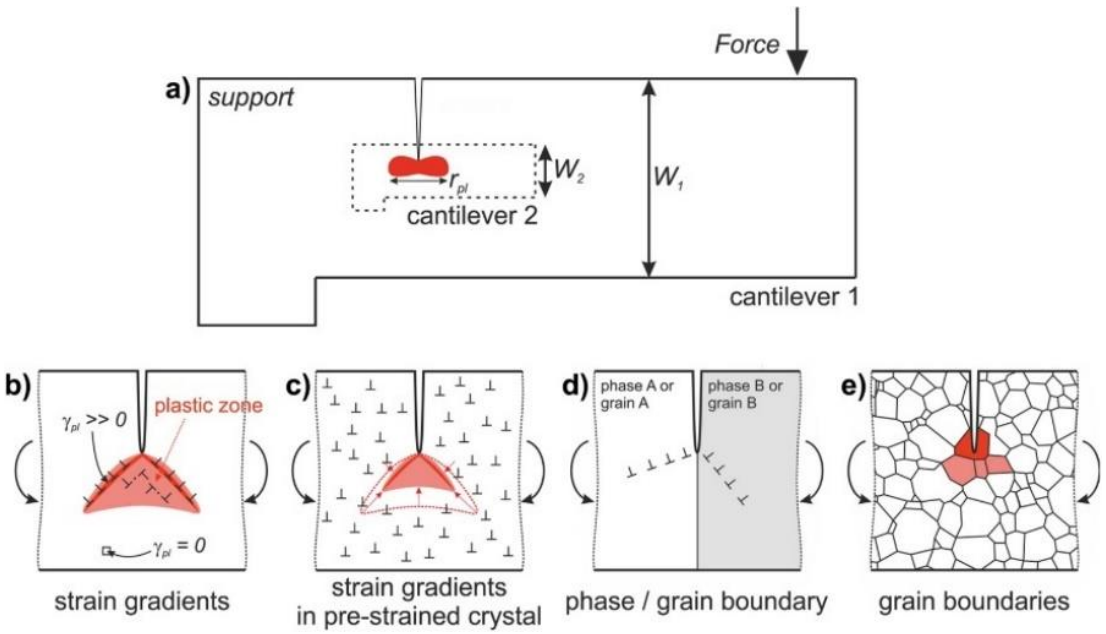

FIGURE 1.40

The development of plastic zones in loaded micro-cantilevers: (a) although cantilever size may change, plastic zone size remains the same for given severity of loading, (b) strain gradient effects, (c) effect of additional plastic pre-straining, (d) testing of single phase or grain boundaries and (e) testing of multiple grains.[304]

When small-scale yielding is not satisfied, the J integral [305] and $CTOD$ [306] are applied in microscale tests to determine fracture toughness, typically via Equations (1-10) and (1-11). The discussions on these methods primarily focus on how to determine the critical conditions at the microscale [306-309]. Standardising such methods is difficult, due to plastic zone effects and case-specific constraints. Direct crack-tip field measurement is needed to further improve the evaluation.

Nevertheless, research based on this method has yielded some significant results. Armstrong, Wilkinson, and Roberts [310] investigated the fracture toughness of grain boundaries in bismuth embrittled copper, demonstrating its advantage in replacing macroscopic bicrystal specimens.

Brinckmann's finite element work demonstrated the influence of anisotropy, Poisson's ratio and beam geometry on K calculation [311], and the impact of pre-crack geometries on test results [312], providing insights into specimen design. Mueller et al. [313] achieved the first measurement of the fracture toughness of nanocrystalline alumina, validating the predictions from theoretical model for grain bridging toughening in this material. Armstrong et al. [314] investigated the mechanical properties of ion-irradiated tungsten, finding a correlation between ion implantation and fracture toughness. Costin et al. [315] were the first to perform micro-fracture testing on an individual microstructural constituent (needle-like ferrite) within a small volume, using hydrogen pre-charging and controlled loading. They found the SIFs to be far below conventional macroscopic thresholds, with toughening mechanisms not fully activated at the microscale. More recent progress has been reviewed by Dehm at al. [316] and Pippan et al. [309].

While previous efforts have highlighted the growing importance of micro-scale fracture testing, it is important to note that recent advances in site-specific micromechanical fracture testing have been largely enabled by high-precision microfabrication techniques, the most notably FIB machining, and high-spatial-resolution testing within SEM. These methods are inherently sophisticated and labour-intensive, posing significant challenges for broader experimental implementation. Figure 1.41 summarises several reported loading geometries for micromechanical fracture testing [291]. Panel (a) shows a single cantilever bending geometry with a pentagonal cross-section loaded by a sharp indenter [310], where the notch shape critically influences fracture stability [313, 317]. Panel (b) illustrates a double clamped beam bending geometry using a blunt tip [288]; while stable crack growth is supported, the flexibility in notch position remains limited [317]. In panel (c), a DCB geometry is loaded by a flat punch [290], where friction and compressive stresses must be accounted for. To address these issues, Sernicola et al. [291] proposed the wedge-loaded DCB geometry (panel d), which enables stable crack growth and helps

to some limitations from FIB-induced damage. Nonetheless, perfect symmetry during sample preparation and loading is rarely achievable at such small scales.

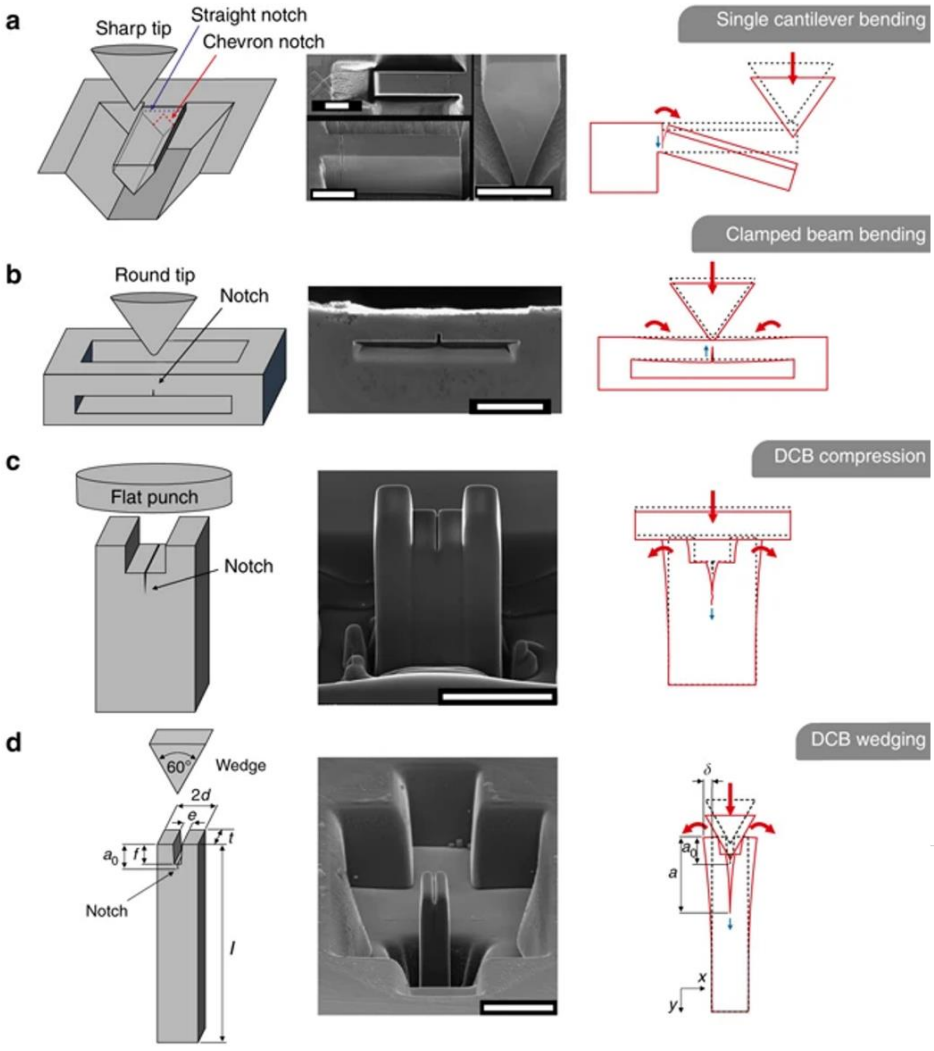

FIGURE 1.41
Loading geometries employed in micromechanical fracture testing. (Adapted from [291])

Overall, these methods demand intricate specimen preparation. FIB processes are not only time-consuming but can also introduce damage near the notch, potentially compromising measurement accuracy. Moreover, some tests employ nanoindenters in load control, which often leads to unstable, abrupt crack propagation. Even when stable cracking is achieved, precise alignment is essential, and test results can suffer from variability and limited repeatability due to setup sensitivity and fabrication artefacts. These challenges underscore the need for simpler and more robust testing approaches that can accommodate brittle fracture, such as cleavage or grain

boundary cracking. Notably, Koko et al. [155] reported quasi-static crack propagation with high-resolution EBSD analysis in an in-situ setting, prompting further interest in integrating advanced measurement techniques with novel micro-fracture testing methods.

In recent years, new advancements have emerged as various characterisation techniques have been employed during experiments to interpret the mechanical behaviour of materials. Ast et al. [153, 170] used HR-EBSD to measure the evolution of the plastic zone. Hirakata et al. [318], Kawai et al. [319], and Takahashi et al. [320] employed TEM for observation of plasticity. These advancements have enabled more precise and direct measurements at the local crack tip, effectively illustrating the impact of plasticity on the crack tip field, providing significant inspirations. While these methods have been successful in analysing the tip fields, challenges such as difficulties in sample preparation, low standardisation, and the need for improved reproducibility remain. Recalling the principles outlined at the beginning of this section, further consideration could focus on how to more effectively combine the testing methods, measurement techniques, and modelling approaches to overcome these challenges.

The increasingly sophisticated full-field micromechanical measurement capabilities, along with the full-field fracture parameter analysis methods discussed previously, offer new possibilities for addressing this issue. If a critical crack can be initiated within the tested material at the microscale, the existing full-field measurement techniques can provide sufficient accuracy to precisely quantify the actual elastic field at the crack tip. Recent studies have shown that HR-EBSD can accurately measure residual stress fields around nanoindentations [321, 322], as shown in Figure 1.42, providing fresh impetus for this thesis to explore the development of novel fracture toughness and fatigue testing methods at microscale using full field measurements.

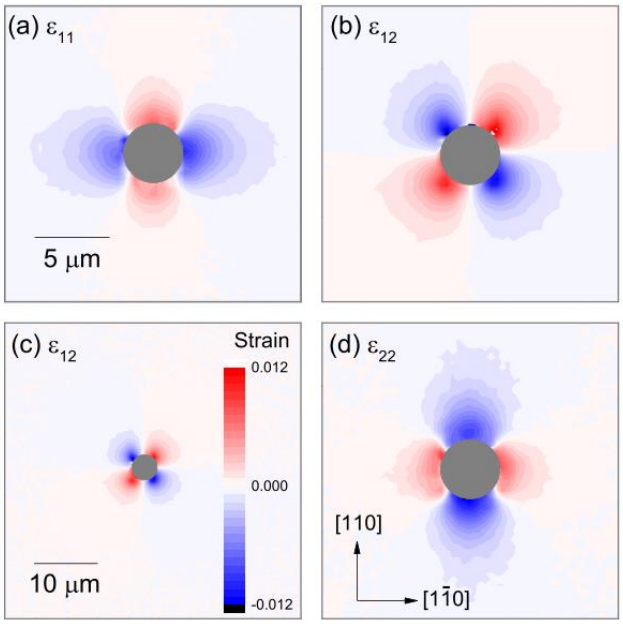

FIGURE 1.42

Colour-filled contour maps of EBSD-measured strain components (a) ε_{11}, (b) and (c) ε_{12}, and (d) ε_{22} adjacent to a spherical indentation in Si. Measured by EBSD. [322]

Chapter 2

Crack Field Analysis by Optical DIC of Short Fatigue Cracks in Zircaloy-4

2.1 Introduction

To ensure the safety and reliability of structural materials, significant emphasis has been placed on investigating crack propagation mechanisms. A classical and widely-used description is the Paris law, which employs the stress intensity factor range, ΔK, as a single-parameter characterisation of the crack-tip mechanical driving force required for fatigue crack growth. However, in many practical cases, the fatigue lifetime associated with short cracks comprises a substantial portion of the total component life. Predictions of fatigue lifetime in this short crack regime based on remote loading conditions are frequently inaccurate, primarily because observed crack growth rates can exhibit considerable variations with crack length. This variability arises fundamentally due to the sensitivity of short cracks to local microstructural environments, where

the crack tip interacts dynamically with evolving local stress fields and encounters microstructural barriers that affect its propagation [188, 196]. Consequently, accurate experimental characterisation of crack-tip stress and strain fields is crucial for deepening the mechanistic understanding of short crack behaviour and for developing physically informed models that can ultimately support the design of improved fatigue-resistant materials [323, 324].

Full-field measurement techniques with sufficient spatial resolution provide effective means for directly measuring the actual mechanical fields in the vicinity of the crack tip. Digital Image Correlation (DIC), first introduced by Peters and Ranson [95], is a widely-used and powerful approach capable of measuring the full-field displacement on a specimen surface. DIC operates by correlating subsets of digital images recorded before and after deformation. The accuracy of displacement measurement relies critically on the precise identification and tracking of subset patterns between reference and deformed images. By employing various correlation algorithms, such as the iterative spatial domain cross-correlation algorithm [106, 109, 110] and the peak-finding algorithm [325], displacement registration with sub-pixel accuracy can be reliably achieved. This capability facilitates detailed observation of short cracks from high-resolution images [326]. When combined with high-magnification optical microscopy or scanning electron microscopy (SEM), DIC can provide even finer spatial resolution, enabling improved characterisation of local deformation fields around microscale cracks.

To analyse the field information obtained by measurements, it was common in the literature to retrieve the crack field using a field fitting approach [190, 327, 328]. Such approaches rely on theoretical solutions, such as the Williams field solution, to determine the field-controlling parameters from experimentally measured displacement fields. In studies focusing on crack-tip fields, Liu et al. [329] employed McNeill's method [97] to determine the stress intensity factors for Inconel 718. For cases involving mixed-mode loading, stress intensity factors were evaluated using extended field fitting methods applied to DIC data [204]. Field fitting approaches have also

been successfully extended to three-dimensional analyses employing digital volume correlation techniques [330]. One limitation inherent to these methods, however, is their sensitivity to the precise definition of the crack tip location [97]. Such sensitivity can lead to uncertainties in estimating stress intensity factors, particularly for cracks with complex geometries or pronounced local plasticity.

An alternative way to deal with the DIC data is the direct evaluation of the J-integral. The JMAN method, proposed by Becker et al. [213, 214], demonstrated the feasibility of using a domain integral in post-processing the measurement data. Other feasible integrals have also been reported in the literature, for example by Moutou Pitti et al. [331]. The path-independent nature of integral-based approaches offers the advantage of determining field-controlling parameters through a selection of integration paths that are comparatively less sensitive to uncertainties in crack-tip location. Additionally, the incorporation of finite element analysis facilitates the treatment of non-linear material behaviour.

Standard finite element software packages can be employed to carry out the integral evaluations mentioned above. Barhli et al. [216] presented a novel method for extracting stress intensity factors through the combined application of digital image correlation (DIC) and finite element simulations, employing the virtual crack extension method. Koko et al. [219] subsequently verified the accuracy of this technique and further developed a related novel method for evaluating stress intensity factors from diffraction-measured strain fields, demonstrated in their study of a long fatigue crack in a compact tension specimen. In the present chapter, the applicability of this combined approach is extended to the investigation of high-magnification displacement fields associated with short fatigue cracks propagating along crystallographic planes in a polycrystalline zirconium alloy (Zircaloy-4). To mitigate the detrimental effects of low-quality data points adjacent to the crack faces, a ‘forbidden’ zone is introduced to exclude these regions from the analysis. The analysis is conducted assuming linear anisotropic elasticity, which incorporates the

crystallographic orientation of the grain containing the crack. However, detailed microstructural effects such as plastic zone evolution, neighbouring grain interactions, and slip character are not explicitly treated. The focus of this work is to examine how data-processing parameters such as subset size, crack-tip position uncertainty, and the extent of the forbidden zone influence the accuracy and consistency of the analysis. This evaluation provides insight into effective strategies for determining the J-integral and stress intensity factors in short fatigue crack studies.

2.2 Material and Methods

This study utilises experimental data from other researchers that have been previously published and described elsewhere [332]. Here, the experimental details most relevant to the current investigation are briefly summarised.

The material was taken from a pair of edge-notched Zircaloy-4 beam samples (Samples A and B), where the edge notch was introduced by electrical discharge machining (EDM). As-received Zircaloy-4 plates, initially with an average grain size of approximately 13.5 μm, were heat-treated at 800 ℃ for 2 weeks to produce a coarse-grained, 'blocky alpha' microstructure with grains on the order of 400 μm. This treatment was carried out to reduce the influence of grain boundaries and to facilitate the observation of crack propagation within individual grains. Their resulting polycrystalline microstructures are shown in Figure 2.1.

For deformation measurement purposes, samples were sprayed with silica speckles of approximately 1 μm diameter. Figure 2.2 illustrates the experimental set-up, providing representative optical and SEM images of the silica speckle pattern on the sample surface. Cyclic loading was applied using a three-point bending arrangement, with a maximum load of 800 N and a load ratio (R-ratio) of 0. Details regarding sample geometry, notch dimensions, and the distance between the two supporting pins are provided in Table 2.1.

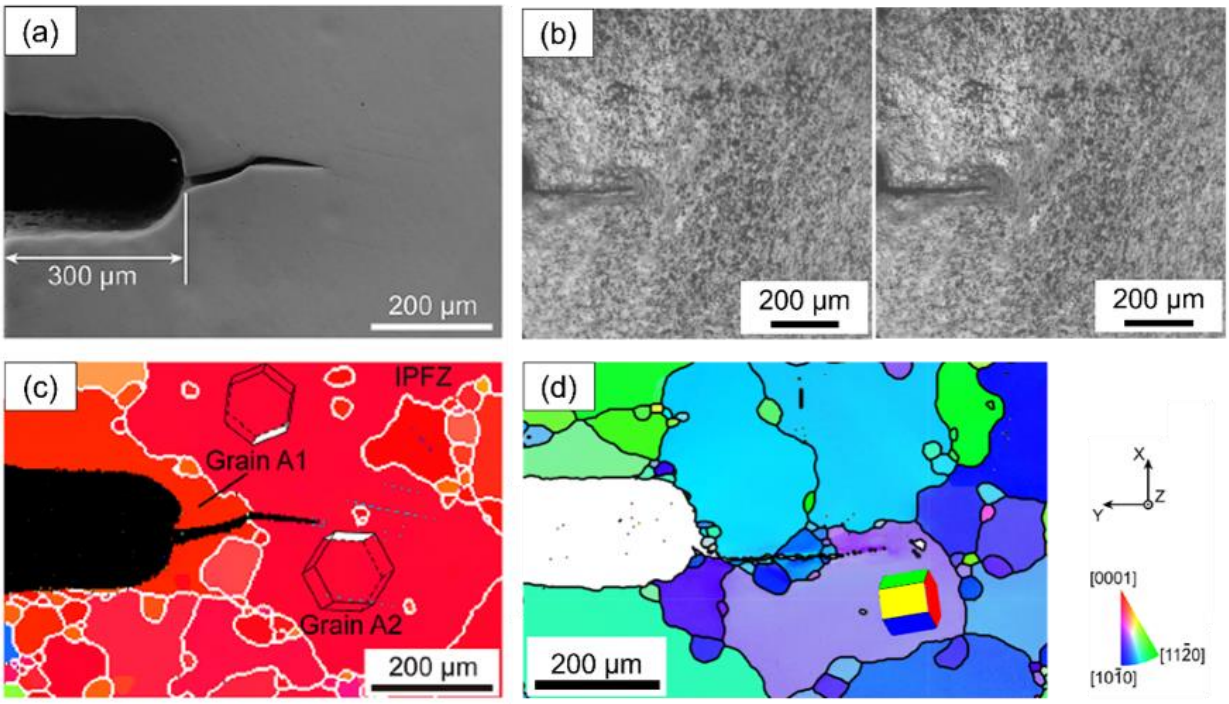

FIGURE 2.1

(a) SEM image of sample A; (b) Optical images of sample B (unloaded and peak-loaded); (c) Inverse pole figure of the z-axis: sample A; (d) Inverse pole figure of the z-axis: sample B.

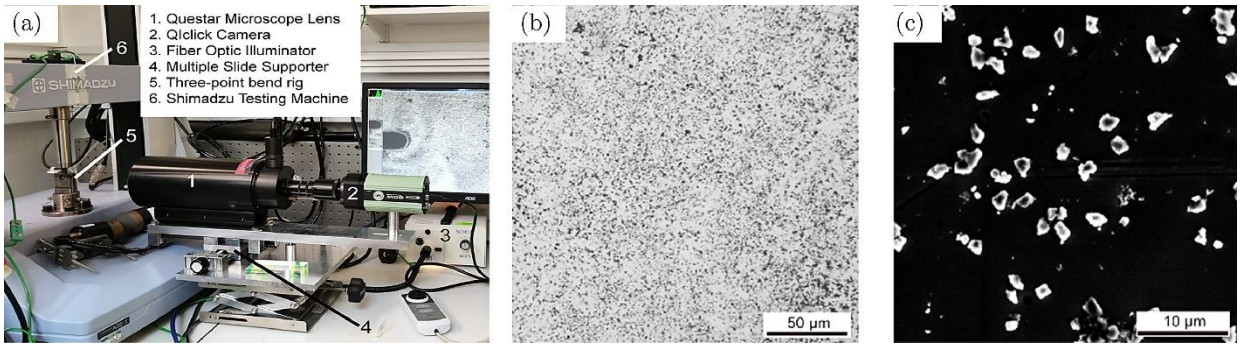

FIGURE 2.2

(a) In-situ micro-scale optical Digital Image Correlation set-up, (b) OM image and (c) SEM image showing the distributed 1 µm silica speckles on the sample surface for DIC measurement.

TABLE 2.1

Geometry, edge-notch shape and distance between supporting pins (separated by 10 mm).

Sample	Geometry (mm)	Notch Shape (µm)
A	Height 3.18, Thickness 3.02, Length 12.01	Notch Height 270, Notch Width 150
B	Height 3.17, Thickness 2.93, Length 12	Notch Height 300, Notch Width 150

In situ observations of the samples were conducted using an optical *Questar*® Microscope Lens (QM-100), and images were captured by a CCD camera with a working distance of approximately 150 mm. The spatial (pixel) resolution of the optical microscopy imaging was 1 μm.

The DIC analyses in this work were performed between successive images captured at unloaded and peak-loaded conditions during a single monotonic fatigue cycle, as illustrated in Figure 2.1 (b), using standard digital image correlation software (*LaVision*® *DaVis 8.4.0*). The legacy mode Fast Fourier Transform correlation was employed with the multi-pass option, where the default final subset size was set to 96×96 pixels with an overlap of 75%. A median filter [333] was applied during vector post-processing to detect and remove spurious displacement vectors. Vectors were excluded if their residual exceeded twice the standard deviation of neighbouring vectors. Empty spaces resulting from this filtering step were subsequently filled by interpolating vectors based on at least two neighbouring valid vectors. The fill-up was an iterative process, in which interpolated vectors obtained in one iteration served as input for subsequent interpolation steps. This chapter presents data obtained for cracks observed at 2400 cycles (Sample A) and 2200 cycles (Sample B), where the measured crack lengths are approximately 230 μm and 252 μm, respectively.

A finite element framework is employed in this study to post-process the displacement field data and calculate the crack driving force, with the detailed procedure illustrated schematically in Figure 2.3. In this method, the finite element model is registered directly to the displacement field obtained by digital image correlation (DIC). Specifically, the finite element mesh is constructed so that each node corresponds exactly to a displacement measurement point from the DIC analysis. The crack-tip position is assessed, and a horizontal crack is subsequently introduced into the mesh. To accurately accommodate the crack geometry, the region in the immediate vicinity of the crack tip is re-meshed.

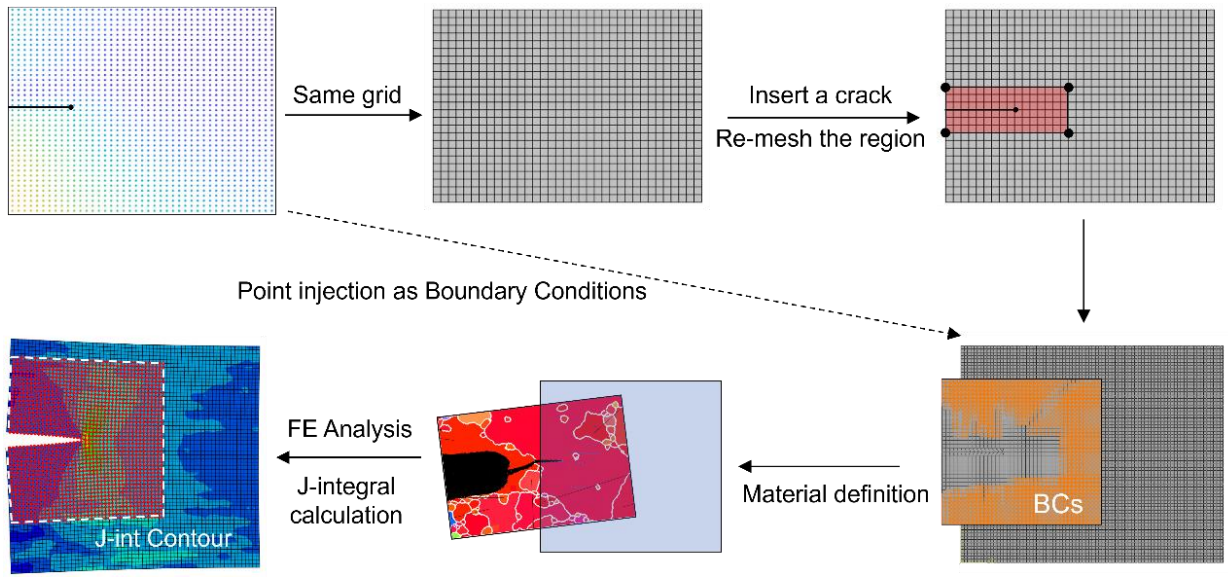

FIGURE 2.3
Steps of the Finite Element post-processing of DIC-obtained displacement field.

In practice, displacement measurements obtained directly at or very near the crack faces are often of lower quality due to speckle pattern deterioration, severe deformation gradients, or image processing artefacts. To address this issue, a 'forbidden zone', defined as a small region immediately surrounding the crack tip and crack faces, is introduced, within which direct DIC displacement data are intentionally excluded from being imposed as boundary conditions. Within this forbidden zone, nodal displacements are instead obtained by enforcing static equilibrium conditions during the finite element solution.

After defining the relevant material properties, with the present study assuming linear anisotropic elasticity, a finite element analysis using CPS4 elements is conducted to determine the resulting stress and strain fields. Finally, the J-integral is calculated using the built-in virtual crack extension algorithms within the finite element software *ABAQUS*® (version 6.14). The variations in both the Mode I and Mode II crack intensity factors range, ΔK_{I} and ΔK_{II}, over a fatigue cycle can then be extracted using the interaction integral method [334], also implemented in *ABAQUS*® (version 6.14).

For Sample A, the crack exhibits a kink within the imaged region, which would result in the crack being inclined relative to the reference axes if DIC and subsequent post-processing were performed directly on the original images. However, as the objective of this analysis is to quantify the J-integral and stress intensity factors associated with crack propagation along the actual local crack direction, the acquired images were cropped and rotated beforehand. This pre-processing step ensures that only a single, straight, horizontal crack segment remains within the region of interest, as illustrated in Figure 2.4 (a). Such image manipulation simplifies and improves the accuracy of the finite element modelling procedure. Aligning the crack horizontally simplifies mesh generation in the finite element model, reducing element distortion around the crack tip region, thereby enhancing the reliability of stress and strain computations. Cropping and rotation also ensure a consistent definition of the local coordinate system aligned with the crack propagation direction. Additionally, they preserve the original spatial resolution, ensuring that the displacement fields used in finite element analyses are unaffected by the image manipulation process. Figure 2.4 (b) presents a typical displacement field obtained by DIC after applying this rotation and cropping process.

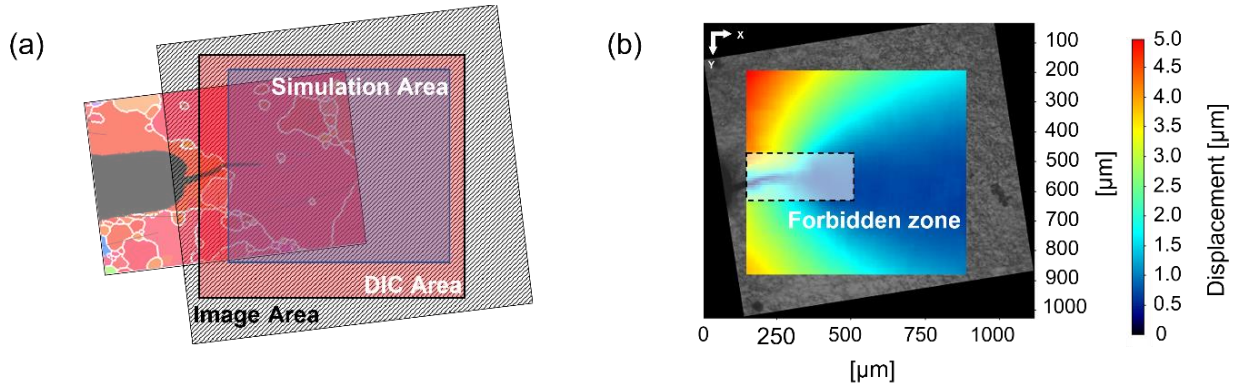

FIGURE 2.4
Rotation and selection of the field data for finite element analysis. (a) Illustration of the original image region together with the cropped and rotated region used for analysis. (b) Displacement field obtained after image processing, with the local coordinate axes shown in the upper left corner. The shaded area indicates the forbidden zone.

An inherent limitation of digital image correlation (DIC) is its difficulty in accurately determining displacement vectors near discontinuities, such as crack faces or sample edges [97]. In these regions, displacement measurements are prone to reduced correlation quality, characterised by low correlation coefficients (typically a normalised correlation value less than 0.95). Consequently, the dimensions of the forbidden zone adopted in this work were established by identifying regions of poor correlation in the DIC data, corresponding approximately to an area of 160×75 pixels for the two image series considered. To ensure robustness and to account for potential variations in data quality across different images, a slightly larger default forbidden zone of 200×100 pixels was selected. Removing data points within this region inevitably alters the spatial extent of the field data available for the calculation of fracture parameters. In practice, this means that the J integral and stress intensity factors are evaluated using high-quality field data located some distance away from the crack tip, rather than using data immediately adjacent to it. As a result, the dimensions of the forbidden zone directly influence the numerical accuracy of J-integral and stress intensity factor calculations, necessitating careful consideration and systematic sensitivity analysis, which is presented next in the discussion section.

2.3 Results and Discussions

For comparison purposes, theoretical estimates of the Mode I stress intensity factor (SIF) range were calculated using the analytical solution specified in the ASTM standard for Single-Edge Bend, SE(B), specimens [14]. This calculation represents the classical approach of estimating the local crack driving force from remote loading and geometric parameters in a standardised specimen. Given the well-defined geometry and loading configuration of SE(B) specimens, such theoretical evaluations serve as a reliable reference against which alternative, field-based methodologies can be assessed. As introduced in the previous chapter, this calculation employs the standard expression for SE(B) specimens, which relates the applied load and geometry to the stress intensity

factor via a shape function. The relevant equations are listed as Equation (2-1) and (2-2), in which P is the load applied on the three-point beam, S is the distance between the supporting pins, W and B the height and thickness of the beam, and a_e is the effective crack length. When used as a benchmark, the comparison not only highlights the potential advantages of the full-field post-processing approach, but may also reveal characteristic behaviours of short fatigue cracks, including possible microstructural sensitivity and crack-tip shielding effects, which are not captured by conventional linear-elastic, geometry-driven formulations.

$$K = \frac{P}{B\sqrt{W} f(\frac{a_e}{W})} \tag{2-1}$$

$$f(\frac{a_e}{W}) = \frac{3\frac{S}{W}\sqrt{\frac{a_e}{W}}}{2\left(1+2\frac{a_e}{W}\right)\left(1-\frac{a_e}{W}\right)^{\frac{3}{2}}}\left[1.99 - \frac{a_e}{W}\left(1-\frac{a_e}{W}\right)\left\{2.15 - 3.93\left(\frac{a_e}{W}\right) + 2.7\left(\frac{a_e}{W}\right)^2\right\}\right] \tag{2-2}$$

Based on the measured specimen geometry, applied load, and effective crack lengths, the Mode I SIF ranges for the two samples were calculated to be 15.36 ± 0.24MPa·m$^{0.5}$ (Sample A) and 16.85 ± 0.27MPa·m$^{0.5}$ (Sample B). These uncertainties reflect combined errors arising from load precision ($\pm 0.5\%$), dimensional measurements of the specimen (± 20 μm), and crack length measurements (± 5 μm).

The Mode I SIF values obtained using the finite element post-processing method based on full-field displacement measurements show close agreement with the theoretical estimates derived from standard SE(B) formulations, as summarised in Table 2.2. This agreement demonstrates the capability of the post-processing approach to reliably quantify Mode I crack-tip mechanical fields in fatigue experiments, without requiring explicit knowledge of the applied load or specimen geometry.

TABLE 2.2

Mode I and mode II stress intensity factors for sample A and B, obtained by this work using subset size 96×96 pixels, overlap of 75% with forbidden zone size 200×100 pixels. The results correspond to cracks observed at 2400 cycles for Sample A and at 2200 cycles for Sample B, where the measured crack lengths are approximately 230 μm and 252 μm, respectively.

Sample	Mode I stress intensity factor range ΔK_I (MPa·m$^{0.5}$)	Mode II stress intensity factor range ΔK_{II} (MPa·m$^{0.5}$)
A	16.98 ± 0.42	0.37 ± 0.21
B	15.95 ± 0.48	0.65 ± 0.64

The local analysis also reveals a minor contribution from Mode II loading. The ability to extract both Mode I and Mode II stress intensity factors, particularly Mode II, offers a valuable opportunity to characterise mixed-mode loading conditions within the local crack coordinate frame using full-field measurements. As the local displacement field governs crack propagation, the proposed method enables direct access to the relevant field-controlling parameters. Understanding the interplay between Mode I and Mode II components is particularly important in materials and geometries where crack paths deviate from the principal loading direction, such as in heterogeneous microstructures or under multiaxial loading. Future investigations may focus on crack growth scenarios involving more pronounced crack-tip kinking, to further elucidate its influence on the local crack growth rate.

Although the two studied cracks experienced comparable, predominantly Mode I loading conditions, they exhibited markedly different growth rates: 0.15 μm /cycle for Sample A and 0.35 μm/cycle for Sample B. As shown in Figure 2.1 (c) and (d), both cracks propagated on prism planes; however, the crack in Sample A advanced perpendicular to the c-axis, while the crack in Sample B propagated parallel to the c-axis. This crystallographic orientation difference may underlie the observed discrepancy in growth rates. Detailed discussions of crack growth behaviour as a function of crystallographic direction can be found in [335]. These observations highlight the

importance of accounting for crystallographic effects in fatigue analyses, particularly in hexagonal close-packed (HCP) materials such as Zircaloy-4.

In digital image correlation (DIC), there is an inherent trade-off between the measurement uncertainty and the spatial resolution of the resultant displacement field. A larger subset size generally reduces displacement uncertainty during the correlation process, as the increased amount of image information within each subset improves the robustness of matching operations [100]. However, this comes at the expense of displacement field resolution, as larger subsets lead to a coarser spatial sampling across the specimen surface. This can limit the ability to resolve fine-scale features or gradients near the crack tip, particularly in the case of short cracks. For calculations involving the J-integral, careful treatment of the crack-tip region is also essential. Previous studies have shown that both the precise location of the crack tip and the presence of low-quality data near discontinuities can significantly affect the reliability of field-based fracture metrics [118, 204]. These issues are particularly relevant when dealing with short cracks, where field gradients are often steep and data quality near the crack tip is highly variable. Therefore, the sensitivity of the computed ΔK values to three key parameters, the DIC subset size, crack-tip position uncertainty, and the size of the forbidden zone, was investigated in further detail in this study.

To investigate the effect of subset size in digital image correlation, four square subset sizes ranging from 48×48 to 128×128 pixels were considered, each with a fixed 75% overlap. Figure 2.5 presents the results, where each data point represents the average ΔK value computed across the full range of integral contours (ranging from 13 to 42, depending on subset size), and the associated error bars indicate the standard deviation across these contours.

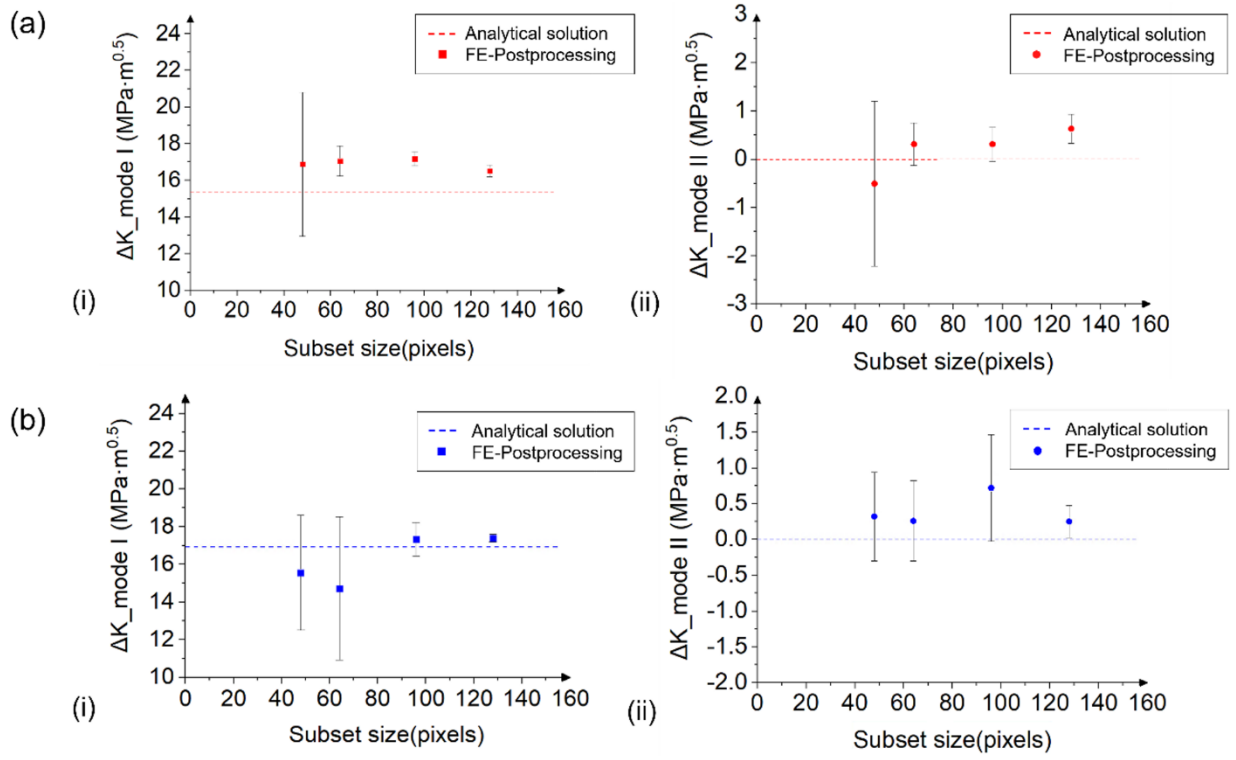

FIGURE 2.5

Effect of DIC subset size on the calculation of stress intensity factors. (red: sample A; blue: sample B; rectangular: mode I; circle: mode II). The horizontal line shows the expected value for pure bending of the specimen.

A clear trend is observed in which the uncertainty in the computed ΔK values increases as the subset size decreases. This effect arises from the reduced number of image features available within smaller subsets, which leads to lower accuracy in the displacement field and thus introduces greater uncertainty in the imposed boundary conditions for the J-integral calculation. For Sample B, a similar pattern is observed, with more stable results consistently obtained at larger subset sizes.

Figure 2.6 (a) illustrates the effect of crack-tip position uncertainty on the computed stress intensity factor range. The DIC analysis was conducted using a subset size of 96×96 pixels with 75% overlap. Based on the resolution of the optical system, the expected uncertainty in locating the crack tip is estimated to be less than 5 μm. To evaluate the sensitivity of the analysis to this uncertainty, the crack-tip position in the finite element model was systematically varied by up to ± 30 μm from the measured location, corresponding to a variation in a/W of approximately 1%.

The results indicate that the computed Mode I stress intensity factor range, ΔK_I, is relatively insensitive to this level of crack-tip positional error. Even in the worst-case scenario involving a 30 μm offset, the mean deviation in ΔK_I remains below 5%. These findings suggest that the finite element post-processing method exhibits a degree of robustness to minor uncertainties in crack-tip positioning, provided the displacement field input is of sufficient quality. Such insensitivity can be advantageous in practical applications, where precise identification of the crack tip in high-magnification imaging may be limited by resolution or contrast, or complicated by the presence of three-dimensional mixed-mode effects, where the observed surface crack tip may not accurately represent the actual crack front.

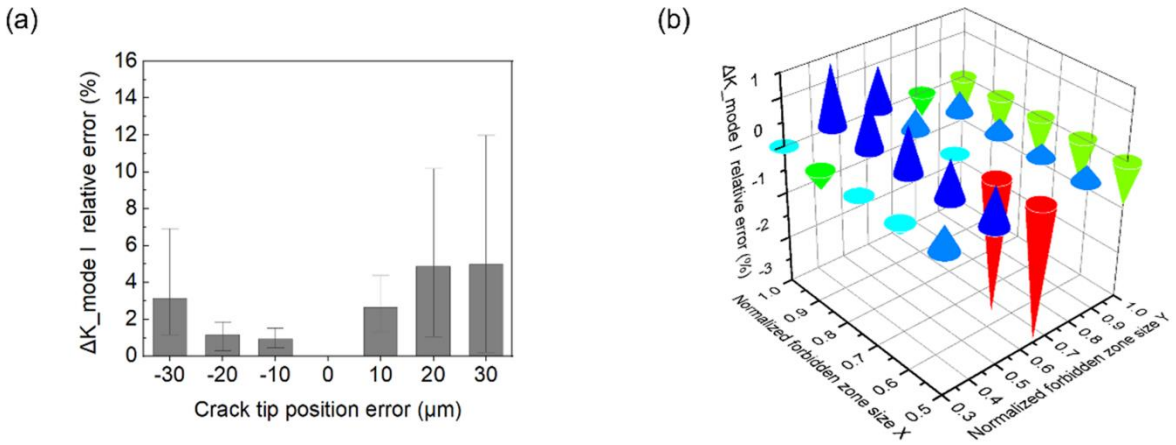

FIGURE 2.6
(a) Effect of erroneous crack tip position on the error of mode I stress intensity factor range; (b) Effect of forbidden zone size on the error of mode I stress intensity factor range.

The forbidden zone is used to exclude displacement field data in the immediate vicinity of the crack. To assess the sensitivity of the results to the size of this zone, a series of forbidden zones with varying lengths and widths was applied to a single image dataset, and the resulting variation in the computed Mode I stress intensity factor range, ΔK_I, was compared, as shown in Figure 2.6 (b). The dataset corresponds to a subset size of 96×96 pixels with 75% overlap, applied to an image of 800×700 pixels.

The dimensions of each forbidden zone were normalised relative to the image size in both the X and Y directions. A representative zone of 0.75×0.6 (240×150 pixels) was selected as the reference case, and the relative error in ΔK_I was calculated with respect to this baseline. The results indicate that variations in the forbidden zone dimensions have only a minor influence on the computed ΔK_I values, suggesting that the analysis method is relatively robust to missing displacement data near the crack. This insensitivity represents a key advantage of using local full-field data to evaluate crack driving forces. The results demonstrate that, even when displacement data in the immediate vicinity of the crack are discarded due to quality concerns, the loading condition at the crack tip can still be uniquely determined from the surrounding field information. This provides the method with notable flexibility and robustness for practical applications.

2.4 Conclusions

For the study of short fatigue cracks, full-field digital image correlation (DIC) measurements have been employed as input boundary conditions for finite element analysis to compute the local J-integral and stress intensity factors under elastic monotonic crack opening. A case study on short cracks in Zircaloy-4 demonstrated that this approach enables characterisation of local crack-tip driving forces without requiring prior knowledge of global parameters such as applied load, total crack length, or specimen geometry. Only the local crack-tip region is utilised, and both Mode I and Mode II stress intensity factors can be extracted. This allows for a detailed evaluation of local crack-tip conditions, including mixed-mode effects, which are often present in short crack growth.

In addition to demonstrating the feasibility of this local approach, the study systematically examined its sensitivity to three key data-processing parameters: DIC subset size, crack-tip position uncertainty, and the dimensions of the forbidden zone. The results show that crack-tip offsets up to ±30 μm lead to changes in ΔK_I of less than 5%, and forbidden zones smaller than about 320×250 pixels produce variations of less than 3%. The subset size mainly affects the

consistency of the computed values, and the results show that sufficiently large subsets yield stable ΔK estimates. With an appropriate choice of subset size, the method remains robust to crack-tip positional uncertainty and to variations in the forbidden-zone dimensions. This robustness reflects a major advantage of the method, namely that the crack-tip loading conditions can be reliably inferred from the surrounding displacement field, even when displacement data in the immediate vicinity of the crack are incomplete, degraded, or entirely absent. As long as high-quality displacement measurements can be obtained at a modest distance from the crack tip, with a speckle pattern, subset size, and imaging configuration that provide sufficient resolution for the loading condition and accuracy required, the method remains effective despite local data loss near the crack face. This makes it well suited for high-resolution, micro-scale experiments in which factors such as speckle deterioration, surface topography or imaging artefacts may compromise measurement quality in the immediate crack-tip region.

Chapter 3

Crack Field Analysis by HR-EBSD and SEM-DIC of Short Fatigue Cracks in Nickel

3.1 Introduction

The previous chapter introduced an approach for evaluating crack driving forces from full-field displacement measurements, enabling the characterisation of local crack-tip driving forces without prior knowledge of global boundary conditions. This versatile framework allows the extraction of mixed-mode stress intensity factors, demonstrating effectiveness in analysing short fatigue cracks.

However, the focus was primarily on validating applicability rather than exploring the underlying mechanisms of short crack growth in greater detail. Interactions between crack-tip plasticity and microstructural features remain insufficiently understood, particularly when examined under more challenging experimental conditions designed to reflect various loading scenarios, or in cases where cracks are surface-breaking rather than through-thickness.

Building on this foundational work, the present study aims to address these gaps through a carefully designed experimental programme. This involves a comprehensive investigation of the detailed response of crack-tip driving forces using multiple full-field measurement techniques. Particular attention is directed towards capturing their in-situ evolution under different remote loading conditions. The aim is to probe deeper into the local interactions influencing short crack propagation and to refine the methodology for broader application and enhanced reliability.

A detailed review of the literature, as presented in Chapter 1, has established that the fundamental distinction between short and long cracks lies in the scale at which their propagation is governed. While long cracks are primarily influenced by macroscopically averaged driving forces and can be described using global parameters such as theoretical ΔK from remote loading, short cracks exhibit highly variable behaviour fundamentally governed by local conditions near the crack tip.

As shown in Chapter 1 (Figure 1.11), short crack growth rates display significant scatter and fail to align with the fitted $\mathrm{d}a/\mathrm{d}N-\Delta K$ relationship established for long cracks. This discrepancy highlights a critical limitation of conventional Paris law, which are incapable of capturing the microstructural sensitivity inherent in short crack propagation. The complexity of short cracks arises from two interrelated mechanisms: crystallographic control and crack-tip plasticity, whose interaction plays a decisive role in determining crack propagation behaviour. A more detailed analysis of these mechanisms is essential and constitutes the central focus of this chapter.

The classification of microstructurally short cracks and mechanically short cracks has been introduced in the Literature Review. Microstructurally short cracks are those whose lengths are comparable to or smaller than characteristic microstructural features. Their propagation is heavily influenced by local crystallographic orientations, grain boundary interactions, and slip transfer mechanisms. The literature has demonstrated that such cracks are particularly sensitive to changes in crystallographic orientation and can be deflected, arrested, or even shielded by microstructural barriers. For instance, Ludwig et al. [235] utilised synchrotron X-ray microtomography (μXCT) to reveal how grain boundary interactions influence crack deflection and arrest in cast aluminium alloys. Birosca [241] employed μXCT and EBSD to characterise cracks in Ti-6246, demonstrating that the local grain structure exerts a dominant influence on crack path evolution. Marrow et al. [188] extended this approach to study magnesium, employing μXCT, digital volume correlation (DVC), and diffraction contrast tomography (DCT) to illustrate how crystallographic crack growth and interactions with twin interfaces affect local crack growth rates.

On the other hand, mechanically short cracks may extend beyond individual microstructural units but remain insufficiently long for their crack-tip plastic zones to be negligible relative to the total crack length. In these cases, local plasticity exerts a significant influence on the crack-tip driving force, particularly under cyclic loading where slip bands are repeatedly activated. The breakdown of classical stress field descriptions, such as the K-dominance assumption, highlights the importance of considering plasticity effects in short crack analysis. Localised plasticity can interact with microstructural barriers, redistribute stresses, and introduce additional energy dissipation mechanisms.

These two mechanisms, crystallographic control and crack-tip plasticity, are not independent but act synergistically to influence short crack propagation. While previous studies have addressed these factors separately, the actual crack driving force resulting from their complex interplay

during fatigue loading remains unclear. A key challenge lies in accurately evaluating this driving force when traditional methods fail to capture its evolution under varying loading conditions.

The local driving force of a short fatigue crack is associated with its growth through well-defined physical explanations. This was proposed by Chan and Lankford [255], who established a power-law correlation between the crack-tip plastic strain range and the stress intensity factor range (ΔK). Their cumulative plastic strain criterion established that crack propagation occurs incrementally when the accumulated local plastic strain within a crack-tip element exceeds a critical threshold (ε_P^*), forming a foundational framework for modelling short fatigue crack growth. Expanding on these principles, Musinski and McDowell [256] introduced Fatigue Indicator Parameters (FIPs) to incorporate microstructural effects into fatigue modelling, an approach that has become instrumental in computational models aimed at predicting microstructure-sensitive crack growth.

It has been proved that the Fatigue Strain (FS) parameter, the elastic-plastic fracture mechanics (EPFM) ΔJ-integral, and the cyclic crack-tip displacement range (ΔCTD) are closely connected as the crack metrics for predicting its propagation [259], particularly in the form of crack-tip opening and sliding displacements. The fundamental mechanism underlying these correlations is the role of plastic strain accumulation at the crack tip, as emphasised by subsequent studies by McDowell and Dunne [248]. Although these parameters have predominantly been used to advance mechanistic understanding and fatigue life modelling, the insights they provide into crack-tip deformation processes offer a valuable foundation for microstructure-sensitive alloy design.

In engineering applications, the fatigue loading experienced by cracked components is rarely an ideal constant-amplitude scenario; instead, it typically involves variable-amplitude and complex load spectra. Consequently, the influence of load history becomes a fundamental factor that must be considered. The crack-tip field of short fatigue cracks also undergoes complex variations under such conditions, representing an area that remains to be thoroughly investigated.

When discussing the load-dependence of fatigue crack growth, it is commonly recognised that a single overload can induce a larger plastic zone and compressive residual stresses at the crack tip, thereby reducing the crack growth rate. In 1971, Elber introduced the concept of crack closure [336]. Some researchers consider plasticity-induced crack closure to be one of the most critical explanations for the retardation effect [337-344], while others argue that this phenomenon may not occur [54]. To address this phenomenon, various studies have proposed alternative explanations such as crack-tip blunting [345], crack deflection [346], strain hardening at the crack tip [347], and residual stresses ahead of the crack tip [54] to elucidate the underlying mechanisms.

Various techniques have been employed to investigate the influence of overload on fatigue crack growth. For instance, Salvati et al. [348] combined EBSD, FIB-DIC, and FEM methods to examine the highly deformed (lattice distortion) region near the overload position, concluding that a complex residual stress field exists around the crack-tip region. Lee et al. [349] used neutron diffraction and electric potential measurements to study crack behaviour after a tensile overload. The electric potential method (DCPD) enabled precise tracking of crack opening loads during fatigue cycles. Their results showed that increased compressive residual stress, crack-tip blunting, and secondary cracks were key factors affecting crack opening behaviour. Additionally, several synchrotron X-ray experiments [350-354] have been carried out to assess the overload-affected crack-tip field. Researchers have employed various approaches, including DIC [355, 356] and X-ray diffraction [350, 351, 353, 354] methods, to gain insights into the underlying mechanisms. Some studies have also attempted to evaluate the stress intensity factor after overload, for example, through fitting of LEFM solutions [353], aiming to further understand the effects of overload on crack growth behaviour.

Since the local crack-tip field ultimately governs crack propagation, accurately characterising this region is essential for comprehensive investigation. Local full-field observations are particularly valuable, as they directly capture the detailed interactions between plasticity, crack-tip

deformation, and microstructural features. Different techniques provide varying types of information, and how the measurement data is processed must be carefully considered to ensure meaningful interpretation. Given the complexity and scale of short fatigue cracks, achieving sufficiently high spatial resolution and sensitivity is crucial for capturing relevant characteristics. Therefore, developing and applying targeted full-field observation techniques, tailored to extract critical parameters from complex measurements, becomes indispensable for advancing the understanding of short crack growth mechanisms under complex loading conditions.

Synchrotron experiments have enabled significant progress in the study of short fatigue crack growth by providing three-dimensional visualisation and field measurements. These techniques have greatly advanced understanding in this area, but researchers are increasingly recognizing limitations related to high costs and resolution constraints. To address these challenges, various SEM-based full-field measurement techniques have been developed, with High-Resolution Electron Backscatter Diffraction (HR-EBSD) strain mapping demonstrating unique advantages in resolution, crystallographic characterisation, and plasticity assessment.

SEM-based techniques excel at capturing localised deformation with high spatial resolution, providing critical insights into microstructural interactions and plasticity. HR-EBSD, particularly effective for examining slip bands and grain boundaries, has been used by Guo, Britton, and Wilkinson [253] to characterise these interactions. Its combination with Differential Aperture X-ray Laue Microdiffraction (DAXM) also enables quantitative assessment of stress concentrations near grain boundaries [138]. Integrating EBSD with Digital Image Correlation (DIC), Carroll et al. [128] achieved sub-grain scale measurements of plastic strain fields during fatigue crack propagation, while Jiang et al. [254] employed SEM-DIC to study strain localisation during early crack propagation. Additionally, Koko et al. applied HR-EBSD to investigate local deformation mechanisms such as twins [220] and slip bands [357], linking strain field evolution to crack-

driving forces. These findings pave the way for this study to advance and tailor these techniques towards more detailed and targeted exploration of short fatigue crack phenomena.

3.2 Methodology

3.2.1. Material, Sample Preparation and Fatigue Crack Initiation

The material used in this study is a nickel-based superalloy with a two-phase equilibrium microstructure consisting of gamma (γ) and gamma-prime (γ') phases. The microstructure observed in SEM is shown in Figure 3.1. The γ phase forms the matrix in which γ' precipitates are embedded. Due to their similar lattice parameters and both possessing a cubic crystal structure, the γ and γ' phases exhibit aligned cubic-lattice edges, resulting in minimal lattice mismatch. This alignment enhances the mechanical compatibility between the phases, contributing to the alloy's high-temperature strength and fatigue resistance.

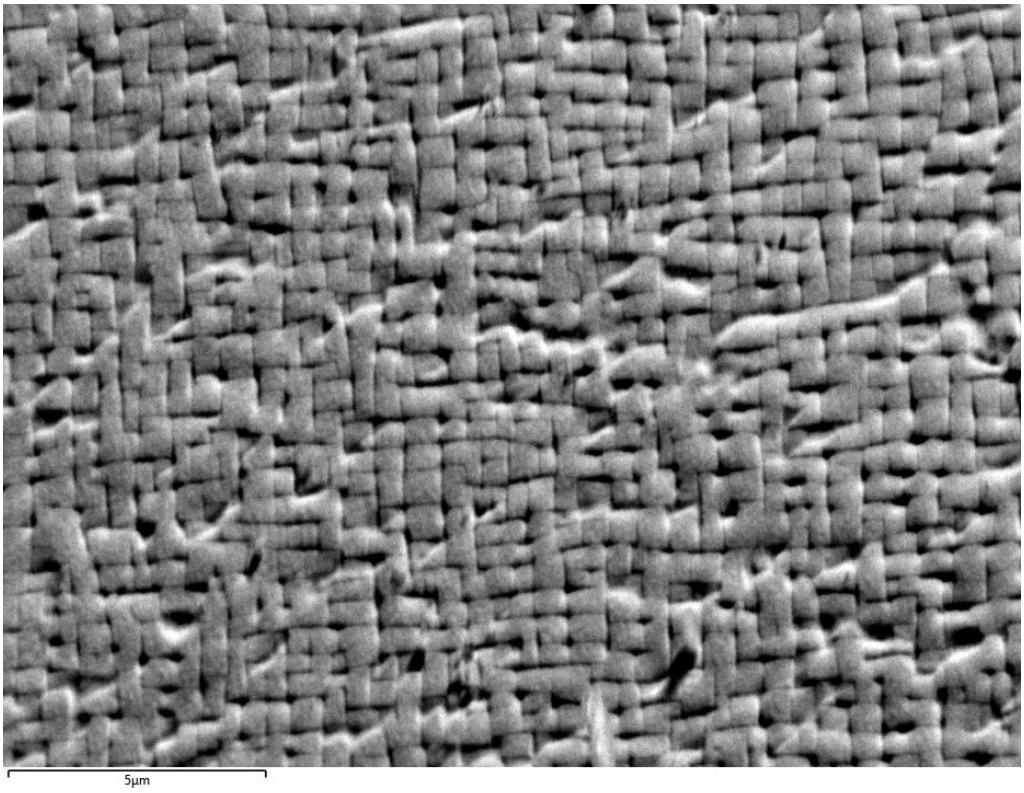

FIGURE 3.1
Forescattered electron (FSE) image showing the microstructure of the two-phase nickel-based superalloy.

Specimens for this study were prepared by laser machining from a single crystal foil of the nickel-based superalloy described above[1], with the surface normal oriented near the [001] direction. The shape and dimensions of the specimens are presented in Figure 3.2. To meet the requirements of HR-EBSD analysis, the specimens underwent electro-polishing to achieve a high-quality surface, capable of producing sharp and well-resolved diffraction patterns essential for precise strain mapping and crystallographic analysis. The polished surface provided excellent imaging quality under SEM, with secondary electron (SE) and forescattered electron (FSE) modes clearly revealing γ and γ' phases and producing suitable random speckle patterns for DIC, as shown in Figure 3.1.

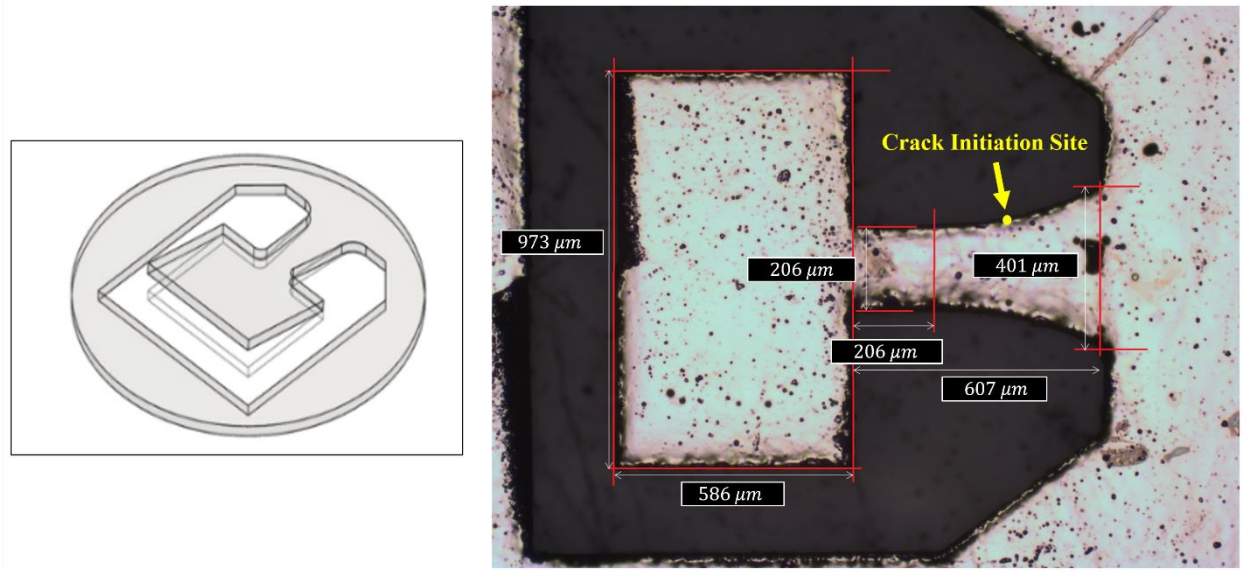

FIGURE 3.2
Geometry (3 mm diameter, 150 ± 0.92 μm thickness) and dimensions of the specimen. All marked dimensions have an uncertainty of ± 3.5 μm from boundary identification.

The electro-polishing process [358] was carried out using an electrolyte solution detailed in Table 3.1. To maintain the electrolyte at a low temperature, a methanol bath cooled via liquid nitrogen was employed, stabilising the temperature at approximately -50 ± 5°C throughout the polishing

[1] *Samples were kindly provided by the Oxford Micromechanics Group. The specimen was designed, machined, and prepared by Robin Scales and Dr Jicheng Gong.*

procedure. A variable-current power source, equipped with a 10-second interval timer, was configured to deliver controlled polishing conditions. The positive terminal (anode) was connected to a platinum-tipped fine reverse-action tweezer holding the specimen, while the negative terminal (cathode) was linked to a submerged steel cage cathode within the electrolyte bath. This setup ensured uniform polishing across the specimen surface, enhancing both diffraction quality and microstructural visibility.

TABLE 3.1
Electropolishing Solution Recipe [358].

Order	Chemicals	Volume [ml]	Volume [%]
1st	Methanol	118	59
2nd	Ethylene Glycol	70	35
3rd	Perchloric Acid	12	6

Subsequently, the specimens were subjected to high-frequency fatigue testing aimed at initiating a fatigue crack[2]. Each specimen was attached to a high-power ultrasonic generator capable of producing mechanical vibrations at a frequency of 20 kHz. In this experiment setup, the outer ring of the specimen aligns with the holder, while the hammerhead part serves to augment its inertia. By carefully designing the inertia mismatch, the hammerhead moves asynchronously with the outer ring of the specimen, exhibiting a phase-shifted motion in response to ultrasonic displacement. This delayed reaction induces cyclic bending within the 'neck' region of the specimen, achieving very-high-frequency tension-compression loading under fully reversed conditions ($R = -1$). The maximum stress is concentrated at the specimen surface, promoting localised fatigue damage initiation [359, 360].

[2] *High-frequency fatigue testing was carried out by Robin Scales. The author was present during the experiment and contributed through discussions, but was not directly involved in conducting the tests.*

A non-contact laser-based monitoring system, complemented by automated analysis tools, was employed to detect crack initiation during fatigue testing [358]. In this setup, a laser beam is directed at the specimen surface to record its vibration, while a camera monitors the movement of the reflected laser spot. By examining the span of the laser spot, as illustrated in Figure 3.3, short fatigue cracks can be detected immediately upon initiation, as they alter the compliance of the specimen. This approach enables precise and timely detection of crack initiation events, typically occurring within a few seconds to several minutes. The high sensitivity and efficiency of the detection method ensure that crack initiation can be captured accurately at the earliest stages, facilitating subsequent investigations of crack-tip fields.

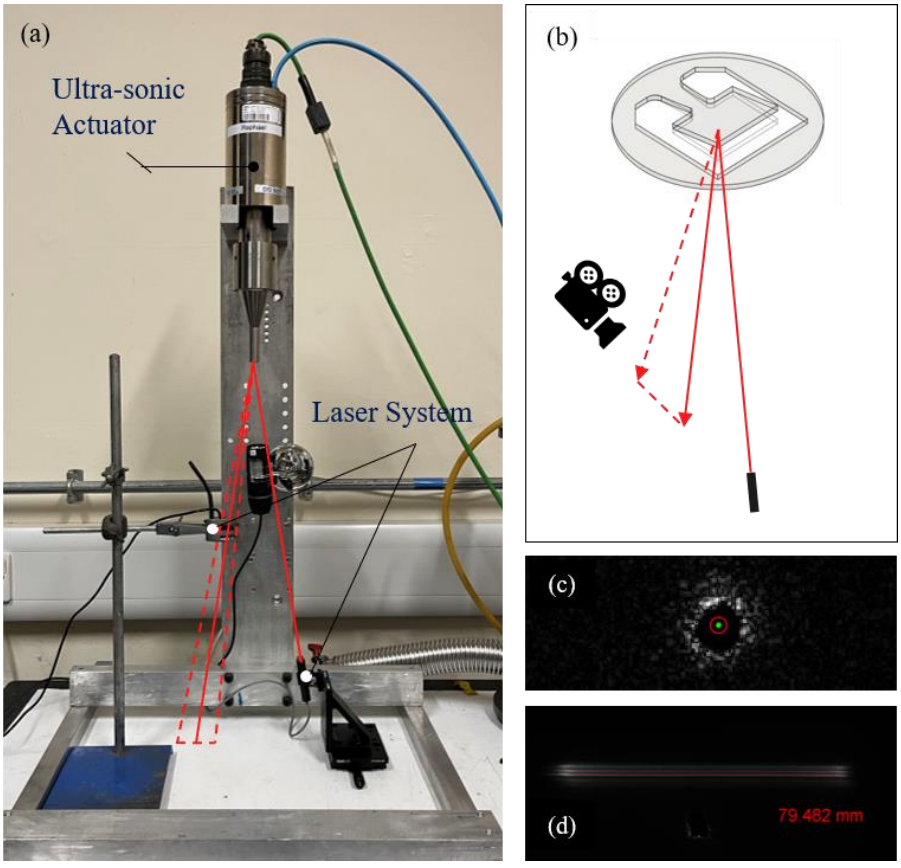

FIGURE 3.3
Experimental setup for fatigue crack initiation: (a) Arrangement of the actuator and laser-based monitoring system. (b) Schematic diagram of the laser optical path. (c) Recorded image and corresponding laser spot fitting. (d) Movement of the laser spot during the experiment.

During fatigue crack initiation, the vibration amplitude was incremented in steps of 50 s duration. Figure 3.4 shows the history of the vibration amplitude during ultrasonic fatigue pre-cracking, where a noticeable increase at about 325 s indicates the onset of crack nucleation. A test specimen with a fatigue crack of approximately 95 µm surface length was then selected. In the uncracked state, the fatigue bending strain and stress amplitudes are in linear proportion to the vibration angle amplitude of the specimen. Hence, an elastic dynamic FEM simulation of the specimen was used to calculate the stress amplitude and its distribution. The vibration angle at the start of the loading step in which crack initiation was detected corresponded to a maximum surface stress amplitude of 282.5 ± 4.5 MPa at the initiation site.

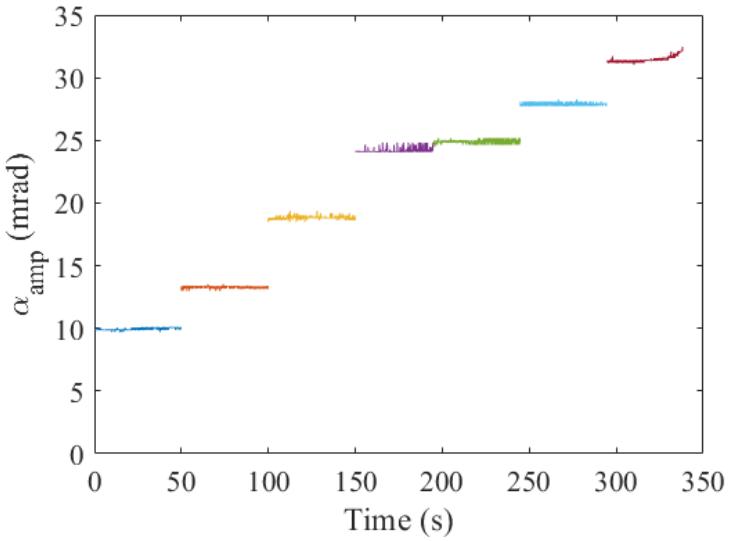

FIGURE 3.4
Vibration amplitude during ultrasonic fatigue pre-cracking. Crack nucleation was detected by the rise in vibration amplitude, α_{amp}, at about 325 seconds.

3.2.2. In-situ Tensile Testing in the SEM

This specimen was carefully mounted onto a 2 kN *Deben*® 70° pre-tilted loading stage, which was installed inside a *Carl Zeiss*® *Merlin* field emission gun scanning electron microscope (FEG-SEM) to facilitate high-resolution imaging and diffraction measurements during mechanical testing. The setup aimed to provide precise control over tensile and fatigue loading conditions while capturing

detailed crack-tip deformation and strain fields with high spatial resolution. The overall configuration within the SEM vacuum chamber, captured by the USB camera installed inside the chamber, is shown in Figure 3.5.

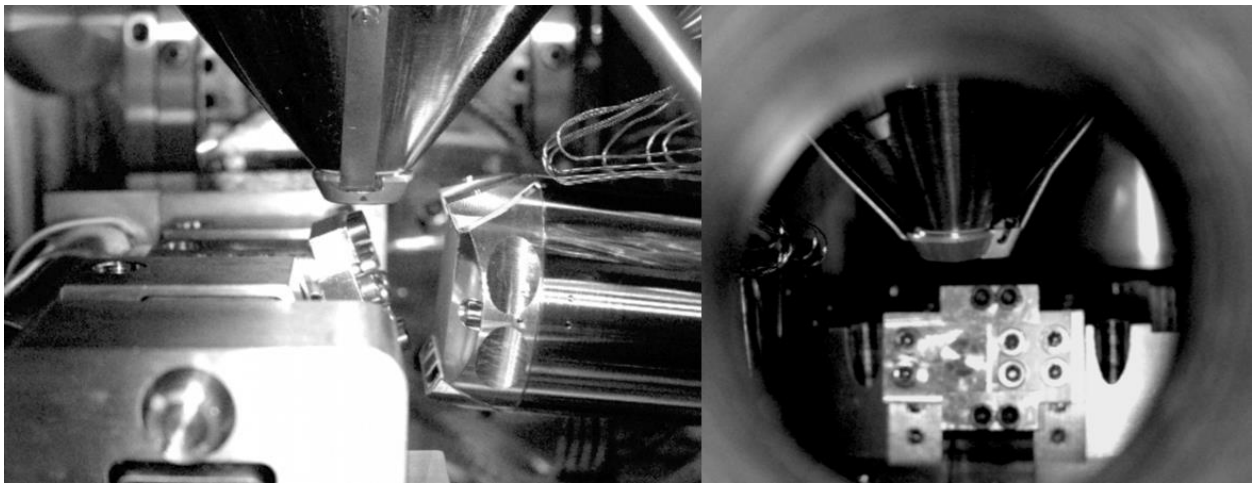

FIGURE 3.5
Overall configuration within the SEM vacuum chamber, captured by the internal USB camera: (a) Side view showing the electron gun, stage, and EBSD detector. (b) View from the EBSD detector's perspective, highlighting the jig positioned on the stage.

To replicate the fatigue load applied to the crack, a custom-designed jig was employed. This jig was specifically manufactured for this project to securely hold the specimen and effectively transmit the load during testing. The load transfer was achieved through two pins that made direct contact with the hammerhead, ensuring stable and reproducible loading conditions. This configuration allowed good alignment of the specimen along the desired loading direction, with the maximum applied force oriented parallel to the near [100] crystallographic direction, i.e., along the 'neck' of the Ni-alloy foil specimen, as shown in Figure 3.6.

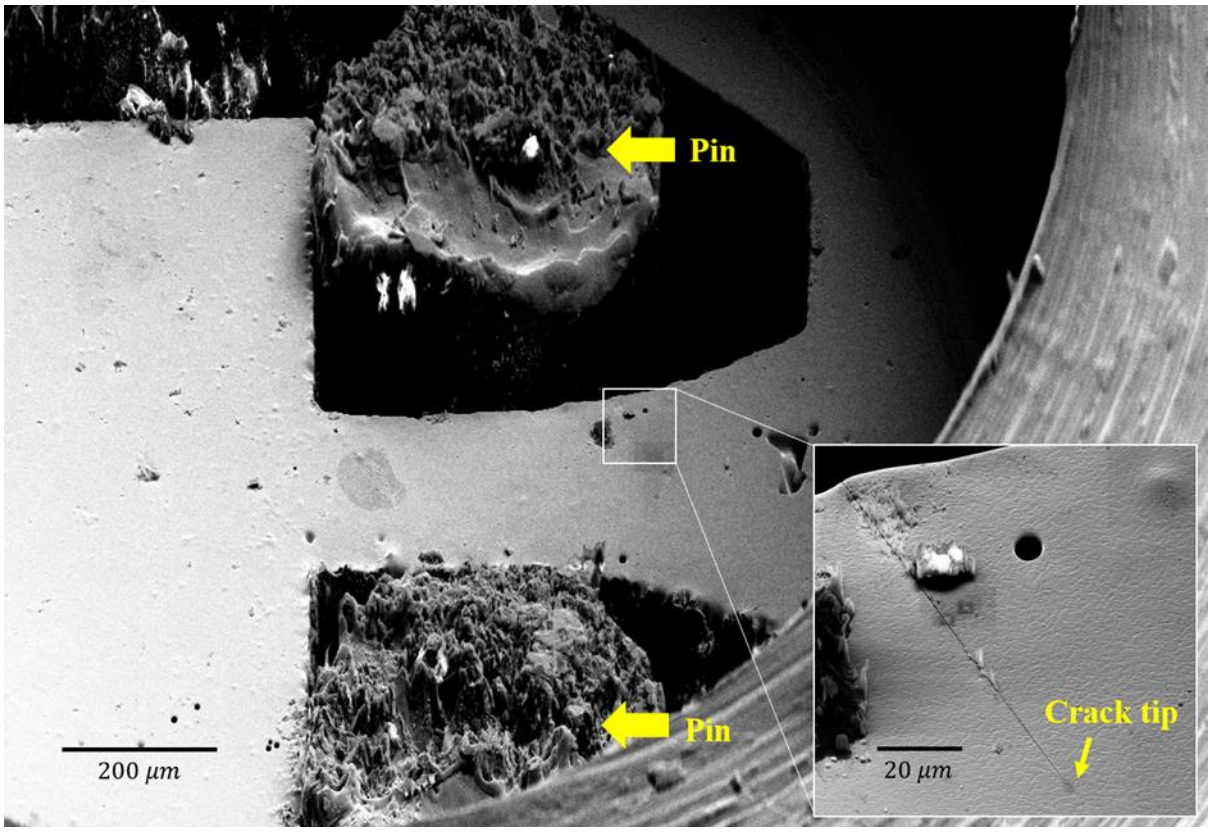

FIGURE 3.6
Secondary electron (SE) image of the tensile loading setup. The force parallel to the 'neck' of the Ni-alloy foil specimen was applied via the two pins (marked). The inset shows a magnified view of the crack.

Before testing, thorough cleaning of the SEM chamber and loading stage was performed to ensure a contamination-free environment, which is critical for achieving high-quality electron imaging and diffraction data. Six cycles of plasma cleaning and purging were carried out, with each cycle lasting approximately one hour. This cleaning procedure aimed to remove residual contaminants on the specimen surface and maintain optimal imaging conditions throughout the experiment.

The testing procedure comprised two separate experiments, both following a structured approach with force control and in-situ measurements, as summarised in Table 3.2 and Figure 3.7.

TABLE 3.2
Summary of the testing procedure.

Experiment 1	
Steps	Tensile Load (N)
0	0.00 (Reference)
1	0.50
2	1.00

Experiment 2					
Cycle 1		Cycle 2		Cycle 3	
Step	Tensile Load (N)	Step	Tensile Load (N)	Step	Tensile Load (N)
0	0.00 (Reference)	5	0.00	10	0.00
1	0.25	6	0.50	11	0.25
2	0.50	7	1.00	12	0.50
3	0.75	8	1.50	13	0.75
4	1.00	9	2.00	14	1.00

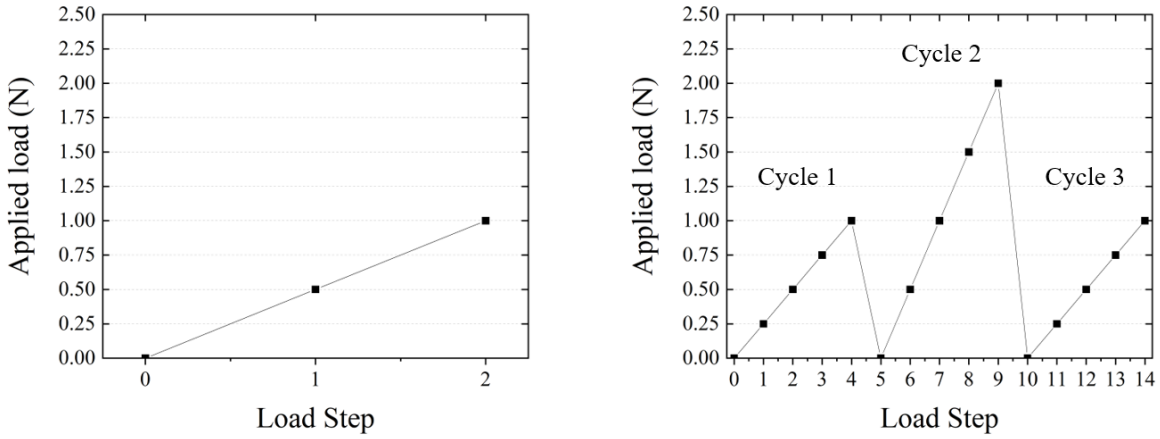

(a) Experiment 1 (b) Experiment 2

FIGURE 3.7
Summary of the testing procedure for the two experiments, showing load step versus applied load.

Experiment 1:

This experiment involved a monotonic loading process consisting of two load steps, in addition to an initial observation (step 0) that established an unloaded reference. The load was incremented from 0 to 1 N in steps of 0.5 N. During each load step, force control was applied until the target load was reached, after which the control mode was switched to displacement control. A 5-minute holding phase followed each load increment to allow stabilisation before measuring the crack-tip filed.

Experiment 1 was designed to validate the experimental setup, explore parameter settings for field measurements, and refine the analysis methods.

Experiment 2:

The second experiment featured a cyclic loading procedure consisting of three complete cycles, each with distinct loading protocols:

Cycle A: This cycle followed a similar monotonic loading process as Experiment 1, with four loading steps of 0 N – 0.25 N – 0.5 N – 0.75N – 1 N. After completing measurements at 1 N, the specimen was unloaded to 0 N to initiate the next cycle.

Cycle B (Overload Cycle): To investigate the influence of overload on short fatigue cracks, the load increment was increased to 0.5 N per step for higher loading levels. The four steps were 0.5 N, 1 N, 1.5 N, and 2 N. After measurements at 2 N, the specimen was unloaded to 0 N before proceeding to the final cycle.

Cycle C: This cycle replicated the monotonic loading pattern of Cycle 1 with the same load steps: 0 N – 0.25 N – 0.5 N – 0.75 N – 1 N.

Experiment 2 was specifically designed to study the effect of overload on short fatigue crack behaviour, incorporating an overload cycle (Cycle B) flanked by two normal cycles (Cycle A and Cycle C) for comparative analysis.

In total, 15 measurements were performed throughout Experiment 2, covering each loading step and the three 0 N reference steps at the beginning of each cycle. As in Experiment 1, force control was applied during loading, followed by a switch to displacement control with a 5-minute load-holding phase to ensure stabilisation before each measurement.

3.2.3. Concurrent HR-EBSD Strain Mapping and DIC of FSE Images

3.2.3.1. ForeScatter Electron Imaging

In conventional SEM-based DIC studies, secondary electron imaging (SEI) is the most commonly used technique. However, when conducting EBSD scans, the sample is typically tilted to a high angle (around 70°), and maintaining a smooth, flat surface is essential to ensure high-quality EBSD patterns. This combination of high tilt and flat surface presents significant challenges for SEI-based DIC, including issues related to poor contrast, image distortion, and reduced signal intensity. Additionally, introducing artificial markers to enhance speckle patterns for DIC would severely compromise EBSD pattern quality, rendering this approach impractical.

To overcome these limitations and enable simultaneous DIC and EBSD analysis, this study leveraged the Forescattered Electron (FSE) detectors integrated into the EBSD system. Forescattered imaging [220, 357] refers to the acquisition of contrast using electrons that are scattered forward from a highly tilted sample surface and collected by the forescattered electron detectors (FSDs) positioned around the EBSD phosphor screen. In this configuration, the FSDs record high-energy electrons emerging at shallow exit angles, producing images that exhibit strong crystallographic, topographic and atomic-number contrast. In the context of DIC, high-quality imaging refers to sufficient spatial resolution, contrast variation and feature fidelity to provide a

reliable speckle pattern. Because FSE imaging reflects intrinsic microstructural contrast rather than an externally applied speckle, the resulting patterns maintain physical authenticity while still enabling correlation across loading steps. This provides a viable route for combined DIC and EBSD measurements without interfering with EBSD acquisition.

FSDs offer unique advantages when imaging microstructures in SEM, particularly at the steep sample tilt used during EBSD. When the primary electron beam interacts with the material, electrons scatter in multiple directions; the FSDs selectively detect those emerging forward from the tilted surface, leading to several distinct contrast mechanisms:

- Topographic Contrast: Variations in surface morphology alter scattering angles, enhancing surface detail through shadowing effects and height differences.
- Atomic Number (Z) Contrast: Differences in atomic density influence scattering cross-sections, allowing heavier elements to produce stronger signals, thereby enabling phase differentiation in multiphase samples.
- Orientation Contrast: Crystallographic orientation differences lead to electron channelling effects, where certain orientations scatter electrons more efficiently towards the detector. This effect is particularly pronounced in polycrystalline materials, where grains of different orientations produce varying contrast.

These contrast mechanisms are relevant to the present material system. In particular, the two-phase nickel-based superalloy examined in this study benefits from the Z-contrast of FSE imaging, which provides sufficient contrast between γ and γ' regions to support DIC tracking without requiring artificial speckle deposition.

Unlike SEI, which detects low-energy electrons (<50 eV) emitted from only the top few nanometres of the sample surface, FSE imaging captures higher-energy forward-scattered electrons originating from deeper interaction volumes. This enhances the ability to detect

crystallographic orientation and atomic density variations that are less accessible through SEI. Most importantly, the consistent alignment of FSE and EBSD systems ensures that FSE imaging can be performed concurrently with EBSD mapping, using the same field of view and imaging conditions.

3.2.3.2. Scan Data Acquisition

In this study, electron backscatter patterns (EBSPs) and forescattered electron (FSE) images were collected concurrently using an *Oxford Instruments Symmetry*® Detector, which offers high-performance capabilities for simultaneous EBSD mapping and FSE imaging. This advanced detector system is equipped with a high-resolution CMOS sensor for EBSP acquisition and multiple forescatter diodes (FSDs) arranged around the central phosphor screen to capture FSE images. The components of a typical high-performance EBSD detector, including the *Symmetry*® Detector used in this study, are illustrated in Figure 3.8.

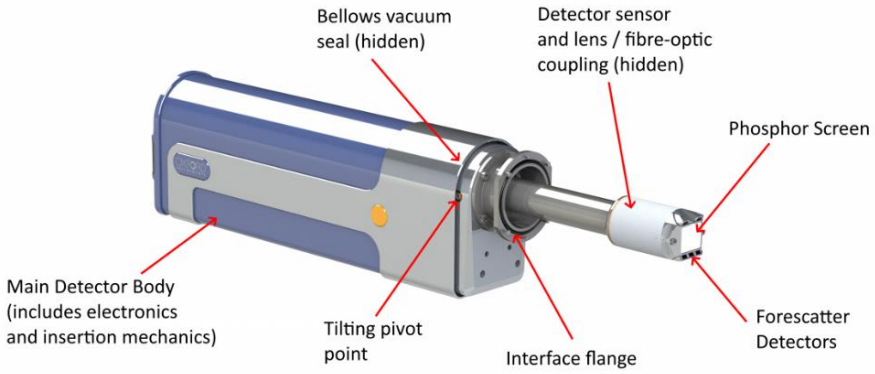

FIGURE 3.8
A typical, high-performance EBSD detector showing the major components.
Available at: https://www.ebsd.com/ebsd-techniques/ebsd-detectors

The simultaneous acquisition of EBSPs and FSE images was achieved under identical imaging conditions, providing consistent field of view and efficient data collection. An accelerating voltage of 20 kV, a beam current of 10 nA, and a working distance of 18 mm were employed throughout the in-situ measurements to ensure optimal diffraction and imaging quality.

For EBSD mapping, Kikuchi patterns were collected using the CMOS sensor with a resolution of 1244 × 1024 pixels in high-resolution mode. A step size of 0.15 µm was utilised over a scan area of 138 × 103 steps, resulting in a mapped region of approximately 20 µm × 15 µm. An exposure time of 4 ms per pattern was applied, with 2-frame averaging employed to enhance signal quality and reduce noise.

Simultaneously, FSE images were captured using the five forescatter diodes (FSDs) positioned around the central phosphor screen (upper left, upper right, lower left, lower centre, and lower right). Among these channels, the lower centre diode was found to produce the highest quality images. The resulting FSE images had a resolution of 1024 × 768 pixels, corresponding to a pixel size of 0.02 µm and a region of interest (ROI) of approximately 20 µm × 15 µm, matching the mapped area of the EBSD scan. Imaging was performed at a magnification of approximately 5400×, with an image dwell time of 5 µs per pixel.

3.2.3.3. HR-EBSD Strain Calculation

The calculation of the elastic strain field was performed through an iterative cross-correlation process between electron backscatter patterns (EBSPs) and a reference pattern ($EBSP_0$) assumed to be stress-free [149]. This analysis was conducted using the commercial software *CrossCourt*® *Rapide* v4.6.

Prior to analysis, raw EBSPs were subjected to background correction using a 'white' scan collected during the experiment. Data points of poor quality were filtered out based on a kernel average misorientation (KAM) criterion, with points exhibiting KAM > 0.4 excluded from analysis. The entire field of view was treated as a single grain, with reference points selected from the unstressed wake region of the crack. During this selection process, regions with low KAM and Band Contrast greater than 120 were preferred, ensuring that the chosen reference area was reasonably strain-free and exhibited satisfactory imaging quality.

Cross-correlation was performed on groups of Regions of Interest (ROIs) within the raw patterns. ROIs were manually selected to focus on sharp, clearly imaged, and well-exposed Kikuchi bands, while avoiding scratched areas or regions with poor exposure and insufficient clarity. This careful selection process aimed to enhance accuracy and reliability during correlation analysis.

To further improve pattern quality and reduce errors, a tailored pattern filter was applied using the built-in algorithm in *CrossCourt*® *Rapide* v4.6. The filtering process involved applying a Fast Fourier Transform (FFT) to the raw EBSPs to identify dominant Kikuchi line components in the frequency domain. Low and high-frequency noise was then filtered out before transforming the patterns back to real space. This approach effectively enhanced feature clarity, improved precision, and minimised errors during the correlation process.

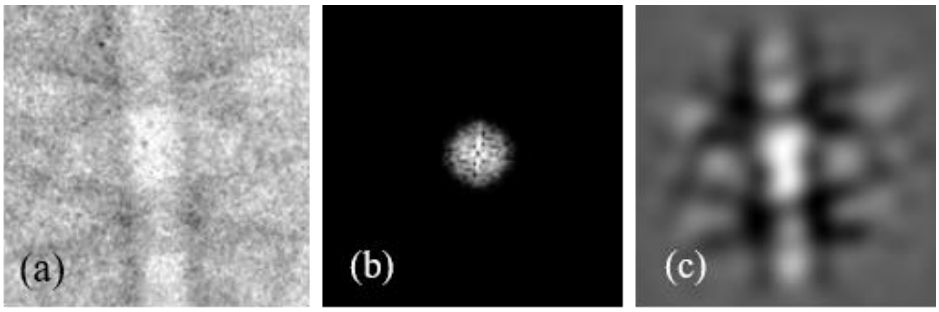

FIGURE 3.9
FFT Filtering to enhance cross-correlation quality. (a) Original pattern ROI affected by noise. (b) FFT transform of the pattern ROI. (c) Filtered pattern ROI obtained by applying inverse FFT.

The analysis consisted of two main stages: a cross-correlation pass to measure relative pattern shifts, and a remapping pass to eliminate large rotations. Following this, the deformation gradient tensor was calculated using measurements of crystal interplanar spacing and zone axes. Assuming no traction perpendicular to the sample surface and applying an elastic material model with single crystal anisotropy, the elastic strain tensor at each point within the scanned area was obtained.

For detailed descriptions of the calculation procedures to obtain the deformation gradients, the reader is referred to [142, 144, 361, 362].

3.2.3.4. Digital Image Correlation

Digital Image Correlation (DIC) of FSE images was performed to calculate the crack-tip displacement field. Using a *xCorrRBMCorrection* code [363], raw images were pre-processed to remove translational rigid body movements and crop to maintain a consistent field of view throughout the testing procedure. The images were carefully calibrated with reference to SE images to establish an accurate pixel-to-length conversion, ensuring reliable quantitative analysis.

The DIC analysis in this work was conducted between reference images (0 N load) and successive images captured at all loading steps, utilizing the Least Squares Matching (LSM) method implemented in the standard DIC software *LaVision® DaVis* 8.4.0.

A subset size of 64 × 64 pixels^2 and a step size of 8 pixels were employed for the analysis. This subset size was selected to ensure sufficient intensity variation and feature density within each subset, enabling robust and accurate correlation. The step size provided a good balance between spatial resolution and computational efficiency. The selection of subsets ensured the inclusion of sufficient speckle patterns, specifically the natural contrast provided by the two-phase microstructure of the material, which was critical for achieving high DIC accuracy.

The analysis was performed using the LSM algorithm as implemented in the software, with the following parameters: a maximum of 100 iterations, a correlation value threshold of 0.3, and 6th-order spline image interpolation for precise displacement calculation. To enhance measurement reliability, outliers were removed based on a threshold criterion where the deviation from the average exceeded 2.5 times the standard deviation. Additionally, a smoothing function involving a 2nd-order polynomial fit over a 7 × 7 pixels^2 area was applied to further reduce noise and improve the consistency of the calculated displacement fields.

3.2.4. Finite Element Post-processing and Direct Evaluation of Energy Integrals from Deformation Gradient

The obtained displacement field can be directly used as boundary conditions in Finite Element (FE) post-processing, as illustrated in Chapter 2. Briefly, the rectangular grid of displacement data served as the input for the FE analysis, with a grid of the same size and spacing constructed to ensure alignment (i.e., one data point per node). Under the assumption of linear anisotropic elasticity, the finite element analysis was performed using CPS4 elements within the *ABAQUS*® software (version 6.14). Direct evaluation of the J-integral was achieved using the built-in algorithms based on the virtual crack extension method. The change in the J-integral between load steps was employed to evaluate variations in the mixed-mode stress intensity factors (SIFs). This was accomplished through a mode-decomposition method [214, 215, 218], which applies an auxiliary field to decompose the constituent field elements. The employed code[3] is available at: *10.5281/zenodo.6411604*.

There are two different approaches to process the strain field data obtained by HR-EBSD. One approach is to integrate the strain field to obtain the corresponding displacement field [220, 357] (code[4] available at: *10.5281/zenodo.6411568*), which can then be applied as boundary conditions in finite element analysis, as described above. The alternative approach is to directly calculate J-integrals and stress intensity factors (SIFs) from the deformation gradient field [155] (code[5] available at: *10.5281/zenodo.6411484*), which corresponds to the strain field through a straightforward relationship. A full derivation of these formulations, along with the corresponding

[3] *Developed by A. Koko*.

[4] *Developed by A. Koko*.

[5] *Developed by A. Koko*.

implementation details, is provided in [364]; the key steps are briefly summarised here for completeness and as framed in the context of the present study.

3.2.4.1. Strain to Displacement Integration and FE Post-processing

The process of determining the displacement field by integrating the strain field is achieved by employing the concepts of the finite element method. This approach involves constructing a discrete system of equations from known deformation measurements, such as deformation gradients or engineering strains, and solving this system to reconstruct the displacement field. The deformation gradient F_{ij} , which quantifies the local changes in geometry between the reference and deformed configurations, serves as the fundamental input for this process.

The deformation gradient F_{ij} is expressed as

$$F_{ij} = \frac{\partial x_i}{\partial X_j} = \delta_{ij} + \frac{\partial u_i}{\partial X_j} \tag{3-1}$$

where $u_i = x_i - X_i$ is the displacement vector, X_i and x_i denote the coordinates in the reference and deformed configurations, respectively, and δ_{ij} is the identity tensor. By utilising the concepts of finite element interpolation, the displacement field is approximated as a linear combination of nodal displacements through shape functions N_I:

$$u_i(X_j, t) = \sum_{I=1}^{N_{nodes}} N_I(X_j) u_i^I(t) \tag{3-2}$$

where N_I are shape functions, and $u_i^I(t)$ are the nodal displacement values. The reference and current coordinates are interpolated using the same shape functions applied to the displacement field. This ensures consistency when evaluating the deformation gradient, as both the original (reference) and deformed coordinates are approximated through the same interpolation scheme. By discretizing the continuous deformation into nodal displacements, the deformation gradient $\frac{\partial x_i}{\partial X_j}$

can be effectively calculated based on how the nodes' positions (X_i^I and x_i^I) change between the reference and deformed configurations.

The finite element discretisation leads to a linear system of equations:

$$A_{ij}d_j = b_i \tag{3-3}$$

Here, A_{ij} is a coefficient matrix constructed from shape functions and their gradients, while d_j is the vector of unknown nodal displacements. The vector b_i represents the discretised deformation gradient data. Specifically, b_i encapsulates the deformation gradient components F_{ij} evaluated at selected computational points within each element. These components are obtained from experimental measurements and are mapped onto the discretised domain through interpolation functions.

The solution method depends on the relationship between the number of equations N_{Eq} and unknowns N_{Un}. When $N_{\mathrm{Eq}} = N_{\mathrm{Un}}$, a unique solution exists if the matrix A_{ij} is full-rank. For overdetermined systems ($N_{\mathrm{Eq}} > N_{\mathrm{Un}}$), a least-squares method is applied, yielding the solution

$$d_j = \left(A_{ij}^T A_{ij}\right)^{-1} A_{ij}^T b_i \tag{3-4}$$

Underdetermined systems ($N_{\mathrm{Eq}} < N_{\mathrm{Un}}$), require additional constraints or regularisation techniques, such as applying the Moore-Penrose pseudoinverse. The quality of the solution can be assessed through the condition number of A_{ij}.

Based on the concepts described above, a 3D volume representing the HR-EBSD-probed membrane layer was defined in MATLAB using hexahedral eight-node elements to construct the mesh. The membrane thickness was set based on values reported for similar Ni-based materials [365-370], with 8.9 nm chosen as a representative value widely adopted in the literature. While convergence improves and out-of-plane displacements decrease with increasing assumed penetration depth, an accurate estimation of this parameter is critical for reliable fracture parameter

calculations. The substantial variability in reported values across the literature reflects the inherent difficulty of precisely defining EBSD depth resolution. Although the chosen thickness may compromise numerical convergence, it aligns with the most frequently reported and broadly accepted value. This aspect and its implications are further discussed later. To enhance computational efficiency and minimise memory usage, the stiffness matrix and related data were assembled at the Gaussian points into a sparse matrix. This approach enabled the use of MATLAB's *lsqminnorm* algorithm to solve for the nodal displacements.

The obtained displacement field was corrected for rigid body movement before applying the mode-decomposition technique. This technique separates the displacement field into three distinct components: symmetric (u^I), in-plane antisymmetric (u^{II}), and out-of-plane antisymmetric (u^{III}) fields. This separation is achieved by superimposing an auxiliary field onto the actual field, where the auxiliary field $\overline{\boldsymbol{u}}$ is generated by mirroring the original field $\boldsymbol{u}$ along the x_1-axis. Through this operation, the symmetry properties of the field are altered in a controlled manner, allowing the original field to be decomposed into the desired components, as shown in the equations below.

$$u = u + \frac{1}{2}\bar{u} - \frac{1}{2}\bar{u} = \underbrace{\frac{1}{2}\begin{pmatrix} u_x + \overline{u_x} \\ u_y - \overline{u_y} \\ u_z + \overline{u_z} \end{pmatrix}}_{mode\ I} + \underbrace{\frac{1}{2}\begin{pmatrix} u_x - \overline{u_x} \\ u_y + \overline{u_y} \\ 0 \end{pmatrix}}_{mode\ II} + \underbrace{\frac{1}{2}\begin{pmatrix} 0 \\ 0 \\ u_z - \overline{u_z} \end{pmatrix}}_{mode\ III} \tag{3-5}$$

The decomposed displacement fields were applied as boundary conditions for finite element (FE) post-processing. This procedure was implemented using two separate 2D FE models.

In the first 2D FE model, the displacement components associated with Mode I and Mode II were applied to compute K_I and K_{II}. During this step, the *Z*-direction displacement component from Mode I was deliberately ignored to focus exclusively on the in-plane stress intensity factors.

The second 2D FE model accounted for the previously ignored *Z*-direction displacement component from Mode I, along with the displacement field from Mode III. This model was used

to compute the anti-symmetric shear K_{III} and its associated symmetric out-of-plane Mode I contribution (K_{I}^{r}).

3.2.4.2. Direct J-integral Evaluation from Deformation Gradient

Another approach involves directly calculating the J-integral from the displacement gradient field, following a similar decomposition scheme used previously. In this procedure, an auxiliary vector field $\boldsymbol{q_1}$ is constructed to define the integration path direction. This vector field is set to unity near the crack tip and gradually approaches zero as it extends away from the crack tip, with a smooth spatial variation along the local x_1 direction, which is aligned with the crack path. Because the calculation is performed entirely within this crack-tip coordinate frame and uses the measured local fields, it does not rely on assumptions regarding the remote loading. Any influences introduced at the remote boundaries, such as effects associated with loading alignment, are inherently reflected in the measured displacement gradients and therefore propagated into the computed J-integral and stress intensity factors. With the crack tip located at the centre of a regularly spaced mesh, the Equivalent Domain Integration (EDI) calculation is simplified. Given the regular grid structure and the assumption of plane stress conditions, the integration can be performed directly over a zero-thickness surface measurement area, without requiring remapping to the element nodes.

Under this framework, the J-integral calculation is expressed as:

$$J = \sum_{el=1}^{N_{el}} \left[\left(\sigma_{11}u_{1,1} + \sigma_{12}u_{2,1} + \sigma_{13}u_{3,1} - W\right)\frac{dq_1}{dx_1} + \left(\sigma_{22}u_{2,1} + \sigma_{12}u_{1,1} + \sigma_{23}u_{3,1}\right)\frac{dq_1}{dx_2} \right] dA \qquad (3\text{-}6)$$

To separate the contributions of different modes, the total displacement gradient $u_{i,j}$ is decomposed into three individual modes:

$$u_{i,j} = u_{i,j}^{I} + u_{i,j}^{II} + u_{i,j}^{III} = \sum_{M=I,II,III} \left(F_{ij}^{M} - \delta_{ij}\right) \qquad (3\text{-}7)$$

where F_{ij}^{M} represents the deformation gradient associated with mode M, and δ_{ij} is the Kronecker delta, representing the identity matrix components.

To extract different modes of the displacement gradient field, a similar mirror operation is applied. By exploiting symmetry and anti-symmetry conditions, the total field $u_{i,j}$ is decomposed into three parts:

$$u_{i,j} = \frac{1}{2}\left(u_{i,j} + \bar{u}_{i,j}\right) + \frac{1}{2}\left(u_{i,j} - \bar{u}_{i,j}\right) \tag{3-8}$$

Since $u_{i,j} = F_{ij} - \delta_{ij}$, the decomposition of $F_{ij}$is expressed as:

$$\begin{aligned} u_{i,j} = \frac{1}{2}&\begin{bmatrix} F_{11} + \bar{F}_{11} - 1 & F_{12} + \bar{F}_{12} & F_{13} + \bar{F}_{13} \\ F_{21} - \bar{F}_{21} & F_{22} - \bar{F}_{22} & F_{23} - \bar{F}_{23} \\ F_{31} + \bar{F}_{31} & F_{32} + \bar{F}_{32} & F_{33} + \bar{F}_{33} - 1 \end{bmatrix} \\ + \frac{1}{2}&\begin{bmatrix} F_{11} - \bar{F}_{11} & F_{12} - \bar{F}_{12} & 0 \\ F_{21} + \bar{F}_{21} & F_{22} + \bar{F}_{22} - 1 & 0 \\ 0 & 0 & F_{33} - \bar{F}_{33} \end{bmatrix} \\ + \frac{1}{2}&\begin{bmatrix} 0 & 0 & F_{13} - \bar{F}_{13} \\ 0 & 0 & F_{23} + \bar{F}_{23} \\ F_{31} - \bar{F}_{31} & F_{32} - \bar{F}_{32} & 0 \end{bmatrix} \end{aligned} \tag{3-9}$$

To calculate the strain energy density W, the Green-Lagrangian strain tensor ϵ_{ij} is derived from the deformation gradient tensor F_{ij}. The Green-Lagrangian strain tensor is defined as

$$\epsilon_{ij} = \frac{1}{2}\left(F_{is}^{T}F_{sj} - \delta_{ij}\right) \tag{3-10}$$

For small deformations or under the assumption of linearised strain, this can be approximated by

$$\epsilon_{ij} \approx \frac{1}{2}\left(u_{i,j} + u_{j,i}\right) \tag{3-11}$$

The mode-specific deviatoric-strain tensors ϵ_{ij}^{M} and the elastic stress tensors σ_{ij}^{M} are related through Hooke's law, which accounts for anisotropic material behaviour using the stiffness matrix. This relationship can be expressed as

$$\sigma_{ij}^{M} = C_{ijkl}\epsilon_{kl}^{M} \tag{3-12}$$

where C_{ijkl} is the fourth-rank anisotropic stiffness tensor, which defines the material's elastic response. By applying Hooke's law independently to each mode, the strain energy density W associated with each mode can be calculated. This mode-specific calculation enables a precise evaluation of the individual mode contributions to the J -integral.

The Mode I, II, III stress intensity factors and the effective K can be calculated directly from the decomposed J -integrals.

$$J = J_{\mathrm{I}} + J_{\mathrm{II}} + J_{\mathrm{III}} = \frac{K_{\mathrm{I}}^2}{E} + \frac{K_{\mathrm{II}}^2}{E} + \frac{K_{\mathrm{III}}^2}{2\mu} \tag{3-13}$$

$$K_{\mathrm{eff}} = \sqrt{JE} \tag{3-14}$$

3.3 Results

3.3.1. Trace Analysis

The material studied in this work is a single-crystal Ni-based superalloy with a face-centred cubic (FCC) structure. In FCC crystals, plastic deformation primarily occurs through dislocation glide along the {111} slip planes in ⟨110⟩ directions. This results in a total of 12 possible slip systems, each defined by a combination of one {111} plane and one ⟨110⟩ direction lying within that plane.

Trace analysis was performed to identify the active slip system(s) associated with the short fatigue crack. A slip trace is the linear feature formed by the intersection of an active slip plane with the sample surface, typically observed as surface steps or slip lines in electron imaging. By projecting the crystallographic slip planes into the sample surface using the known crystal orientation, theoretical slip traces can be calculated and compared with those observed experimentally.

The results of the trace analysis are shown in Figure 3.10. In this figure, the experimentally observed slip traces are overlaid on a forescatter electron image of the sample surface. The

crystallographic orientation of the single-crystal sample is illustrated using a unit cell schematic, and all candidate slip traces are shown along with their corresponding Schmid factors.

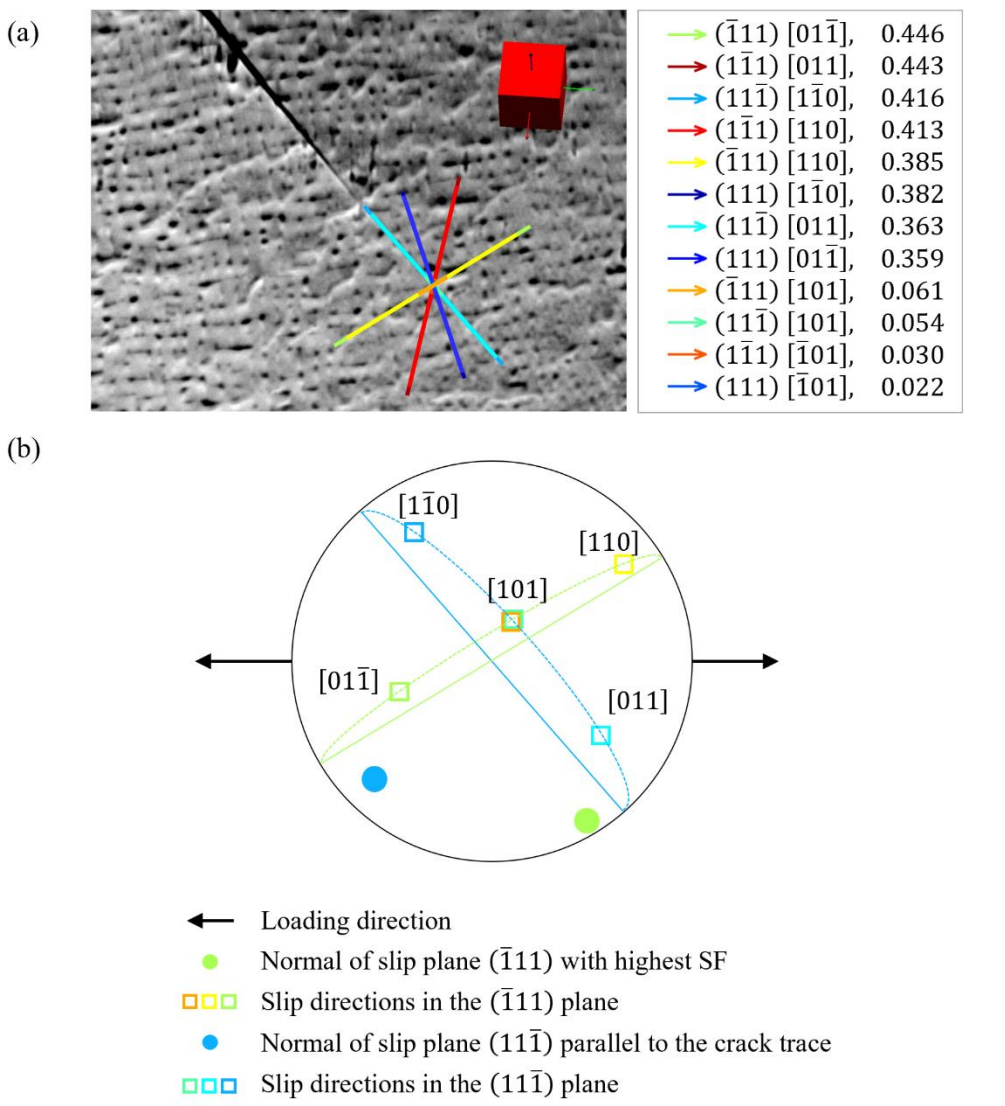

FIGURE 3.10

a) Slip trace analysis, with slip systems overlaid on the FSE image and Schmid factors listed; b) pole figure showing the loading direction, slip plane with the highest Schmid factor, the $(11\bar{1})$ crack plane and the corresponding slip directions in the crack plane. The $(\bar{1}11)$ slip systems are also shown.

The Schmid factor (SF) quantifies the mechanical favourability of a slip system under a given loading condition. It is calculated as:

$$SF = \left| \left(\vec{L_c} \cdot \vec{n_i} \right) \left(\vec{L_c} \cdot \vec{d_i} \right) \right| \tag{3-15}$$

where $\vec{n_i}$ is the slip plane normal and $\vec{d_i}$ is the slip direction, both expressed in the crystal frame, and L_c is the loading direction transformed into the crystal frame using the sample's orientation

matrix. A higher Schmid factor indicates that a slip system is more likely to be activated under the applied uniform load.

As illustrated in Figure 3.10, The crack is parallel to the trace of $(11\bar{1})$, which is almost orthogonal to the specimen surface and inclined at approximately 45° to the loading direction. To better understand the active deformation mechanisms, a pole figure was constructed, showing the loading direction, the slip plane normals and slip directions of the systems with the highest Schmid factors. This orientation suggests that the crack is not aligned with a principal loading direction, and therefore experiences mixed-mode loading, which includes both opening (Mode I) and shear (Mode II or III) components. However, since the crack acts as a strong local stress concentrator, the assumption of uniform stress used in classical Schmid analysis is no longer valid near the crack tip. Therefore, while Schmid factor analysis provides useful insight into potential slip activity, it does not fully capture the complex stress state driving crack propagation. This information was incorporated into the finite element (FE) model to evaluate the theoretical stress intensity factors associated with the experimentally observed crack orientation.

In addition to the primary slip plane identified, trace analysis revealed several other competitive slip systems with comparable Schmid factors. These systems may also participate in local plastic deformation near the crack tip, where the evolution of slip bands is influenced not only by shear-driven activity but also by the opening displacement field associated with Mode I loading. Their combined contribution could therefore affect the subsequent crack-path development under cyclic loading.

3.3.2. Estimate of Expected *J* and *K* from Remote Boundary Conditions

To estimate the expected *J*-integral values, a finite element model of a section of the test specimen was developed in *ABAQUS*® (version 6.14). The model included a crack with the same location, length, and orientation as in the experiment. A tensile load of 1.00 N was applied to the

hammerhead to represent the remote boundary condition ("Remote BC"), in line with the experimental setup. Linear elastic material properties were assigned, with orthotropic stiffness defined based on EBSD orientation data: $D_{1111} = D_{2222} = D_{3333} = 251.3\,GPa$, $D_{1122} = D_{1133} = D_{2233} = 160.9\,GPa$, and $D_{1212} = D_{1313} = D_{2323} = 129.4\,GP$ [358, 371]. The mesh was locally refined to accommodate the geometry of the crack. The simulation used C3D20 elements and the resulting displacement fields are presented in Figure 3.11 and Figure 3.12. The calculated stress intensity factors (SIFs), which increase linearly with load, are summarised in Table 3.3.

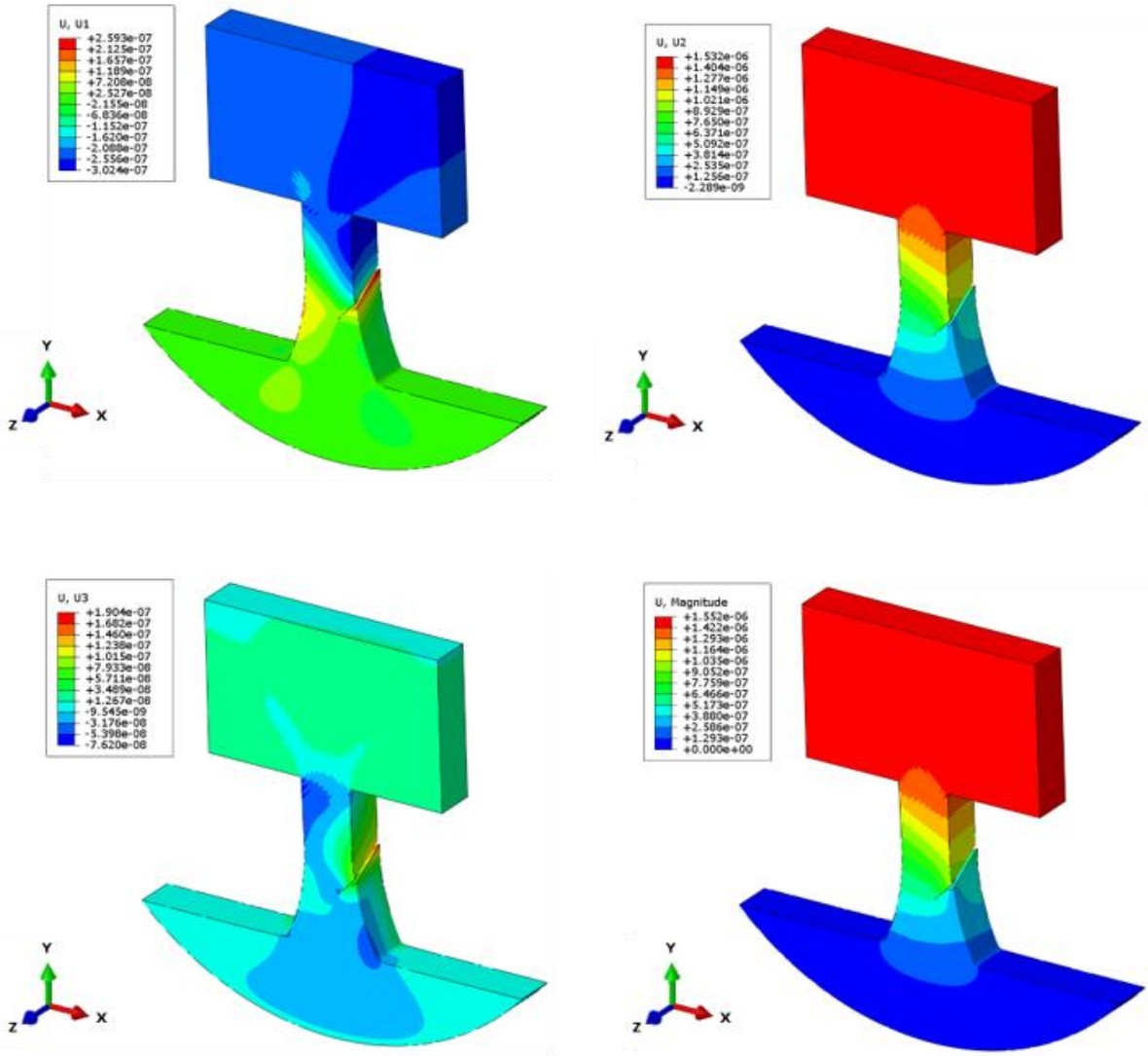

FIGURE 3.11

3D finite element model with a tensile load of 1.00 N applied to the hammerhead as a remote boundary condition. Displacement fields U1, U2, U3, and total displacement magnitude shown (view from one side of the specimen).

TABLE 3.3

Summary of the stress intensity factors and J-integral from finite element model with tensile load 1 N.

Tensile Load 1.00N, Pure Elastic Model	
J	$120.11\ J/m^2$
K_{I}	$4.57\ \mathrm{MPa}\sqrt{m}$
K_{II}	$1.29\ \mathrm{MPa}\sqrt{m}$
K_{III}	$1.97\ \mathrm{MPa}\sqrt{m}$

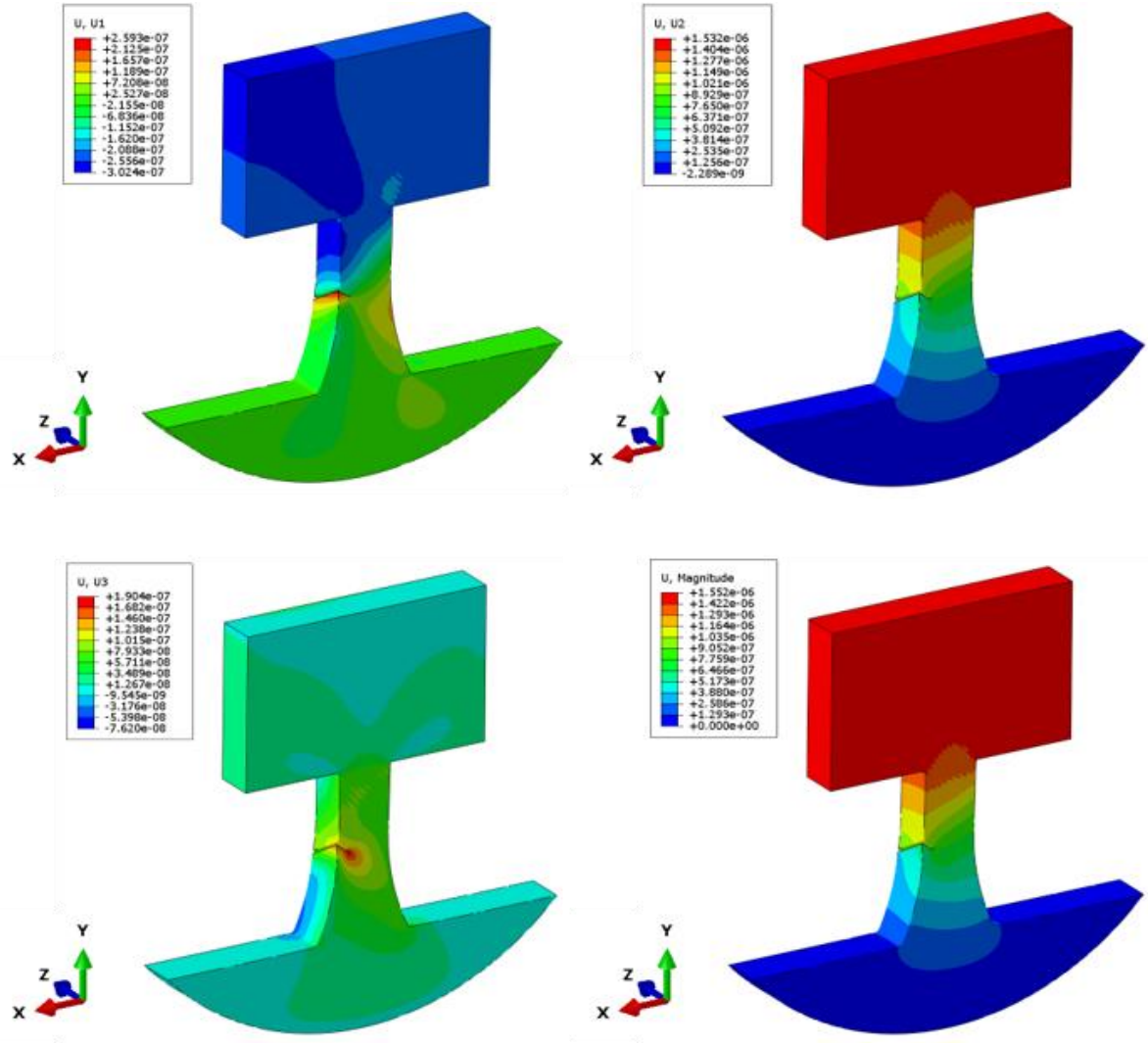

FIGURE 3.12

3D finite element model with a tensile load of 1.00 N applied to the hammerhead as a remote boundary condition. Displacement fields U1, U2, U3, and total displacement magnitude shown (view from the opposite side of the specimen).

This finite element model based on the assumption of linear elasticity was used to provide a theoretical estimate of the crack driving force observed in the experiment. The 3D model strictly followed the actual orientation of the crack plane and revealed a mixed-mode loading condition. The J-integral and SIFs (per N of applied load) were evaluated from the calculated 3D displacement field (using the equivalent domain integral and interaction integral methods natively implemented in ABAQUS) as $J = 120.11$ J m^{-2} N^{-1}, $K_{\mathrm{I}} = 4.57$ MPa m$^{1/2}$ N^{-1}, $K_{\mathrm{II}} = 1.29$ MPa m$^{1/2}$ N^{-1} and $K_{\mathrm{III}} = 1.97$ MPa m$^{1/2}$ N^{-1}. The remote tensile loading of the crack is thus predicted to be dominantly mode I, with lesser but equivalent mode II and mode III components.

3.3.3. Crack Field Analysis of a Monotonic Loading Case

In Experiment 1, once the applied load reached the target at each step, the control mode switched to displacement control. After waiting for the load to stabilise, in situ measurements were initiated. Throughout the experiment, the field of view remained locked at the same location around the crack tip region, with magnification kept constant.

During measurement, ForeScatter Electron (FSE) images were first captured, followed immediately by an EBSD scan. The region covered by the image and the scan was perfectly matched. Figure 3.13 presents three FSE images taken throughout Experiment 1. The crack is clearly visible within the field of view, and the material exhibits satisfactory phase contrast, meeting the requirements of a random speckle pattern suitable for DIC analysis. The three images were corrected for rigid body movement and registered to precisely the same field of view (using a *xCorrRBMCorrection* code [363]). Close inspection of the imaged short fatigue crack reveals a discernible opening as the load increases.

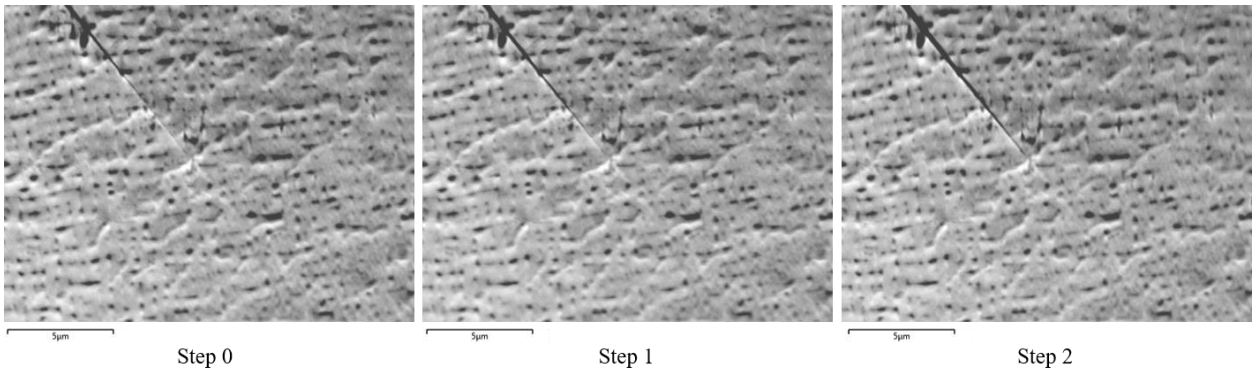

FIGURE 3.13
FSE images taken during Experiment 1.

Digital image correlation (DIC) was performed using the FSE images, and the resulting displacement field is presented in Figure 3.14. A rectangular region focusing on the crack tip was cropped from the original data and rotated to orient the crack horizontally, using built-in functions in *LaVision® DaVis 8.4.0*. This operation was performed to simplify the FE post-processing. Before being applied as boundary conditions in the FE model, rigid body movement correction was applied once again. Figure 3.14 compares the original displacement fields u_x and u_y with the corrected displacement fields $cor.u_x$ and $cor.u_y$ at Step 2. The displacement field reveals a mixed-mode loading condition, characterised by a relatively prominent Mode I component and a minor Mode II component.

The calculation of crack driving force supports the aforementioned observations. The energy integral calculation was performed within a selected area that conformed to the boundaries of the available data. The contour is centred at the crack tip, and the contour number increases with each additional layer of elements contained within it, as shown in Figure 3.15. Specifically, Contour 1 encompasses the element layer immediately surrounding the crack tip, Contour 2 includes an additional layer outside of that, and so on. The crack tip location was determined visually from the FSE images. To minimise potential displacement errors near the crack, a mask was applied around the crack vicinity during the analysis. The J-integral, along with the Mode I (K_{I}) and Mode II (K_{II}) stress intensity factors (SIFs) obtained from the analysis, are presented in Figure 3.15.

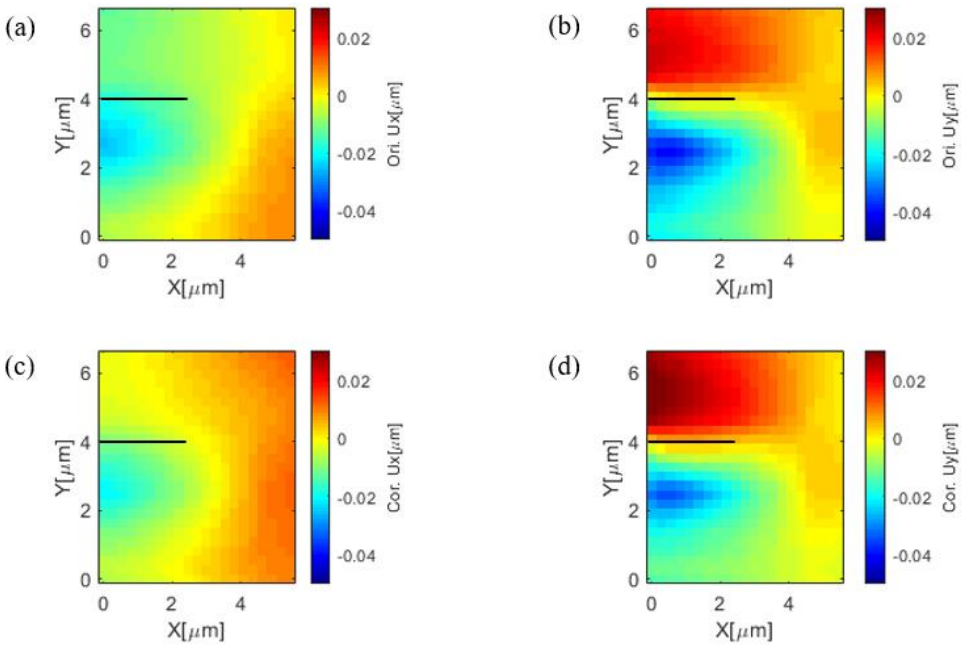

FIGURE 3.14

Displacement fields obtained from DIC at Step 2. (a) Original displacement field u_x. (b) Original displacement field u_y. (c) Corrected displacement field $cor.u_x$ after rigid body movement correction. (d) Corrected displacement field $cor.u_y$ after rigid body movement correction. The black line indicates the location of the crack.

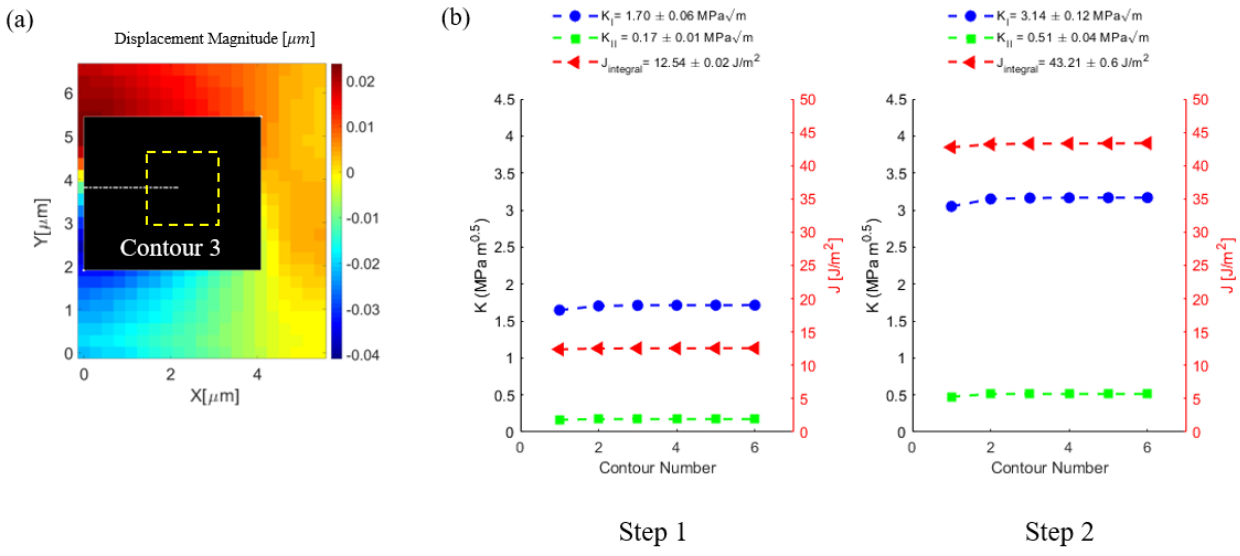

FIGURE 3.15

(a) Contour definition in the DIC-obtained displacement field, cantered at the crack tip. The dashed line indicates a representative contour (No. 3); the black region denotes a forbidden zone near the crack where displacement data were excluded from boundary conditions. (b) J-integral and stress intensity factors evaluated from the field. Good convergence was achieved due to the exclusion of the near-tip zone. Results shown correspond to contours with the best convergence; uncertainties are indicated.

The stress tensor fields calculated using the HR-EBSD method for the peak load step in Experiment 1 (1.00 N) are shown in Figure 3.16. Localised stress concentrations are observed near the crack tip. The stress maps exhibit scattered noise distributed across the entire field of view. A detailed post-experimental analysis revealed that the quality of scan set in this experiment was not optimal. In particular, relatively short exposure times during pattern acquisition, compounded by carbon deposition on the specimen surface during scanning, led to a slightly reduced signal-to-noise ratio in the diffraction patterns. Although the cross-correlation analysis yielded acceptable results, there remains potential for further enhancement in pattern quality. A comparison with subsequent experiments will further illustrate this issue. In the σ_{12} map, a relatively elevated stress field is observed on one side of the crack, which is attributed to localised lattice rotation and rigid-body-like movement induced by asymmetric crack opening. These effects arise due to different constraint across the crack flanks during crack propagation. To reduce such artefacts, a remapping step, performed as a second-pass cross-correlation in the HR-EBSD analysis, was applied. In this step, the test pattern is rotated toward the reference orientation using a finite rotation matrix estimated from the initial correlation. This alignment reduces the apparent lattice misorientation, allowing the subsequent cross-correlation to isolate elastic strain more accurately. Although remapping helped to mitigate the artefact, it did not completely eliminate it.

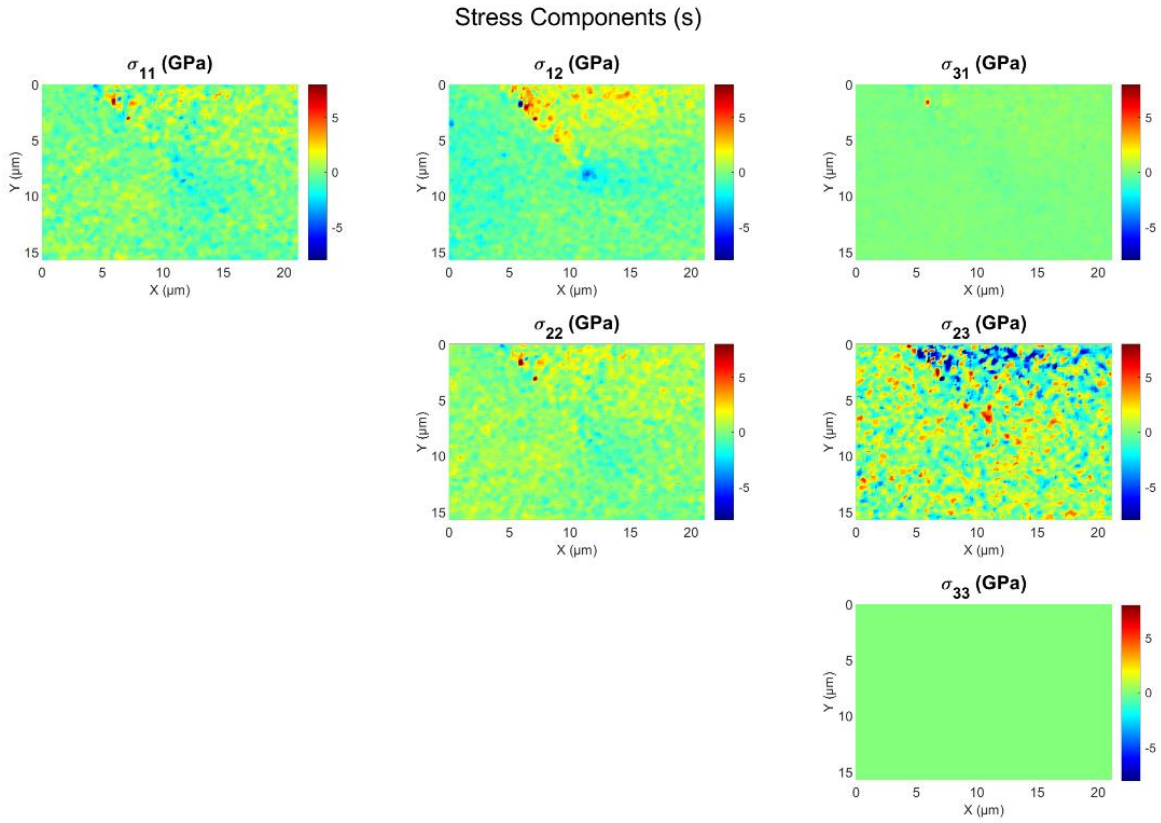

FIGURE 3.16
Elastic stress tensor maps measured at the peak load step (1.00 N) in Experiment 1.

Based on the obtained strain fields, two methods were employed to characterise the crack driving force. Figure 3.17 presents the results obtained using the finite element (FE) post-processing method, while Figure 3.18 shows the results from the direct deformation gradient decomposition approach. The average values and standard deviations of the stress intensity factors and J-integral are reported above each plot.

Table 3.4 further summarises the integral results using two different post-processing approaches, together with results obtained from the DIC-measured displacement field, for direct comparison. These results are also plotted in Figure 3.19.

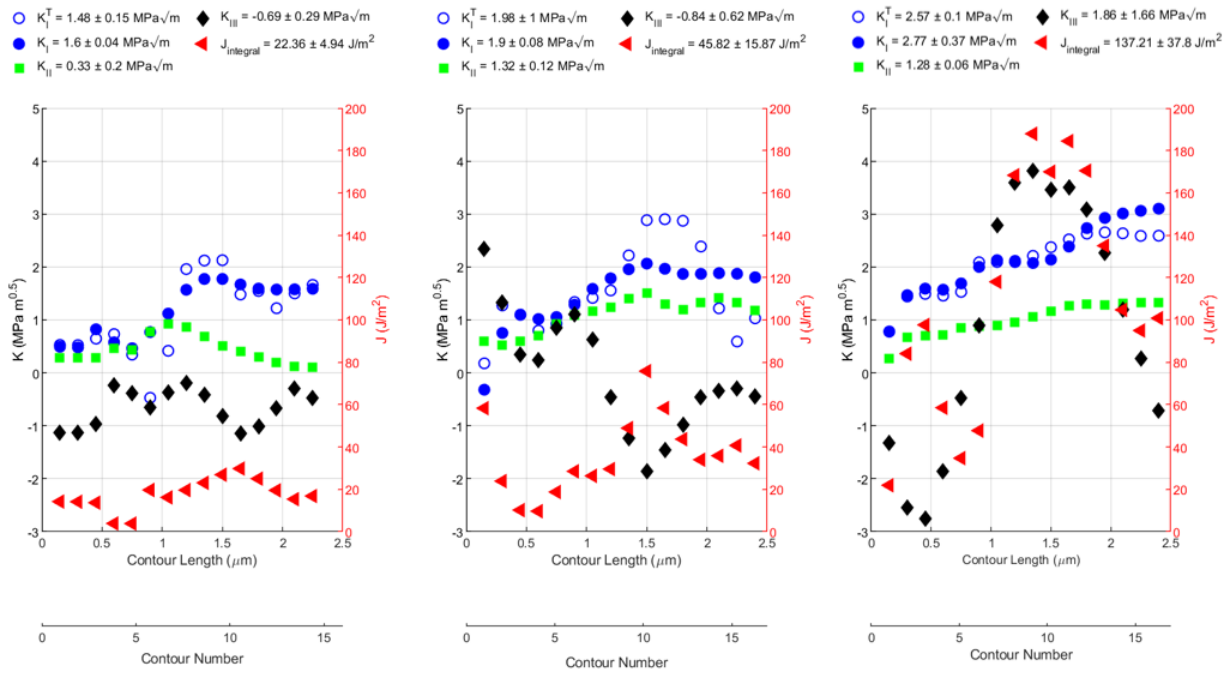

FIGURE 3.17

J-integral and stress intensity factors evaluated from different contours using the finite element (FE) post-processing method. Note that K_I^T denotes the total Mode I contribution, combining the in-plane K_I and the symmetric out-of-plane component K_I^r, obtained from separate 2D models.

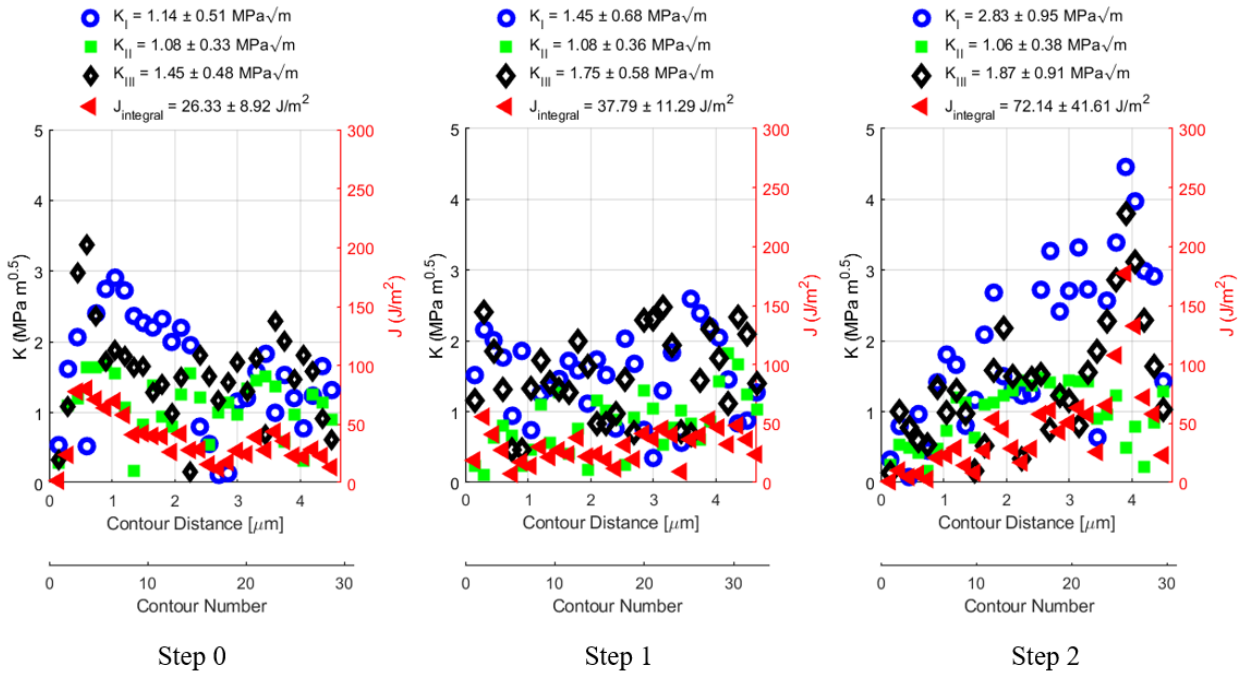

FIGURE 3.18

J-integral and stress intensity factors evaluated using the direct approach without integration.

TABLE 3.4

Summary of the stress intensity factor (MPa·m$^{0.5}$) and J-integral (J·m^{-2}) results from different methods. Note that the ΔK values are calculated as the difference between each step and the reference.

Load (N)	J-integral (EBSD+FE)	J-integral (EBSD+Direct)	J-integral (remote BC)	J-integral (DIC)
0	22.36 ± 4.94	26.33 ± 6.92	0	–
0.50	45.82 ± 15.87 ($\Delta J = 23.46$)	37.79 ± 11.29 ($\Delta J = 11.46$)	60.06	12.54 ± 0.02
1.00	137.21 ± 37.8 ($\Delta J = 114.85$)	72.14 ± 41.61 ($\Delta J = 45.81$)	120.11	43.21 ± 0.60

Load (N)	K_{I} (EBSD+FE)	K_{I} (EBSD+Direct)	K_{I} (remote BC)	K_{I} (DIC)
0	1.48 ± 0.15	1.14 ± 0.51	0	–
0.50	1.96 ± 1.0 ($\Delta K_{\mathrm{I}} = 0.30$)	1.45 ± 0.68 ($\Delta K_{\mathrm{I}} = 0.31$)	2.29	1.70 ± 0.06
1.00	2.57 ± 0.1 ($\Delta K_{\mathrm{I}} = 1.17$)	2.83 ± 0.95 ($\Delta K_{\mathrm{I}} = 1.69$)	4.57	3.14 ± 0.12

Load (N)	K_{II} (EBSD+FE)	K_{II} (EBSD+Direct)	K_{II} (remote BC)	K_{II} (DIC)
0	0.33 ± 0.2	1.08 ± 0.33	0	–
0.50	1.32 ± 0.12 ($\Delta K_{\mathrm{II}} = 0.99$)	1.08 ± 0.36 ($\Delta K_{\mathrm{II}} = 0$)	0.65	0.17 ± 0.01
1.00	1.28 ± 0.06 ($\Delta K_{\mathrm{II}} = 0.95$)	1.06 ± 0.38 ($\Delta K_{\mathrm{II}} = -0.02$)	1.29	0.51 ± 0.04

Load (N)	K_{III} (EBSD+FE)	K_{III} (EBSD+Direct)	K_{III} (remote BC)	K_{III} (DIC)
0	-0.69 ± 0.29 (false)	1.45 ± 0.48	0	–
0.50	-0.84 ± 0.62 (false)	1.75 ± 0.58 ($\Delta K_{\mathrm{III}} = 0.30$)	0.99	–
1.00	1.86 ± 1.66 (false)	1.87 ± 0.91 ($\Delta K_{\mathrm{III}} = 0.42$)	1.97	–

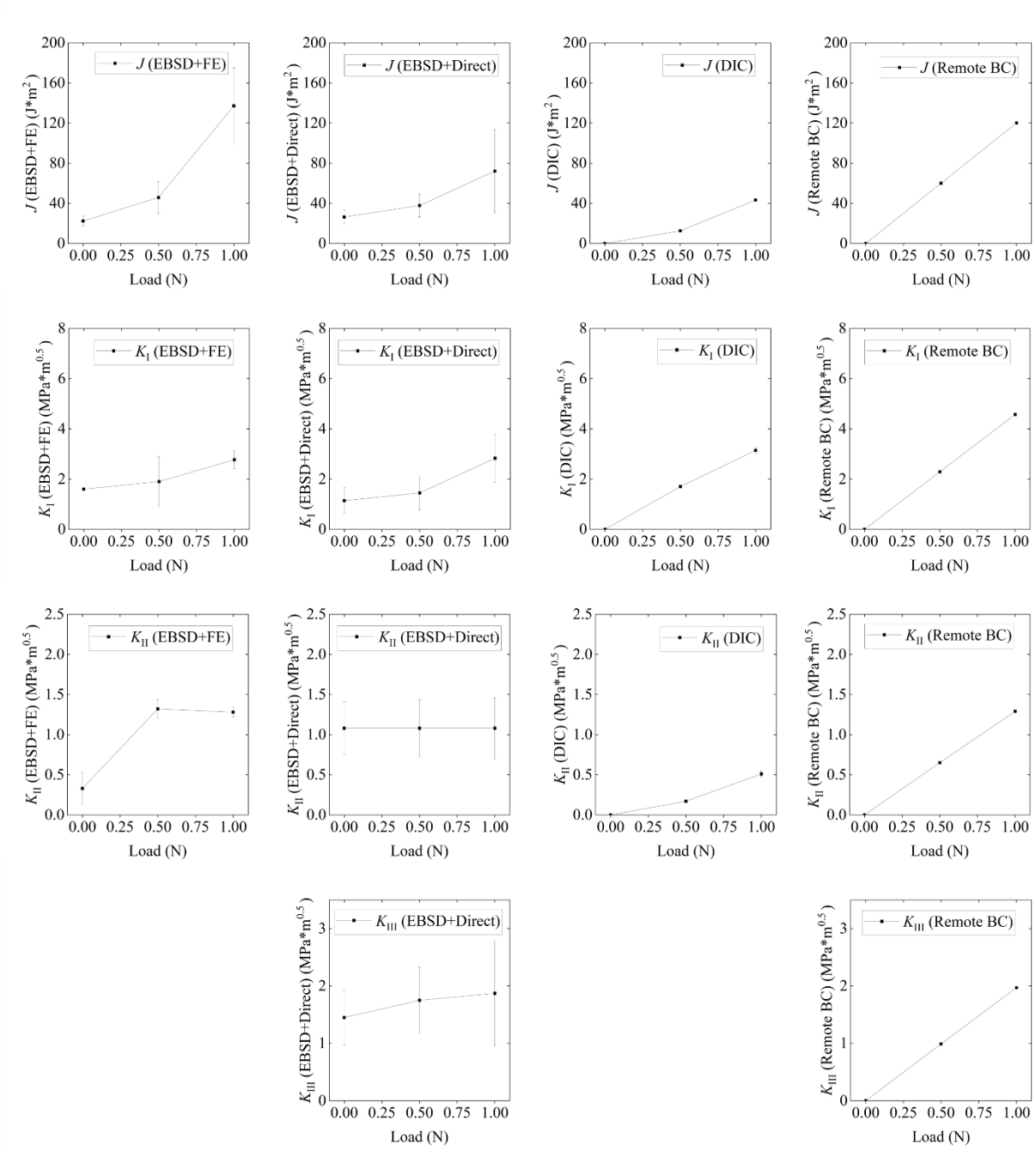

FIGURE 3.19
Summary of the *J*-integral and Mode I, II, and III stress intensity factors for experiment 1.

For the EBSD+FE-based method, the statistical values were calculated using data from the converged region, defined as contours starting from No. 8 onward, in order to minimise the influence of the crack tip plastic zone. For the direct evaluation method without integration, the values were computed from the scattered data while also avoiding those corresponding to the near-

tip region typically covered by the first 5-10 contours. Outliers, defined as points exceeding 2.5 times the standard deviation from the mean, were excluded from the analysis.

Both methods reveal a monotonic increase in Mode I loading with increasing applied load, consistent with the proportional relationship between the crack tip elastic field and the remote load. However, the trends differ slightly: the FE-based method, which integrates the strain field to recover displacements before contour integration, produces a more uniform increase in K_{I}, likely due to regularisation reducing sensitivity to local noise. In contrast, the direct evaluation method shows a steeper rise at step 2, possibly due to amplified fluctuations arising from noise in the strain field. This method is inherently more susceptible to convergence issues, as errors in the measured strain propagate through both stress calculation and subsequent integration. These effects are discussed further in a later section.

For Mode II loading, both methods show a trend of initial increase followed by a plateau. This behaviour suggests that, as the load increases, the Mode II stress intensity factor also increases until a critical level is reached, at which point crack-tip slip systems are activated and plastic activity occurs. As a result, K_{II} saturates. The saturated value can therefore be interpreted as the critical load required to activate the relevant slip system near the crack tip. Although slip activation provides the most physically consistent explanation, it should be acknowledged that load misalignment during testing could also contribute to the observed plateau.

In contrast, the evaluation of Mode III stress intensity factors shows a marked discrepancy between the two methods. As previously discussed, the FE-based method models the sample surface as a thin membrane and assumes a finite electron beam penetration depth for the backscattered electrons. The estimated K_{III} values are strongly dependent on this assumption [220, 364]. For the data in this study, K_{III} values obtained by the FE-based method exhibit significant fluctuations and lack convergence, indicating strong path dependence. This suggests that the out-of-plane driving force may not be accurately captured under the current depth assumptions. Another potential

source of error is that the finite element calculation of displacement may not have fully incorporated the discontinuity associated with the crack surface within the measured field, which could also affect the accuracy of the energy integral evaluations.

Compared to the FE-based method, the direct evaluation approach appears to offer a more reliable estimate of K_{III}, yielding more reasonable and consistent results. Like K_{II}, K_{III} represents a shear-driven component and may also exhibit saturation behaviour as the corresponding slip system is activated.

A broader comparison, including the results from remote boundary conditions and DIC, is considered. Several observations can be made from Table 3.4 and Figure 3.19. The comparison demonstrates that results obtained from different measurement techniques are generally consistent with one another and also align reasonably well with the theoretical predictions from numerical simulation. This suggests that the employed methods for measuring and evaluating crack tip fields are effective. Note that non-zero K values are observed at zero applied load when using EBSD data. This is attributed to residual strains captured by HR-EBSD, which reflect pre-existing stress states in the material prior to external loading.

Among all results, the purely elastic finite element model yields the highest values of both K_{I} and the J-integral. This is expected, as the model assumes perfect alignment of the tensile load and also does not account for stress redistribution by plastic deformation at the crack tip and thus represents an idealised case of a singular elastic field. The elastic model also exhibits significantly higher $K_{\mathrm{I}}/K_{\mathrm{II}}$ and $K_{\mathrm{I}}/K_{\mathrm{III}}$ ratios, reflecting its inability to capture the complexity of the local crack tip fields.

In contrast, the EBSD-based results show smaller $K_{\mathrm{I}}/K_{\mathrm{II}}$ and $K_{\mathrm{I}}/K_{\mathrm{III}}$ ratios, highlighting the presence of substantial crack tip plastic activity and the important role of shear loading in this region, which are known to be key factors controlling short fatigue crack propagation [372]. The

DIC-based evaluation, however, fails to adequately reflect these features as well. This may be attributed to the difficulty of isolating elastic shear-mode deformation from the total strain field, particularly when plastic strains are not explicitly resolved. Additionally, as a two-dimensional analysis, DIC assumes all deformation occurs within the image plane. However, out-of-plane displacements, especially near crack tips or highly deformed regions, can distort the surface pattern or shift the apparent position of features, leading to errors in in-plane displacement and strain measurements. These effects may result in inaccurate estimation of local fields, particularly when assessing crack driving forces.

Moreover, the K_{I} values derived from DIC are consistently higher than those from EBSD, particularly when considering the residual-field-corrected ΔK values. This discrepancy indicates that DIC captures the combined effect of elastic and plastic deformation, whereas EBSD measurements are more sensitive to the purely elastic lattice response. The contribution of plastic strain in DIC data results in a larger crack opening, which leads to an overestimation of K_{I} when interpreted within an elastic framework. In the EBSD data, this plastic activity appears as a saturation behaviour in the evolution of K_{II} and K_{III}, where the shear components no longer increase with further applied load. This suggests that the shear stresses at the crack tip have reached the threshold necessary to activate slip systems, and additional loading does not significantly enhance lattice deformation. Such behaviour reflects the fundamentally different characteristics of crack-tip field measurements obtained by EBSD, which are closely linked to the actual local loads acting on the crystal lattice of the material.

3.3.4. Crack Field Analysis across an Overload Cycle

Building upon the previous experiment, the electron beam and detector settings were optimised to enhance Kikuchi pattern quality. Specifically, the exposure time was doubled, and the relative positioning between the detector and the loading stage was adjusted to improve the quality of

Kikuchi patterns on the screen, an effect closely linked to refinement of the pattern centre. These adjustments improved the signal-to-noise ratio, thereby increasing the reliability of the cross-correlation analysis of the diffraction data. Using the same specimen, a more complex loading sequence was implemented to facilitate crack-tip field characterisation across three loading cycles. During the experiment, forescatter electron (FSE) images (included in the Appendix) and high-resolution EBSD diffraction data were acquired at each loading step under applied load conditions, enabling in situ observation of the crack-tip response throughout the entire loading sequence. This section presents the results of the data processing and analysis.

The loading plan consists of three cycles: a single overload cycle bracketed by two moderate loading cycles, serving as pre- and post-loading steps to investigate the effect of overload on crack-tip behaviour. The elastic strain tensor fields and total GND density maps calculated via HR-EBSD are presented in Figure 3.20 (spanning multiple pages).

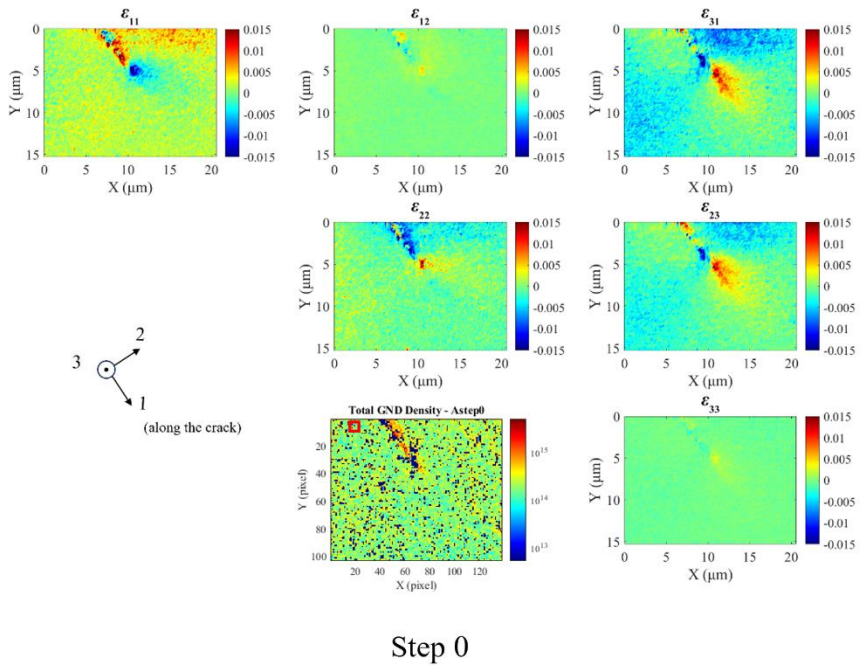

FIGURE 3.20

Elastic strain tensor fields and total GND density maps obtained by HR-EBSD for Cycle A at loading steps 0, 1, 2, 3, and 4. In the total GND density maps, dark areas correspond to missing data where patterns were filtered out due to poor quality. Reference points were selected from the unstressed wake region of the crack, assuming a strain-free condition near the free surface. The selected location, indicated by a small red square, lies within a low GND density area and avoids filtered data points. The maps are distributed across multiple pages for clarity.

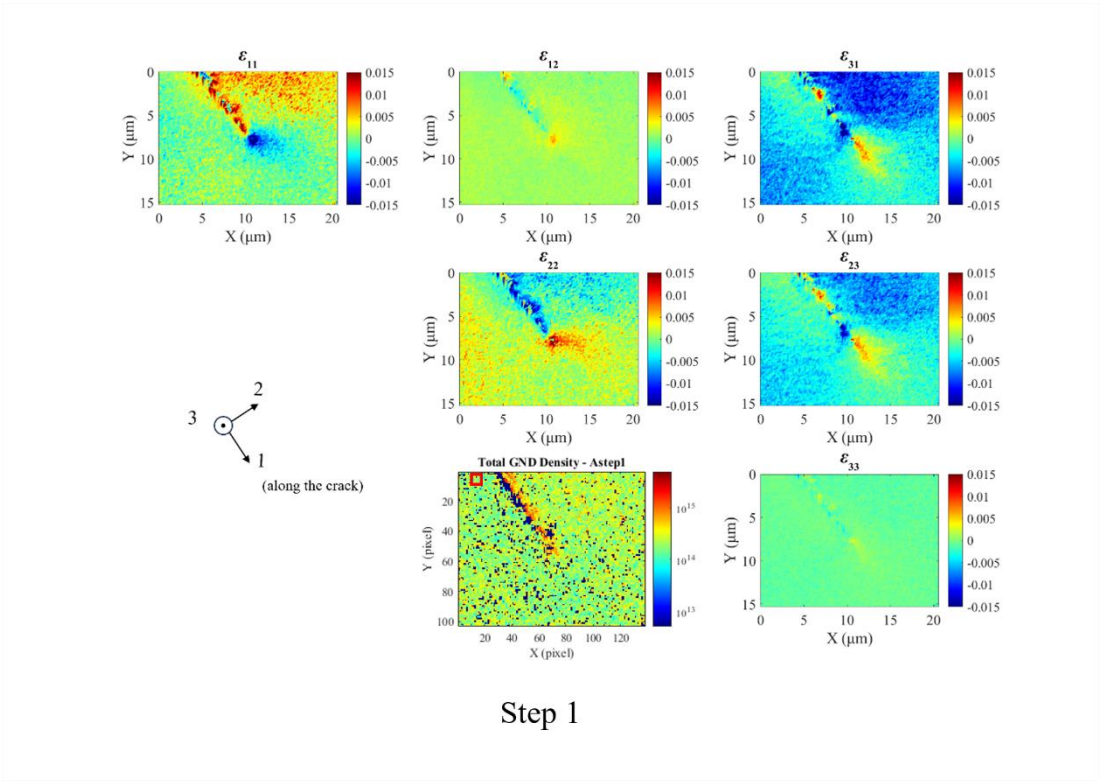

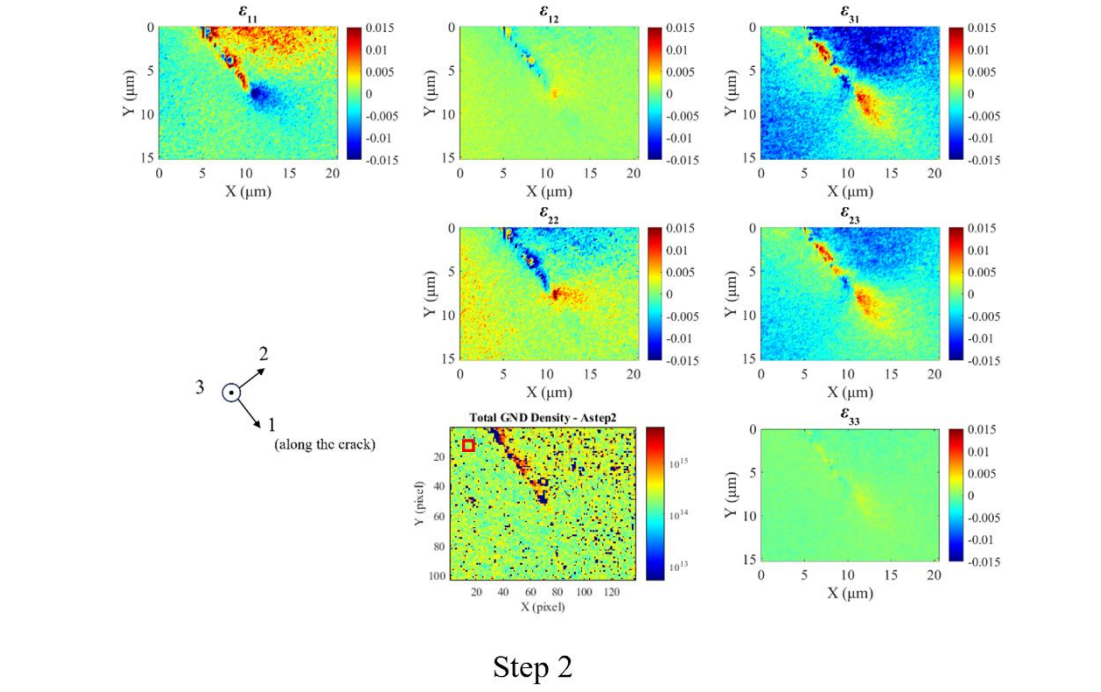

FIGURE 3.20

Elastic strain tensor fields and total GND density maps obtained by HR-EBSD for Cycle A at loading steps 0, 1, 2, 3, and 4. In the total GND density maps, dark areas correspond to missing data where patterns were filtered out due to poor quality. Reference points were selected from the unstressed wake region of the crack, assuming a strain-free condition near the free surface. The selected location, indicated by a small red square, lies within a low GND density area and avoids filtered data points. The maps are distributed across multiple pages for clarity.

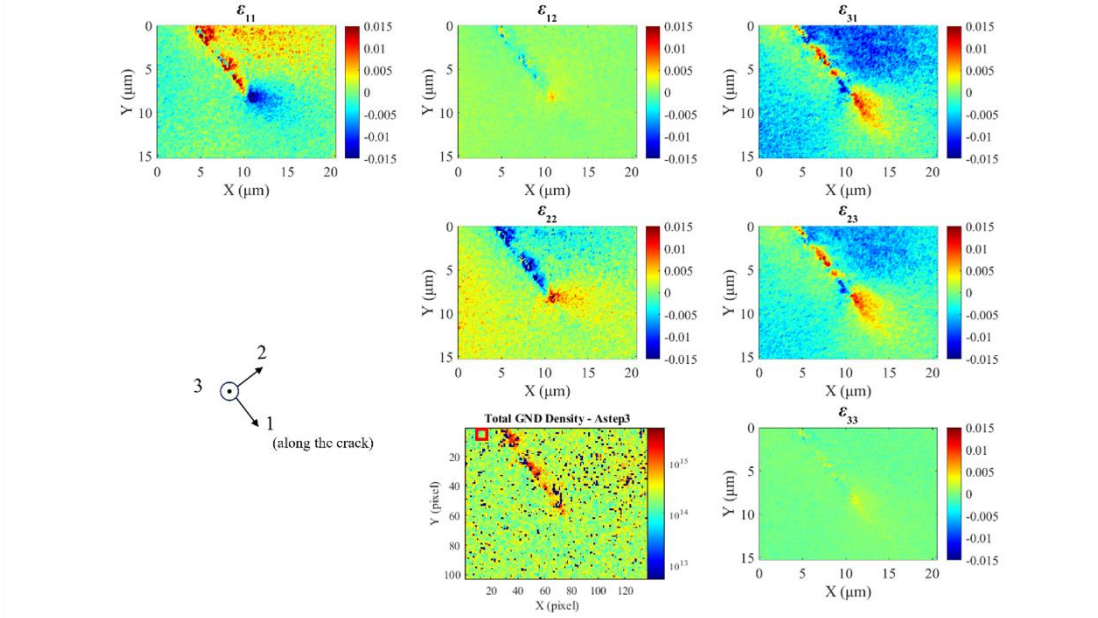

Step 3

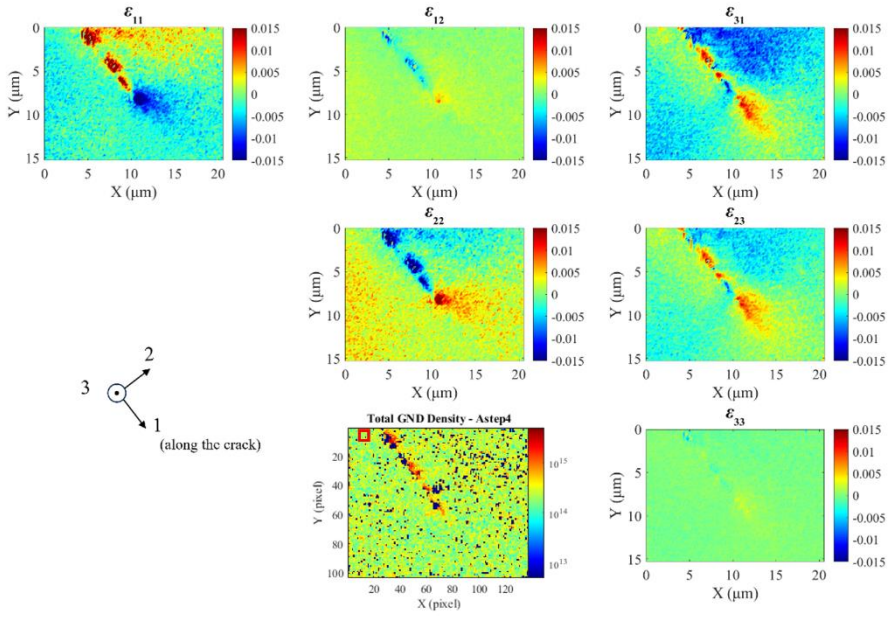

Step 4

FIGURE 3.20

Elastic strain tensor fields and total GND density maps obtained by HR-EBSD for Cycle A at loading steps 0, 1, 2, 3, and 4. In the total GND density maps, dark areas correspond to missing data where patterns were filtered out due to poor quality. Reference points were selected from the unstressed wake region of the crack, assuming a strain-free condition near the free surface. The selected location, indicated by a small red square, lies within a low GND density area and avoids filtered data points. The maps are distributed across multiple pages for clarity.

In the GND density maps, dark regions correspond to data points filtered out due to reduced pattern quality. Reference points for strain calculation were selected from the unstressed wake region of the crack, assuming an approximately strain-free condition near the free surface. The selected location, indicated by a red box, lies in a low GND density area and avoids filtered data points. For conciseness, only the results from the first loading cycle (Cycle A) are shown here, while the strain fields corresponding to the remaining cycles are provided in the Appendix. Compared to Experiment 1, the quality of the diffraction signals has improved, enabling clearer visualisation of strain concentration near the crack tip. As the remote load increases, changes in the magnitude of the crack-tip strain field are observed, demonstrating the effectiveness of the in-situ measurement approach.

It is important to note that the measured strain tensor fields represent elastic strains derived from changes in interplanar spacing, which distinguishes diffraction-based strain mapping from other full-field strain measurement techniques. The results indicate that the elastic strain concentration at the crack tip is confined to a region approximately 10 μm × 10 μm in size, which is significantly smaller than the total crack length of approximately 95 μm.

The J-integral and Mode I, II, and III stress intensity factors were calculated from the HR-EBSD measured strain fields using the direct method, which involves decomposition of the deformation gradient followed by contour integration. This approach circumvents the need for numerical integration of displacement fields or assumptions about electron beam penetration depth, and is therefore considered more faithful to the experimental data. Unlike FE-based field reconstruction, which inherently smooths the measured fields and requires explicit modelling of physical discontinuities such as crack faces, the direct method operates directly on the experimentally measured deformation gradients. It avoids introducing model-based artefacts or uncertainties associated with boundary condition definitions and deformation volume approximations. As a result, it yields energy integrals, particularly Mode III components, that more accurately reflect

the true local response captured in the experiments, provided that the underlying data quality is sufficiently good.

For each loading step, at least 20 integration contours were used to evaluate the J-integral and stress intensity factors. The contour paths were consistently defined, expanding outward concentrically from the crack tip. While individual paths exhibit a degree of fluctuation, the results effectively capture the local crack-tip field, and the overall trends demonstrate good convergence. Statistical processing followed the same method as in Experiment 1, with the mean and standard deviation of each parameter indicated above the corresponding scatter plots. These statistical values serve as an effective representation of the crack driving force, summarising the key features of the measured, and sometimes scattered, data. The results are presented in Figure 3.21.

Figure 3.22 and Figure 3.23 present the displacement fields obtained from digital image correlation (DIC) analysis of forescattered electron (FSE) images and the corresponding results of J-integral and Mode I and II stress intensity factor calculations based on finite element post-processing. The displacement fields used in this analysis were corrected for rigid body translation and rotation and show an increasing magnitude with increasing applied load, a trend that is also reflected in the calculated integral values.

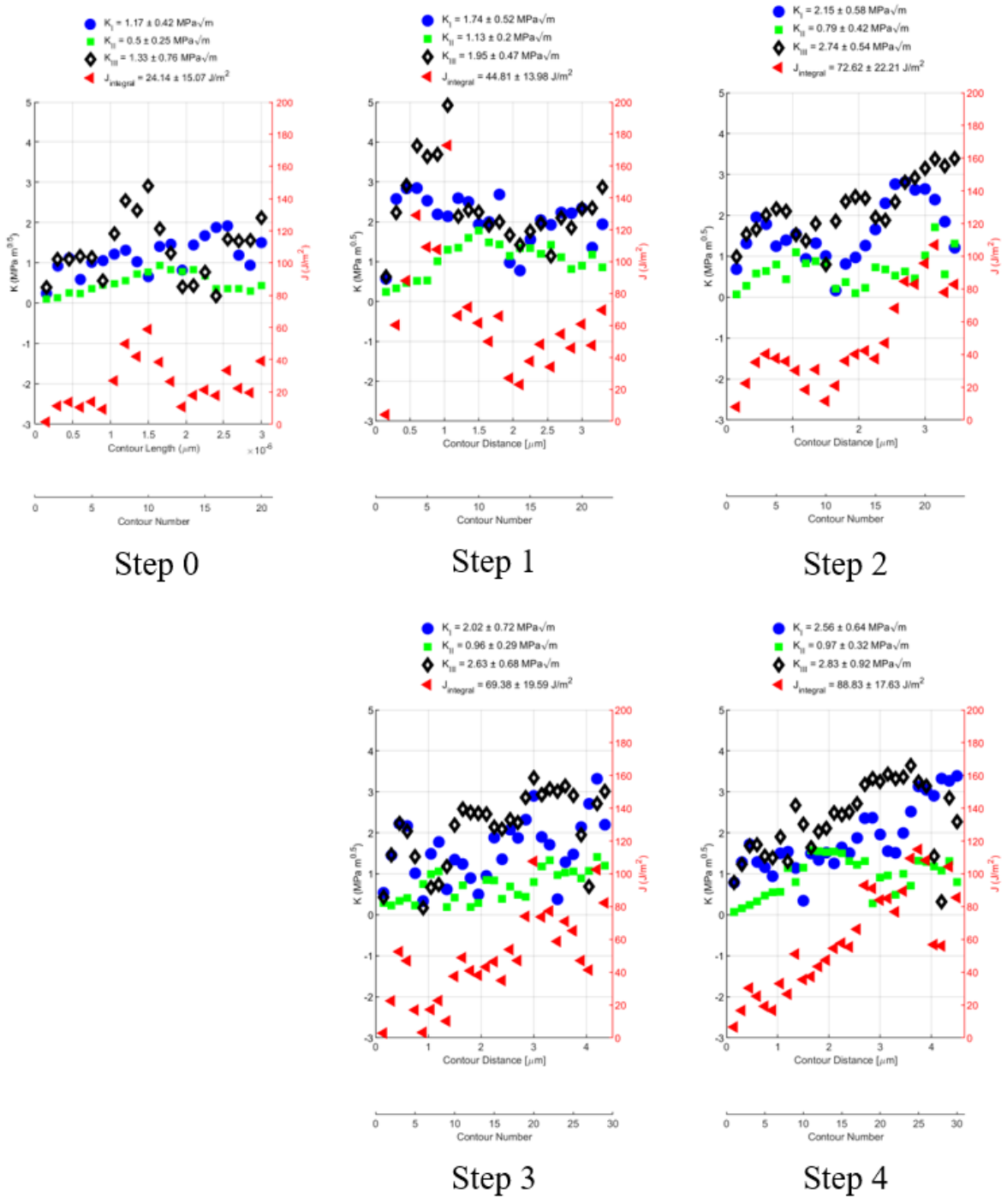

FIGURE 3.21

J-integral and Mode I, II, and III stress intensity factors evaluated using the direct approach based on HR-EBSD strain maps for Experiment 2, Cycle A.

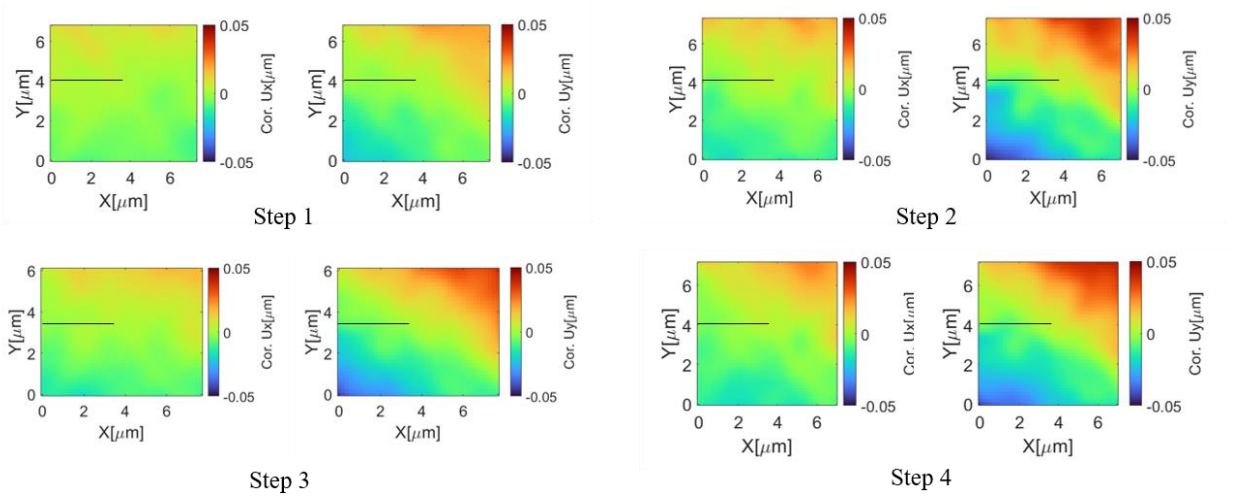

FIGURE 3.22

Displacement fields obtained from DIC analysis of forescattered electron (FSE) images for Experiment 2, Cycle A. The displacement fields were corrected for rigid body motion. Black lines indicate the crack.

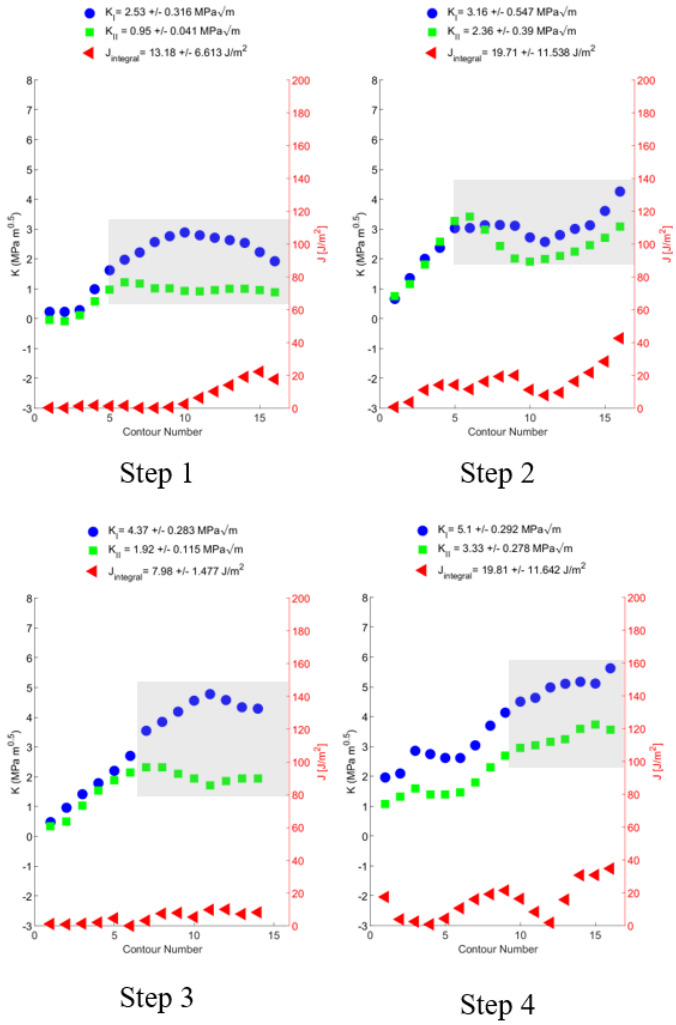

FIGURE 3.23

J-integral and Mode I and II stress intensity factors calculated using a finite element model with DIC-derived displacement fields as boundary conditions, for Experiment 2, Cycle A. No masking was applied. The grey area indicates the region where good convergence was achieved.

In this case, no masking was applied during the crack driving force evaluation; the full displacement field from the DIC analysis was used as boundary conditions in the finite element model. Although data near the crack surface can introduce variations, it did not significantly affect the convergence of the integral results. Convergence was assessed across all contours, and values were extracted from the region showing stable behaviour, excluding the first few contours close to the crack tip.

It is important to note that the displacement field measured by DIC corresponds to the total deformation, including both elastic and plastic contributions. In contrast, the finite element simulation assumes linear elasticity. As a result, the calculated crack driving force does not represent the actual physical value but rather provides an upper-bound estimate based on the total displacement field. Additionally, as a two-dimensional measurement technique, DIC cannot account for potential out-of-plane displacements, which may further compromise the accuracy of the calculated results. Nevertheless, despite these limitations, the DIC-based evaluation serves as a valuable reference for comparison and trend validation across different measurement approaches.

Figure 3.24 summarises all the J-integral and Mode I, II, and III stress intensity factor results obtained from HR-EBSD measurements. These results reflect the purely elastic response at the crack tip under external loading. As shown in the plots for Cycle A, K_{I} increases monotonically with the applied load, whereas K_{II} rises in the first step but quickly reaches a plateau, stabilising at around 1 MPa$\sqrt{m}$ in the subsequent steps. Similarly, K_{III} increases over the first two steps and then saturates at approximately 2.7 MPa$\sqrt{m}$. The saturation of K_{II} and K_{III} is indicative of the activation of slip systems associated with Mode II and Mode III loading. Once these slip systems are activated, part of the intensified stress concentration at the crack tip is relieved. This may explain the observed reduction in the rate of increase of K_{I} at specific loading steps, as the redistribution of stress due to plastic deformation could weaken the continued Mode I response. It is also noted that nonzero initial K values were measured at Step 0. This residual field reflects the

presence of stress and strain introduced by the fatigue pre-cracking process, during which the sample was subjected to cyclic loading prior to the current in-situ experiment.

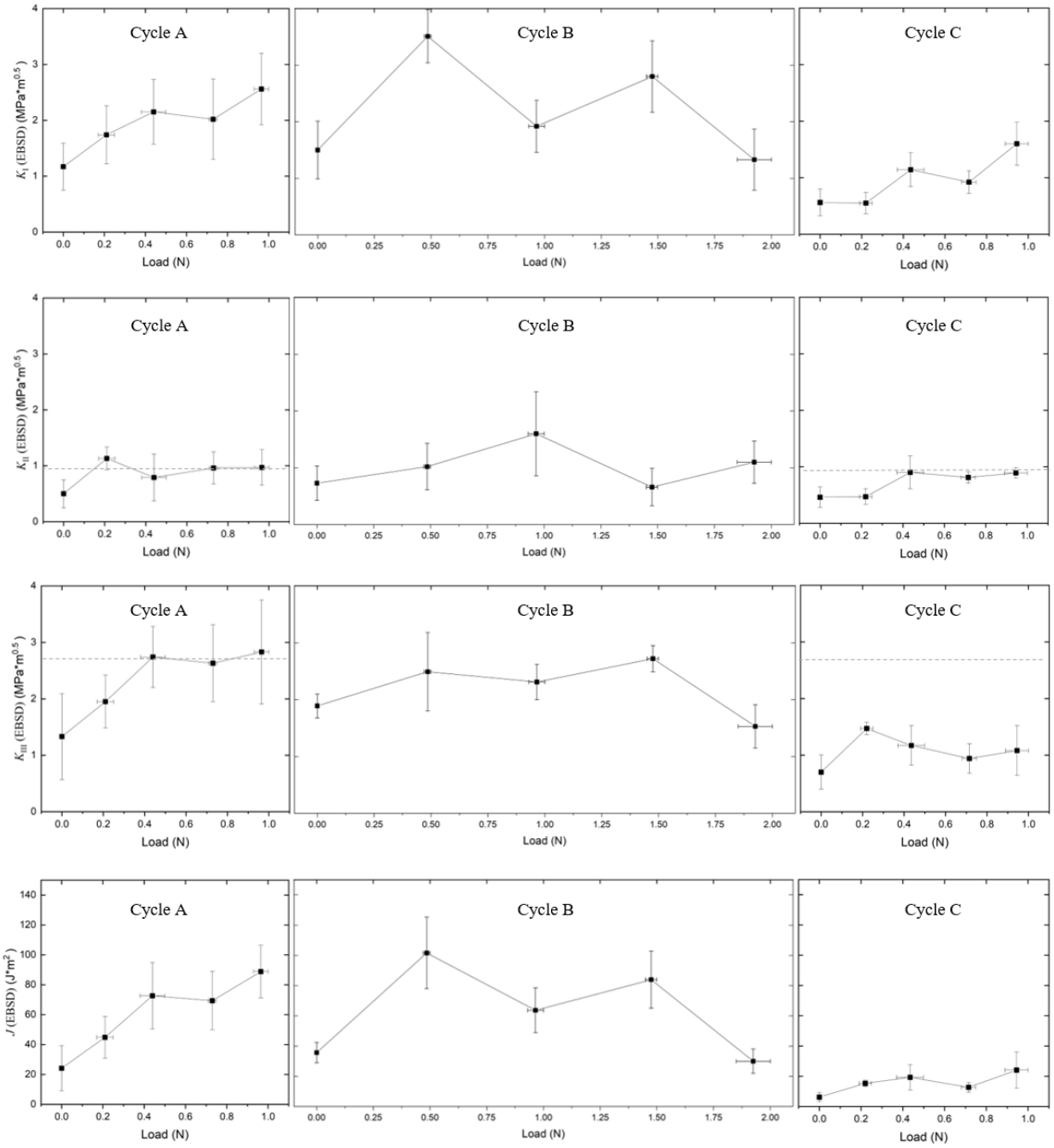

FIGURE 3.24
Summary of the J-integral and Mode I, II, and III stress intensity factors calculated from HR-EBSD strain fields for Experiment 2.

In contrast to Cycle A, the crack-tip elastic fields in the overload cycle (Cycle B) exhibit markedly different behaviour. At the beginning of Cycle B, residual stresses result in a higher initial stress

state compared to the previous cycle. This suggests that plastic deformation had occurred during Cycle A, leaving behind a residual stress field that effectively "remembers" the previous loading history. Supporting this interpretation, a notable change in K_{II} and K_{III} is observed at the end of Cycle A as the load is removed, indicating the presence of cyclic plasticity at the crack tip. This plasticity is associated with the creation of new crack surfaces during cyclic loading. The magnitude of the residual shear components would be expected to scale with the crack growth increment, as it is proportional to the accumulated cyclic strain at the crack tip. As loading progresses in Cycle B, K_{I} rises rapidly and exceeds the maximum value observed in Cycle A, while K_{II} and K_{III} also increase quickly, reaching the saturation levels previously established. With further increase in applied load, the crack-tip loading mode undergoes a notable transition. A sharp increase in K_{II} is observed, while both K_{I} and K_{III} decrease significantly, with the reduction in K_{I} being particularly pronounced. As the loading continues, another shift in loading mode occurs: K_{II} begins to decrease, whereas K_{I} and K_{III} rise again (Step 3). At peak load, this pattern repeats, with K_{II} increasing once more and both K_{I} and K_{III} decreasing further.

This sequence of transitions suggests a highly dynamic response of the crack-tip region under overload, potentially indicating intermittent activation of significant plastic deformation mechanisms triggered by elevated Mode II loading. Following each apparent plastic event, substantial relaxation of the elastic crack-tip field, as reflected by the J-integral change, is observed. This behaviour may be associated with localised plastic shear deformation near the crack tip.

The crack-tip elastic fields in Cycle C also exhibit several notable features. In general, the loading mode in Cycle C follows a similar pattern to that of Cycle A, and the overall trends are broadly comparable. However, the observed differences between the two cycles highlight the lasting influence of the preceding overload cycle (Cycle B). First, the initial crack-tip stress state in Cycle C appears to be lower than that in the previous two cycles. This may be attributed to the significant

relaxation of the elastic field observed at the end of Cycle B, likely accompanied by the removal or rearrangement of accumulative lattice defects during unloading.

An interesting phenomenon occurs at the first loading step: neither K_{I} nor K_{II} increases significantly in response to the applied load. This suggests the important effect of the overload cycle, within which the presence of mobile dislocations may have accommodated the applied stress, effectively shielding the crack tip from further elastic strain accumulation. This mechanism may be a key reason behind the well-known retardation of crack growth following an overload event, and it represents an important experimental observation captured in this study.

From Cycle C loading step 2 (Step 12) onward, the Mode I and II loading behaviour in Cycle C resembles that of Cycle A: K_{II} quickly saturates at a similar level, and K_{I} continues to increase with applied load. However, the Mode III behaviour in Cycle C diverges significantly. After the overload cycle, K_{III} appears to stabilise at a lower plateau value compared to previous cycles. This reduction in Mode III response may reflect the accumulation of shear-induced plastic deformation during the overload, which alters the local stress redistribution at the crack tip. As a result, further Mode III loading could be accommodated more readily by plastic mechanisms, leading to a lower elastic driving force captured by K_{III}.

Overall, the J-integral results in Cycle C reflect a substantially constrained elastic field at the crack tip, suggesting that the plastic deformation accumulated during overload has a pronounced influence on subsequent crack-tip behaviour and the resistance to further crack propagation.

Although the overload behaviour in Cycles B and C is complex, consistent Changes in K_{II} and K_{III} are observed between the unloading at the end of the previous cycle and the initial loading step of the subsequent cycle. These changes are indicative of reversed plasticity at the crack tip, associated with the build-up and relaxation of the elastic field. Interestingly, the extent of these changes

appears to be smaller following the overload, which may cause a retardation in the crack growth rate.

As a comparison, Figure 3.25 summarises the *J*-integral and Mode I and II stress intensity factors calculated from the DIC-derived displacement fields throughout the experiment. It should be noted that results obtained via DIC may be affected by plastic deformation, out-of-plane displacement, and the inherent limitations of two-dimensional measurement, which reduce the accuracy of crack-tip driving force quantification. Accordingly, this dataset is presented solely for qualitative comparison, and no detailed interpretation is attempted in order to avoid over-interpretation.

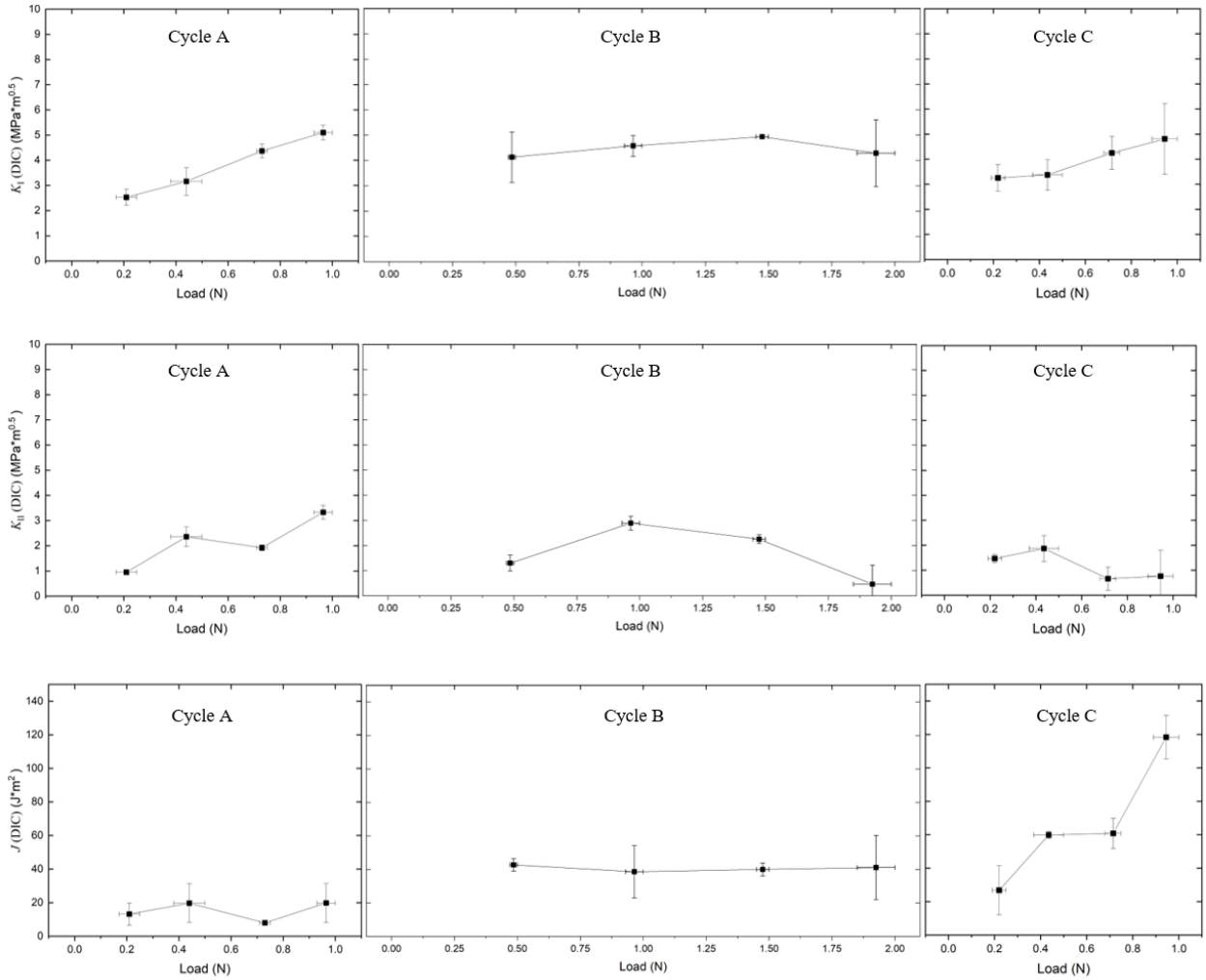

FIGURE 3.25
Summary of the *J*-integral and Mode I, II stress intensity factors calculated from DIC displacement fields for Experiment 2.

The J-integral values computed from the DIC data show a general increase over the three loading cycles, indicating a cumulative growth in the total deformation at the crack tip. The Mode I stress intensity factor K_{I} increases with load in both Cycle A and Cycle C, reflecting progressive opening of the crack faces under applied loading. Notably, the initial K_{I} value in Cycle C is higher than that in Cycle A, suggesting the presence of residual plastic deformation carried over from the first two cycles.

In contrast to the behaviour observed in HR-EBSD-derived elastic strain fields, the Mode II component K_{II} does not exhibit a clear saturation trend. Instead, it shows complex variations throughout the loading process. This distinction highlights the difference between total strain captured by DIC and purely elastic strain captured by HR-EBSD. The observed fluctuations in K_{II} may reflect transitions in mixed-mode loading at the crack tip; however, these values should be interpreted with caution, given the limited ability of DIC to accurately resolve the mixed-mode loading in crack-tip fields.

3.4 Discussion

3.4.1. Reference Pattern Selection and Pattern Processing for HR-EBSD

High-resolution electron backscatter diffraction (HR-EBSD) is a highly sensitive technique capable of measuring elastic strain and lattice rotations with sub-micro-strain precision. However, this level of sensitivity also means that the accuracy of the results is strongly dependent on the quality of the acquired diffraction patterns, which in turn is influenced by the sample surface condition, scanning parameters, and pre-processing strategies. In practice, ensuring reliable strain field estimation requires special attention to several aspects of the HR-EBSD workflow.

EBSD scans require exceptionally clean and well-prepared sample surfaces, as well as optimised detector settings that ensure high-quality pattern acquisition. In this study, careful sample

preparation, including mechanical polishing and etching, was employed. Nonetheless, during in situ loading, a limited number of scan points with low-quality patterns inevitably emerged. These are typically caused by local contamination, deposition of carbon or oxides, surface topography changes, or other mechanical damage. Such points can produce poor diffraction signals due to underexposure or pattern distortion, introducing significant noise into the calculated strain fields, especially near the crack tip where precision is critical.

To mitigate this, a pre-processing filter based on the kernel average misorientation (KAM) parameter was applied to remove low-quality points from the dataset, as shown in Figure 3.26. This thresholding strategy proved effective in excluding unreliable regions and significantly improved the stability and clarity of the resulting strain maps.

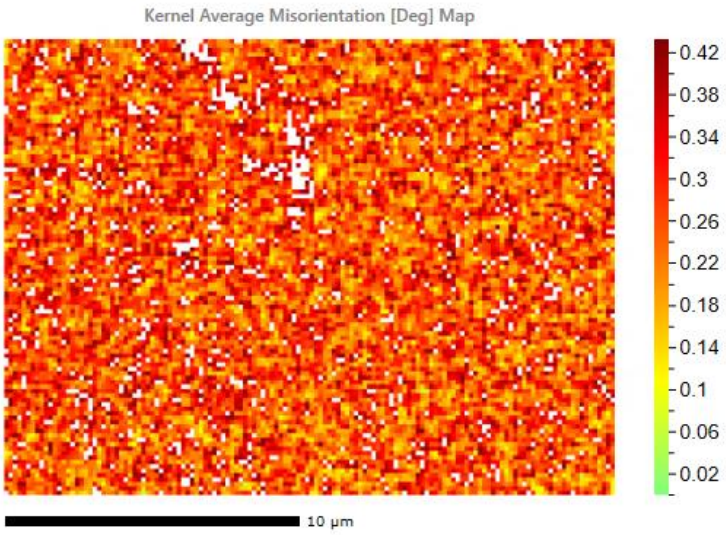

FIGURE 3.26
Kernel Average Misorientation (KAM) map of the EBSD dataset. White (missing) points indicate regions that were filtered out due to low pattern quality, based on a KAM threshold applied during pre-processing.

In addition to local defects, the detector itself may contribute systematic issues such as uneven exposure or background gradients across the field of view. These effects can significantly degrade the fidelity of the Kikuchi patterns and interfere with the cross-correlation process, which forms the basis of HR-EBSD strain calculation. Since the method relies on detecting small shifts in Kikuchi band positions, any background noise or distortion can lead to erroneous strain estimates.

To address this, pattern filtering was performed prior to correlation. In particular, fast Fourier transform (FFT)-based filtering was implemented to enhance pattern clarity in the frequency domain. This approach selectively suppressed background noise and enhanced the definition of Kikuchi lines, leading to visibly improved pattern quality upon inverse transformation (see Figure 3.9). The improved pattern contrast not only facilitated more accurate cross-correlation but also helped ensure the robustness of the calculated strain fields, especially in regions of high gradient near the crack tip.

In addition to filtering, the careful selection of the region of interest (ROI) is equally critical to the overall quality of the HR-EBSD analysis. Due to variations in surface conditions and local pattern contrast, not all scanned areas are equally suitable for high-precision strain evaluation. In this study, ROIs were selected based on visual inspection and pattern quality metrics to ensure that only well-resolved areas were used in the analysis. Applying FFT filtering to these high-quality regions further enhanced the accuracy of the correlation process. The combination of ROI selection and targeted filtering was found to be the most effective strategy for minimising error propagation and preserving fine strain features in the vicinity of the crack tip.

In addition to pre-processing, the selection of the reference pattern is one of the most critical factors affecting the accuracy of strain measurements in HR-EBSD. The quality and deformation state of the reference pattern directly determine the precision of the cross-correlation analysis and define the baseline for all strain results. Despite its importance, the selection of an optimal reference pattern remains an unresolved challenge within the EBSD research community, particularly for in-situ or mechanically loaded samples. Defining a truly strain-free point in a deformed material is inherently difficult. Different strategies have been proposed [150, 373], including the use of simulated (virtual) patterns as references. Koko's work [149], for example, provides a detailed investigation into selection criteria and practical considerations for reference pattern definition.

The focus of the present study is to identify a viable strategy for reference selection suitable for in-situ HR-EBSD experiments. Ideally, a single reference pattern should be used consistently across all loading steps. This would ensure that strain fields derived at different stages share a common baseline, thereby enabling direct comparisons. However, this approach has proven difficult to implement in practice.

Even in cases where a reliable, strain-free reference point can be identified under zero load conditions, and where experimental parameters such as stage position and detector settings are kept constant throughout the experiment, using a single global reference pattern introduces a systematic and progressively varying background strain across the field of view. This is illustrated in Figure 3.27. The root cause lies in tiny but unavoidable shifts in the spatial geometry between the specimen and the detector during loading, due to load transfer mechanisms between the grips and the sample. These shifts introduce geometric artefacts that are indistinguishable from true strain in the correlation process, rendering the single-reference strategy unsuitable for high-accuracy in-situ measurements under current hardware constraints.

Nevertheless, with future advancements such as real-time tracking of the crack tip and dynamic reconstruction of the specimen-detector geometry using parameters like pattern centre and sample-to-detector distance, it may become feasible to implement a consistent reference across multiple loading steps. Such developments would also allow for the subtraction of systematic and progressively varying background strains, thereby making absolute measurement of the residual stress fields possible.

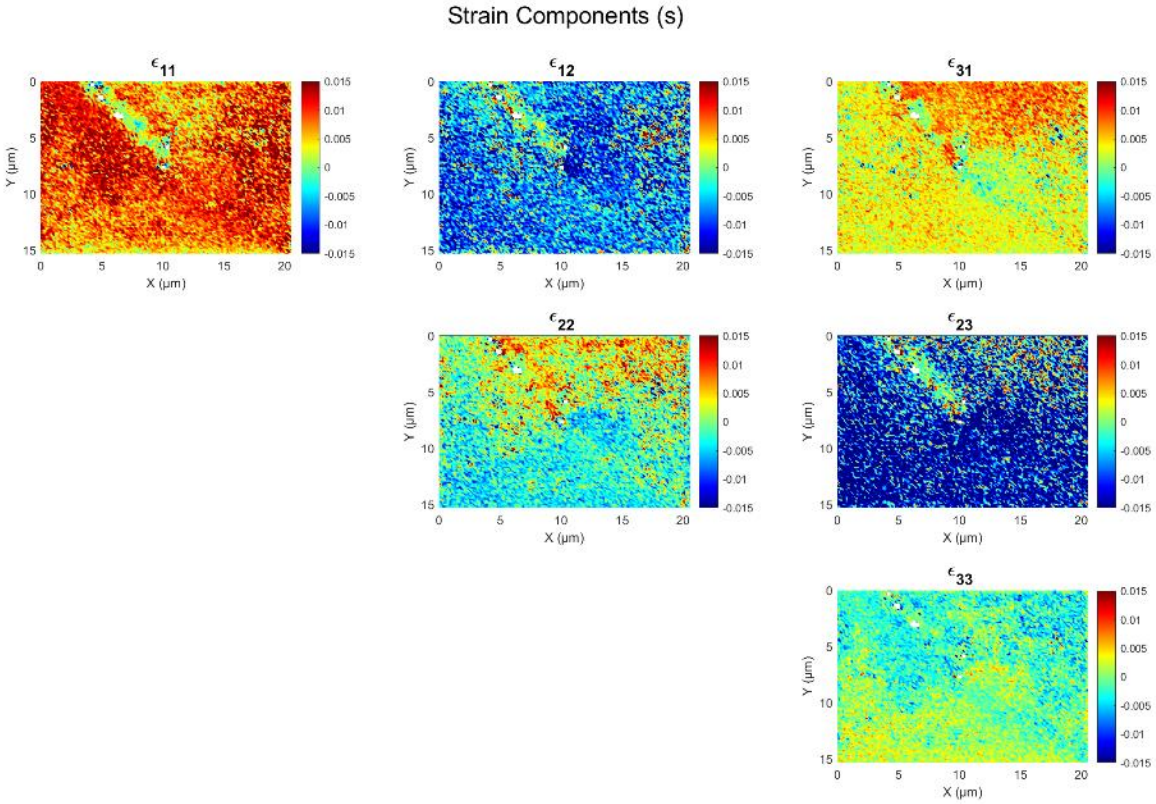

FIGURE 3.27
Erroneous strain field resulting from the use of a single reference diffraction pattern for all loading steps.

Given the current limitations, the present study adopts a stepwise reference selection strategy. For each loading step, a local strain-free reference was selected to enable accurate strain quantification. This was achieved by exploiting a characteristic feature of the crack-tip field: in the crack wake region near the free surface, a small zone can reasonably be assumed to be free of elastic strain. Combined with high-confidence evaluation of pattern quality, this approach enabled accurate characterisation of the elastic strain field surrounding the crack tip at each loading stage.

3.4.2. The Advantage of ForeScatter Electron Imaging in SEM-DIC

Forescatter electron (FSE) imaging in the scanning electron microscope (SEM) primarily utilises electron channelling contrast (ECC) and atomic-number (Z) contrast to generate image features. ECC arises due to differences in crystal orientation and local lattice distortions, making FSE imaging particularly sensitive to microstructural details such as grain orientations, boundaries, and sub-grain structures. Moreover, the Z-contrast mechanism enhances the visibility of phases with

different atomic numbers, significantly improving the differentiation between microstructural constituents compared to secondary electron (SE) imaging. These combined contrast mechanisms result in clearer and more robust identification of intrinsic surface features, thereby substantially reducing subset matching errors during digital image correlation (DIC) and enhancing the accuracy of strain measurements.

In contrast, conventional SE imaging predominantly reflects surface topography and roughness, factors which are susceptible to disturbances by deformation and sample preparation. Consequently, SE images often introduce significant errors in subset tracking during DIC analyses, especially under large deformations or complex loading conditions. By emphasising crystallographic and compositional information rather than purely surface morphology, FSE imaging reduces the influence of surface roughness and mitigates errors introduced by moderate out-of-plane deformation, leading to potentially more reliable in-plane strain measurements.

An additional advantage of FSE imaging in SEM-DIC experiments is the potential to use intrinsic microstructural features as natural speckle patterns. Grain structures, slip traces, and phase boundaries all represent viable natural speckles. In the present study, the contrast from a two-phase microstructure was utilised. This choice eliminated the need for artificial pattern deposition techniques, such as nanoparticle spraying, which can interfere with simultaneous electron backscatter diffraction (EBSD) analysis. The combined use of EBSD and DIC is particularly beneficial, as EBSD provides high-resolution elastic strain measurements alongside crystallographic orientation data, whereas DIC captures the total strain field, including both elastic and plastic deformation. Thus, the complementary strengths of EBSD and DIC enable comprehensive microstructural and mechanical characterisation without requiring additional image registration steps.

Furthermore, FSE imaging exhibits high sensitivity to localised strain concentrations, making it effective for directly observing deformation phenomena such as slip bands, crack-tip plasticity,

and grain boundary deformation. This sensitivity enhances the capability of SEM-DIC methods in studying detailed deformation processes at microstructural scales.

Nevertheless, it should be noted that the advantages of FSE imaging become most evident when out-of-plane deformation is limited. In the current study, significant out-of-plane displacements were present due to the loading configuration, restricting the accuracy of two-dimensional DIC analysis. Thus, although the present experiment does not fully exploit this particular advantage of FSE imaging, it clearly demonstrates the potential of this technique. Under conditions with less pronounced out-of-plane displacement, the combination of FSE imaging with intrinsic microstructural features could further enhance the precision and reliability of strain mapping at the microscale.

3.4.3. Comparison of J-integral Calculation from Deformation Gradient with/without FE Integration

As introduced previously, two post-processing approaches were applied to the EBSD data for evaluating the crack-tip driving force. Fundamentally, HR-EBSD provides measurements of the deformation gradient through high-resolution pattern correlation. One approach involves integrating the measured strain field derived from the deformation gradient to reconstruct the displacement field, which is subsequently employed as boundary conditions in finite element analysis, enabling the computation of the J-integral in the same way as DIC-based methods.

The second approach, which is the primary methodology employed in this chapter, directly calculates the stress field from the experimentally measured deformation gradient using a linear elastic constitutive law. The resulting stress and strain fields are then used to evaluate the J-integral via contour integration, which involves terms including the strain energy. This method is conceptually closer to the experimental measurements, as it directly leverages the stress and strain

fields derived from diffraction-based elastic strain measurements without the intermediate step of displacement integration.

An important advantage of this direct approach is its fidelity to the experimentally measured data. Nevertheless, this methodology inherently amplifies measurement errors through a two-step process: first, experimental inaccuracies or noise in the measured strain fields directly translate into errors in the derived stress fields; subsequently, these errors are further magnified when performing the contour integration required to compute the J-integral. Consequently, for high-precision measurements, significant effort must be directed towards minimising noise and ensuring data quality throughout data acquisition and processing. The present study has demonstrated that, with careful implementation, this direct method effectively characterises the elastic crack-tip fields in situ, although careful attention must always be paid to the sensitivity to experimental noise.

Moreover, the feasibility of this approach depends on the availability of experimentally measured elastic strain fields obtained from diffraction-based techniques, such as HR-EBSD. If the experimental data consist only of displacement fields, the ideal procedure is to use FE analysis to compute the corresponding stress and strain fields, from which the J-integral can then be evaluated. As discussed in Chapter 2, such FE-based post-processing has notable robustness advantages in high-precision crack driving force evaluation, including mitigating uncertainties related to crack-tip positioning and suppressing the influence of localised poor-quality data.

In cases where the experimental measurement provides only strain, the displacement field must be reconstructed first before such a procedure can be applied. This first step using FE simulation to retrieve displacement was not implemented for Experiment 2 due to limitations associated with the model. Specifically, the model employed a simplified three-dimensional geometry with assumptions about electron penetration thickness that led to unreliable predictions of out-of-plane displacements, affecting the accuracy of the Mode III stress intensity factor. Additionally, the

model did not explicitly incorporate the discontinuities associated with the crack faces, which are essential for capturing the correct near-tip fields.

Although these challenges influenced the decision not to implement the displacement reconstruction method in the current study, the FE-based approach holds potential if these issues can be effectively resolved. If refined to incorporate detailed crack geometry and calibrated thickness assumptions, it could serve as a powerful tool for filtering noisy data and recovering a smoother crack-tip field. This "FE-filter" concept, where experimental data are regularised through constrained simulation, has been explored by researchers [218] and may offer a promising pathway for enhancing the reliability of fracture mechanics analyses based on diffraction measurements in the future.

3.4.4. Actual Mixed-mode Loading Conditions of a Fatigue Crack Across an Overload Cycle

The experimental results presented in this chapter provide valuable insights into crack-tip deformation mechanisms under different loading conditions. Under monotonic loading (Cycle A), the data reveal clear activation of primary slip systems, as indicated by the observed saturation behaviour of the Mode II and Mode III stress intensity factors. Initially, increasing the applied load leads to intensified stress concentrations at the crack tip, showing as predominant Mode I loading. This is consistent with the expected elastic behaviour, where crack opening (Mode I) dominates the initial deformation response. However, as loading progresses, the activation of primary slip systems associated with Mode II and Mode III effectively limits further increases in these shear-mode stress intensity factors, indicating local yielding and plastic deformation at the crack tip.

During the overload cycle (Cycle B), the crack-tip deformation behaviour becomes significantly more complex. Unlike the monotonic loading scenario, the overload introduces substantial plasticity, altering the shear mode contributions markedly. This is evidenced by pronounced

fluctuations in K_{II} and K_{III}, coupled with significant relaxation in Mode I loading (K_I). Such relaxation indicates substantial redistribution of stresses and strains due to extensive plastic activity triggered by overload conditions. Upon unloading, residual strains are expected to dominate the crack-tip stress state. This residual stress field represents a critical factor governing subsequent mechanical behaviour, as evidenced in Cycle C. The presence of residual strains significantly influenced the initial loading conditions of Cycle C, notably delaying the activation of Mode I and Mode II loading responses. Interestingly, the extent of reversed plasticity appears to decrease following the overload, which may reflect changes in the residual stress field that reduce the local driving forces for crack advance, thereby contributing to a retardation in the subsequent crack growth rate. However, considering the uncertainties associated with the measured stress intensity factors and the potential limitations in accurately capturing each individual crack-tip field, particularly the residual fields, these findings prompt a cautious interpretation, which is best understood as preliminary insights into complex crack-tip behaviour.

A comparison with displacement fields obtained through digital image correlation (DIC) reveals important limitations and strengths of the DIC method in capturing crack driving forces. While DIC effectively captures overall displacement fields around the crack, it inherently integrates both elastic and plastic deformation components, resulting in systematically higher Mode I stress intensity factor values compared to HR-EBSD measurements. Moreover, the inherent inability of DIC to accurately resolve out-of-plane displacement further compounds errors in crack-tip driving force quantification. Consequently, although valuable for qualitative comparison and validation of trends, DIC-based evaluations must be interpreted cautiously, recognizing the limitations associated with capturing pure elastic crack-tip fields.

Comparisons between experimentally derived values and theoretical predictions based on remote boundary condition simulations offer additional insights. The purely elastic FE model provides idealised upper-bound estimates for K_I and the J-integral due to the absence of plasticity-induced

stress redistribution. These results exhibit markedly higher K_I/K_{II} and K_I/K_{III} ratios, reflecting the model's inability to represent the complex interplay of different loading modes at the crack tip. Experiment results, especially those derived from HR-EBSD, show more balanced contributions of shear modes, highlighting significant plastic activity at the crack tip. This discrepancy underscores the necessity of accounting for local activities when accurately quantifying stress fields and propagation of a short fatigue crack.

In summary, the experimental observations reinforce the critical role of slip system activation and plastic deformation in governing crack-tip mechanics under various loading conditions. Monotonic loading primarily activates the dominant slip systems, while overload conditions introduce additional shear deformation that significantly redistributes the local stress and strain fields, leading to reduced reversed plasticity at the crack tip and a consequent retardation of crack growth. Residual strains from overload cycles significantly influence subsequent loading responses, emphasising the importance of history-dependent deformation processes. Additionally, although DIC provides valuable displacement field information, careful interpretation is required to avoid misrepresentation of the underlying elastic-plastic mechanics at the crack tip.

3.5 Conclusion

This chapter presents a detailed experimental investigation into the crack-tip fields of short fatigue cracks in a single crystal nickel-based superalloy using a combination of High-Resolution Electron Backscatter Diffraction (HR-EBSD) and Scanning Electron Microscopy-Digital Image Correlation (SEM-DIC). Two complementary experiments were designed to explore both monotonic and overload-induced loading conditions, providing insight into the activation of slip systems, the evolution of crack-tip fields, and the role of residual plasticity.

Under monotonic loading, the results clearly demonstrate the activation of primary slip systems, with Mode II and Mode III components exhibiting saturation behaviour. This saturation reflects

the onset of plastic deformation mechanisms that relieve stress concentration at the crack tip. The overload cycle reveals a more complex response, including stress and strain redistribution, relaxation, and load-mode transitions. Post-overload, the reduced shear plasticity and delayed elastic response observed at the crack tip are consistent with the classical overload-induced retardation effect.

An important methodological advancement introduced in this study is the use of Forescattered Electron (FSE) images for DIC analysis. This approach enables concurrent acquisition of high-quality images suitable for both DIC and EBSD within the same SEM setup and field of view. Compared to conventional secondary electron imaging, FSE imaging provides improved phase and orientation contrast under high-tilt EBSD conditions, without compromising diffraction pattern quality. As such, it presents a practical and effective solution for achieving high-resolution, co-registered full-field measurements in in-situ micro-mechanical testing.

HR-EBSD-based measurements provided high-resolution mapping of the elastic strain fields, enabling accurate decomposition of the deformation gradient and reliable calculation of J-integral and stress intensity factors. In comparison, DIC-based evaluations offered a broader picture of the total displacement field, capturing both elastic and plastic contributions. However, the presence of out-of-plane motion and the inability to isolate elastic shear modes introduced uncertainties into the DIC-based quantification of crack driving forces.

Despite these differences, the overall trends observed from both techniques are consistent and align well with theoretical expectations derived from finite element simulations using remote boundary conditions. Notably, the purely elastic FE model overestimates the crack driving force due to the absence of stress redistribution effects, emphasising the value of experimental investigations that capture local crack tip activities.

In summary, the results presented in this chapter highlights the critical importance of local full-field measurement in understanding the micromechanical behaviour of short fatigue cracks. While HR-EBSD offers high spatial fidelity in capturing elastic fields, its integration with FSE-based DIC enhances the interpretation of total deformation in a practical and innovative way. The observed influence of overload and the persistence of residual fields highlight the complex, history-dependent nature of short crack propagation, pointing to the need for further investigation. The findings of this chapter serve as a foundation for refining experimental techniques and modelling strategies aimed at capturing the detailed and complex behaviour of cracks at the microscale under realistic loading conditions.

Chapter 4

Fracture Toughness Testing by Analysis of Indentation Crack Fields in Silicon

4.1 Introduction

Micro-mechanical testing is playing an increasingly critical role in the design of next-generation engineering materials. As materials are pushed to operate in extreme environments, such as in aerospace [297, 374, 375], microelectronics [265, 266], and energy storage systems [272, 273], their mechanical integrity at small length scales becomes an essential design factor. In particular, ceramics and advanced composites, which offer desirable combinations of low density, high

hardness, and thermal stability, often suffer from low fracture toughness and brittle failure. These limitations are most pronounced at interfaces and grain boundaries [376, 377], which are known to control crack initiation and propagation but are difficult to study in isolation.

Unlike conventional bulk fracture toughness testing (reviewed in detail in Chapter 1), micro-mechanical testing allows direct evaluation of mechanical properties at the scale of individual microstructural features, such as grain boundaries, thin films, or phase interfaces. This is essential for systems where fracture behaviour is size-dependent or interface-dominated, including protective coatings [269, 270], batteries materials [272, 273, 378], microelectromechanical systems (MEMS) [267], and layered electronics [265, 266]. However, measuring fracture toughness at these scales poses significant challenges: the preparation of defect-free specimens with controlled geometry, the need to decouple substrate effects and residual stress contributions, and the difficulty of probing localised properties without averaging over complex microstructures.

Efforts to characterise fracture toughness at small length scales initially built upon classical indentation techniques, with the Lawn-Evans-Marshall (LEM) model [276-279] serving as a foundational approach. This model relates indentation load and resulting crack length to fracture resistance through a semi-empirical formulation involving hardness, elastic modulus, and crack geometry. While this technique proved effective for brittle bulk ceramics, its extension to small volumes, such as thin films or localised microstructural regions, revealed intrinsic limitations. The complex stress field beneath the indenter [280], the influence of plasticity [301, 302], and the geometry-dependent nature of crack systems [300] introduce significant uncertainty. Moreover, residual stresses and substrate effects in thin films [284] further compromise the validity of this method, rendering it unreliable for many advanced engineering materials.

To address these limitations, a new generation of micromechanical testing methods has been developed, leveraging focused ion beam (FIB) milling and nanoindentation to fabricate well-controlled micro-specimens. These techniques enable localised testing of fracture properties with

unprecedented spatial resolution, and critically, they allow for the targeting of specific microstructural features, such as grain boundaries [310, 379, 380], interfaces [318, 320, 381], or individual phases [153, 304]. Among these, the micro-cantilever bending test and the micro-pillar splitting method have become the most prominent.

In the micro-cantilever approach, a notched beam is milled from the material and subjected to bending via nanoindentation. Fracture toughness is derived using analytical expressions from linear or elastic–plastic fracture mechanics, with the aid of finite element models [300] to account for geometric complexity. This method has demonstrated strong utility in characterising intergranular fracture [304], radiation damage effects [314], and dislocation-driven toughening processes [307]. However, it is sensitive to notch geometry, ion damage, and residual stress relaxation [269, 312], all of which require careful control.

The micro-pillar splitting technique, on the other hand, is based on indenting cylindrical pillars, typically with a high aspect ratio, until catastrophic cracking occurs. The critical load at which splitting takes place is used to calculate fracture toughness through a calibrated relationship involving the pillar geometry and material properties. This approach eliminates the need to measure crack length, simplifies data interpretation, and reduces the impact of residual stresses [292, 293]. Due to its ease of implementation and statistical robustness, pillar splitting has gained popularity, especially for evaluating fracture toughness of hard coatings [382], oxide films[297], and battery materials [272, 273, 378].

Despite significant progress, these approaches remain constrained by practical and conceptual limitations. The majority of existing methods rely heavily on sophisticated FIB-based specimen preparation, which, while offering geometric control and site specificity, requires multiple milling stages, precise geometric control, and careful post-processing. Such demand imposes significant barriers to statistically robust studies. Additionally, many of the established test geometries, such as cantilevers [310], clamped beams [288], or DCBs [291], are inherently optimised for controlled

mode I fracture, and are thus not well suited to more complex or realistic loading conditions where mixed-mode fracture may occur.

Beyond fabrication and loading constraints, there is also the issue of interpretability. Most existing micromechanical tests focus on extracting single-point fracture toughness values, often derived under idealised assumptions of symmetry, notch sharpness, or material homogeneity [291]. However, real fracture processes, especially those involving brittle cleavage or intergranular cracking, rarely conform to such idealisations. In these cases, understanding the spatial evolution of stress and strain fields around the crack tip becomes just as important as the critical stress intensity itself. Unfortunately, current techniques provide limited access to such information, often relying on indirect or post-mortem assessments.

Furthermore, the mechanical response of brittle materials at small scales is often influenced by localised factors such as notch-induced residual stresses, FIB damage zones, and interface decohesion, all of which introduce uncertainty in test repeatability and accuracy. These effects are particularly problematic for grain boundary fracture studies, where the inherent variability in boundary type, orientation, and chemistry further complicates experimental design.

Given these limitations, there is a growing need for alternative testing approaches that reduce experimental complexity while enabling mechanistic understanding of crack behaviour at small scales. In this context, the study by Koko et al. [155] represents a new strategy. By integrating in situ high-resolution electron backscatter diffraction (HR-EBSD) with the observation of quasi-static crack propagation, they demonstrated a new pathway for characterising fracture toughness in brittle materials. Rather than relying on standard specimen geometries or indirect toughness models, their approach directly couples full-field strain mapping with crack driving force analysis, offering both local fracture metrics and insight into crack evolution mechanisms.

Building on these insights, the present work seeks to develop a simplified yet rigorous micromechanical testing approach that leverages full-field data and crack driving force evaluation to characterise brittle fracture processes. The method aims to bridge the gap between experimental feasibility and mechanistic fidelity, offering a pathway toward more universal application in studying microstructurally governed fracture, especially in materials where cleavage or boundary-controlled cracking dominates.

4.2 Methodology

4.2.1. Material, Single Indent and Its Residual Field

The material used in this study was a single-crystal silicon wafer with (001) crystallographic orientation. The wafer was n-type, doped with phosphorus, exhibiting a nominal resistivity of $90.0\ \Omega \cdot cm$ and a thickness of approximately $695\ \mu m$. This type is widely employed in both electronics and micromechanical testing due to its well-defined structure and consistent mechanical response.

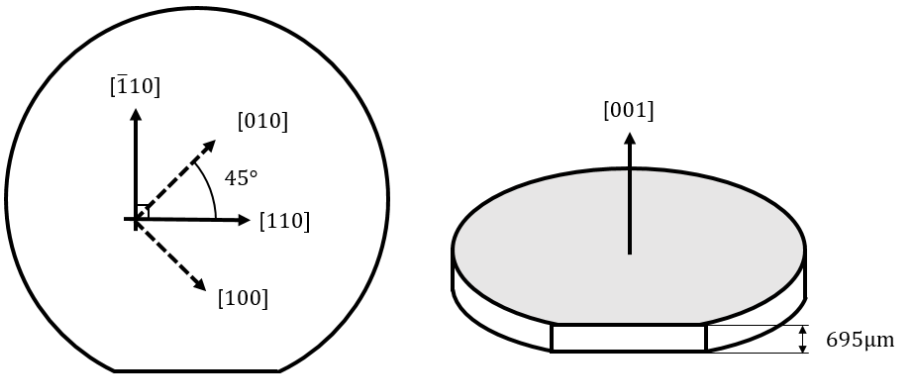

FIGURE 4.1
Schematic of the n-type single-crystal silicon wafer with (100) crystallographic orientation, used in this study.

Pure silicon is intrinsically non-conductive. To make it functionally usable, controlled doping is required. In this case, phosphorus atoms, each with five valence electrons, have been introduced into the silicon lattice. These atoms donate free electrons to the conduction band without disrupting

the cubic crystal structure, thus forming an extrinsic n-type semiconductor. The resulting moderate conductivity is especially advantageous for SEM observations, as it minimises surface charging without the need for additional conductive coatings.

The wafer was sectioned into specimens approximately 6 mm × 6 mm in size and mounted on pin stubs using conductive adhesive Silver DAG. The as-received surface was mirror-flat and required no further preparations. It provided an ideal surface for indentation tests and EBSD strain analysis, with sharp and reliable diffraction patterns obtained directly. Crack paths were also clearly visible under SEM due to the high surface quality.

Monocrystalline silicon is commonly used as a model material in micro-scale fracture toughness measurements due to its characteristic elastic-to-brittle failure mode. Under room temperature conditions, it often deforms elastically until abrupt fracture, with negligible plasticity. Silicon has a cubic crystal structure and its fracture behaviour is strongly anisotropic, with cracks tending to propagate along preferred crystallographic planes such as {110} or {111} [383, 384]. This anisotropy allows controlled observation of crack initiation and propagation mechanisms. Additionally, the material is nearly defect-free at the microscale, and free of grain boundaries, ensuring uniformity in mechanical response and improving test reproducibility.

To inform the experimental design, preliminary indentation tests were first conducted using both spherical and Berkovich indenters. Under appropriate loading conditions, spherical indentation is capable of generating a residual stress field around the contact zone [321, 322], while Berkovich indentation can initiate radial cracks at its sharply defined corners [280]. The material used in this study, (001) oriented monocrystalline silicon, exhibits strong crystallographic directionality in its fracture behaviour. When subjected to impact at the centre, (001) silicon wafers typically fracture into four quadrants, indicating preferred crack propagation along the ⟨110⟩ directions, which are orthogonal on the (001) plane.

This crystallographic regularity enables alignment between the indenter orientation and the underlying lattice directions, using the edges of the fractured samples as a reference for alignment, as shown in Figure 4.2. By characterising the wafer orientation and controlling the sample cutting process accordingly, it is possible to align the Berkovich indenter's radial direction with a ⟨110⟩ cleavage direction. Such alignment facilitates controlled crack initiation and propagation along specific crystallographic planes, enhancing the repeatability and interpretability of the indentation fracture experiments.

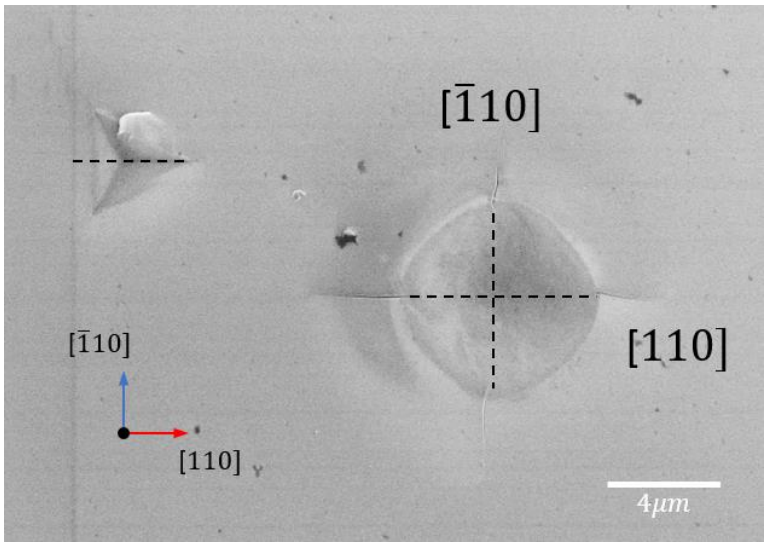

FIGURE 4.2
Preferred crack propagation along the ⟨110⟩ directions around a spherical indent, with the Berkovich indent aligned parallel to the cleavage direction.

Nanoindentation was conducted using an *Agilent G200 Nano Indenter*® equipped with diamond Berkovich and spherical tips. The Berkovich tip had a nominal radius of 20 µm, while the spherical tip had a nominal radius of 10 µm. The instrument was operated in quasi-static mode, following the Oliver and Pharr method [385]. The purpose of the testing was to introduce well-controlled residual stress fields around the indents and to examine the conditions under which cracks initiate. Indentation depths ranged from 500 nm to 1000 nm for spherical indents, and from 400 nm to 800 nm for Berkovich indents. A constant displacement rate was used throughout each test (20 s loading time at a constant rate, 5 s hold time). All indents were spaced at least 200 µm apart to avoid interaction effect. HR-EBSD analysis was carried out after the indentation tests.

4.2.2. Crack Arrest in Residual Field using Dual Indentation

From the body of literature discussing the limitations of the Lawn-Evans-Marshall (LEM) method, two central issues can be summarised: first, the idealised conditions assumed by the model, such as the formation of long, half-penny or 'Palmqvist'/radial cracks under well-defined loading and material responses, are often difficult to achieve in practice; second, the approach lacks accuracy in evaluating the actual crack driving force. These limitations constrain the wider applicability of the LEM method, despite its unmatched advantages in simplicity and minimal material requirement for toughness evaluation.

This study aims to address these challenges by developing a methodology that retains the practical advantages of indentation-based fracture toughness measurements, while overcoming their inherent limitations. Building on observations from single-indent studies, the proposed methodology employs spherical indentation to generate a controlled and stable residual stress field, combined with Berkovich indentation to initiate radial cracks from its sharply defined corners. By strategically positioning the Berkovich indent relative to the spherical indent, cracks may be intentionally introduced and, ideally, driven and subsequently arrested by the residual stress field. If successful, this dual-indentation approach, when integrated with full-field HR-EBSD measurements, would allow the crack-tip driving force to be accurately quantified at the arrest point, thereby providing a rigorous and reliable method for evaluating fracture toughness.

This dual-indentation approach is designed to exploit spatially controlled interaction between the crack and the residual stress field. To investigate this interaction, Berkovich indents are placed at varying distances outside the spherical indent, allowing systematic evaluation of how the residual stress field influences crack propagation.

In addition, configurations are studied in which the Berkovich indent is placed inside the spherical indent. In this case, the crack initiated by the Berkovich tip propagates entirely within the residual

stress field. The stress intensity factor at the crack tip is then evaluated using HR-EBSD measurements, serving as a quantitative validation of the method.

4.2.3. HR-EBSD Measurements and *J*-integral Analysis

After the indentation tests, EBSD measurements were performed using a *Carl Zeiss*® *Merlin* field emission gun scanning electron microscope (FEG-SEM), equipped with an *Oxford Instruments Symmetry*® detector featuring a high-resolution CMOS sensor for EBSP acquisition. All scans were conducted under an accelerating voltage of 20 kV, a beam current of 10 nA, and a working distance of 18.5 mm. Kikuchi patterns were collected in high-resolution mode with an image resolution of 1244×1024 pixels.

Two types of scan configurations were employed depending on the field of view:

- For large-area mapping, the scan field was selected to fully capture the dual-indent region. A step size in the range of 0.15 µm – 0.20 µm was used over a grid of approximately 160×120 steps, resulting in a mapped area of $\sim 32\ \mu m \times 24\ \mu m$. An exposure time of 5 ms – 10 ms per pattern was used without frame averaging. Due to the as-received mirror-finished surface, signal quality was excellent.
- For high-resolution mapping near crack tips, a smaller field of view was adopted. A step size of 60 nm was applied over a scan grid of approximately 160×120 steps, yielding a mapped area of $\sim 9.6\ \mu m \times 7.2\ \mu m$. A longer exposure time of 10 ms was used, also without frame averaging, to ensure high-quality pattern acquisition near the crack tip.

With the obtained data, HR-EBSD strain calculation was performed in a similar way as described in Section 3.2.3.3. The elastic strain field was extracted using the commercial software *CrossCourt*® *Rapide* v4.6, following an iterative cross-correlation procedure between electron backscatter patterns (EBSPs) and a reference pattern assumed to be stress-free. Prior to analysis, raw patterns were subjected to background correction using a "white scan". This refers to a

reference scan acquired over a large field of view without significant crystallographic texture. It captures the background intensity distribution, which is subtracted from the raw patterns to enhance the signal quality and remove systematic background features. The entire field of view was treated as a single grain, and reference patterns were selected from the edge of the scan remote from the indents and crack to ensure minimal residual strain. Cross-correlation was conducted on carefully selected regions of interest (ROIs) with well-defined Kikuchi bands, while avoiding poor-quality areas. To enhance the accuracy of correlation, a built-in FFT filtering routine in *CrossCourt*® *Rapide* v4.6 was applied to suppress low- and high-frequency noise and improve pattern clarity. The final strain tensors were calculated from the deformation gradient field under the assumption of plane-stress boundary conditions and elastic anisotropy of the single crystal.

The J-integral analysis was performed using the direct evaluation method illustrated in Section 3.2.4.2, based on the full-field deformation gradient data obtained from HR-EBSD. An auxiliary vector field $\boldsymbol{q_1}$ was defined to localise the integration path, and the Equivalent Domain Integral (EDI) method was applied over the measurement region. The strain energy density was computed from the Green-Lagrangian strain tensor, derived from the deformation gradient. The total J-integral was decomposed into mode-specific components (Mode I, II, III) using symmetry operations applied to the displacement gradient field. Each mode was analysed independently through Hooke's law with anisotropic stiffness, allowing accurate computation of the mode-specific energy release rates and the corresponding stress intensity factors. The elastic stiffness tensor used for silicon is defined by $C_{11} = 165.78$ GPa, $C_{12} = 63.94$ GPa, and $C_{44} = 79.62$ GPa.

This approach enabled a quantitative evaluation of the mixed-mode crack-tip driving force under residual stress-dominated conditions.

4.2.4. Maximum Potential Energy Release Rate Method

To evaluate fracture toughness under mixed-mode loading, it is necessary to adopt a criterion that accounts for the combined effects of modes I, II, and III. The Maximum Potential Energy Release Rate (MPERR) method [386-389] provides a unified and physically meaningful fracture criterion under such conditions. Unlike traditional criteria (e.g., Maximum Circumferential Stress [390] or Minimum Strain Energy Density [391, 392]), which are either restricted to planar cases or fail to incorporate mode III effects adequately, MPERR offers a three-dimensional, energy-based framework that predicts both the critical fracture condition and the effective fracture toughness in mixed-mode situations. It was previously used successfully in a study of a quasi-static (131) cleavage crack in Si, observed in situ by HR-EBSD and analysed using the direct evaluation method [155].

The MPERR criterion defines fracture as occurring when the combination of applied stress intensity factors satisfies the following normalised elliptical relationship:

$$\left(\frac{K_{\mathrm{I}}}{K_{\mathrm{IC}}}\right)^2 + \left(\frac{K_{\mathrm{II}}}{K_{\mathrm{IIC}}}\right)^2 + \left(\frac{K_{\mathrm{III}}}{K_{\mathrm{IIIC}}}\right)^2 = 1 \tag{4-1}$$

Here, K_{IC}, K_{IIC},K_{IIIC} represent the critical stress intensity factors in pure mode I, II, and III, respectively. These are expressed relative to a unified effective toughness K_{eff} as follows:

$$K_{\mathrm{IC}} = K_{\mathrm{eff}}, \quad K_{\mathrm{IIC}} = \frac{\sqrt{3}}{2} K_{\mathrm{eff}}, \quad K_{\mathrm{IIIC}} = \frac{\sqrt{\mathrm{k}+1}}{2} K_{\mathrm{eff}} \tag{4-2}$$

Where the parameter k accounts for Poisson's ratio effects under plane stress conditions:

$$k = \frac{3-\nu}{1+\nu} \tag{4-3}$$

In addition, the mode mixity is quantified by an angle ψ, defined as

$$\psi = tan^{-1}\left(\frac{K_{\mathrm{III}}}{\sqrt{K_{\mathrm{I}}^2 + K_{\mathrm{II}}^2}}\right) \tag{4-4}$$

This formulation ensures that the influence of out-of-plane shear (mode III) is fully incorporated in both the critical fracture condition and the directionality of crack growth. The MPERR method is particularly advantageous for analysing fracture in three-dimensional anisotropic materials, where mode coupling and mixed-mode effects are significant. Its closed-form criterion also makes it suitable for direct comparison with experimental measurements and for use in numerical simulations.

4.3 Results

4.3.1. Single Indent Control

A series of single-indentation tests were conducted to investigate strategies for controlling spherical indentation to generate the desired residual stress field, as well as for effectively introducing cracks using Berkovich indentation. The indentation tests were performed using a predefined depth limit, with indentation depths progressively reduced to identify the critical conditions. The objective was to identify the maximum load for spherical indentation that does not induce cracking, and the minimum load for Berkovich indentation that reliably initiates radial cracks at the corners. In this study, precise control of the applied load was not the primary objective, as the actual conditions were to be quantitatively characterised through HR-EBSD measurements afterwards. Figure 4.3 illustrates representative arrays of single indents performed in this study.

As shown in Figure 4.3, an indentation depth limit of 600 nm was selected for spherical indents to generate the residual stress field used in subsequent tests. This depth was chosen because it does not induce cracking, thereby preserving the integrity and symmetry of the residual stress distribution. For Berkovich indents, a depth limit of 300 nm or 400 nm was employed, depending on whether a pre-existing crack was desired for the specific test configuration.

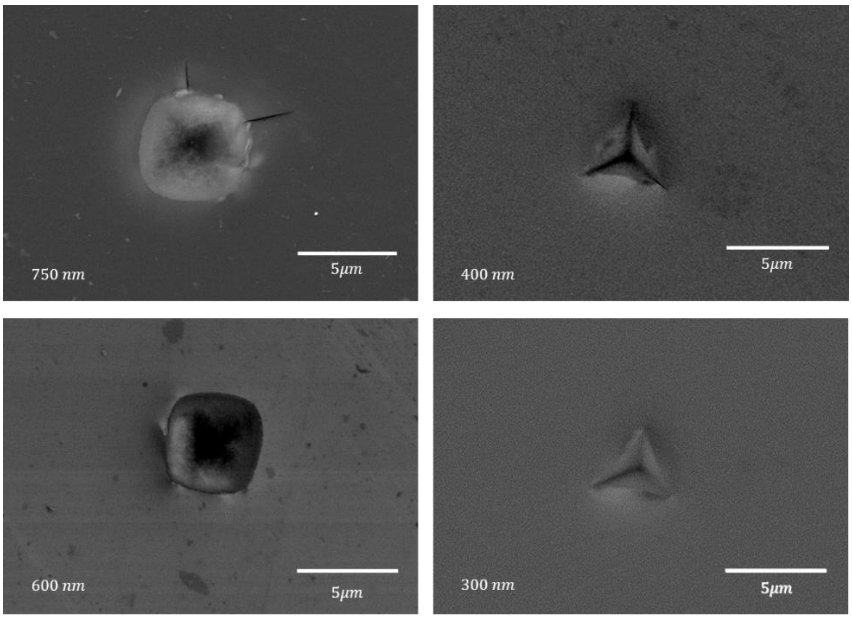

FIGURE 4.3
Secondary electron (SE) images of single indentation tests. The indentation depth limit applied in each experiment is indicated in the lower left corner of each image.

Figure 4.4 presents a representative residual stress field surrounding a spherical indent. It can be observed that the spherical indentation induces an in-plane tensile hoop stress field, which can be exploited to drive crack propagation when combined with a second, strategically placed indent. This characteristic forms the basis for the dual-indentation approach developed in this study.

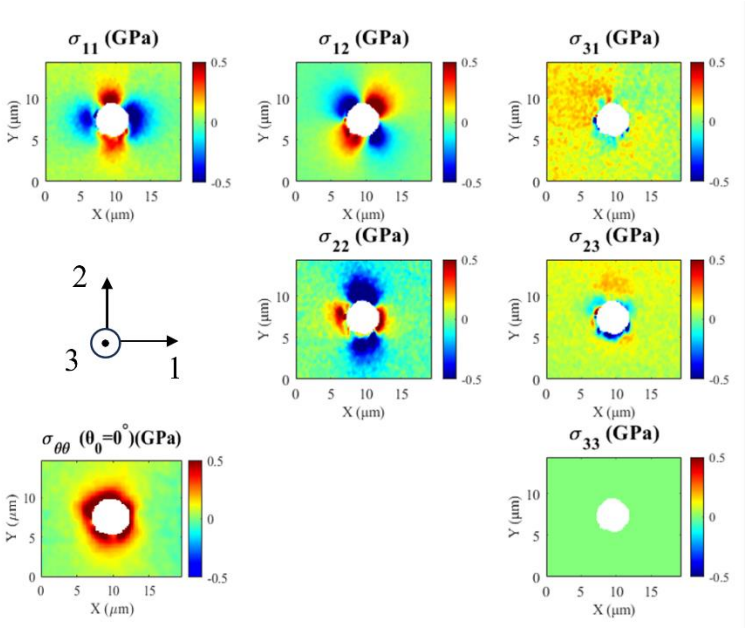

FIGURE 4.4
Full residual stress tensor field generated by a 600nm depth spherical indent on silicon (001), obtained from HR-EBSD strain mapping and calculated based on an anisotropic elastic model.

4.3.2. Dual Indent Interaction: Inward Propagation

To investigate crack-residual stress interaction, a series of dual-indentation experiments were performed using a spherical indent to generate a residual stress field. A relatively small depth limit was selected for the Berkovich indent to ensure that it would not independently initiate a crack. The Berkovich indents were placed at various distances from the spherical indent, with one vertex aligned along a ⟨110⟩ direction, that is, radially inwards to the centre of the spherical indent. This configuration allows the residual stress field to provide a tensile hoop stress perpendicular to the preferred crack propagation plane.

Figure 4.5 presents typical results of these dual-indentation tests. In the case of large spacing (7.83μm), no crack initiation was observed. At an intermediate distance (6.45μm), a crack initiated from the Berkovich indent and propagated partially toward the spherical indent but eventually stopped within a short distance (4.92μm). When the spacing was further reduced, the crack propagated continuously and penetrated into the spherical indent, forming a through-crack.

High-magnification observations reveal additional insights into the crack-stress interaction. In the close-spacing case, the crack is fully opened along its entire length, indicating that it is strongly affected by the residual tensile stress field. In the intermediate-spacing case, the crack tip appears nearly closed, while the rear part of the crack remains slightly open, suggesting a gradual reduction in tensile stress along its path. These observations serve as supporting evidence that the residual stress field directly influenced crack propagation. Although the Berkovich indentation was removed after initiating the crack, its effect on the stress field during subsequent propagation is minimal. This is because the residual stress field generated by the spherical indent dominates the local mechanical environment, and any stress redistribution due to Berkovich removal is both localised and small in magnitude. Therefore, it is reasonable to infer that the crack tip approaches a critical state when it stops, with the local crack driving force reduced to just below the material's fracture toughness.

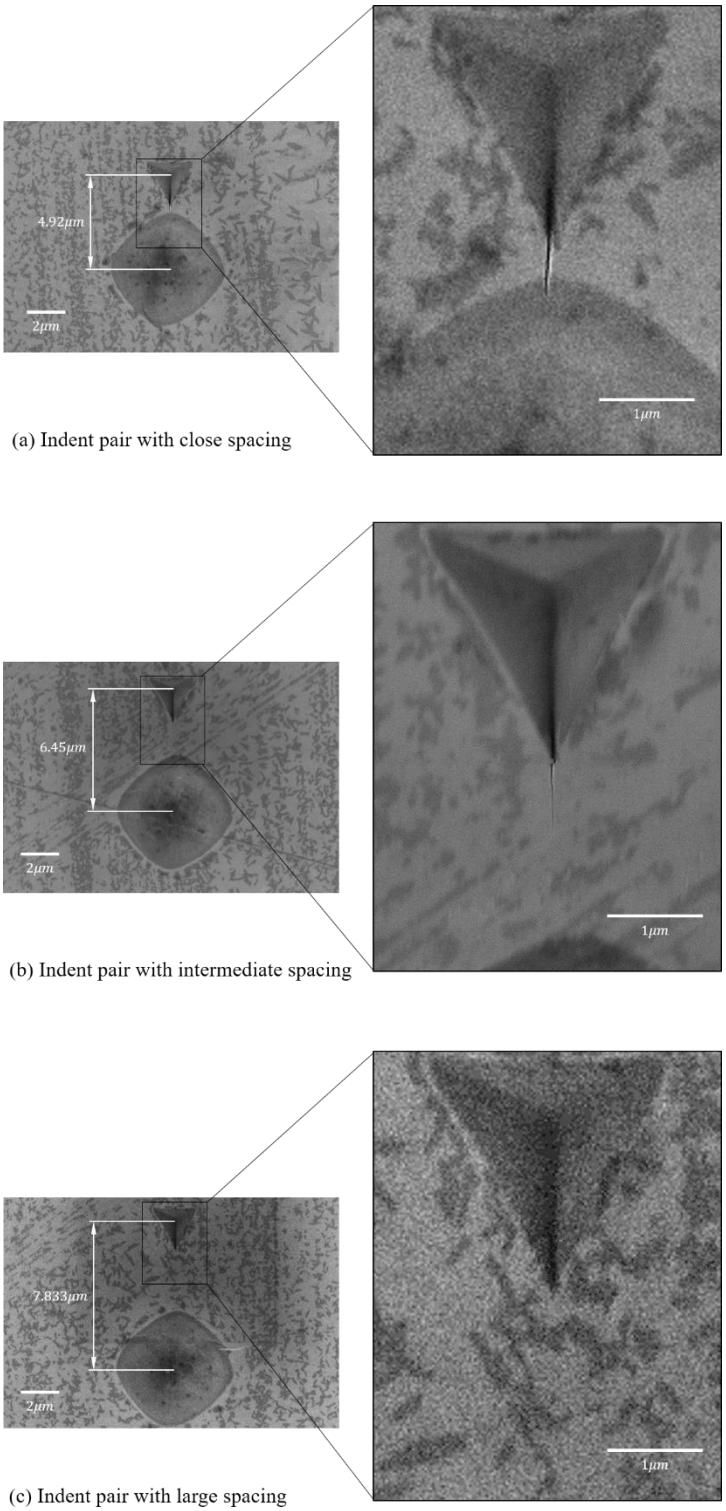

FIGURE 4.5

Dual indent interaction. (a) Indent pair with close spacing: a crack initiates from the Berkovich indent and propagates into the spherical indent, forming a through-crack. (b) Indent pair with intermediate spacing: a crack initiates from the Berkovich indent but is arrested before reaching the spherical indent. (c) Indent pair with large spacing: no crack initiation is observed.

Note that the surface patterns visible in the image are not intentional decorations, but are likely artefacts resulting from minor surface contamination or residual effects from prior processing steps. These features do not affect the mechanical testing results and are unrelated to the deformation behaviour studied.

To further illustrate the interaction between cracks and the residual stress field, full-field measurements were conducted following the dual-indentation tests. Figure 4.6 presents the measured σ_{11} stress fields for the representative tests shown previously in Figure 4.5, highlighting the in-plane tensile stress acting perpendicular to the crack path. As seen in Figure 4.6, at close spacing, the crack experiences a strong tensile stress resulting from the combined effects of both indents. At intermediate spacing, the tensile stress level near the crack is slightly reduced compared to the close-spacing case, yet it remains relatively high. Furthermore, the residual stress distribution originally introduced by the spherical indent is significantly altered after crack initiation and propagation, reflecting clear interaction between crack growth and the surrounding stress field. In the large-spacing case, this redistribution of residual stress can also be observed but is confined to regions close to the Berkovich indent, where its stress field remains largely unchanged from the single-indent condition due to the lack of significant interaction with the spherical indent's stress field.

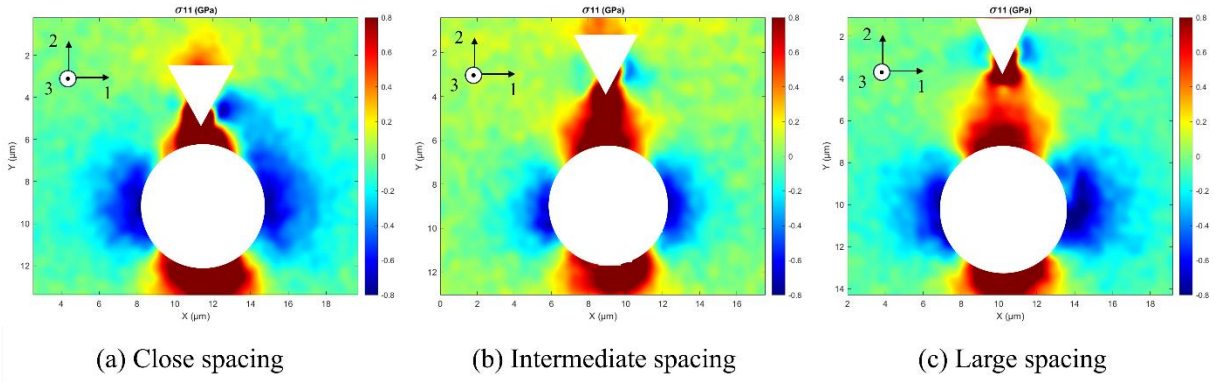

(a) Close spacing (b) Intermediate spacing (c) Large spacing

FIGURE 4.6

Stress field (σ_{11}) measured by HR-EBSD for dual-indent interaction (4.92 μm, 6.45μm, 7.83 μm distance). The 11 direction is parallel to the *x*-axis in the image.

This analysis demonstrates that crack propagation behaviour within a residual stress field varies distinctly depending on the extent of their interaction. By strategically exploiting this interaction, it becomes possible to achieve controlled crack propagation conditions approaching a critical state, thereby providing a robust foundation for accurate fracture toughness evaluations.

4.3.3. Dual Indent Interaction: Outward Propagation

In the previous tests, although the desired crack–stress field interaction was successfully observed when the Berkovich indent was placed outside and oriented toward the spherical indent, achieving a stable arrested crack at a critical state required careful control. This complexity arises primarily because the crack propagation direction is against the residual stress gradient, meaning the crack tip propagates into regions of increasing tensile stress magnitude, as shown in Figure 4.7.

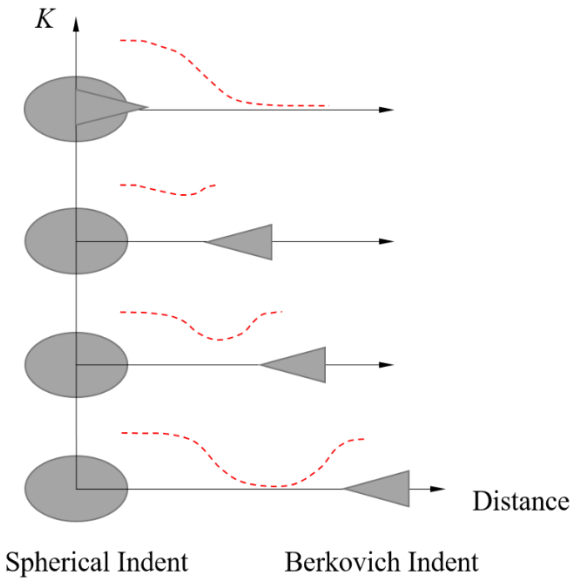

FIGURE 4.7
Schematic plot of the expected K values as a function of crack tip location within the superimposed residual stress field of the dual indents. The residual stress field decays gradually with distance from the spherical indent, while it diminishes rapidly away from the Berkovich indent. This spatial variation governs the local crack driving force.

An alternative indentation arrangement was investigated, where the Berkovich indent was positioned *inside* the spherical indent. In this new configuration, the Berkovich indent vertex was oriented radially outward, with one of its corners placed precisely at or slightly beyond the edge of the spherical indentation. The indentation load was carefully selected to be just sufficient to initiate a crack at the Berkovich indent corner. Under this arrangement, the crack naturally propagates outward, moving along the decreasing residual tensile stress gradient. Consequently, the crack driving force progressively decreases until the crack spontaneously arrests, establishing

a clearly defined critical state. Although the crack initiates under the influence of the Berkovich load, its effect is expected to diminish rapidly with distance and is therefore considered to have a negligible influence on the subsequent crack propagation and arrest behaviour.

Following this new indentation arrangement, a total of eight dual-indentation tests were successfully conducted. The results from all tests are presented in Figure 4.8, which shows the secondary electron (SE) images of the indented regions. Enlarged views highlighting the crack-tip areas are also included. The approximate positions of the crack tips were visually identified from the SE images, and the visible crack lengths were measured using *ImageJ*, based on the scale bars recorded in the images. The measured lengths are annotated directly on the enlarged views and the results are plotted in Figure 4.9 as a function of the distance between the centres of the two indentations. Further interpretation, including the trace analysis and crack path, is provided in the Discussion section.

The eight tests were conducted under slightly varying conditions. Test A served as a preliminary trial, in which the spherical indent was made using an indentation depth limit of 600 nm. However, in several subsequent tests, it was observed that this depth occasionally led to the formation of cracks around the spherical indent. This may be related to tip degradation over time, which could have resulted in deviations from the ideal, uniform hemispherical indentation shape. In addition, limitations associated with the long-serving instrument, such as slight misalignment or reduced stability during loading, may have also contributed to these crack formations.

To prevent such cracking, which could compromise the integrity of the residual stress field and reduce the consistency of the tests, the indentation depth limit for the spherical indent was slightly reduced to 550 nm in the remaining seven tests (Tests B to H). This adjustment improved the overall stability and reproducibility of the experimental conditions.

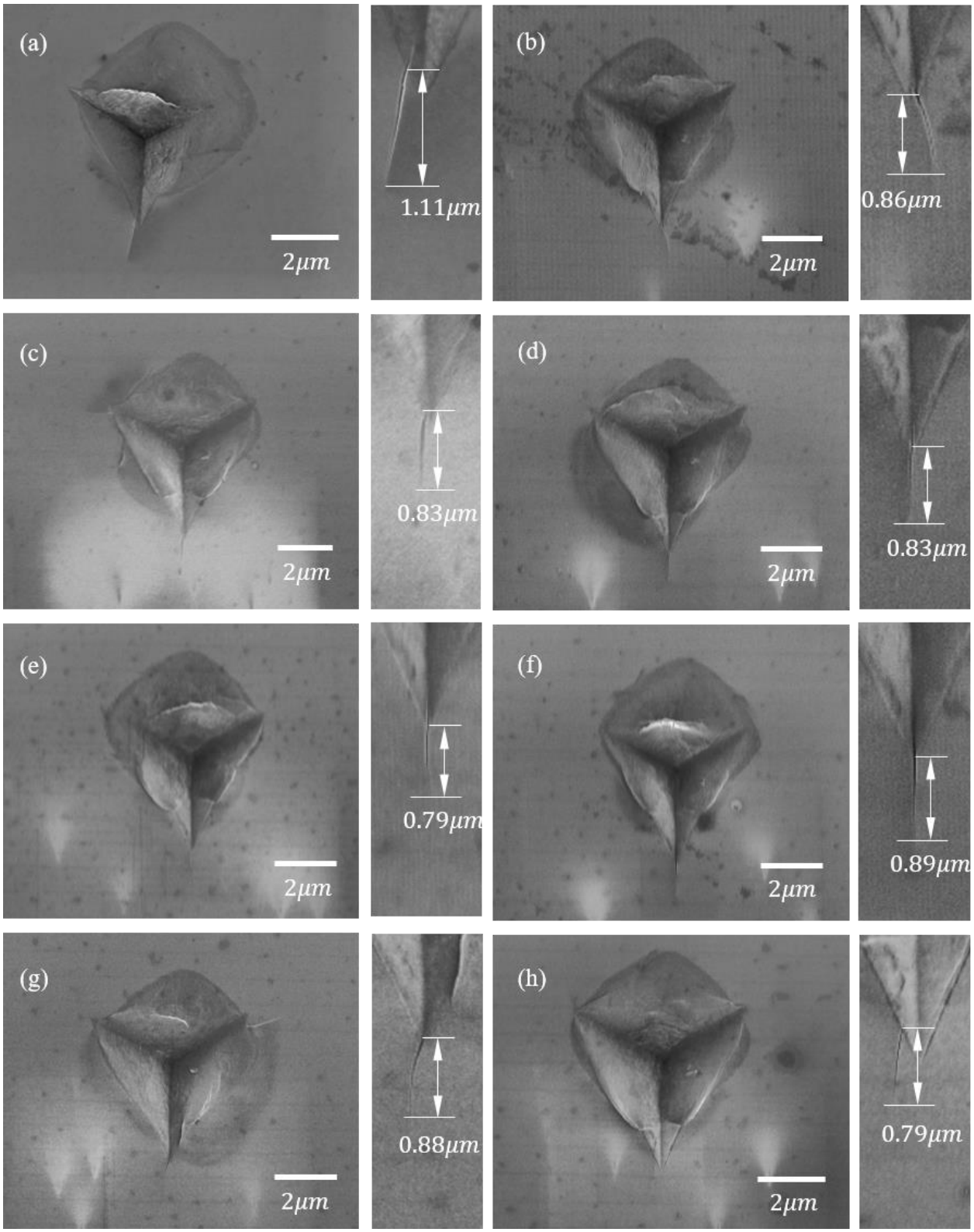

FIGURE 4.8

Secondary electron images of eight dual-indentation tests (Tests A-H) conducted using the modified indentation configuration. Enlarged views highlight the region near the crack tips. Visible crack lengths were measured and are annotated on each image.

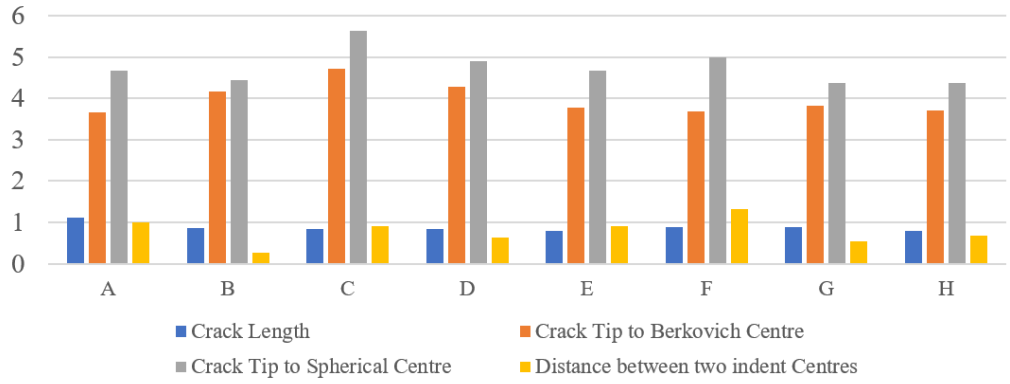

FIGURE 4.9
Plot of measured crack length for different distances between the centres of the two indentations. (in μm)

During SE imaging, the sample was oriented such that the ⟨110⟩ crystallographic directions coincided with the horizontal and vertical axes of the image within the limits of stage alignment accuracy. The precise orientation relationship between the crack paths and the crystal planes was later determined through detailed trace analysis (Discussion Section). Due to these limitations in the equipment, the exact placement of the Berkovich indents varied slightly from test to test. However, all indents generally satisfied the two key conditions of being oriented radially and having the corner located on or slightly beyond the edge of the spherical indent.

In all eight tests, the initiated cracks propagated approximately along the ⟨110⟩ crystallographic directions, with slight deviations observed from sample to sample. The crack surfaces consistently exhibited a transition from being more open near the initiation point to closed toward the crack tip, which aligns with the intended residual stress interaction in the experimental design. Minor variations in crack length and initiation position were observed, likely due to slight differences in the relative placement between the spherical and Berkovich indents in each test.

These variations, together with potential fluctuations in loading conditions and instrument performance, introduced a degree of uncertainty in the crack formation process. Nevertheless, the crack-tip mechanical conditions in each test were subsequently characterised using full-field HR-EBSD measurements, which provided the necessary input for further quantitative evaluation of the crack-driving force.

Typical crack-tip stress fields from Test A are shown in Figure 4.10 and Figure 4.11. In the scan presented in Figure 4.10, a step size of 0.15 µm was used to capture a relatively large field of view, and the full set of stress tensor components is displayed. Figure 4.11 focuses on the near-tip region with higher spatial resolution, using a step size of 0.06 µm. This scan highlights the in-plane shear stress component, which is overlaid on the corresponding secondary electron image to illustrate the local stress distribution around the crack. The reference point for stress calculation was chosen at the edge of the field of view, remote from the indents, and assumed to be strain-free. In addition to geometric separation, regions with low Kernel Average Misorientation (KAM) and Band Contrast values greater than 120 were preferred, ensuring that the selected reference area was both mechanically unaffected and of good imaging quality.

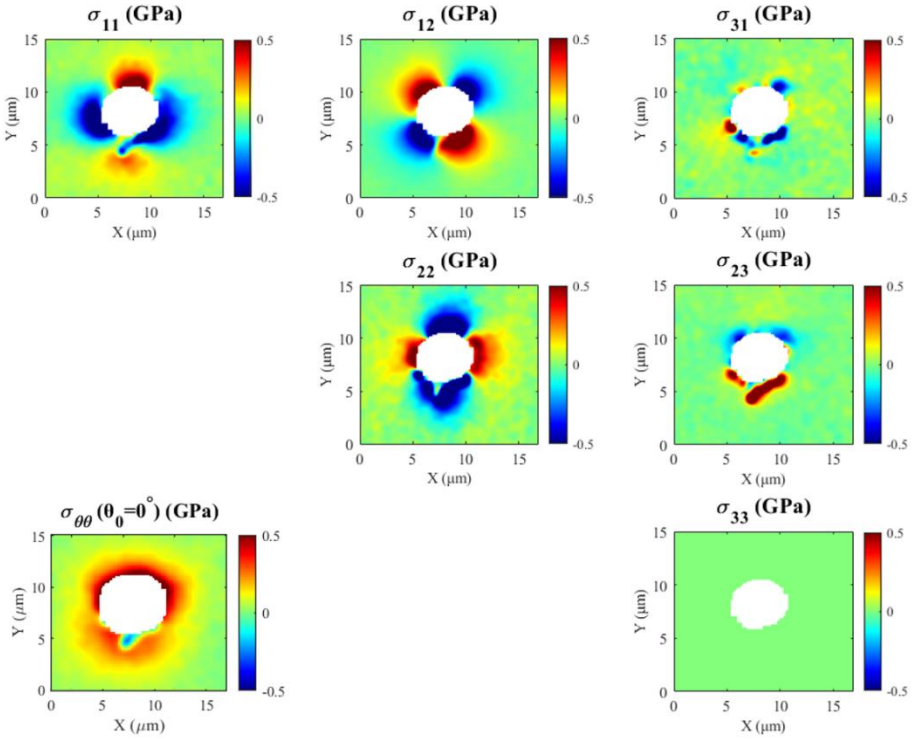

FIGURE 4.10

Full-field stress tensor components around the indent pair in Test A, measured by HR-EBSD, together with an in-plane hoop stress map (bottom left, plotted in polar coordinates centred at the indent, with θ = 0° along the positive x-axis). The sample is single-crystal silicon with a (001) surface orientation. Indents were introduced to a depth of approximately 600 nm. A step size of 0.15 µm was used to capture a relatively large field of view. The Berkovich nano-indent was positioned inside a previous spherical nano-indent, as shown in Figure 4.8 (a).

Figure 4.11 clearly reveals that the residual stress field undergoes a redistribution after crack initiation and propagation (compared with Figure 4.4). σ_{12} is presented in particular because this shear component changes sign across the crack plane, which makes it a sensitive indicator of how the stress field responds to crack propagation. The boundary between positive and negative in-plane shear stress (σ_{12}) aligns with the crack path, indicating a strong interaction between the crack and the residual stress field. Near the crack tip, the stress field decays rapidly, suggesting that the attainment of a critical crack-tip state (or crack arrest) is governed by the local reduction in residual stress magnitude.

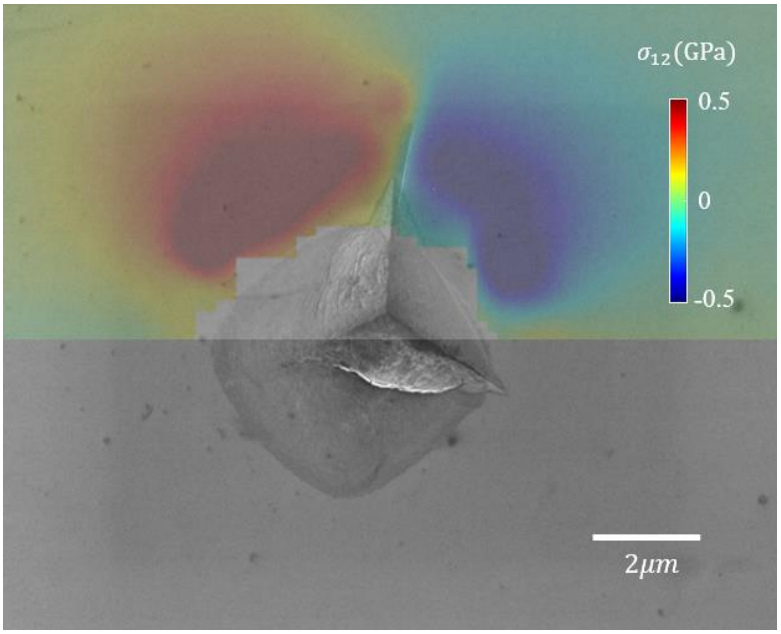

FIGURE 4.11
In-plane shear stress distribution (σ_{12}) in the crack vicinity region of Test A, measured by HR-EBSD with a step size of 0.06 μm. The stress field is overlaid on the SE image.

J-integral analysis was performed based on the HR-EBSD results for all eight tests. For each case, a local region surrounding the crack tip was cropped, and the data were rotated to align the crack horizontally with the tip positioned at the centre of the domain, as illustrated in Figure 4.12. The corresponding contour integral results are presented in Figure 4.14 and Figure 4.15. The maximum number of contours was limited by the crack length and the proximity of the indents. In all cases, the integral values show good convergence with increasing contour number. The mean and

standard deviation of the converged stress intensity factors are summarised in Table 4.1 and also annotated above each plot in Figure 4.14 and Figure 4.15. A histogram of the data is presented in Figure 4.13. Outliers exceeding 2.5 times the standard deviation from the mean were excluded from the averaging process.

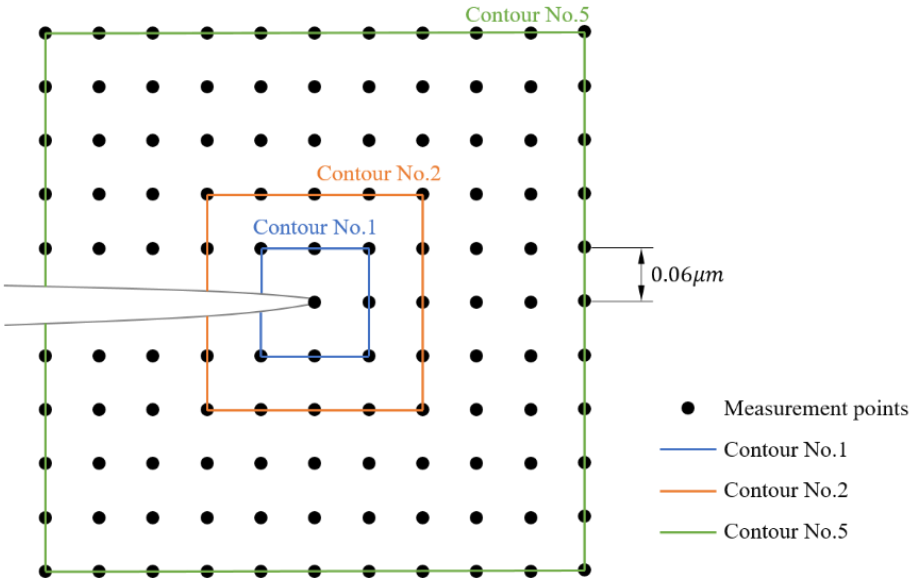

FIGURE 4.12
Schematic illustration of the contour definition used in the crack-tip measurement field. The cropped region is centred at the crack tip, with the crack aligned horizontally.

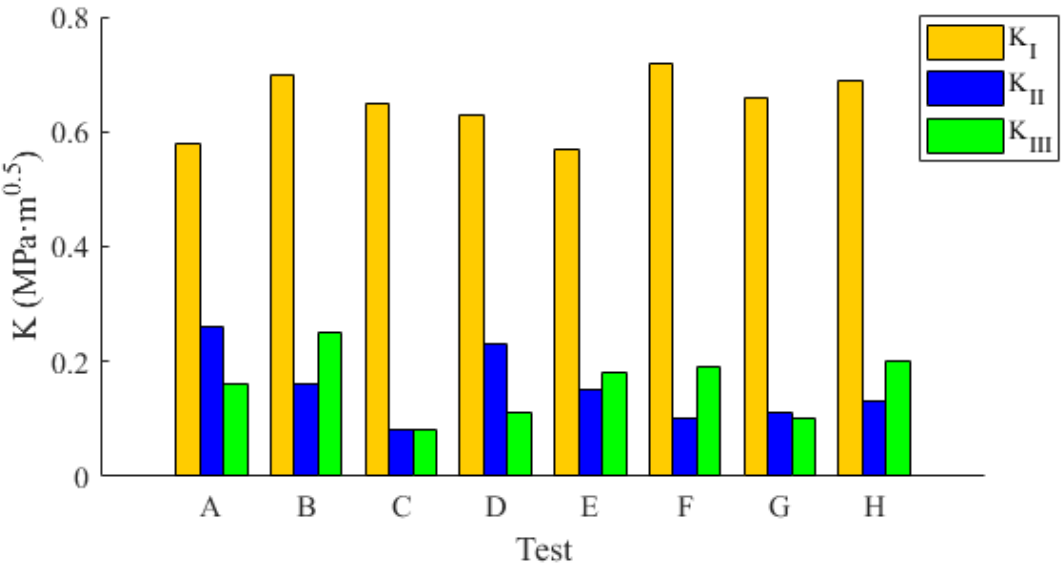

FIGURE 4.13
Histograms of the stress intensity factors K_{I}, K_{II}, K_{III} measured from eight tests.

TABLE 4.1
Summary of the mixed mode stress intensity factors, J-integral and ψ for the eight indentation tests.

Test	K_{I} (MPa·m$^{0.5}$)	K_{II} (MPa·m$^{0.5}$)	K_{III} (MPa·m$^{0.5}$)	J (J/m^2)	ψ (°)
A	0.58 ± 0.11	0.26 ± 0.11	0.16 ± 0.05	2.70 ± 0.80	14.1
B	0.7 ± 0.05	0.16 ± 0.05	0.25 ± 0.08	3.48 ± 0.57	19.2
C	0.65 ± 0.05	0.08 ± 0.03	0.08 ± 0.03	2.48 ± 0.33	7.0
D	0.63 ± 0.08	0.23 ± 0.05	0.11 ± 0.06	2.65 ± 0.64	9.3
E	0.57 ± 0.07	0.15 ± 0.02	0.18 ± 0.09	2.79 ± 0.60	17.0
F	0.72 ± 0.06	0.10 ± 0.06	0.19 ± 0.08	4.31 ± 0.65	14.6
G	0.66 ± 0.04	0.11 ± 0.05	0.10 ± 0.07	3.27 ± 0.55	8.5
H	0.69 ± 0.04	0.13 ± 0.05	0.20 ± 0.06	3.21 ± 0.39	15.9

For each indent pair, the contour integral results were evaluated in the local crack-tip coordinate system, meaning that the stress intensity factors correspond directly to the crack-tip field and are not affected by the coordinate rotation used to align the crack for numerical integration. Good convergence was consistently achieved starting from contour 6 to 8. All cases exhibit mode I-dominated loading, with minor contributions from modes II and III, indicating a mixed-mode stress state near the crack tip. The extracted mode I stress intensity factor (K_{I}) ranges from 0.57 to 0.72 MPa·m$^{0.5}$, with a mean value of 0.65 ±0.019 MPa·m$^{0.5}$. The mode II component (K_{II}) falls between 0.08 and 0.26 MPa·m$^{0.5}$ (mean: 0.15 ±0.022 MPa·m$^{0.5}$), while the mode III component (K_{III}) ranges from 0.08 to 0.25 MPa·m$^{0.5}$ (mean: 0.16 ±0.020 MPa·m$^{0.5}$).

Compared to K_{I}, the values of K_{II} and K_{III} are relatively small and exhibit greater variability. This increased scatter is likely due to the fact that even minor measurement noise can introduce significant relative errors when the magnitudes of K_{II} and K_{III} are low. Nevertheless, both shear-mode components remain secondary in contribution compared to the dominant mode I loading.

Experimental results demonstrate that the new configuration is straightforward to implement, yields stable crack formation, and exhibits good repeatability across multiple tests. The integration of full-field HR-EBSD measurements enables effective extraction of crack-tip stress and strain fields, allowing for the quantitative evaluation of mixed-mode stress intensity factors with high spatial resolution.

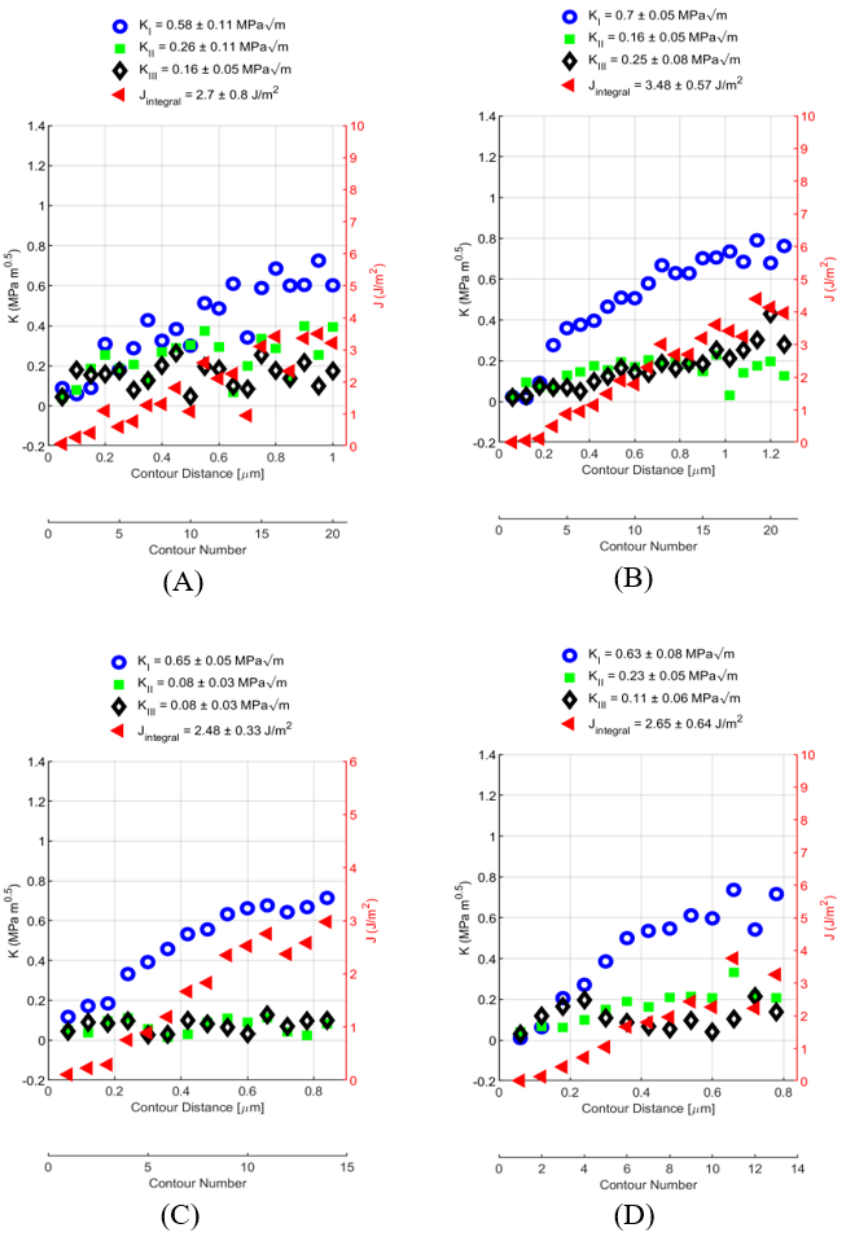

FIGURE 4.14

Contour integral results for the dual-indentation tests A to D, based on HR-EBSD measurements. Convergence was achieved at approximately 0.5 μm from the crack tip, and the mean and standard error of the *J*-integral and mixed mode stress intensity factors were obtained from contours beyond this.

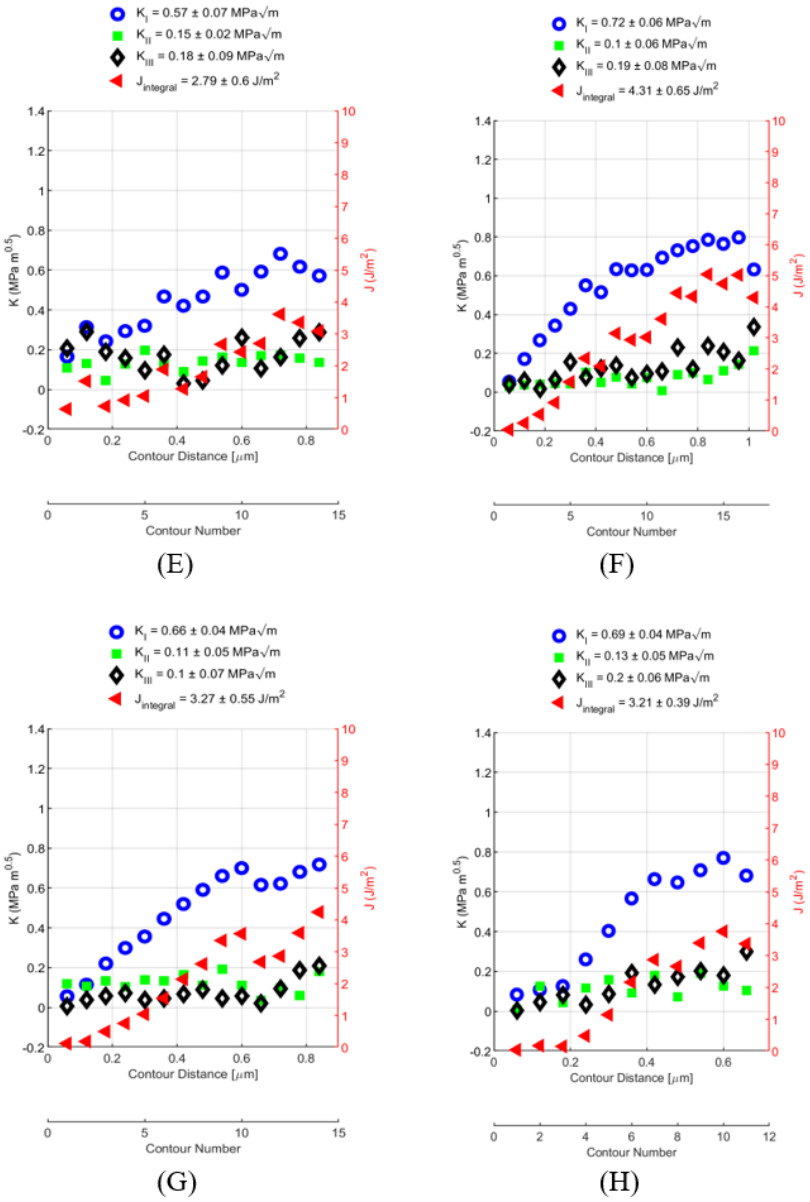

FIGURE 4.15

Contour integral results for the dual-indentation tests E to H, based on HR-EBSD measurements. Convergence was achieved at approximately 0.5 μm from the crack tip, and the mean and standard error of the *J*-integral and mixed mode stress intensity factors were obtained from contours beyond this.

4.4 Discussion

4.4.1. Cleavage Favourably Propagates in the {111} Plane

To better understand the crystallographic nature of crack propagation under the dual-indentation configuration, trace analysis was performed for all eight tests. The results are shown in Figure 4.16, where each secondary electron (SE) image is overlaid with the complete set of {111}⟨110⟩ trace

directions. For each image, traces of the {111} cleavage planes were plotted. Due to the crystallographic symmetry of single-crystal silicon and the specific sample orientation used in this study, many of these traces overlap, revealing well-defined preferred paths for crack propagation.

The trace analysis reveals that in the majority of cases, the cracks propagated along directions that closely align with ⟨110⟩ traces of the {111} planes, which are known to be the preferred cleavage planes in single-crystal silicon. This confirms that under the stress state induced by the dual-indentation configuration, cracks tend to follow energetically favourable paths corresponding to intrinsic crystal cleavage planes. These observations also validate the experimental design, where the Berkovich indents were intentionally aligned to facilitate crack propagation along these cleavage directions.

However, two notable exceptions were observed in Test B and Test G, where the crack traces exhibited deviation from a single, well-defined cleavage direction. In both cases, the crack initially propagated along a direction not aligned with any of the {111} traces but eventually returned to a {111} orientation. While this might appear as a change in cleavage plane, it is more likely attributed to crack propagation on an alternative, higher-energy cleavage plane before re-aligning with the preferred low-energy {111} plane. Importantly, the apparent changes in trace direction observed in the mapped images are based on data taken close to the crack, where local lattice rotation due to crack opening and strain can influence orientation measurements. The overall crystal orientation across the sample is expected to remain consistent, and there is no indication of large orientation gradients or multiple grains in these regions.

In Test G, similar to Test B, the crack likely propagated transiently along another less-favourable cleavage plane before returning to the primary {111} path. Such behaviour reflects the crack's sensitivity to local stress and microstructural interactions near the indentation, while ultimately favouring re-alignment with the energetically preferred {111} cleavage planes. While cleavage in silicon is most commonly observed on {111} planes, other crystallographic planes such as {131}

have also been reported in the literature (e.g., [155].), and may occasionally become active depending on the local stress state and crack geometry.

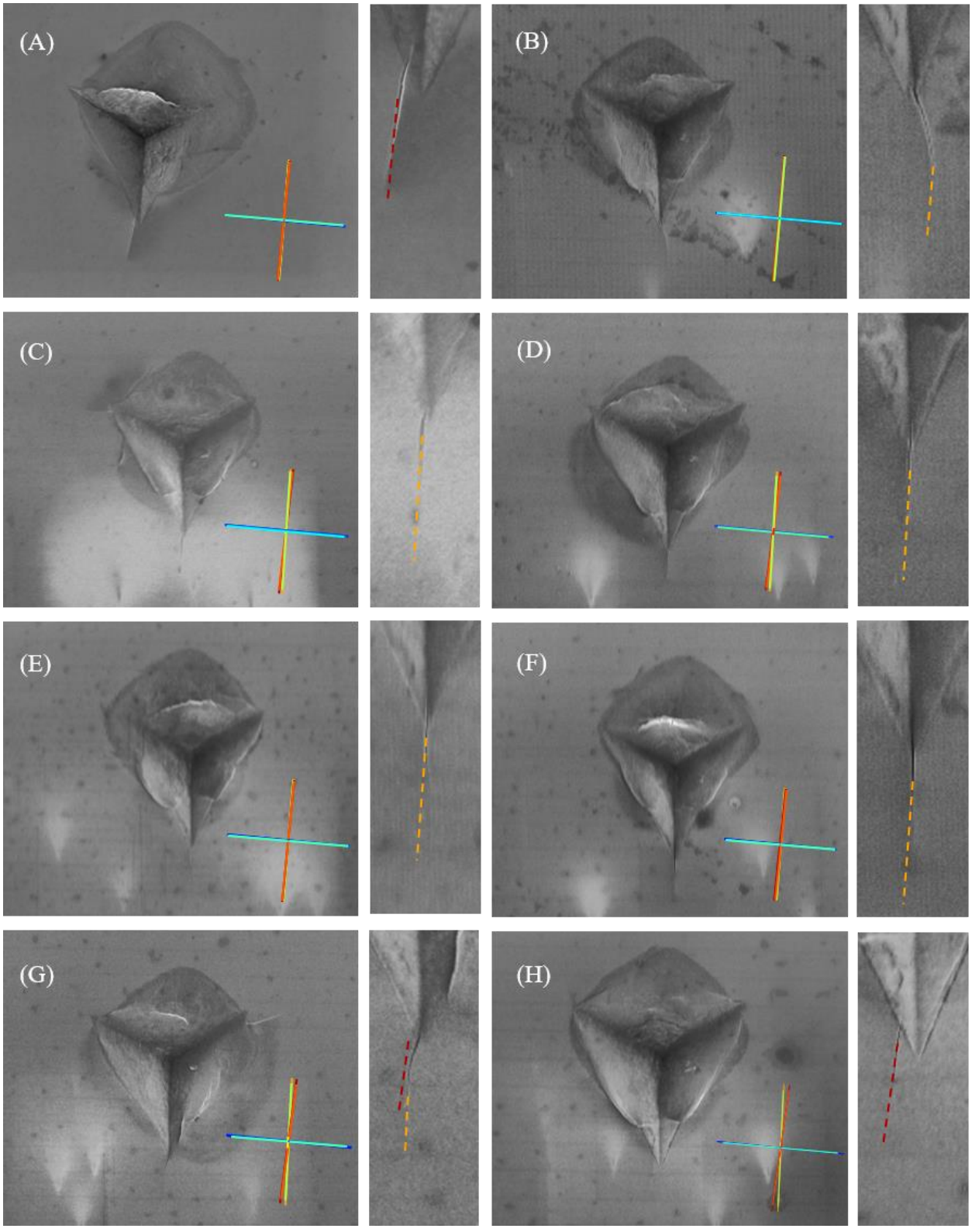

FIGURE 4.16
Crack trace analysis for all eight dual-indentation tests (Tests A–H). Secondary electron (SE) images are overlaid with the complete set of {111} trace directions.

These findings illustrate that while cleavage along the {111} planes dominates in the majority of cases, local stress variations and crystallographic orientation can give rise to more complex crack trajectories. The ability to resolve such behaviour through high-resolution trace analysis adds an important layer of understanding to the crack–crystal interaction mechanisms in indentation-induced fracture. Moreover, the observed transitions and deviations further emphasise the need for full-field characterisation techniques when interpreting crack propagation behaviour, especially in anisotropic materials.

4.4.2. MPERR Method Evaluation

The present study reveals that all evaluated crack-driving conditions involve mixed-mode loading, characterised by simultaneous contributions from opening (mode I), sliding (mode II), and tearing (mode III) mechanisms. Such mixed-mode scenarios are inherent to indentation-induced cracks, owing to the anisotropic nature of the material and the complex local stress fields generated by the dual-indentation configurations. To obtain a representative measure of the fracture toughness of silicon, especially for cleavage planes such as the {111} plane examined in this study, the Maximum Potential Energy Release Rate (MPERR) criterion was applied. This approach incorporates a three-dimensional fracture criterion that accounts for the relative contributions of all three loading modes, enabling rigorous quantification of fracture resistance under realistic mixed-mode conditions.

Using the MPERR criterion, an optimal critical mode I stress intensity factor K_{Ic} was determined through a least-squares fitting process. Specifically, the optimal value ($K_{\mathrm{Ic}}^{\mathrm{opt}}$) was obtained by minimising the deviation of experimental data points from the three-dimensional fracture surface defined by MPERR:

$$K_{\mathrm{Ic}}^{\mathrm{opt}} = \arg\min_{K_{\mathrm{Ic}}} \sum_{i=1}^{n} \left[\left(\frac{K_{\mathrm{I}}^{(i)}}{K_{\mathrm{I}c}} \right)^2 + \left(\frac{K_{\mathrm{II}}^{(i)}}{K_{\mathrm{II}c}} \right)^2 + \left(\frac{K_{\mathrm{III}}^{(i)}}{K_{\mathrm{III}c}} \right)^2 - 1 \right]^2 \tag{4-5}$$

where

$$K_{\mathrm{IIc}} = \frac{\sqrt{3}}{2} K_{\mathrm{Ic}}, \quad K_{\mathrm{IIIc}} = \frac{\sqrt{k+1}}{2} K_{\mathrm{Ic}} \tag{4-6}$$

and this yielded

$$K_{\mathrm{Ic}}^{\mathrm{opt}} = 0.711\ \mathrm{MPa} \cdot \mathrm{m}^{1/2} \tag{4-7}$$

In addition, each individual test allows direct calculation of a local critical mode I stress intensity factor, denoted as $K_{\mathrm{Ic}}^{(\mathrm{i})}$. Due to inevitable experimental scatter and effect of data quality on J-integral convergence, these individual estimates exhibited moderate variability. The individual computed values from the eight valid datasets were:

Test	$K_{\mathrm{Ic}}^{(\mathrm{i})}(\mathrm{MPa} \cdot \mathrm{m}^{1/2})$	Test	$K_{\mathrm{Ic}}^{(\mathrm{i})}(\mathrm{MPa} \cdot \mathrm{m}^{1/2})$
A	0.677	E	0.629
B	0.777	F	0.760
C	0.663	G	0.681
D	0.695	H	0.741

Figure 4.17 visualises the three-dimensional MPERR fracture surface together with all eight experimental data points plotted in $(K_{\mathrm{I}}/K_{\mathrm{I}c})$-$(K_{\mathrm{II}}/K_{\mathrm{I}c})$-$(K_{\mathrm{III}}/K_{\mathrm{I}c})$ space. The proximity of each point to the fitted surface illustrates the validity of the assumed fracture criterion and the consistency of the extracted $K_{\mathrm{I}c}$ across varying mixed-mode conditions.

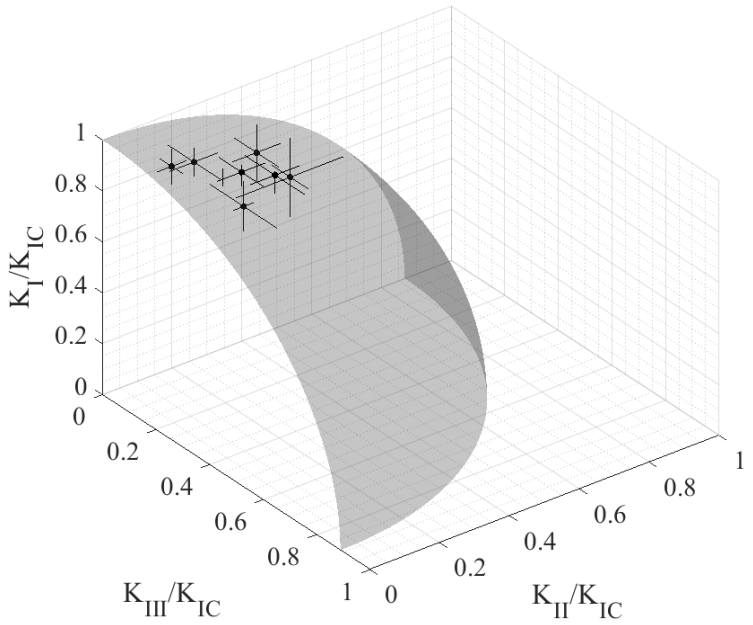

FIGURE 4.17
Three-dimensional fracture surface defined by the MPERR criterion, plotted in normalised $K_{\mathrm{I}}/K_{\mathrm{Ic}}$, $K_{\mathrm{II}}/K_{\mathrm{Ic}}$, $K_{\mathrm{III}}/K_{\mathrm{Ic}}$ space. The surface corresponds to the condition $\left(\frac{K_{\mathrm{I}}}{K_{\mathrm{Ic}}}\right)^2 + \left(\frac{K_{\mathrm{II}}}{K_{\mathrm{IIc}}}\right)^2 + \left(\frac{K_{\mathrm{III}}}{K_{\mathrm{IIIc}}}\right)^2 = 1$. Experimental data points from the eight dual-indentation tests are overlaid.

Statistical analysis of these local measurements provides deeper insights into the consistency and reliability of the fracture toughness estimate. The mean ($\overline{K_{\mathrm{Ic}}}$) and standard deviation (s) of individual tests were calculated as:

$$\overline{K_{\mathrm{Ic}}} = 0.703\ \mathrm{MPa}\cdot\mathrm{m}^{1/2}, \quad s = 0.051\ \mathrm{MPa}\cdot\mathrm{m}^{1/2} \tag{4-8}$$

This yields a coefficient of variation (CV):

$$\mathrm{CV} = \frac{s}{\overline{K_{Ic}}} \times 100\% = 7.29\% \tag{4-9}$$

This relatively low coefficient of variation indicates that the measured fracture toughness values are clustered despite the mixed-mode variability, suggesting a stable fracture resistance across different indentation configurations.

To further establish statistical confidence, a 95% confidence interval (CI) was constructed as follows:

$$\mathrm{CI}_{95\%} = \overline{K_{\mathrm{Ic}}} \pm t_{0.975,n-1}\frac{s}{\sqrt{n}} \tag{4-10}$$

With $n = 8$ and $t_{0.975,7} = 2.365$, the calculated 95% confidence interval is:

$$\mathrm{CI}_{95\%} = [0.660,\ 0.746]\ \mathrm{MPa}\cdot\mathrm{m}^{1/2} \tag{4-11}$$

Notably, the globally fitted $K_{\mathrm{Ic}}^{\mathrm{opt}} = 0.711\ \mathrm{MPa}\cdot\mathrm{m}^{1/2}$ lies within this confidence interval, supporting its representativeness and robustness with respect to local variations.

Comparison was also made with mode I fracture toughness values for silicon cleavage planes reported in the literature. According to Masolin et al. [384], the reported K_{Ic} values for the $\{100\}$, $\{110\}$, and $\{111\}$ planes are summarised in Table 4.2. These were obtained using various experimental techniques, including indentation, four-point bending, and double-cantilever beam (DCB) tests. The value for the $\{111\}$ plane corresponds to the crystallographic orientation of the cleavage surfaces observed in the present study.

TABLE 4.2
Reported mode I fracture toughness values for single crystal silicon cleavage at room temperature

Fracture Plane	$\{100\}$	$\{110\}$	$\{111\}$
Reported K_{Ic} ($\mathrm{MPa}\cdot\mathrm{m}^{1/2}$)	0.75–1.29	0.68–1.19	0.62–1.22

The MPERR-derived value obtained in this study is therefore in good agreement with this reference value, falling within an acceptable range given typical experimental and methodological uncertainties. This agreement confirms the accuracy of the implemented experimental and analytical procedures.

4.4.3. Formation and Arrest of an Indentation Crack in Critical State

The dual-indentation strategy developed in this study addresses two major limitations inherent in the classical indentation-based fracture toughness method, particularly the Lawn-Evans-Marshall (LEM) approach. While the LEM method provides a convenient framework for estimating fracture

toughness from radial crack lengths, it relies on a number of idealised assumptions that are difficult to satisfy in practical scenarios. The present work rethinks and reconstructs the indentation testing approach by leveraging controllable residual stress fields and full-field HR-EBSD measurements to achieve more reliable and quantitative fracture assessment.

First, in the LEM model, it is assumed that the desired half-penny cracks extend under a critical loading condition, with propagation driven primarily by residual tensile stresses generated during unloading. However, this assumption is not guaranteed to hold in practice. In many materials, radial cracks may initiate during loading rather than under residual stress, or may be the result of complex local stress concentrations rather than a well-defined, repeatable residual field. As a result, the actual crack-tip condition during propagation is often unclear, making the measured crack length an unreliable indicator of fracture toughness, except when supported by calibration from similar studies.

In contrast, the dual-indentation method developed in this work enables the intentional introduction of cracks driven specifically by a controlled residual stress field, and in particular, enables the crack to arrest in a near-critical condition. By adjusting the position and load of the Berkovich indent relative to the residual stress field generated by the spherical indent, cracks can be made to propagate along the stress gradient and stop naturally where the local driving force falls below the fracture resistance. This overcomes the first fundamental limitation of conventional methods by ensuring that the crack-tip condition corresponds to a known and physically meaningful mechanical state.

Second, the LEM model assumes that radial cracks are dominated by pure mode I (opening) loading, and accordingly calculates fracture toughness under this simplifying assumption. However, actual crack-tip loading conditions in indentation scenarios are often more complex, involving mixed-mode contributions (modes I, II, and III), especially in anisotropic or non-

uniform materials. Ignoring the contributions of shear modes may lead to inaccurate evaluations of crack driving force and material resistance.

The present study resolves this issue by integrating full-field HR-EBSD strain mapping with contour-integral-based J-integral analysis, enabling the quantitative decomposition of the crack-tip loading into mode I, II, and III stress intensity factors. The results from eight systematically varied dual-indentation tests clearly demonstrate that while mode I remains dominant, non-negligible mode II and III components are present in all cases. Importantly, these components can be extracted and analysed, allowing fracture toughness to be assessed under realistic, non-ideal loading conditions. This capability represents a significant advancement over traditional indentation methods, which cannot account for mixed-mode loading without additional assumptions or modelling. In principle, this approach could also be extended to study intergranular cracking, where the local crack-tip fields along grain boundaries could be characterised under complex loading modes. However, such applications would introduce additional experimental challenges, such as the selection of an appropriate reference for stress calculations in heterogeneous microstructures, and theoretical complexities related to defining path-independent integrals like the J-integral along interfaces with discontinuous material properties.

In summary, by directly addressing the uncertainties in crack-driving force and loading mode inherent in classical indentation fracture mechanics, the dual-indentation approach developed in this work establishes a more flexible, quantitative, and reliable framework for fracture toughness evaluation, particularly well-suited for small-scale, anisotropic, or residual-stress-sensitive materials. It is noted that, ideally, HR-EBSD measurements would be performed while the crack remains loaded by the indenter to capture the actual stress and strain fields under applied loading. However, such in-situ measurements are currently not feasible due to experimental limitations.

4.5 Conclusion

This chapter presented a novel dual-indentation methodology for evaluating the fracture toughness of single-crystal silicon under mixed-mode loading conditions. The approach addresses key limitations of classical indentation methods, particularly the Lawn-Evans-Marshall (LEM) model, by enabling cracks to be introduced and arrested under a well-controlled residual stress field, and by directly measuring the crack-tip driving forces through full-field HR-EBSD.

By combining spherical and Berkovich indentations, the study demonstrated that it is possible to control the location of indentation-induced cracks and residual fields to achieve designed interactions. Two dual-indentation configurations were explored: placing the Berkovich indent either outside or inside the spherical indent. In both cases, cracks were found to propagate in a predictable manner along {111} cleavage planes and arrest naturally, forming well-defined critical states suitable for fracture toughness quantification.

HR-EBSD measurements enabled high-resolution mapping of the elastic strain fields around the crack tip. Through decomposition of the deformation gradient and evaluation of the J-integral, mode-specific stress intensity factors (K_{I}, K_{II}, and K_{III}) were extracted, revealing consistent mode I-dominated mixed-mode loading conditions. The Maximum Potential Energy Release Rate (MPERR) criterion was applied to unify these observations into a single critical fracture surface. The fitted mode I toughness value $K_{\mathrm{Ic}}^{\mathrm{opt}} = 0.711\ \mathrm{MPa} \cdot \mathrm{m}^{1/2}$ agreed well with literature values for the {111} cleavage plane of silicon.

Importantly, the methodology demonstrated excellent stability, repeatability, and scalability. It requires minimal sample preparation, avoids the need for FIB milling, and retains the simplicity and practicality of indentation-based methods, while achieving rigorous and spatially resolved fracture mechanics analysis. As such, this dual-indentation framework lays the foundation for a

versatile and reliable tool for micromechanical fracture toughness testing in brittle materials, particularly when crack behaviour is influenced by residual stress and crystallographic anisotropy.

Chapter 5

General Discussion

5.1 Full-Field Measurements: Comparison and Future Perspectives

Accurate quantification of crack tip fields is fundamental to understanding and predicting fracture behaviour, especially in the case of short cracks whose propagation is governed by highly localised microstructural conditions. Traditional global approaches, based on remote boundary conditions and simplified assumptions, are increasingly insufficient for analysing such complex, scale-sensitive phenomena. Instead, full-field measurement techniques have become indispensable tools, providing rich spatially-resolved data on strain and displacement fields at or near the crack tip. In this study, several advanced full-field methods were employed, including high-resolution electron backscatter diffraction (HR-EBSD) and digital image correlation (DIC) in a scanning electron microscope (SEM), with an emphasis on their in situ implementation and complementary strengths.

HR-EBSD stands out for its ability to measure the elastic strain and lattice rotation fields with exceptional angular sensitivity, typically around 10^{-4} radians, and sub-micron spatial resolution. By analysing shifts in Kikuchi patterns through cross-correlation techniques, HR-EBSD directly extracts the deformation gradient tensor, from which physically meaningful quantities such as elastic strain, geometrically necessary dislocation (GND) density and stress intensity factors can be calculated. One of the key advantages of this method, as highlighted in this study, is its ability to resolve the **elastic** field surrounding crack tips by quantifying local lattice strain and rotation. This capability is crucial for accurately evaluating the actual driving force at the crack tip.

Furthermore, HR-EBSD enables microstructure-sensitive analysis by providing crystallographic orientation maps concurrently. This is useful for assessing the influence of crystallographic features on the local mechanical response. In the context of short fatigue cracks or indentation-induced cracks, HR-EBSD has revealed local strain concentration, loading mode mixity, and the interaction between crack propagation paths and underlying crystallographic features.

Digital image correlation in the SEM, particularly when implemented with Forescatter Electron Imaging (FSE), offers a highly stable and spatially resolved approach to tracking displacement fields around microstructural features and crack tips. FSE images offer a high signal-to-noise ratio and reveal fine surface features that are well-suited for sub-pixel accuracy in DIC tracking. Compared to optical DIC, SEM-DIC achieves superior spatial resolution often down to tens or hundreds of nanometres, which is essential for capturing sharp displacement and strain gradients near cracks in small-scale specimens. However, this technique also has notable limitations. The measurement of out-of-plane displacement effects remains relatively underexplored, and the accuracy of results is highly sensitive to electron beam instability, which can compromise pattern quality and tracking reliability.

The integration of HR-EBSD and SEM-DIC represents a particularly promising approach for comprehensive crack field characterisation. Their complementary nature, HR-EBSD capturing lattice strain and rotation, and SEM-DIC providing full-field surface displacement, enables detailed insight into the mechanical response around crack tip. Crack opening measurement is also possible in future studies, and incorporating it into this framework would offer additional information. The crack opening profile is sensitive to the inelastic deformation that develops ahead of the crack tip and therefore provides an experimental measure of the extent of crack-tip plasticity. Its evolution can also be linked to the local mode mixity and the effective stress intensity acting on the crack.

As both techniques can be performed concurrently within the same SEM setup and region of interest, their co-registration provides a complete picture of the deformation field at the microscale, encompassing both elastic and plastic components. Moreover, it allows for a direct, experimentally grounded validation of numerical models that attempt to predict crack growth under complex, small-scale conditions.

Another defining strengths of both HR-EBSD and SEM-DIC lies in their adaptability to in situ experimental setups within the SEM environment. This capability enables the continuous observation of evolving crack fields under controlled mechanical loading, offering insights that are inaccessible through post-mortem analysis. In situ techniques allow researchers to directly monitor crack initiation, arrest, repropagation, and interaction with microstructural features such as grain boundaries or second-phase particles. This leads to greater data consistency and higher confidence in the derived conclusions.

Looking ahead, the continued advancement of full-field measurement techniques is expected to open new avenues for high-fidelity crack analysis. In particular, three-dimensional (3D) strain field characterisation is gaining increasing attention, and will be further discussed in the following

sections of Further Work. The integration of multiple measurement techniques, as demonstrated in this study through the combined use of DIC and EBSD, holds considerable promise. Collaborative application of complementary methods can overcome the intrinsic limitations of any single technique, enhancing both spatial resolution and data dimensionality.

Comparative studies summarised in the literature review also point to the benefits of such multi-modal strategies. For instance, certain limitations of the present methodology, such as the challenge of capturing out-of-plane displacement fields, may be addressed through the incorporation of techniques like Atomic Force Microscopy (AFM). These developments will lay the foundation for fully integrated digital fracture frameworks, in which both experimental measurements and computational modelling co-evolve, mutually reinforcing predictive capability and mechanistic insight.

5.2 Evaluation of crack driving force: Advantages and Challenges

5.2.1. Comparison of the Two Applied Methods

Two main strategies have been developed for extracting fracture parameters from measured strain fields: finite element (FE)-based field reconstruction, and direct computation from experimental data without intermediate modelling. Each offers distinct advantages and presents specific challenges, particularly when applied to short crack analysis.

A key strength of FE-based field reconstruction is its robustness to experimental noise, as the FE framework naturally smooths the data while enforcing mechanical equilibrium and compatibility. Additionally, its flexibility in handling various measurement inputs and constitutive models makes it particularly well-suited for use in such contexts.

However, this study has also revealed that FE-based field reconstruction introduces some accompanying issues. Most critically, the physical features of the deformation field, particularly

discontinuities such as crack faces, must be explicitly modelled. Failing to do so can lead to inaccuracies in the computed driving forces. A further limitation is that the FE solution inherently enforces mechanical equilibrium and compatibility, which are baseline continuum mechanics assumptions that may not strictly hold in regions affected by localised damage, crystal plasticity, or measurement uncertainty. As a result, the reconstructed field may impose mechanically admissible behaviour that is smoother or more idealised than the true deformation state. In three-dimensional applications, particular attention must be paid to the definition of boundary conditions derived from experimental data. For instance, when working with strain fields measured by EBSD, an accurate estimation of the electron penetration depth is essential to define the appropriate deformation volume for displacement integration. Any mismatch between the modelled and actual deformation domain may render the computed results physically unrepresentative.

By contrast, direct methods which compute the J-integral or stress intensity factors directly from deformation gradient tensors without intermediate modelling offer a more straightforward and computationally efficient path. These methods make no assumptions about boundary conditions and are computationally more efficient. However, they are highly sensitive to experimental data quality, particularly noise. Because the energy integral involves stress calculation and spatial integration, even small measurement errors can be amplified, leading to divergence or scattered results. This sensitivity becomes a significant concern when working with high-gradient fields near crack tips, where numerical instability can obscure the true material behaviour.

Thus, while direct methods reduce modelling assumptions, they require a higher standard of experimental data, particularly with regard to spatial resolution, noise levels, and field continuity. This discussion aims to highlight the importance of these experimental details in ensuring accurate and reliable fracture parameter evaluation.

5.2.2. Common Challenges in Experiment–Simulation Integration

5.2.2.1. Reference State and Zero-Strain Calibration

A critical prerequisite for field-based fracture analysis is the definition of a zero-strain reference state. In HR-EBSD, the chosen reference pattern sets the baseline against which all strain and rotation fields are calculated. However, due to the nature of the measurement, absolute elastic strain is difficult to determine, and the results often reflect relative variations. If the selected reference point already contains residual strain or stress, the entire field may be offset, leading to systematic errors in energy integral evaluations.

Similarly, in DIC, the reference image must be captured in a truly unloaded and stable state. Any drift or residual stress can introduce non-zero displacements, which may be misinterpreted as mechanical deformation. This challenge is further compounded in in situ experiments, where maintaining environmental stability and load control is more difficult.

5.2.2.2. Data Quality and Noise Management

High-resolution full-field methods, particularly HR-EBSD, are highly sensitive to noise introduced during data acquisition and processing. Sources of noise include:

- Limited pattern resolution or contrast (e.g., in FSE imaging or low-index EBSD zones)
- Geometric inconsistencies between the sample and detector setup
- Surface preparation quality and topography artefacts
- Environmental vibrations and beam instabilities

These effects can distort strain and rotation fields, particularly in regions with steep gradients or low pattern quality. This, in turn, can result in physically unrealistic local spikes in deformation gradients or lattice curvature, which may dominate integral quantities such as the J-integral.

Common strategies for managing these issues include local smoothing, Fourier-based or finite element filtering, and removal of low-quality data points. However, each filtering step must be applied with caution to preserve genuine gradients near the crack tip and avoid introducing artificial delocalisation.

A key point emphasised throughout the chapters is that the quality of data pre-processing, prior to any fracture parameter evaluation, is as crucial as the measurement technique itself. Poor handling of noise can not only reduce accuracy but also lead to qualitatively misleading interpretations.

5.2.2.3. Comparability and Data Integration

Another challenge in full-field fracture analysis is ensuring comparability across datasets and techniques. Differences in spatial resolution, field type (displacement vs. strain), and measurement principles (DIC vs. HR-EBSD) make direct comparison complex. Quantities such as J or K computed from different fields may vary not only due to material or geometry, but also because of differences in data structure and integration methodology.

To improve reliability and interpretation, it is increasingly necessary to combine multiple field types into a unified framework. Multi-technique analysis facilitates cross-validation of critical findings and helps relate different aspects of crack tip activity. The development of standardised post-processing framework and shared spatial registration schemes will be crucial for ensuring consistent, transferable results across different studies and techniques.

5.3 Further Work

5.3.1. Towards Three-Dimensional Crack Field Characterisation

The examples examined in this thesis clearly demonstrate that crack propagation is fundamentally a three-dimensional process. Despite the use of two-dimensional measurements, the deformation and fracture behaviour observed, such as out-of-plane displacements and mixed mode loading

conditions, reflect complex interactions that evolve through the thickness of the material. These findings underscore the need to move beyond two-dimensional studies and towards a full three-dimensional characterisation of crack fields.

Future efforts should therefore focus on extending full-field methods into the third dimension to capture the true nature of crack tip mechanics. Synchrotron-based techniques such as Differential Aperture X-ray Micro-diffraction (DAXM) [138] and Bragg Coherent Diffraction Imaging (BCDI) [393] offer promising capabilities for volumetric mapping of internal lattice strain and orientation gradients in bulk crystals. These non-destructive methods are uniquely suited for identifying strain localisation ahead of buried cracks, and for tracking the development of internal fracture surfaces during in situ loading. However, several challenges remain, including limited spatial and temporal resolution, restricted sample geometries, and the need for complex experimental setups and data reconstruction procedures, all of which currently constrain routine application of these three-dimensional methods.

At finer length scales, combining Transmission Kikuchi Diffraction (TKD) [394, 395] with high-resolution TEM imaging [396] enables sub-100 nm resolution for mapping strain fields in thin sections, such as ion-irradiated layers or diffusion-modified interfaces. These approaches are particularly relevant for materials in which fracture is strongly influenced by near-surface phenomena or irradiation damage.

Nevertheless, several challenges must be addressed to enable the routine application of these techniques. One critical issue is the reliable identification of crack features, such as complex, non-planar crack fronts and tortuous paths, as well as crystallographic elements like grain boundary networks or phase interfaces, all within three-dimensional datasets. Moreover, translating these raw 3D fields into usable fracture mechanics quantities requires the development of extended formulations of fracture parameters. Simultaneously, the computational and visualisation

frameworks necessary to reconstruct, segment, and interpret such datasets must be significantly improved.

Overall, transitioning from 2D to 3D field-based fracture analysis represents not just a technical enhancement, but a fundamental step toward capturing the true micromechanical landscape of fracture. This shift will be essential for studying complex materials and geometries where anisotropy, heterogeneity, and spatial constraints dominate crack evolution.

5.3.2. Expanding the Application of the Proposed Methods to Complex Damage Scenarios

The methods developed in this work, particularly the full-field evaluation of crack driving forces and the dual-indentation approach, provide a versatile framework that can be extended to address more complex and application-driven fracture problems. While the current study focuses primarily on fatigue cracks under controlled overload conditions and tailored indentation cracks in model material silicon, the same methodology can be adapted to investigate a broader range of damage mechanisms that are highly relevant in engineering contexts.

One possible direction is the study of grain boundary cracking and grain boundary engineering [316, 397]. By introducing cracks deliberately along targeted grain boundaries using the indentation method, it becomes possible to systematically quantify grain boundary strength and identify the microstructural conditions that promote or inhibit crack propagation. Such experiments, combined with high-resolution strain mapping, could support the development of grain boundary design strategies for improved resistance to intergranular fracture, especially in polycrystalline ceramics used in critical structural applications.

A second promising application is the analysis of cracking in corrosive environments [398, 399]. Such failures often involve complex interactions between mechanical loading and chemical

processes at the crack tip. Field-based methods could enable in situ tracking of strain accumulation and crack tip field evolution under these conditions, providing new insights into crack initiation thresholds and localised embrittlement mechanisms. Practical challenges remain, however, including surface degradation from corrosion or oxidation products that can obscure imaging contrast and reduce measurement fidelity, making reliable field acquisition more difficult in such environments.

The methodology is also well-suited to evaluating fracture toughness degradation in service-exposed or irradiated materials, especially when only limited sample volumes are available [314, 400, 401]. Micro-scale indentation-induced cracking provides a means of probing damage in materials subjected to extreme conditions such as radiation, high temperature or prolonged mechanical loading, making it especially valuable for research on nuclear and aerospace materials and other high-value systems where conventional mechanical testing is difficult.

Realising the full potential of these research applications will require the development of customised laboratory-based in situ platforms. One promising direction is an in situ indentation system capable of applying well-defined loading while simultaneously capturing full-field deformation data. Such a system would increase the precision with which local crack-tip fields can be resolved, enabling real-time observation of crack initiation and short-crack evolution under controlled microstructural or environmental variations. This would provide a powerful tool for mechanistic studies of material degradation.

Extending their use to more complex and microstructure-sensitive fracture scenarios would deepen our understanding of small-scale cracking processes and provide insights that can inform microstructure-guided strategies for improving material performance.

5.3.3. Bridging Experiment and Modelling

A key direction for future work lies in building stronger links between experimentally measured fields and computational models of fracture. The field-based methods developed in this thesis, particularly the evaluation of crack driving forces directly from deformation gradients, offer an opportunity to move beyond qualitative validation and toward quantitative, model-driven prediction of fracture behaviour.

One promising avenue is the development of locally calibrated constitutive models based on full-field data [402, 403]. By extracting spatially resolved strain and rotation fields near crack tips, it becomes possible to infer local mechanical responses and identify heterogeneity in material behaviour. These data can be used to inform or calibrate microstructure-sensitive constitutive laws, such as those used in crystal plasticity finite element (CPFE) models [404] or cohesive zone formulations [405, 406]. This is particularly important for complex material systems like high-entropy alloys, nanostructured metals, or irradiated materials, where conventional constitutive assumptions often fail.

Perhaps most significantly, field-based fracture parameters can serve as a powerful bridge between experiment and multiscale modelling [407]**.** By supplying direct input on crack tip fields such as local energy dissipation, plastic strain gradients, or mixed-mode stress intensity factor, these measurements can constrain and guide simulations at both the microscale (e.g., dislocation-based models) and the macroscale (e.g., continuum damage mechanics). This integration lays the foundation for building predictive digital twins of materials under realistic loading and environmental conditions, in which experimental data continuously inform and update simulation models.

To realise this vision, further work is needed to develop standardised interfaces between experimental datasets and modelling platforms, as well as uncertainty quantification strategies to account for experimental noise and variability. Nonetheless, the integration of high-fidelity field measurements with physically grounded models represents a critical step toward more predictive, mechanistic, and application-relevant fracture simulation frameworks.

Chapter 6

Conclusion

This study presents a comprehensive investigation into the micromechanics of short crack propagation and fracture toughness evaluation using advanced full-field experimental techniques. By integrating Digital Image Correlation (DIC), High-Resolution Electron Backscatter Diffraction (HR-EBSD), and Finite Element (FE) post-processing, a robust framework has been developed to directly evaluate crack-tip fields and extract fracture parameters under varied and complex loading conditions.

The experimental observations in this work provide further insight into the complexity of short crack propagation, particularly in scenarios that deviate from conventional assumptions, such as overload-induced effects, and microstructural heterogeneity. By leveraging high-resolution full-field techniques, this study enables direct assessment of fracture parameters, such as the J-integral and mode-specific stress intensity factors, based on the actual near-tip deformation fields. These techniques allow for a more transparent characterisation of local loading conditions, avoiding the assumptions inherent in conventional, global-based models. The results underscore how crack behaviour at early stages is strongly influenced by the interaction between microstructure and localised plasticity, which cannot be effectively captured through remote load measurements alone. This deeper understanding of local fields surrounding short cracks not only informs the interpretation of crack driving forces but also offers a reliable basis for refining experimental techniques and modelling strategies.

In the context of microscale fracture toughness characterisation, this study establishes a dual-indentation strategy that enables precise control over crack nucleation and arrest within a tailored residual stress field. Applied to single-crystal silicon, this methodology leverages the interaction between spherical and Berkovich indentations to reproducibly generate cracks that propagate and arrest along well-defined crystallographic planes. The resulting crack configurations represent stable, near-critical states suitable for quantitative analysis. By combining this controlled crack formation with HR-EBSD-based strain field measurements and energy integral analysis, the methodology facilitates direct extraction of mode-specific stress intensity factors under mixed-mode conditions. The use of the Maximum Potential Energy Release Rate (MPERR) framework provides a consistent, physically grounded criterion for identifying the fracture surface and evaluating crack stability. Notably, the method retains the accessibility and simplicity of traditional indentation testing while effectively addressing their key limitations. These results demonstrate the feasibility of extending indentation-based approaches toward more rigorous, versatile, and reproducible toughness measurements at the microscale.

Collectively, the experimental strategies and analytical methodologies established in this work contribute to a more realistic and microstructure-sensitive understanding of both crack field and crack propagation. By bridging local experimental data with fracture mechanics principles, this thesis lays a methodological foundation for future studies involving complex failure scenarios, such as those influenced by anisotropy, residual stress, or environmental effects.

In summary, this work refines the application of full-field experimental methods in fracture mechanics and contributes to the quantitative analysis of crack-tip conditions in small-scale and non-standard test configurations. The outcomes are expected to inform both the development of more predictive fatigue and fracture models and the design of testing strategies for emerging materials operating under demanding mechanical conditions.

Reference

[1] D. Wilson, Z. Zheng, and F. P. E. Dunne, "A microstructure-sensitive driving force for crack growth," *J Mech Phys Solids*, vol. 121, pp. 147-174, 2018/12/01/ 2018, doi: https://doi.org/10.1016/j.jmps.2018.07.005.

[2] C. E. Inglis, "Stresses in a plate due to presence of cracks and sharp coners," *Transactions of the Royal Institute of Naval Architectes*, vol. 60, pp. 219-241, 1913.

[3] A. A. Griffith, "The phenomena of rupture and flow in solids," *Philosophical Transactions of the Royal Society of London*, vol. 221, 1921.

[4] G. R. Irwin, "Fracture Dynamics, Fracturing of Metals," 1948.

[5] E. Orowan, "Fracture and strength of solids," *Reports on Progress in Physics*, vol. 12, no. 1, 1949.

[6] G. R. Irwin, "Onset of fast crack propagation in high strenght steel and aluminum alloys," *Naval Research Laboratory*, vol. 4763, 1956.

[7] G. R. Irwin, "Analysis of Stresses and Strains Near the End of a Crack Traversing a Plate," *Journal of Applied Mechanics*, vol. 24, no. September, 1957.

[8] M. L. Williams, "On the Stress Distribution at the Base of a Stationary Crack," *Journal of Applied Mechanics*, vol. 24, pp. 109-114, 1957. [Online]. Available: https://www.semanticscholar.org/paper/bf85be73df7eb5449a8c856c5ec2fcc2487b04dd.

[9] I. N. Sneddon and N. S. Ian, "The Distribution of Stress in the Neighbourhood of a Crack in an Elastic Solid," *Proceedings of The Royal Society A: Mathematical, Physical and Engineering Sciences*, 1946, doi: 10.1098/rspa.1946.0077.

[10] H. Tada, P. C. Paris, and G. R. Irwin, *The Stress Analysis of Cracks Handbook, Third Edition*. New York: ASME Press, 2000.

[11] M. Yukitaka, *Stress Intensity Factors Handbook*. Oxford: Pergamon Press, 1987.

[12] C. Betego´n and J. W. Hancock, "Two-Parameter Characterization of Elastic-Plastic Crack-Tip Fields," *Journal of Applied Mechanics*, vol. 58, no. 1, pp. 104-110, 1991, doi: 10.1115/1.2897135.

[13] J. Sumpter, E. Hackett, K.-H. Schwalbe, and R. Dodds, Jr, "An Experimental Investigation of the T Stress Approach," in *Constraint Effects in Fracture*, vol. STP1171-EB: ASTM International, 1993, p. 0.

[14] T. L. Anderson, *Fracture Mechanics: Fundamentals and Applications*, Fourth Edition (4th ed.) ed. CRC Press, 2017.

[15] A. A. Wells, "The Condition of Fast Fracture in Aluminum Alloys with Particular Reference to Comet Failures," 1955.

[16] A. A. Wells, "Unstable Crack Propagation in Metals: Cleavage and Fast Fracture," *Proceedings of the Crack Propagation Symposium*, 1961.

[17] D. H. and W. B. M. Winne, "Application of the Griffith-Irwin Theory of Crack Propagation to the Bursting Behavior of Disks, Including Analytical and Experimental Studies," *Transactions of the American Society of Mechanical Engineers*, vol. 80, pp. 1643-1655, 1958.

[18] G. R. Irwin, "Linear fracture mechanics, fracture transition, and fracture control," *Engineering Fracture Mechanics*, vol. 1, no. 2, pp. 241-257, 1968, doi: https://doi.org/10.1016/0013-7944(68)90001-5.

[19] G. R. Irwin, "Plastic zone near a crack and fracture toughness," *Proceedings of the 7th sagamore ordnance materials conference*, pp. 463–478, 1960.

[20] D. S. Dugdale, "Yielding in Steel Sheets Containing Slits," *J Mech Phys Solids*, vol. 8, pp. 100–104, 1960.

[21] G. I. Barenblatt, "The Mathematical Theory of Equilibrium Cracks in Brittle Fracture," *Advances in Applied Mechanics*, vol. VII, pp. 55–129, 1962.

[22] A. A. Wells, "Application of fracture mechanics at and beyond general yielding," *Br Weld J*, vol. 10, pp. 563-70, 1963.

[23] F. F. Goodier JN, "Plastic energy dissipation in crack propagation.," *Fracture of solids*, pp. 103–18, 1963. 103–18.

[24] S. D. Burdekin FM, "The crack opening displacement approach to fracture mechanics in yielding materials," *J Strain Anal*, vol. 1, 145-53, 1966.

[25] M. Dawes, J. Landes, J. Begley, and G. Clarke, "Elastic-Plastic Fracture Toughness Based on the COD and J-Contour Integral Concepts," in *Elastic-Plastic Fracture*, vol. STP668-EB: ASTM International, 1979, p. 0.

[26] J. R. Rice, "A path independent integral and the approximate analysis of strain concentration by notches and cracks," *J Appl Mech*, vol. 35, pp. 379–86., 1968.

[27] J. W. Hutchinson, "Singular behaviour at the end of a tensile crack in a hardening material," *J Mech Phys Solids*, vol. 16, no. 1, pp. 13-31, 1968, doi: https://doi.org/10.1016/0022-5096(68)90014-8.

[28] J. R. Rice and G. F. Rosengren, "Plane strain deformation near a crack tip in a power-law hardening material," *J Mech Phys Solids*, vol. 16, no. 1, pp. 1-12, 1968, doi: https://doi.org/10.1016/0022-5096(68)90013-6.

[29] R. McMeeking, D. Parks, J. Landes, J. Begley, and G. Clarke, "On Criteria for J-Dominance of Crack-Tip Fields In Large-Scale Yielding," in *Elastic-Plastic Fracture*, vol. STP668-EB: ASTM International, 1979, p. 0.

[30] C. F. Shih and M. D. German, "Requirements for a one parameter characterization of crack tip fields by the HRR singularity," *International Journal of Fracture*, vol. 17, no. 1, pp. 27-43, 1981/02/01 1981, doi: 10.1007/BF00043119.

[31] J. R. Rice, R. M. McMeeking, D. M. Parks, and E. P. Sorensen, "Recent finite element studies in plasticity and fracture mechanics," *Computer Methods in Applied Mechanics and Engineering*, vol. 17-18, pp. 411-442, 1979/02/01/ 1979, doi: https://doi.org/10.1016/0045-7825(79)90026-4.

[32] A. M. Al-Ani and J. W. Hancock, "J-Dominance of short cracks in tension and bending," *J Mech Phys Solids*, vol. 39, no. 1, pp. 23-43, 1991/01/01/ 1991, doi: https://doi.org/10.1016/0022-5096(91)90029-N.

[33] D. Parks, "Three-dimensional aspects of HRR-dominance," *Proceedings of the conference of european symposium on elastic–plastic fracture mechanics: defect assessment in components—fundamentals and applications*, October 9–12, pp. 205–31., 1989.

[34] C. F. Shih, "Relationships between the J-integral and the crack opening displacement for stationary and extending cracks," *J Mech Phys Solids*, vol. 29, pp. 305-326, 1981, doi: 10.1016/0022-5096(81)90003-x.

[35] B. W. Srawley JE, "Fracture toughness testing methods.," *Fracture toughness testing and its applications. ASTM STP 381. American Society for Testing and Materials*, pp. 133–96, 1965.

[36] W. F. Brown, Jr, J. E. Srawley, and C. E-24, "Plane Strain Crack Toughness Testing of High Strength Metallic Materials," in *Plane Strain Crack Toughness Testing of High Strength Metallic Materials*, vol. STP410-EB: ASTM International, 1966, p. 0.

[37] "Standard Test Method for Linear-Elastic Plane-Strain Fracture Toughness of Metallic Materials," *ASTM E1737-96*, 2024.
[38] G. Clarke, W. Andrews, P. Paris, D. Schmidt, J. Rice, and P. Paris, "Single Specimen Tests for JIc Determination," in *Mechanics of Crack Growth*, vol. STP590-EB: ASTM International, 1976, p. 0.
[39] H. Ernst, P. Paris, J. Landes, and R. Roberts, "Estimations on J-Integral and Tearing Modulus T from a Single Specimen Test Record," in *Fracture Mechanics*, vol. STP743-EB: ASTM International, 1981, p. 0.
[40] "Standard test method for J-integral characterization of fracture toughness," *ASTM E1737-96*, 1996.
[41] "Standard test method for measurement of fracture toughness," *ASTM E1737-96*, 1997.
[42] P. C. Paris and F. Erdogan, "A Critical Analysis of Crack Propagation Laws," *Journal of BasicEngineering*, vol. 85, pp. 528–534, 1960.
[43] R. G. Foreman, V. E. Keary, and R. M. Engle, "Numerical Analysis of Crack Propagation in Cyclic Loaded Structures," *Journal of Basic Engineering*, vol. 89, pp. 459-46, 1967.
[44] J. Weertman, "Rate of growth of fatigue cracks calculated from the theory of infinitesimal dislocations distributed on a plane," *International Journal of Fracture Mechanics*, vol. 2, no. 2, pp. 460-467, 1966/06/01 1966, doi: 10.1007/BF00183823.
[45] M. Klesnil and P. Lukas, "Influence of Strength and Stress History on Growth and Stabilisation of Fatigue Cracks," *Engineering Fracture Mechanics*, vol. 4, pp. 77-92, 1972.
[46] R. J. Donahue, H. M. Clark, P. Atanmo, R. Kumble, and A. J. McEvily, "Crack opening displacement and the rate of fatigue crack growth," *International Journal of Fracture Mechanics*, vol. 8, no. 2, pp. 209-219, 1972/06/01 1972, doi: 10.1007/BF00703882.
[47] A. J. McEvily, "On Closure in Fatigue Crack Growth," *ASTM STP 982, American Society for Testing and Materials*, pp. 35–43, 1988.
[48] K. Walker and M. Rosenfeld, "The Effect of Stress Ratio During Crack Propagation and Fatigue for 2024-T3 and 7075-T6 Aluminum," in *Effects of Environment and Complex Load History on Fatigue Life*, vol. STP462-EB: ASTM International, 1970, p. 0.
[49] R. G. Forman and S. R. Mettu, "Behavior of Surface and Corner Cracks Subjected to Tensile and Bending Loads in Ti – 6Al – 4V Alloy," *ASTM STP 1131, American Society for Testing and Materials*, pp. 519–546, 1992.
[50] K. Tanaka and Y. Nakai, "Propagation and Non-Propagation of Short Fatigue Cracks at a Sharp Notch," *Fatigue Fract Eng M*, vol. 6, pp. 315-327, 1983, doi: 10.1111/j.1460-2695.1983.tb00347.x.
[51] K. Tanaka, R. Wei, and R. Gangloff, "Mechanics and Micromechanics of Fatigue Crack Propagation," in *Fracture Mechanics: Perspectives and Directions (Twentieth Symposium)*, vol. STP1020-EB: ASTM International, 1989, p. 0.
[52] M. H. El Haddad, T. H. Topper, and K. N. Smith, "Prediction of non propagating cracks," *Engineering Fracture Mechanics*, vol. 11, no. 3, pp. 573-584, 1979/01/01/ 1979, doi: https://doi.org/10.1016/0013-7944(79)90081-X.
[53] O. E. Wheeler, "Spectrum Loading and Crack Growth," *Journal of Basic Engineering*, vol. 94, no. 1, pp. 181-186, 1972, doi: 10.1115/1.3425362.
[54] K. Sadananda, A. K. Vasudevan, R. L. Holtz, and E. U. Lee, "Analysis of overload effects and related phenomena," *Int J Fatigue*, vol. 21, pp. S233-S246, 1999/09/01/ 1999, doi: https://doi.org/10.1016/S0142-1123(99)00094-8.
[55] L. Guerra-Rosa, C. Moura Branco, and J. C. Radon, "Monotonic and cyclic crack tip plasticity," *Int J Fatigue*, vol. 6, no. 1, pp. 17-24, 1984/01/01/ 1984, doi: https://doi.org/10.1016/0142-1123(84)90004-5.
[56] A. H. Purcell and J. Weertman, "Crack tip area in fatigued copper single crystals," *Metallurgical transactions*, vol. 5, no. 8, pp. 1805-1809, 1974/08/01 1974, doi: 10.1007/BF02644144.

[57] R. L. Smith and G. E. Sandly, "An Accurate Method of Determining the Hardness of Metals, with Particular Reference to Those of a High Degree of Hardness," *Proceedings of the Institution of Mechanical Engineers,* vol. 102, no. 1, pp. 623-641, 1922/06/01 1922, doi: 10.1243/PIME_PROC_1922_102_033_02.

[58] M. Kikukawa, M. Jono, K. Tanaka, and M. Takatani, "Measurement of Fatigue Crack Propagation and Crack Closure at Low Stress Intensity Level by Unloading Elastic Compliance Method (In Japanese)," *Journal of the Society of Materials Science,* vol. 25, pp. 899-903, 1976.

[59] M. N. James, M. N. Pacey, L. W. Wei, and E. A. Patterson, "Characterisation of plasticity-induced closure—crack flank contact force versus plastic enclave," *Engineering Fracture Mechanics,* vol. 70, no. 17, pp. 2473-2487, 2003/11/01/ 2003, doi: https://doi.org/10.1016/S0013-7944(02)00273-4.

[60] R. J. Sanford and J. W. Dally, "A general method for determining mixed-mode stress intensity factors from isochromatic fringe patterns," *Engineering Fracture Mechanics,* vol. 11, no. 4, pp. 621-633, 1979/01/01/ 1979, doi: https://doi.org/10.1016/0013-7944(79)90123-1.

[61] A. McDonach, J. McKelvie, P. MacKenzie, and C. A. Walker, "Improved Moiré Interferometry and Applications in Fracture Mechanics, Residual Stress and Damaged Composites," *Experimental Techniques,* vol. 7, no. 6, pp. 20-24, 1983, doi: https://doi.org/10.1111/j.1747-1567.1983.tb01766.x.

[62] G. Nicoletto, "FATIGUE CRACK TIP STRAINS IN 7075-T6 ALUMINUM ALLOY," *Fatigue Fract Eng M,* vol. 10, no. 1, pp. 37-49, 1987, doi: https://doi.org/10.1111/j.1460-2695.1987.tb01147.x.

[63] C. W. Smith, D. Post, and G. Nicoletto, "Experimental stress-intensity distributions in three-dimensional cracked-body problems," *Exp Mech,* vol. 23, no. 4, pp. 378-382, 1983/12/01 1983, doi: 10.1007/BF02330051.

[64] T. G. F. Gray and P. M. MacKenzie, "Fatigue crack closure investigation using Moiré interferometry," *Int J Fatigue,* vol. 12, no. 5, pp. 417-423, 1990/09/01/ 1990, doi: https://doi.org/10.1016/0142-1123(90)90007-2.

[65] P. Stanley and J. M. Dulieu-Smith, "The determination of crack-tip parameters from thermoelastic data," *Experimental Techniques,* vol. 20, no. 2, pp. 21-23, 1996/03/01 1996, doi: 10.1111/j.1747-1567.1996.tb01490.x.

[66] A. S. Patiki and E. A. Patterson, "Thermoelastic stress analysis of fatigue cracks subject to overloads," *Fatigue Fract Eng M,* vol. 33, no. 12, pp. 809-821, 2010, doi: https://doi.org/10.1111/j.1460-2695.2010.01471.x.

[67] D. Palumbo, R. De Finis, F. Ancona, and U. Galietti, "Damage monitoring in fracture mechanics by evaluation of the heat dissipated in the cyclic plastic zone ahead of the crack tip with thermal measurements," *Engineering Fracture Mechanics,* vol. 181, pp. 65-76, 2017/08/01/ 2017, doi: https://doi.org/10.1016/j.engfracmech.2017.06.017.

[68] P. Manogg, *Anwendung der Schattenoptik zur Untersuchung des Zerreißvorgangs von Platten*. Freiburg, Germany, 1964.

[69] P. Manogg, "Schattenoptische Messung der spezifischen Bruchenergie während des Bruchvorgangs bei Plexiglas," *Proc. Int. Conf. on the Physics of Non-Crystalline Solids,* pp. 481–490, 1964.

[70] J. F. Kalthoff, J. Beinert, and S. Winkler, "Analysis of Fast Running and Arresting Cracks by the Shadow Optical Method of Caustics," *Optical Methods in Mechanics of Solids,* 1980.

[71] J. F. Kalthoff, W. Boehme, and S. Winkler, "Analysis of impact fracture phenomena by means of the shadow optical method of caustics," 1982.

[72] J. Beinert and J. F. Kalthoff, "Experimental determination of dynamic stress intensity factors by shadow patterns," in *Experimental evaluation of stress concentration and*

intensity factors: Useful methods and solutions to Experimentalists in fracture mechanics, G. C. Sih Ed. Dordrecht: Springer Netherlands, 1981, pp. 281-330.

[73] P. S. Theocaris and N. Joakimides, "Some properties of generalized epicycloids applied to fracture mechanics," *Zeitschrift für angewandte Mathematik und Physik ZAMP*, vol. 22, no. 5, pp. 876-890, 1971/09/01 1971, doi: 10.1007/BF01591815.

[74] P. S. Theocaris, "The reflected caustics method for the evaluation of mode III stress intensity factor," *International Journal of Mechanical Sciences*, vol. 23, no. 2, pp. 105-117, 1981/01/01/ 1981, doi: https://doi.org/10.1016/0020-7403(81)90075-8.

[75] A. J. Rosakis and L. B. Freund, "Optical Measurement of the Plastic Strain Concentration at a Crack Tip in a Ductile Steel Plate," *Journal of Engineering Materials and Technology*, vol. 104, no. 2, pp. 115-120, 1982, doi: 10.1115/1.3225045.

[76] A. J. Rosakis, C. C. Ma, and L. B. Freund, "Analysis of the Optical Shadow Spot Method for a Tensile Crack in a Power-Law Hardening Material," *Journal of Applied Mechanics*, vol. 50, no. 4a, pp. 777-782, 1983, doi: 10.1115/1.3167145.

[77] E. G. Coker, L. N. G. Filon, H. T. Jessop, and D. A. Wiegand, "A Treatise on Photoelasticity," *Physics Today*, vol. 11, no. 10, pp. 38-40, 1958, doi: 10.1063/1.3062240.

[78] R. S. Hegazy, M. I. Mohamed, and G. M. Mahmoud, "An accurate method for determining stress intensity factor by caustic," *MRS Advances*, vol. 7, no. 10, pp. 229-234, 2022/04/01 2022, doi: 10.1557/s43580-022-00253-y.

[79] A. J. Rosakis and L. B. Freund, "The Effect of Crack-Tip Plasticity on the Determination of Dynamic Stress-Intensity Factors by the Optical Method of Caustics," *Journal of Applied Mechanics*, vol. 48, no. 2, pp. 302-308, 1981, doi: 10.1115/1.3157613.

[80] C. Bull and R. Hermann, "Fatigue crack growth and closure in aluminum alloys," *Scripta Metallurgica et Materialia*, vol. 30, no. 10, pp. 1337-1342, 1994/05/15/ 1994, doi: https://doi.org/10.1016/0956-716X(94)90269-0.

[81] R. A. Tomlinson and E. A. Patterson, "A STUDY OF RESIDUAL CAUSTICS GENERATED FROM FATIGUE CRACKS," *Fatigue Fract Eng M*, vol. 20, no. 10, pp. 1467-1479, 1997, doi: https://doi.org/10.1111/j.1460-2695.1997.tb01503.x.

[82] E. Anastassakis, A. Pinczuk, E. Burstein, F. H. Pollak, and M. Cardona, "Effect of static uniaxial stress on the Raman spectrum of silicon," *Solid State Communications*, vol. 8, no. 2, pp. 133-138, 1970/01/15/ 1970, doi: https://doi.org/10.1016/0038-1098(70)90588-0.

[83] W. Ingrid De, "Micro-Raman spectroscopy to study local mechanical stress in silicon integrated circuits," *Semiconductor Science and Technology*, vol. 11, no. 2, p. 139, 1996/02/01 1996, doi: 10.1088/0268-1242/11/2/001.

[84] S. Ganesan, A. A. Maradudin, and J. Oitmaa, "A lattice theory of morphic effects in crystals of the diamond structure," *Annals of Physics*, vol. 56, no. 2, pp. 556-594, 1970/02/01/ 1970, doi: https://doi.org/10.1016/0003-4916(70)90029-1.

[85] V. T. Srikar, A. K. Swan, M. S. Unlu, B. B. Goldberg, and S. M. Spearing, "Micro-Raman measurement of bending stresses in micromachined silicon flexures," *Journal of Microelectromechanical Systems*, vol. 12, no. 6, pp. 779-787, 2003, doi: 10.1109/JMEMS.2003.820280.

[86] M. D. Vaudin, Y. B. Gerbig, S. J. Stranick, and R. F. Cook, "Comparison of nanoscale measurements of strain and stress using electron back scattered diffraction and confocal Raman microscopy," *Applied Physics Letters*, vol. 93, no. 19, 2008, doi: 10.1063/1.3026542.

[87] R. P. Koseski *et al.*, "Micro-scale measurement and modeling of stress in silicon surrounding a tungsten-filled through-silicon via," *Journal of Applied Physics*, Article vol. 110, no. 7, 2011, Art no. 073517, doi: 10.1063/1.3644971.

[88] U. Schmidt, W. Ibach, J. Müller, K. Weishaupt, and O. Hollricher, "Raman spectral imaging—A nondestructive, high resolution analysis technique for local stress

measurements in silicon," *Vibrational Spectroscopy*, vol. 42, no. 1, pp. 93-97, 2006/10/18/ 2006, doi: https://doi.org/10.1016/j.vibspec.2006.01.005.

[89] L. H. Friedman *et al.*, "Assessing strain mapping by electron backscatter diffraction and confocal Raman microscopy using wedge-indented Si," *Ultramicroscopy*, vol. 163, pp. 75-86, 2016/04/01/ 2016, doi: https://doi.org/10.1016/j.ultramic.2016.02.001.

[90] Y. Zhang, D. P. Mohanty, and V. Tomar, "Analyses of Nanoscale to Microscale Strength and Crack-Tip Stresses Using Nanomechanical Raman Spectroscopy in IN-617," in *Challenges in Mechanics of Time Dependent Materials, Volume 2*, Cham, B. Antoun *et al.*, Eds., 2017// 2017: Springer International Publishing, pp. 9-16.

[91] Y. Zhang, C. Prakash, and V. Tomar, "In-situ Crack Tip Stress Measurement at High Temperature in IN-617 Using Combined Nano-Indentation and Nano-Mechanical Raman Spectroscopy," *Fracture, Fatigue, Failure and Damage Evolution, Volume 6*, 2018.

[92] Y. Zhang, D. P. Mohanty, and V. Tomar, "Visualizing In Situ Microstructure Dependent Crack Tip Stress Distribution in IN-617 Using Nano-mechanical Raman Spectroscopy," *JOM*, vol. 68, no. 11, pp. 2742-2747, 2016/11/01 2016, doi: 10.1007/s11837-016-2099-3.

[93] R. J. Moon, M. Hoffman, J. Rödel, S. Tochino, and G. Pezzotti, "Evaluation of crack-tip stress fields on microstructural-scale fracture in Al–Al2O3 interpenetrating network composites," *Acta Mater*, vol. 57, no. 2, pp. 570-581, 2009/01/01/ 2009, doi: https://doi.org/10.1016/j.actamat.2008.09.043.

[94] G. Pezzotti, H. Ichimaru, L. P. Ferroni, K. Hirao, and O. Sbaizero, "Raman Microprobe Evaluation of Bridging Stresses in Highly Anisotropic Silicon Nitride," *Journal of the American Ceramic Society*, vol. 84, no. 8, pp. 1785-1790, 2001, doi: https://doi.org/10.1111/j.1151-2916.2001.tb00915.x.

[95] W. H. Peters and W. F. Ranson, "Digital Imaging Techniques In Experimental Stress Analysis," *Optical Engineering*, 1982, doi: 10.1117/12.7972925.

[96] M. A. Sutton, W. J. Wolters, W. H. Peters, W. F. Ranson, and S. R. McNeill, "Determination of displacements using an improved digital correlation method," *Image and Vision Computing*, 1983, doi: 10.1016/0262-8856(83)90064-1.

[97] S. R. McNeill, W. H. Peters, and M. A. Sutton, "Estimation of stress intensity factor by digital image correlation," *Engineering Fracture Mechanics*, vol. 28, no. 1, pp. 101-112, 1987/01/01/ 1987, doi: https://doi.org/10.1016/0013-7944(87)90124-X.

[98] H. Lu and P. D. Cary, "Deformation measurements by digital image correlation : Implementation of a second-order displacement gradient," *Exp Mech*, vol. 40, no. 4, pp. 393-400, 2000/12/01 2000, doi: 10.1007/bf02326485.

[99] B. Pan, "Digital image correlation for surface deformation measurement: historical developments, recent advances and future goals," *Measurement Science and Technology*, vol. 29, no. 8, p. 082001, 2018.

[100] M. Bornert *et al.*, "Assessment of Digital Image Correlation Measurement Errors: Methodology and Results," *Exp Mech*, vol. 49, no. 3, pp. 353-370, 2009/06/01 2009, doi: 10.1007/s11340-008-9204-7.

[101] L. David *et al.*, "Quality assessment of speckle patterns for digital image correlation," *Optics and Lasers in Engineering*, vol. 44, no. 11, pp. 1132-1145, 2006/11/01/ 2006, doi: https://doi.org/10.1016/j.optlaseng.2005.10.004.

[102] H. Haddadi and S. Belhabib, "Use of rigid-body motion for the investigation and estimation of the measurement errors related to digital image correlation technique," *Optics and Lasers in Engineering*, vol. 46, no. 2, pp. 185-196, 2008/02/01/ 2008, doi: https://doi.org/10.1016/j.optlaseng.2007.05.008.

[103] S. Yaofeng and P. J. H. L., "Study of optimal subset size in digital image correlation of speckle pattern images," *Optics and Lasers in Engineering*, vol. 45, no. 9, pp. 967-974, 2007/09/01/ 2007, doi: https://doi.org/10.1016/j.optlaseng.2007.01.012.

[104] M. A. Sutton, M. Cheng, W. H. Peters, Y. J. Chao, and S. R. McNeill, "Application of an optimized digital correlation method to planar deformation analysis," *Image and Vision Computing*, 1986, doi: 10.1016/0262-8856(86)90057-0.

[105] B. Pan, K. Qian, H. Xie, and A. Asundi, "Two-dimensional digital image correlation for in-plane displacement and strain measurement: a review," *Measurement science and technology*, vol. 20, no. 6, p. 062001, 2009.

[106] H. A. Bruck, S. R. McNeill, M. A. Sutton, and W. H. Peters, "Digital image correlation using Newton-Raphson method of partial differential correction," *Exp Mech*, 1989, doi: 10.1007/bf02321405.

[107] P. F. Luo, Y. J. Chao, M. A. Sutton, and W. H. Peters, "Accurate measurement of three-dimensional deformations in deformable and rigid bodies using computer vision," *Exp Mech*, 1993, doi: 10.1007/bf02322488.

[108] Z. Sun, J. Lyons, and S. R. McNeill, "Measuring Microscopic Deformations with Digital Image Correlation," *Optics and Lasers in Engineering*, 1997, doi: 10.1016/s0143-8166(96)00041-3.

[109] G. Vendroux and W. G. Knauss, "Submicron deformation field measurements: Part 2. Improved digital image correlation," *Exp Mech*, 1998, doi: 10.1007/bf02321649.

[110] G. Vendroux and W. G. Knauss, "Submicron deformation field measurements: Part 1. Developing a digital scanning tunneling microscope," *Exp Mech*, 1998, doi: 10.1007/bf02321262.

[111] A. Pilch, A. Mahajan, and T. Chu, "Measurement of Whole-Field Surface Displacements and Strain Using a Genetic Algorithm Based Intelligent Image Correlation Method," *Journal of Dynamic Systems Measurement and Control-transactions of The Asme*, 2004, doi: 10.1115/1.1789968.

[112] H. W. Schreier and M. A. Sutton, "Systematic errors in digital image correlation due to undermatched subset shape functions," *Exp Mech*, 2002, doi: 10.1007/bf02410987.

[113] P. Zhou and K. E. Goodson, "Subpixel displacement and deformation gradient measurement using digital image/speckle correlation (DISC)," *Optical Engineering*, 2001, doi: 10.1117/1.1387992.

[114] M. A. Sutton, S. R. McNeill, J. D. Helm, and Y. J. Chao, "Advances in Two-Dimensional and Three-Dimensional Computer Vision," in *Photomechanics*, P. K. Rastogi Ed. Berlin, Heidelberg: Springer Berlin Heidelberg, 2000, pp. 323-372.

[115] H. W. Schreier, J. R. Braasch, and M. A. Sutton, "Systematic errors in digital image correlation caused by intensity interpolation," *Optical Engineering*, 2000, doi: 10.1117/1.1314593.

[116] Y. Sun, J. H. L. Pang, C. K. Wong, and F. Su, "Finite element formulation for a digital image correlation method," *Applied Optics*, 2005, doi: 10.1364/ao.44.007357.

[117] G. Besnard, F. Hild, and S. Roux, ""Finite-Element" Displacement Fields Analysis from Digital Images: Application to Portevin-Le Châtelier Bands," *Exp Mech*, 2006, doi: 10.1007/s11340-006-9824-8.

[118] S. Roux, J. Réthoré, and F. Hild, "Digital image correlation and fracture: an advanced technique for estimating stress intensity factors of 2D and 3D cracks," *Journal of Physics D*, 2009, doi: 10.1088/0022-3727/42/21/214004.

[119] F. Hild and S. Roux, "Digital Image Correlation: from Displacement Measurement to Identification of Elastic Properties – a Review," *Strain*, 2006, doi: 10.1111/j.1475-1305.2006.00258.x.

[120] J. Q. d. Fonseca, P. Mummery, and P. J. Withers, "Full-field strain mapping by optical correlation of micrographs acquired during deformation," *Journal of Microscopy*, 2005, doi: 10.1111/j.1365-2818.2005.01461.x.

[121] M. A. Sutton *et al.*, "Scanning Electron Microscopy for Quantitative Small and Large Deformation Measurements Part II: Experimental Validation for Magnifications from 200 to 10,000," *Exp Mech*, 2007, doi: 10.1007/s11340-007-9041-0.
[122] M. A. Sutton, N. Li, D. C. Joy, A. P. Reynolds, and X. Li, "Scanning Electron Microscopy for Quantitative Small and Large Deformation Measurements Part I: SEM Imaging at Magnifications from 200 to 10,000," *Exp Mech*, 2007, doi: 10.1007/s11340-007-9042-z.
[123] N. Li, M. A. Sutton, X. Li, and H. W. Schreier, "Full-field Thermal Deformation Measurements in a Scanning Electron Microscope by 2D Digital Image Correlation," *Exp Mech*, 2008, doi: 10.1007/s11340-007-9107-z.
[124] M. A. Tschopp, B. B. Bartha, W. J. Porter, P. T. Murray, and S. B. Fairchild, "Microstructure-dependent local strain behavior in polycrystals through in situ scanning electron microscope tensile experiments," *Materials Science*, 2009, doi: 10.1007/s11661-009-9938-6.
[125] T. Zhu *et al.*, "Quantitative Stereovision in a Scanning Electron Microscope," *Exp Mech*, 2011, doi: 10.1007/s11340-010-9378-7.
[126] A. D. Kammers and S. Daly, "Small-scale patterning methods for digital image correlation under scanning electron microscopy," *Measurement Science and Technology*, 2011, doi: 10.1088/0957-0233/22/12/125501.
[127] A. D. Kammers and S. Daly, "Digital Image Correlation under Scanning Electron Microscopy: Methodology and Validation," *Exp Mech*, 2013, doi: 10.1007/s11340-013-9782-x.
[128] J. D. Carroll, W. Abuzaid, J. Lambros, and H. Sehitoglu, "High resolution digital image correlation measurements of strain accumulation in fatigue crack growth," *Int J Fatigue*, vol. 57, pp. 140-150, 2013/12/01/ 2013, doi: https://doi.org/10.1016/j.ijfatigue.2012.06.010.
[129] F. D. Gioacchino and J. Q. d. Fonseca, "Plastic Strain Mapping with Sub-micron Resolution Using Digital Image Correlation," *Exp Mech*, vol. 53, pp. 743–754, 2013, doi: 10.1007/s11340-012-9685-2.
[130] F. D. Gioacchino and J. Q. d. Fonseca, "An experimental study of the polycrystalline plasticity of austenitic stainless steel," *Int J Plasticity*, 2015, doi: 10.1016/j.ijplas.2015.05.012.
[131] J. A. Venables and C. J. Harland, "Electron back-scattering patterns—A new technique for obtaining crystallographic information in the scanning electron microscope," *Philosophical Magazine*, 1973, doi: 10.1080/14786437308225827.
[132] B. L. Adams, "Orientation imaging microscopy: application to the measurement of grain boundary structure," *Materials Science and Engineering: A*, vol. 166, no. 1, pp. 59-66, 1993/07/15/ 1993, doi: https://doi.org/10.1016/0921-5093(93)90310-B.
[133] A. J. Wilkinson, "Methods for determining elastic strains from electron backscatter diffraction and electron channelling patterns," *Mater Sci Tech-Lond*, 1997, doi: 10.1179/mst.1997.13.1.79.
[134] K. Z. Troost, P. v. d. Sluis, and D. J. Gravesteijn, "Microscale elastic-strain determination by backscatter Kikuchi diffraction in the scanning electron microscope," *Applied Physics Letters*, 1993, doi: 10.1063/1.108758.
[135] A. J. Wilkinson, "Measurement of elastic strains and small lattice rotations using electron back scatter diffraction," *Ultramicroscopy*, 1996, doi: 10.1016/0304-3991(95)00152-2.
[136] A. J. Wilkinson, G. Meaden, and D. J. Dingley, "High resolution mapping of strains and rotations using electron backscatter diffraction," (in English), *Mater Sci Tech-Lond*, vol. 22, no. 11, pp. 1271-1278, Nov 2006, doi: 10.1179/174328406x130966.
[137] A. J. Wilkinson, G. Meaden, and D. J. Dingley, "High-resolution elastic strain measurement from electron backscatter diffraction patterns: New levels of sensitivity," (in

English), *Ultramicroscopy*, vol. 106, no. 4-5, pp. 307-313, Mar 2006, doi: 10.1016/j.ultramic.2005.10.001.

[138] Y. Guo *et al.*, "Measurements of stress fields near a grain boundary: Exploring blocked arrays of dislocations in 3D," *Acta Mater*, vol. 96, pp. 229-236, 2015/09/01/ 2015, doi: https://doi.org/10.1016/j.actamat.2015.05.041.

[139] G. Miyamoto, A. Shibata, T. Maki, and T. Furuhara, "Precise measurement of strain accommodation in austenite matrix surrounding martensite in ferrous alloys by electron backscatter diffraction analysis," *Acta Mater*, 2009, doi: 10.1016/j.actamat.2008.10.050.

[140] P. S. Bate, R. D. Knutsen, I. Brough, and F. J. Humphreys, "The characterization of low-angle boundaries by EBSD," *Journal of Microscopy*, 2005, doi: 10.1111/j.1365-2818.2005.01513.x.

[141] S. Villert, C. Maurice, C. Wyon, and R. Fortunier, "Accuracy assessment of elastic strain measurement by EBSD," *Journal of Microscopy*, 2009, doi: 10.1111/j.1365-2818.2009.03120.x.

[142] T. B. Britton and A. J. Wilkinson, "Measurement of residual elastic strain and lattice rotations with high resolution electron backscatter diffraction," (in English), *Ultramicroscopy*, vol. 111, no. 8, pp. 1395-1404, 2011, doi: 10.1016/j.ultramic.2011.05.007.

[143] C. Maurice, J. H. Driver, and R. Fortunier, "On solving the orientation gradient dependency of high angular resolution EBSD," *Ultramicroscopy*, 2012, doi: 10.1016/j.ultramic.2011.10.013.

[144] T. B. Britton and A. J. Wilkinson, "High resolution electron backscatter diffraction measurements of elastic strain variations in the presence of larger lattice rotations," (in English), *Ultramicroscopy*, vol. 114, pp. 82-95, 2012, doi: 10.1016/j.ultramic.2012.01.004.

[145] T. B. Britton *et al.*, "Assessing the precision of strain measurements using electron backscatter diffraction – part 1: Detector assessment," *Ultramicroscopy*, 2013, doi: 10.1016/j.ultramic.2013.08.005.

[146] T. B. Britton *et al.*, "Assessing the precision of strain measurements using electron backscatter diffraction--part 2: experimental demonstration," *Ultramicroscopy*, 2013, doi: 10.1016/j.ultramic.2013.08.006.

[147] P. Karamched and A. J. Wilkinson, "High resolution electron back-scatter diffraction analysis of thermally and mechanically induced strains near carbide inclusions in a superalloy," *Acta Mater*, 2011, doi: 10.1016/j.actamat.2010.09.030.

[148] T. Vermeij, M. D. Graef, and J. P. M. Hoefnagels, "Demonstrating the potential of accurate absolute cross-grain stress and orientation correlation using electron backscatter diffraction," *Scripta Materialia*, 2019, doi: 10.1016/j.scriptamat.2018.11.030.

[149] A. Koko, V. Tong, A. J. Wilkinson, and T. J. Marrow, "An iterative method for reference pattern selection in high-resolution electron backscatter diffraction (HR-EBSD)," *Ultramicroscopy*, vol. 248, p. 113705, 2023/06/01/ 2023, doi: https://doi.org/10.1016/j.ultramic.2023.113705.

[150] A. Deal, I. Spinelli, A. Chuang, Y. Gao, and T. Broderick, "Measuring residual stress in Ti-6Al-4V with HR-EBSD, using reference patterns from annealed material," *Mater Charact*, vol. 175, p. 111027, 2021/05/01/ 2021, doi: https://doi.org/10.1016/j.matchar.2021.111027.

[151] H. Abdolvand and A. J. Wilkinson, "Assessment of residual stress fields at deformation twin tips and the surrounding environments," *Acta Mater*, 2016, doi: 10.1016/j.actamat.2015.11.036.

[152] T. Zhang, D. M. Collins, F. P. E. Dunne, and B. A. Shollock, "Crystal plasticity and high-resolution electron backscatter diffraction analysis of full-field polycrystal Ni superalloy strains and rotations under thermal loading," *Acta Mater*, 2014, doi: 10.1016/j.actamat.2014.07.036.

[153] J. Ast, G. Mohanty, Y. Guo, J. Michler, and X. Maeder, "In situ micromechanical testing of tungsten micro-cantilevers using HR-EBSD for the assessment of deformation evolution," *Materials & Design*, vol. 117, pp. 265-266, 2017/03/05/ 2017, doi: https://doi.org/10.1016/j.matdes.2016.12.052.

[154] A. Arabi-Hashemi, Y. Guo, J. Michler, D. Casari, C. Leinenbach, and X. Maeder, "Stress induced martensite variants revealed by in situ high resolution electron backscatter diffraction (HR-EBSD)," *Materials & Design*, vol. 151, pp. 83-88, 2018/08/05/ 2018, doi: https://doi.org/10.1016/j.matdes.2018.04.006.

[155] A. Koko, T. H. Becker, E. Elmukashfi, N. M. Pugno, A. J. Wilkinson, and T. J. Marrow, "HR-EBSD analysis of in situ stable crack growth at the micron scale," *J Mech Phys Solids*, vol. 172, p. 105173, 2023/03/01/ 2023, doi: https://doi.org/10.1016/j.jmps.2022.105173.

[156] B.-L. Adams and J. Kacher, "EBSD-Based Microscopy: Resolution of Dislocation Density," *Computers, Materials \& Continua*, vol. 14, no. 3, pp. 185--196, 2009. [Online]. Available: http://www.techscience.com/cmc/v14n3/22513.

[157] D. P. Field, C. C. Merriman, N. Allain-Bonasso, and F. Wagner, "Quantification of dislocation structure heterogeneity in deformed polycrystals by EBSD," *Modelling and Simulation in Materials Science and Engineering*, vol. 20, no. 2, p. 024007, 2012/02/24 2012, doi: 10.1088/0965-0393/20/2/024007.

[158] W. Pantleon, "Resolving the geometrically necessary dislocation content by conventional electron backscattering diffraction," *Scripta Materialia*, vol. 58, no. 11, pp. 994-997, 2008/06/01/ 2008, doi: https://doi.org/10.1016/j.scriptamat.2008.01.050.

[159] E. Demir, D. Raabe, N. Zaafarani, and S. Zaefferer, "Investigation of the indentation size effect through the measurement of the geometrically necessary dislocations beneath small indents of different depths using EBSD tomography," *Acta Mater*, vol. 57, no. 2, pp. 559-569, 2009/01/01/ 2009, doi: https://doi.org/10.1016/j.actamat.2008.09.039.

[160] A. J. Wilkinson and D. Randman, "Determination of elastic strain fields and geometrically necessary dislocation distributions near nanoindents using electron back scatter diffraction," *Philosophical Magazine*, 2010, doi: 10.1080/14786430903304145.

[161] J. Jiang, T. B. Britton, and A. J. Wilkinson, "Measurement of geometrically necessary dislocation density with high resolution electron backscatter diffraction: Effects of detector binning and step size," *Ultramicroscopy*, 2013, doi: 10.1016/j.ultramic.2012.11.003.

[162] M. D. Vaudin, G. Stan, Y. B. Gerbig, and R. F. Cook, "High resolution surface morphology measurements using EBSD cross-correlation techniques and AFM," *Ultramicroscopy*, vol. 111, no. 8, pp. 1206-1213, 2011/07/01/ 2011, doi: https://doi.org/10.1016/j.ultramic.2011.01.039.

[163] A. J. Wilkinson, "Examination of fatigue crack plastic zones using scanning-electron-microscope-based electron diffraction techniques," *Philosophical Magazine Letters*, vol. 74, no. 3, pp. 145-152, 1996, doi: 10.1080/095008396180290.

[164] T. B. Britton, S. Birosca, M. Preuss, and A. J. Wilkinson, "Electron backscatter diffraction study of dislocation content of a macrozone in hot-rolled Ti-6Al-4V alloy," *Scripta Materialia*, 2010, doi: 10.1016/j.scriptamat.2010.01.010.

[165] A. J. Wilkinson, E. Clarke, T. B. Britton, P. Littlewood, and P. Karamched, "High-resolution electron backscatter diffraction: An emerging tool for studying local deformation," (in English), *J Strain Anal Eng*, vol. 45, no. 5, pp. 365-376, 2010, doi: 10.1243/03093247jsa587.

[166] T. B. Britton, H. Liang, F. P. E. Dunne, and A. J. Wilkinson, "The effect of crystal orientation on the indentation response of commercially pure titanium: experiments and simulations," *Proceedings of The Royal Society A: Mathematical, Physical and Engineering Sciences*, vol. 466, no. 2115, pp. 695-719, Mar 8 2010, doi: 10.1098/rspa.2009.0455.

[167] A. J. Wilkinson, E. E. Clarke, T. B. Britton, P. Littlewood, and P. S. Karamched, "High-resolution electron backscatter diffraction: an emerging tool for studying local deformation," (in English), *J Strain Anal Eng*, vol. 45, no. 5, pp. 365-376, 2010, doi: 10.1243/03093247jsa587.

[168] J. Jiang, J. Yang, T. Zhang, F. P. E. Dunne, and T. B. Britton, "On the mechanistic basis of fatigue crack nucleation in Ni superalloy containing inclusions using high resolution electron backscatter diffraction," *Acta Mater*, vol. 97, pp. 367-379, 2015/09/15/ 2015, doi: https://doi.org/10.1016/j.actamat.2015.06.035.

[169] T. Zhang, J. Jiang, B. A. Shollock, T. B. Britton, and F. P. E. Dunne, "Slip localization and fatigue crack nucleation near a non-metallic inclusion in polycrystalline nickel-based superalloy," *Materials Science and Engineering: A*, vol. 641, pp. 328-339, 2015/08/12/ 2015, doi: https://doi.org/10.1016/j.msea.2015.06.070.

[170] J. Ast, M. N. Polyakov, G. Mohanty, J. Michler, and X. Maeder, "Interplay of stresses, plasticity at crack tips and small sample dimensions revealed by in-situ microcantilever tests in tungsten," *Materials Science and Engineering: A*, vol. 710, pp. 400-412, 2018/01/05/ 2018, doi: https://doi.org/10.1016/j.msea.2017.10.096.

[171] É. Maire and P. J. Withers, "Quantitative X-ray tomography," *International Materials Reviews*, 2014, doi: 10.1179/1743280413y.0000000023.

[172] J. Rannou *et al.*, "Three dimensional experimental and numerical multiscale analysis of a fatigue crack," *Computer Methods in Applied Mechanics and Engineering*, vol. 199, no. 21, pp. 1307-1325, 2010/04/01/ 2010, doi: https://doi.org/10.1016/j.cma.2009.09.013.

[173] B. K. Bay, T. S. Smith, D. P. Fyhrie, and M. Saad, "Digital volume correlation : Three-dimensional strain mapping using X-ray tomography," *Exp Mech*, 1999, doi: 10.1007/bf02323555.

[174] H. Leclerc, J. N. Périé, F. Hild, and S. Roux, "Digital volume correlation: what are the limits to the spatial resolution?," *Mechanics & Industry*, 2012, doi: 10.1051/meca/2012025.

[175] M. Gates, J. Lambros, and M. T. Heath, "Towards High Performance Digital Volume Correlation," *Exp Mech*, 2011, doi: 10.1007/s11340-010-9445-0.

[176] T. S. Smith, B. K. Bay, and M. M. Rashid, "Digital volume correlation including rotational degrees of freedom during minimization," *Exp Mech*, 2002, doi: 10.1007/bf02410982.

[177] S. A. McDonald, G. Dedreuil-Monet, Y. Yao, A. Alderson, and P. J. Withers, "In situ 3D X-ray microtomography study comparing auxetic and non-auxetic polymeric foams under tension," *Physica Status Solidi B-basic Solid State Physics*, 2011, doi: 10.1002/pssb.201083975.

[178] S. Roux, F. Hild, P. Viot, and D. Bernard, "Three dimensional image correlation from X-Ray computed tomography of solid foam," *Composites Part A-applied Science and Manufacturing*, 2008, doi: 10.1016/j.compositesa.2007.11.011.

[179] F. Pierron, S. A. McDonald, D. Hollis, P. J. Withers, and A. Alderson, "Assessment of the Deformation of Low Density Polymeric Auxetic Foams by X-Ray Tomography and Digital Volume Correlation," *Applied Mechanics and Materials*, 2011, doi: 10.4028/www.scientific.net/amm.70.93.

[180] F. Hild, É. Maire, S. Roux, and J. F. Witz, "Three-dimensional analysis of a compression test on stone wool," *Acta Mater*, 2009, doi: 10.1016/j.actamat.2009.03.038.

[181] F. Forsberg, R. Mooser, M. Arnold, E. Hack, and P. Wyss, "3D micro-scale deformations of wood in bending: Synchrotron radiation μCT data analyzed with digital volume correlation," *Journal of Structural Biology*, 2008, doi: 10.1016/j.jsb.2008.08.004.

[182] S. A. McDonald, L. C. R. Schneider, A. C. F. Cocks, and P. J. Withers, "Particle movement during the deep penetration of a granular material studied by X-ray microtomography," *Scripta Materialia*, 2006, doi: 10.1016/j.scriptamat.2005.09.042.

[183] S. A. Hall *et al.*, "Discrete and continuum analysis of localised deformation in sand using X-ray mu CT and volumetric digital image correlation," *Geotechnique*, 2010, doi: 10.1680/geot.2010.60.5.315.
[184] F. Tagliaferri *et al.*, "Observing strain localisation processes in bio-cemented sand using x-ray imaging," *Granular Matter*, 2011, doi: 10.1007/s10035-011-0257-4.
[185] S. R. Stock, A. Guvenilir, T. M. Breunig, J. H. Kinney, and M. C. Nichols, "Computed tomography part III: Volumetric, High-Resolution X-Ray analysis of fatigue crack closure," *JOM*, 1995, doi: 10.1007/bf03221124.
[186] H. Toda *et al.*, "A 3D measurement procedure for internal local crack driving forces via synchrotron X-ray microtomography," *Acta Mater*, vol. 52, no. 5, pp. 1305-1317, 2004/03/08/ 2004, doi: https://doi.org/10.1016/j.actamat.2003.11.014.
[187] H. Toda *et al.*, "Assessment of the fatigue crack closure phenomenon in damage-tolerant aluminium alloy by in-situ high-resolution synchrotron X-ray microtomography," *Philosophical Magazine*, Article vol. 83, no. 21, pp. 2429-2448, 2003, doi: 10.1080/1478643031000115754.
[188] T. J. Marrow, M. Mahmoud, H. Teruo, and E. T. George, "A quantitative three-dimensional in situ study of a short fatigue crack in a magnesium alloy," *Int J Fatigue*, vol. 66, pp. 183-193, 2014, doi: 10.1016/j.ijfatigue.2014.04.003.
[189] P. J. Withers, J. A. Bennett, Y. C. Hung, and M. Preuss, "Crack opening displacements during fatigue crack growth in Ti–SiC fibre metal matrix composites by X-ray tomography," *Mater Sci Tech-Lond*, 2006, doi: 10.1179/174328406x114108.
[190] N. Limodin, J. Réthoré, J. Y. Buffière, A. Gravouil, F. Hild, and S. Roux, "Crack closure and stress intensity factor measurements in nodular graphite cast iron using three-dimensional correlation of laboratory X-ray microtomography images," *Acta Mater*, 2009, doi: 10.1016/j.actamat.2009.05.005.
[191] N. Limodin *et al.*, "Influence of closure on the 3D propagation of fatigue cracks in a nodular cast iron investigated by X-ray tomography and 3D volume correlation," *Acta Mater*, 2010, doi: 10.1016/j.actamat.2010.01.024.
[192] K. I. Ignatiev, G. R. Davis, J. C. Elliott, and S. R. Stock, "MicroCT (microtomography) quantification of microstructure related to macroscopic behaviour: Part 1 - Fatigue crack closure measured in situ in AA 2090 compact tension samples," *Mater Sci Tech-Lond*, 2006, doi: 10.1179/174328406x114144.
[193] T. M. Breunig, J. H. Kinney, and S. R. Stock, "MicroCT (microtomography) quantification of microstructure related to macroscopic behaviour. Part 2 - Damage in SiC-Al monofilament composites tested in monotonic tension and fatigue," *Mater Sci Tech-Lond*, 2006, doi: 10.1179/174328406x114153.
[194] Y. Barranger, P. Doumalin, J.-C. Dupré, A. Germaneau, and V. Valle, "Analyse à cœur des champs de déplacement obtenus sur une éprouvette fissurée," 2009. [Online]. Available: https://www.semanticscholar.org/paper/2da8a2ee5d9ccc28819ae8d462584c91fe0edb1f.
[195] P. J. Withers, P. López-Crespo, A. Kyrieleis, and Y. C. Hung, "Evolution of crack-bridging and crack-tip driving force during the growth of a fatigue crack in a Ti/SiC composite," *Proceedings of The Royal Society A: Mathematical, Physical and Engineering Sciences*, 2012, doi: 10.1098/rspa.2012.0070.
[196] A. King *et al.*, "Three-dimensional in situ observations of short fatigue crack growth in magnesium," *Acta Mater*, vol. 59, no. 17, pp. 6761-6771, Oct 2011, doi: 10.1016/j.actamat.2011.07.034.
[197] M. Mostafavi *et al.*, "Three-dimensional crack observation, quantification and simulation in a quasi-brittle material," *Acta Mater*, 2013, doi: 10.1016/j.actamat.2013.07.011.

[198] M. Mostafavi, S. A. McDonald, P. Mummery, and T. J. Marrow, "Observation and quantification of three-dimensional crack propagation in poly-granular graphite," *Engineering Fracture Mechanics,* 2013, doi: 10.1016/j.engfracmech.2012.11.023.

[199] M. Mostafavi, S. A. McDonald, H. Çetinel, P. Mummery, and T. J. Marrow, "Flexural strength and defect behaviour of polygranular graphite under different states of stress," *Carbon,* 2013, doi: 10.1016/j.carbon.2013.03.025.

[200] M. Mostafavi, R. Bradley, D. E. J. Armstrong, and T. J. Marrow, "Quantifying yield behaviour in metals by X-ray nanotomography," *Scientific Reports,* vol. 6, no. 1, p. 34346, 2016/10/04 2016, doi: 10.1038/srep34346.

[201] F. P. Chiang and A. Asundi, "A white light speckle method applied to the determination of stress intensity factor and displacement field around a crack tip," *Engineering Fracture Mechanics,* vol. 15, no. 1, pp. 115-121, 1981/01/01/ 1981, doi: https://doi.org/10.1016/0013-7944(81)90110-7.

[202] J. M. Huntley and J. E. Field, "Measurement of crack tip displacement field using laser speckle photography," *Engineering Fracture Mechanics,* vol. 30, no. 6, pp. 779-790, 1988/01/01/ 1988, doi: https://doi.org/10.1016/0013-7944(88)90139-7.

[203] J. Abanto-Bueno and J. Lambros, "Investigation of crack growth in functionally graded materials using digital image correlation," *Engineering Fracture Mechanics,* vol. 69, no. 14, pp. 1695-1711, 2002/09/01/ 2002, doi: https://doi.org/10.1016/S0013-7944(02)00058-9.

[204] S. Roux and F. Hild, "Stress intensity factor measurements from digital image correlation: post-processing and integrated approaches," *International Journal of Fracture,* 2006, doi: 10.1007/s10704-006-6631-2.

[205] S. Yoneyama, Y. Morimoto, and M. Takashi, "Automatic Evaluation of Mixed-mode Stress Intensity Factors Utilizing Digital Image Correlation," *Strain,* vol. 42, no. 1, pp. 21-29, 2006, doi: https://doi.org/10.1111/j.1475-1305.2006.00246.x.

[206] P. Lopez-crespo, A. Shterenlikht, J. R. Yates, E. A. Patterson, and P. J. Withers, "Some experimental observations on crack closure and crack-tip plasticity," *Fatigue Fract Eng M,* vol. 32, no. 5, pp. 418-429, 2009, doi: https://doi.org/10.1111/j.1460-2695.2009.01345.x.

[207] J. R. Yates, M. Zanganeh, and Y. H. Tai, "Quantifying crack tip displacement fields with DIC," *Engineering Fracture Mechanics,* vol. 77, no. 11, pp. 2063-2076, 2010/07/01/ 2010, doi: https://doi.org/10.1016/j.engfracmech.2010.03.025.

[208] M. S. Kirugulige and H. V. Tippur, "Measurement of Fracture Parameters for a Mixed-Mode Crack Driven by Stress Waves using Image Correlation Technique and High-Speed Digital Photography," *Strain,* vol. 45, no. 2, pp. 108-122, 2009, doi: https://doi.org/10.1111/j.1475-1305.2008.00449.x.

[209] F. Yusof and P. J. Withers, "Real-time acquisition of fatigue crack images for monitoring crack-tip stress intensity variations within fatigue cycles," *The Journal of Strain Analysis for Engineering Design,* vol. 44, no. 2, pp. 149-158, 2009/02/01 2008, doi: 10.1243/03093247JSA440.

[210] R. Hamam, F. Hild, and S. Roux, "Stress Intensity Factor Gauging by Digital Image Correlation: Application in Cyclic Fatigue," *Strain,* vol. 43, no. 3, pp. 181-192, 2007, doi: https://doi.org/10.1111/j.1475-1305.2007.00345.x.

[211] J. Poissant and F. Barthelat, "A Novel “Subset Splitting” Procedure for Digital Image Correlation on Discontinuous Displacement Fields," *Exp Mech,* vol. 50, no. 3, pp. 353-364, 2010/03/01 2010, doi: 10.1007/s11340-009-9220-2.

[212] J. Réthoré, A. Gravouil, F. Morestin, and A. Combescure, "Estimation of mixed-mode stress intensity factors using digital image correlation and an interaction integral," *International Journal of Fracture,* 2005, doi: 10.1007/s10704-004-8141-4.

[213] T. H. Becker, T. J. Marrow, and R. B. Tait, "Damage, crack growth and fracture characteristics of nuclear grade graphite using the Double Torsion technique," *J Nucl Mater*, vol. 414, no. 1, pp. 32-43, Jul 1 2011, doi: 10.1016/j.jnucmat.2011.04.058.

[214] T. H. Becker, M. Mostafavi, R. B. Tait, and T. J. Marrow, "An approach to calculate the J-integral by digital image correlation displacement field measurement," *Fatigue Fract Eng M*, vol. 35, no. 10, pp. 971-984, 2012, doi: 10.1111/j.1460-2695.2012.01685.x.

[215] S. M. Barhli *et al.*, "Obtaining the J-integral by diffraction-based crack-field strain mapping," *Procedia structural integrity*, vol. 2, pp. 2519-2526, 2016, doi: 10.1016/j.prostr.2016.06.315.

[216] S. M. Barhli, M. Mostafavi, A. F. Cinar, D. Hollis, and T. J. Marrow, "J-Integral Calculation by Finite Element Processing of Measured Full-Field Surface Displacements," *Exp Mech*, vol. 57, no. 6, pp. 997-1009, Jul 2017, doi: 10.1007/s11340-017-0275-1.

[217] T. H. Becker, M. R. Molteno, and T. J. Marrow, "Procedure for accurate calculation of the J-integral from digital volume correlation displacement data," *Strain*, 2020, doi: 10.1111/str.12337.

[218] T. H. Becker and T. J. Marrow, "A Robust Finite Element-based Filter for Digital Image and Volume Correlation Displacement Data," *Exp Mech*, 2021, doi: 10.1007/s11340-021-00718-5.

[219] A. Koko, P. Earp, T. Wigger, J. Tong, and T. J. Marrow, "J-integral analysis: An EDXD and DIC comparative study for a fatigue crack," *Int J Fatigue*, vol. 134, May 2020, doi: 10.1016/j.ijfatigue.2020.105474.

[220] A. Koko, E. Elmukashfi, K. Dragnevski, A. J. Wilkinson, and T. J. Marrow, "J-integral analysis of the elastic strain fields of ferrite deformation twins using electron backscatter diffraction," *Acta Mater*, vol. 218, Oct 1 2021, doi: 10.1016/j.actamat.2021.117203.

[221] S. Pearson, "Initiation of fatigue cracks in commercial aluminium alloys and the subsequent propagation of very short cracks," *Engineering Fracture Mechanics*, vol. 7, no. 2, pp. 235-247, 1975/06/01/ 1975, doi: https://doi.org/10.1016/0013-7944(75)90004-1.

[222] K. Tokaji, T. Ogawa, and Y. Harada, "EVALUATION ON LIMITATION OF LINEAR ELASTIC FRACTURE MECHANICS FOR SMALL FATIGUE CRACK GROWTH," *Fatigue Fract Eng M*, vol. 10, no. 4, pp. 281-289, 1987, doi: https://doi.org/10.1111/j.1460-2695.1987.tb00207.x.

[223] S. M. Ohr, "An electron microscope study of crack tip deformation and its impact on the dislocation theory of fracture," *Materials Science and Engineering*, vol. 72, no. 1, pp. 1-35, 1985/06/01/ 1985, doi: https://doi.org/10.1016/0025-5416(85)90064-3.

[224] A. Navarro and E. R. de los Rios, "Short and long fatigue crack growth: A unified model," *Philosophical Magazine A*, vol. 57, no. 1, pp. 15-36, 1988/06/01 1988, doi: 10.1080/01418618808204496.

[225] K. Sadananda and A. K. Vasudevan, "Short crack growth and internal stresses," *Int J Fatigue*, vol. 19, no. 93, pp. 99-108, 1997/06/01/ 1997, doi: https://doi.org/10.1016/S0142-1123(97)00057-1.

[226] A. Boyd-Lee and J. E. King, "SHORT FATIGUE CRACK PATH DETERMINANTS IN POLYCRYSTALLINE Ni-BASE SUPERALLOYS," *Fatigue Fract Eng M*, vol. 17, no. 1, pp. 1-14, 1994, doi: https://doi.org/10.1111/j.1460-2695.1994.tb00768.x.

[227] T. Zhai, A. J. Wilkinson, and J. W. Martin, "A crystallographic mechanism for fatigue crack propagation through grain boundaries," *Acta Mater*, vol. 48, no. 20, pp. 4917-4927, 2000/12/04/ 2000, doi: https://doi.org/10.1016/S1359-6454(00)00214-7.

[228] T. Zhai, X. P. Jiang, J. X. Li, M. D. Garratt, and G. H. Bray, "The grain boundary geometry for optimum resistance to growth of short fatigue cracks in high strength Al-alloys," *Int J Fatigue*, vol. 27, no. 10, pp. 1202-1209, 2005/10/01/ 2005, doi: https://doi.org/10.1016/j.ijfatigue.2005.06.021.

[229] A. Sugeta, Y. Uematsu, A. Hashimoto, and M. Jono, "Atomic force microscopy of fatigue crack growth behavior in the low K region," *Int J Fatigue,* vol. 26, no. 11, pp. 1159-1168, 2004/11/01/ 2004, doi: https://doi.org/10.1016/j.ijfatigue.2004.04.001.

[230] R. Pippan, "Dislocation emission and fatigue crack growth threshold," *Acta Metallurgica et Materialia,* vol. 39, no. 3, pp. 255-262, 1991/03/01/ 1991, doi: https://doi.org/10.1016/0956-7151(91)90304-J.

[231] R. Pippan, "The condition for the cyclic plastic deformation of the crack tip: the influence of dislocation obstacles," *International Journal of Fracture,* vol. 58, no. 4, pp. 305-318, 1992/12/01 1992, doi: 10.1007/BF00048951.

[232] A. J. Wilkinson and S. G. Roberts, "A dislocation model for the two critical stress intensities required for threshold fatigue crack propagation," *Scripta Materialia,* vol. 35, no. 11, pp. 1365-1371, 1996/12/01/ 1996, doi: https://doi.org/10.1016/1359-6462(96)00301-6.

[233] H. H. M. Cleveringa, E. Van der Giessen, and A. Needleman, "A discrete dislocation analysis of mode I crack growth," *J Mech Phys Solids,* vol. 48, no. 6, pp. 1133-1157, 2000/06/01/ 2000, doi: https://doi.org/10.1016/S0022-5096(99)00076-9.

[234] C. Bjerkén and S. Melin, "A study of the influence of grain boundaries on short crack growth during varying load using a dislocation technique," *Engineering Fracture Mechanics,* vol. 71, no. 15, pp. 2215-2227, 2004/10/01/ 2004, doi: https://doi.org/10.1016/j.engfracmech.2003.10.006.

[235] W. Ludwig, J. Y. Buffière, S. Savelli, and P. Cloetens, "Study of the interaction of a short fatigue crack with grain boundaries in a cast Al alloy using X-ray microtomography," *Acta Mater,* vol. 51, no. 3, pp. 585-598, 2003/02/07/ 2003, doi: https://doi.org/10.1016/S1359-6454(02)00320-8.

[236] C. Holzapfel, W. Schäf, M. Marx, H. Vehoff, and F. Mücklich, "Interaction of cracks with precipitates and grain boundaries: Understanding crack growth mechanisms through focused ion beam tomography," *Scripta Materialia,* vol. 56, no. 8, pp. 697-700, 2007/04/01/ 2007, doi: https://doi.org/10.1016/j.scriptamat.2006.12.025.

[237] W. Schäf, M. Marx, and A. F. Knorr, "Influence of microstructural barriers on small fatigue crack growth in mild steel," *Int J Fatigue,* vol. 57, pp. 86-92, 2013/12/01/ 2013, doi: https://doi.org/10.1016/j.ijfatigue.2012.11.006.

[238] T. J. Marrow, J. Y. Buffiere, P. J. Withers, G. Johnson, and D. Engelberg, "High resolution X-ray tomography of short fatigue crack nucleation in austempered ductile cast iron," *Int J Fatigue,* vol. 26, no. 7, pp. 717-725, 2004/07/01/ 2004, doi: https://doi.org/10.1016/j.ijfatigue.2003.11.001.

[239] E. Ferrié, J. Y. Buffière, and W. Ludwig, "3D characterisation of the nucleation of a short fatigue crack at a pore in a cast Al alloy using high resolution synchrotron microtomography," *Int J Fatigue,* vol. 27, no. 10, pp. 1215-1220, 2005/10/01/ 2005, doi: https://doi.org/10.1016/j.ijfatigue.2005.07.015.

[240] J. Y. Buffiere, E. Ferrie, H. Proudhon, and W. Ludwig, "Three-dimensional visualisation of fatigue cracks in metals using high resolution synchrotron X-ray micro-tomography," *Mater Sci Tech-Lond,* vol. 22, no. 9, pp. 1019-1024, 2006/09/01 2006, doi: 10.1179/174328406X114135.

[241] S. Birosca, J. Y. Buffiere, F. A. Garcia-Pastor, M. Karadge, L. Babout, and M. Preuss, "Three-dimensional characterization of fatigue cracks in Ti-6246 using X-ray tomography and electron backscatter diffraction," *Acta Mater,* vol. 57, no. 19, pp. 5834-5847, 2009/11/01/ 2009, doi: https://doi.org/10.1016/j.actamat.2009.08.009.

[242] N. Limodin *et al.*, "3D X-ray Microtomography Volume Correlation to Study Fatigue Crack Growth," *Advanced Engineering Materials,* vol. 13, no. 3, pp. 186-193, 2011, doi: https://doi.org/10.1002/adem.201000235.

[243] M. Herbig *et al.*, "3-D growth of a short fatigue crack within a polycrystalline microstructure studied using combined diffraction and phase-contrast X-ray tomography," *Acta Mater*, vol. 59, no. 2, pp. 590-601, 2011/01/01/ 2011, doi: https://doi.org/10.1016/j.actamat.2010.09.063.

[244] T. P. Chapman *et al.*, "Characterisation of short fatigue cracks in titanium alloy IMI 834 using X-ray microtomography," *Acta Mater*, vol. 99, pp. 49-62, 2015/10/15/ 2015, doi: https://doi.org/10.1016/j.actamat.2015.07.069.

[245] Y. Gao, J. S. Stölken, M. Kumar, and R. O. Ritchie, "High-cycle fatigue of nickel-base superalloy René 104 (ME3): Interaction of microstructurally small cracks with grain boundaries of known character," *Acta Mater*, vol. 55, no. 9, pp. 3155-3167, 2007/05/01/ 2007, doi: https://doi.org/10.1016/j.actamat.2007.01.033.

[246] C. Santus and D. Taylor, "Physically short crack propagation in metals during high cycle fatigue," *Int J Fatigue*, vol. 31, no. 8, pp. 1356-1365, 2009/08/01/ 2009, doi: https://doi.org/10.1016/j.ijfatigue.2009.03.002.

[247] M. D. Chapetti, "Fatigue propagation threshold of short cracks under constant amplitude loading," *Int J Fatigue*, vol. 25, no. 12, pp. 1319-1326, 2003/12/01/ 2003, doi: https://doi.org/10.1016/S0142-1123(03)00065-3.

[248] D. L. McDowell and F. P. E. Dunne, "Microstructure-sensitive computational modeling of fatigue crack formation," *Int J Fatigue*, vol. 32, no. 9, pp. 1521-1542, 2010/09/01/ 2010, doi: https://doi.org/10.1016/j.ijfatigue.2010.01.003.

[249] P. Hansson and S. Melin, "Grain boundary influence on short fatigue crack growth rate," *International Journal of Fracture*, vol. 165, no. 2, pp. 199-210, 2010/10/01 2010, doi: 10.1007/s10704-010-9512-7.

[250] V. V. C. Wan, D. W. MacLachlan, and F. P. E. Dunne, "Integrated experiment and modelling of microstructurally-sensitive crack growth," *Int J Fatigue*, vol. 91, pp. 110-123, 2016/10/01/ 2016, doi: https://doi.org/10.1016/j.ijfatigue.2016.05.027.

[251] A. Rovinelli, M. D. Sangid, H. Proudhon, Y. Guilhem, R. A. Lebensohn, and W. Ludwig, "Predicting the 3D fatigue crack growth rate of small cracks using multimodal data via Bayesian networks: In-situ experiments and crystal plasticity simulations," *J Mech Phys Solids*, vol. 115, pp. 208-229, 2018/06/01/ 2018, doi: https://doi.org/10.1016/j.jmps.2018.03.007.

[252] R. A. Brockman, R. M. Hoffman, P. J. Golden, W. D. Musinski, S. K. Jha, and R. John, "A computational framework for microstructural crack propagation," *Int J Fatigue*, vol. 152, p. 106397, 2021/11/01/ 2021, doi: https://doi.org/10.1016/j.ijfatigue.2021.106397.

[253] Y. Guo, T. B. Britton, and A. J. Wilkinson, "Slip band–grain boundary interactions in commercial-purity titanium," *Acta Mater*, vol. 76, pp. 1-12, 2014/09/01/ 2014, doi: https://doi.org/10.1016/j.actamat.2014.05.015.

[254] R. Jiang, F. Pierron, S. Octaviani, and P. A. S. Reed, "Characterisation of strain localisation processes during fatigue crack initiation and early crack propagation by SEM-DIC in an advanced disc alloy," *Materials Science and Engineering: A*, vol. 699, pp. 128-144, 2017/06/24/ 2017, doi: https://doi.org/10.1016/j.msea.2017.05.091.

[255] K. S. Chan and J. Lankford, "A crack-tip strain model for the growth of small fatigue cracks," *Scripta Metallurgica*, vol. 17, no. 4, pp. 529-532, 1983/04/01/ 1983, doi: https://doi.org/10.1016/0036-9748(83)90346-0.

[256] W. D. Musinski and D. L. McDowell, "Simulating the effect of grain boundaries on microstructurally small fatigue crack growth from a focused ion beam notch through a three-dimensional array of grains," *Acta Mater*, vol. 112, pp. 20-39, 2016/06/15/ 2016, doi: https://doi.org/10.1016/j.actamat.2016.04.006.

[257] K. Miller, R. Piascik, J. Newman, Jr, and N. Dowling, "The Three Thresholds for Fatigue Crack Propagation," in *Fatigue and Fracture Mechanics: 27th Volume*, vol. STP1296-EB: ASTM International, 1997, p. 0.

[258] T. Hoshide and D. F. Socie, "Mechanics of mixed mode small fatigue crack growth," *Engineering Fracture Mechanics*, vol. 26, no. 6, pp. 841-850, 1987/01/01/ 1987, doi: https://doi.org/10.1016/0013-7944(87)90033-6.

[259] D. L. McDowell and J.-Y. Berard, "A δJ-BASED APPROACH TO BIAXIAL FATIGUE," *Fatigue Fract Eng M*, vol. 15, no. 8, pp. 719-741, 1992, doi: https://doi.org/10.1111/j.1460-2695.1992.tb00053.x.

[260] M. W. Brown and K. J. Miller, "A Theory for Fatigue Failure under Multiaxial Stress-Strain Conditions," *Proceedings of the Institution of Mechanical Engineers*, vol. 187, no. 1, pp. 745-755, 1973, doi: 10.1243/pime_proc_1973_187_161_02.

[261] F. O. Riemelmoser, P. Gumbsch, and R. Pippan, "Dislocation Modelling of Fatigue Cracks: An Overview," *MATERIALS TRANSACTIONS*, vol. 42, no. 1, pp. 2-13, 2001, doi: 10.2320/matertrans.42.2.

[262] R. Pippan, F. Riemelmoser, O., and H. Kreuzer, "Effect of the discrete nature of plasticity on fatigue crack propagation," *J. Phys. IV France*, vol. 11, no. PR5, pp. Pr5-77-Pr5-84, 2001. [Online]. Available: https://doi.org/10.1051/jp4:2001510.

[263] K. S. Chan, J. Lankford, and D. L. Davidson, "A Comparison of Crack-Tip Field Parameters for Large and Small Fatigue Cracks," *Journal of Engineering Materials and Technology*, vol. 108, no. 3, pp. 206-213, 1986, doi: 10.1115/1.3225868.

[264] K. Hussain, E. R. De los Rios, and A. Navarro, "A two-stage micromechanics model for short fatigue cracks," *Engineering Fracture Mechanics*, vol. 44, no. 3, pp. 425-436, 1993/02/01/ 1993, doi: https://doi.org/10.1016/0013-7944(93)90034-P.

[265] C. Wu, C. Wei, and Y. Li, "In Situ Mechanical Characterization of the Mixed-Mode Fracture Strength of the Cu/Si Interface for TSV Structures," *Micromachines*, vol. 10, no. 2, p. 86, 2019. [Online]. Available: https://www.mdpi.com/2072-666X/10/2/86.

[266] L. Xi, C. Qiao, D. Pradeep, C. Ritwik, R. R. Tummala, and S. K. Sitaraman, "Failure mechanisms and optimum design for electroplated copper Through-Silicon Vias (TSV)," in *2009 59th Electronic Components and Technology Conference*, 26-29 May 2009 2009, pp. 624-629, doi: 10.1109/ECTC.2009.5074078.

[267] V. T. Srikar and S. M. Spearing, "A critical review of microscale mechanical testing methods used in the design of microelectromechanical systems," *Exp Mech*, vol. 43, no. 3, pp. 238-247, 2003/09/01 2003, doi: 10.1007/BF02410522.

[268] M. Trueba *et al.*, "Fracture characterization of thin-films by dual tip indentation," *Acta Mater*, vol. 71, pp. 44-55, 2014/06/01/ 2014, doi: https://doi.org/10.1016/j.actamat.2014.03.011.

[269] J. P. Best, Z. Johannes, W. J. M., S. Rachel, M. Marcus, and J. Michler, "Small-scale fracture toughness of ceramic thin films: the effects of specimen geometry, ion beam notching and high temperature on chromium nitride toughness evaluation," *Philosophical Magazine*, vol. 96, no. 32-34, pp. 3552-3569, 2016/12/01 2016, doi: 10.1080/14786435.2016.1223891.

[270] J. Schaufler, C. Schmid, K. Durst, and M. Göken, "Determination of the interfacial strength and fracture toughness of a-C:H coatings by in-situ microcantilever bending," *Thin Solid Films*, vol. 522, pp. 480-484, 2012/11/01/ 2012, doi: https://doi.org/10.1016/j.tsf.2012.08.031.

[271] K. Matoy *et al.*, "A comparative micro-cantilever study of the mechanical behavior of silicon based passivation films," *Thin Solid Films*, vol. 518, no. 1, pp. 247-256, 2009/11/02/ 2009, doi: https://doi.org/10.1016/j.tsf.2009.07.143.

[272] A.-N. Wang, J. F. Nonemacher, G. Yan, M. Finsterbusch, J. Malzbender, and M. Krüger, "Mechanical properties of the solid electrolyte Al-substituted Li7La3Zr2O12 (LLZO) by utilizing micro-pillar indentation splitting test," *Journal of the European Ceramic Society*, vol. 38, no. 9, pp. 3201-3209, 2018/08/01/ 2018, doi: https://doi.org/10.1016/j.jeurceramsoc.2018.02.032.

[273] M. Z. Mughal, R. Moscatelli, H.-Y. Amanieu, and M. Sebastiani, "Effect of lithiation on micro-scale fracture toughness of LixMn2O4 cathode," *Scripta Materialia*, vol. 116, pp. 62-66, 2016/04/15/ 2016, doi: https://doi.org/10.1016/j.scriptamat.2016.01.023.

[274] S. Bulychev, V. Alekhin, M. Shorshorov, A. Ternovskii, and G. Shnyrev, "Determining Young's modulus from the indentor penetration diagram," *Ind. Lab.*, vol. 41, no. 9, pp. 1409-1412, 1975.

[275] D. Newey, M. A. Wilkins, and H. M. Pollock, "An ultra-low-load penetration hardness tester," *Journal of Physics E: Scientific Instruments*, vol. 15, no. 1, p. 119, 1982/01/01 1982, doi: 10.1088/0022-3735/15/1/023.

[276] B. Lawn and R. Wilshaw, "Indentation fracture: principles and applications," *Journal of Materials Science*, vol. 10, no. 6, pp. 1049-1081, 1975/06/01 1975, doi: 10.1007/BF00823224.

[277] A. G. Evans and E. A. Charles, "Fracture Toughness Determinations by Indentation," *Journal of the American Ceramic Society*, vol. 59, no. 7-8, pp. 371-372, 1976, doi: https://doi.org/10.1111/j.1151-2916.1976.tb10991.x.

[278] D. B. Marshall and B. R. Lawn, "Residual stress effects in sharp contact cracking," *Journal of Materials Science*, vol. 14, no. 8, pp. 2001-2012, 1979/08/01 1979, doi: 10.1007/BF00551043.

[279] B. R. Lawn, A. G. Evans, and D. B. Marshall, "Elastic/Plastic Indentation Damage in Ceramics: The Median/Radial Crack System," *Journal of the American Ceramic Society*, vol. 63, no. 9-10, pp. 574-581, 1980, doi: https://doi.org/10.1111/j.1151-2916.1980.tb10768.x.

[280] J. H. Lee, Y. F. Gao, K. E. Johanns, and G. M. Pharr, "Cohesive interface simulations of indentation cracking as a fracture toughness measurement method for brittle materials," *Acta Mater*, vol. 60, no. 15, pp. 5448-5467, 2012/09/01/ 2012, doi: https://doi.org/10.1016/j.actamat.2012.07.011.

[281] K. E. Johanns, J. H. Lee, Y. F. Gao, and G. M. Pharr, "An evaluation of the advantages and limitations in simulating indentation cracking with cohesive zone finite elements," *Modelling and Simulation in Materials Science and Engineering*, vol. 22, no. 1, p. 015011, 2013/12/20 2014, doi: 10.1088/0965-0393/22/1/015011.

[282] S. Bruns, K. E. Johanns, H. U. R. Rehman, G. M. Pharr, and K. Durst, "Constitutive modeling of indentation cracking in fused silica," *Journal of the American Ceramic Society*, vol. 100, no. 5, pp. 1928-1940, 2017, doi: https://doi.org/10.1111/jace.14734.

[283] R. F. Cook and G. M. Pharr, "Direct Observation and Analysis of Indentation Cracking in Glasses and Ceramics," *Journal of the American Ceramic Society*, vol. 73, no. 4, pp. 787-817, 1990, doi: https://doi.org/10.1111/j.1151-2916.1990.tb05119.x.

[284] B. Merle and M. Göken, "Fracture toughness of silicon nitride thin films of different thicknesses as measured by bulge tests," *Acta Mater*, vol. 59, no. 4, pp. 1772-1779, 2011/02/01/ 2011, doi: https://doi.org/10.1016/j.actamat.2010.11.043.

[285] E. I. Preiß, B. Merle, and M. Göken, "Understanding the extremely low fracture toughness of freestanding gold thin films by in-situ bulge testing in an AFM," *Materials Science and Engineering: A*, vol. 691, pp. 218-225, 2017/04/13/ 2017, doi: https://doi.org/10.1016/j.msea.2017.03.037.

[286] E. I. Preiß, F. Gannott, M. Göken, and B. Merle, "Scaling of the fracture toughness of freestanding metallic thin films with the yield strength," *Materials Research Letters*, vol. 6, no. 10, pp. 607-612, 2018/10/03 2018, doi: 10.1080/21663831.2018.1520749.

[287] J. J. Schwiedrzik, J. Ast, L. Pethö, X. Maeder, and J. Michler, "A new push-pull sample design for microscale mode 1 fracture toughness measurements under uniaxial tension," *Fatigue Fract Eng M*, vol. 41, no. 5, pp. 991-1001, 2018, doi: https://doi.org/10.1111/ffe.12741.

[288] B. N. Jaya, V. Jayaram, and S. K. Biswas, "A new method for fracture toughness determination of graded (Pt,Ni)Al bond coats by microbeam bend tests," *Philosophical Magazine*, vol. 92, no. 25-27, pp. 3326-3345, 2012/09/01 2012, doi: 10.1080/14786435.2012.669068.

[289] E. D. Hintsala, S. Bhowmick, X. Yueyue, R. Ballarini, S. A. S. Asif, and W. W. Gerberich, "Temperature dependent fracture initiation in microscale silicon," *Scripta Materialia*, vol. 130, pp. 78-82, 2017/03/15/ 2017, doi: https://doi.org/10.1016/j.scriptamat.2016.11.016.

[290] S. Liu, J. M. Wheeler, P. R. Howie, X. T. Zeng, J. Michler, and W. J. Clegg, "Measuring the fracture resistance of hard coatings," *Applied Physics Letters*, vol. 102, no. 17, 2013, doi: 10.1063/1.4803928.

[291] G. Sernicola *et al.*, "In situ stable crack growth at the micron scale," *Nature Communications*, vol. 8, no. 1, p. 108, 2017/07/24 2017, doi: 10.1038/s41467-017-00139-w.

[292] M. Sebastiani, K. E. Johanns, E. G. Herbert, F. Carassiti, and G. M. Pharr, "A novel pillar indentation splitting test for measuring fracture toughness of thin ceramic coatings," *Philosophical Magazine*, vol. 95, no. 16-18, pp. 1928-1944, 2015/06/23 2015, doi: 10.1080/14786435.2014.913110.

[293] M. Sebastiani, K. E. Johanns, E. G. Herbert, and G. M. Pharr, "Measurement of fracture toughness by nanoindentation methods: Recent advances and future challenges," *Current Opinion in Solid State and Materials Science*, vol. 19, no. 6, pp. 324-333, 2015/12/01/ 2015, doi: https://doi.org/10.1016/j.cossms.2015.04.003.

[294] F. Hofmann, R. J. Harder, W. Liu, Y. Liu, I. K. Robinson, and Y. Zayachuk, "Glancing-incidence focussed ion beam milling: A coherent X-ray diffraction study of 3D nano-scale lattice strains and crystal defects," *Acta Mater*, vol. 154, pp. 113-123, 2018/08/01/ 2018, doi: https://doi.org/10.1016/j.actamat.2018.05.018.

[295] M. Ghidelli, M. Sebastiani, K. E. Johanns, and G. M. Pharr, "Effects of indenter angle on micro-scale fracture toughness measurement by pillar splitting," *Journal of the American Ceramic Society*, vol. 100, no. 12, pp. 5731-5738, 2017, doi: https://doi.org/10.1111/jace.15093.

[296] C. M. Lauener, L. Petho, M. Chen, Y. Xiao, J. Michler, and J. M. Wheeler, "Fracture of Silicon: Influence of rate, positioning accuracy, FIB machining, and elevated temperatures on toughness measured by pillar indentation splitting," *Materials & Design*, vol. 142, pp. 340-349, 2018/03/15/ 2018, doi: https://doi.org/10.1016/j.matdes.2018.01.015.

[297] G. Bolelli *et al.*, "Damage progression in thermal barrier coating systems during thermal cycling: A nano-mechanical assessment," *Materials & Design*, vol. 166, p. 107615, 2019/03/15/ 2019, doi: https://doi.org/10.1016/j.matdes.2019.107615.

[298] D. Di Maio and S. G. Roberts, "Measuring fracture toughness of coatings using focused-ion-beam-machined microbeams," *Journal of Materials Research*, vol. 20, no. 2, pp. 299-302, 2005/02/01 2005, doi: 10.1557/JMR.2005.0048.

[299] T. P. Halford, K. Takashima, Y. Higo, and P. Bowen, "Fracture tests of microsized TiAl specimens," *Fatigue Fract Eng M*, vol. 28, no. 8, pp. 695-701, 2005, doi: https://doi.org/10.1111/j.1460-2695.2005.00893.x.

[300] F. Iqbal, J. Ast, M. Göken, and K. Durst, "In situ micro-cantilever tests to study fracture properties of NiAl single crystals," *Acta Mater*, vol. 60, no. 3, pp. 1193-1200, 2012/02/01/ 2012, doi: https://doi.org/10.1016/j.actamat.2011.10.060.

[301] M. D. Uchic, D. M. Dimiduk, J. N. Florando, and W. D. Nix, "Sample dimensions influence strength and crystal plasticity," *Science*, Article vol. 305, no. 5686, pp. 986-989, 2004, doi: 10.1126/science.1098993.

[302] O. Kraft, P. A. Gruber, R. Mönig, and D. Weygand, "Plasticity in Confined Dimensions," *Annual Review of Materials Research*, vol. 40, no. Volume 40, 2010, pp. 293-317, 2010, doi: https://doi.org/10.1146/annurev-matsci-082908-145409.

[303] D. Kupka and E. T. Lilleodden, "Mechanical Testing of Solid–Solid Interfaces at the Microscale," *Exp Mech*, vol. 52, no. 6, pp. 649-658, 2012/07/01 2012, doi: 10.1007/s11340-011-9530-z.

[304] J. Ast, M. Göken, and K. Durst, "Size-dependent fracture toughness of tungsten," *Acta Mater*, vol. 138, pp. 198-211, 2017/10/01/ 2017, doi: https://doi.org/10.1016/j.actamat.2017.07.030.

[305] S. Wurster, C. Motz, and R. Pippan, "Characterization of the fracture toughness of micro-sized tungsten single crystal notched specimens," *Philosophical Magazine*, vol. 92, no. 14, pp. 1803-1825, 2012/05/11 2012, doi: 10.1080/14786435.2012.658449.

[306] Y. Deng and A. Barnoush, "Hydrogen embrittlement revealed via novel in situ fracture experiments using notched micro-cantilever specimens," *Acta Mater*, vol. 142, pp. 236-247, 2018/01/01/ 2018, doi: https://doi.org/10.1016/j.actamat.2017.09.057.

[307] C. Bohnert, N. J. Schmitt, S. M. Weygand, O. Kraft, and R. Schwaiger, "Fracture toughness characterization of single-crystalline tungsten using notched micro-cantilever specimens," *Int J Plasticity*, vol. 81, pp. 1-17, 2016/06/01/ 2016, doi: https://doi.org/10.1016/j.ijplas.2016.01.014.

[308] J. Ast, T. Przybilla, V. Maier, K. Durst, and M. Göken, "Microcantilever bending experiments in NiAl — Evaluation, size effects, and crack tip plasticity," *Journal of Materials Research*, vol. 29, no. 18, pp. 2129-2140, 2014/09/01 2014, doi: 10.1557/jmr.2014.240.

[309] R. Pippan, S. Wurster, and D. Kiener, "Fracture mechanics of micro samples: Fundamental considerations," *Materials & Design*, vol. 159, pp. 252-267, 2018/12/05/ 2018, doi: https://doi.org/10.1016/j.matdes.2018.09.004.

[310] D. E. J. Armstrong, A. J. Wilkinson, and S. G. Roberts, "Micro-mechanical measurements of fracture toughness of bismuth embrittled copper grain boundaries," *Philosophical Magazine Letters*, vol. 91, no. 6, pp. 394-400, 2011/06/01 2011, doi: 10.1080/09500839.2011.573813.

[311] S. Brinckmann, C. Kirchlechner, and G. Dehm, "Stress intensity factor dependence on anisotropy and geometry during micro-fracture experiments," *Scripta Materialia*, vol. 127, pp. 76-78, 2017/01/15/ 2017, doi: https://doi.org/10.1016/j.scriptamat.2016.08.027.

[312] S. Brinckmann, K. Matoy, C. Kirchlechner, and G. Dehm, "On the influence of microcantilever pre-crack geometries on the apparent fracture toughness of brittle materials," *Acta Mater*, vol. 136, pp. 281-287, 2017/09/01/ 2017, doi: https://doi.org/10.1016/j.actamat.2017.07.014.

[313] M. G. Mueller, V. Pejchal, G. Žagar, A. Singh, M. Cantoni, and A. Mortensen, "Fracture toughness testing of nanocrystalline alumina and fused quartz using chevron-notched microbeams," *Acta Mater*, vol. 86, pp. 385-395, 2015/03/01/ 2015, doi: https://doi.org/10.1016/j.actamat.2014.12.016.

[314] D. E. J. Armstrong, C. D. Hardie, J. S. K. L. Gibson, A. J. Bushby, P. D. Edmondson, and S. G. Roberts, "Small-scale characterisation of irradiated nuclear materials: Part II nanoindentation and micro-cantilever testing of ion irradiated nuclear materials," *J Nucl Mater*, vol. 462, pp. 374-381, 2015/07/01/ 2015, doi: https://doi.org/10.1016/j.jnucmat.2015.01.053.

[315] W. L. Costin, O. Lavigne, A. Kotousov, R. Ghomashchi, and V. Linton, "Investigation of hydrogen assisted cracking in acicular ferrite using site-specific micro-fracture tests," *Materials Science and Engineering: A*, vol. 651, pp. 859-868, 2016/01/10/ 2016, doi: https://doi.org/10.1016/j.msea.2015.11.044.

[316] G. Dehm, B. N. Jaya, R. Raghavan, and C. Kirchlechner, "Overview on micro- and nanomechanical testing: New insights in interface plasticity and fracture at small length scales," *Acta Mater*, vol. 142, pp. 248-282, 2018/01/01/ 2018, doi: https://doi.org/10.1016/j.actamat.2017.06.019.

[317] B. N. Jaya, C. Kirchlechner, and G. Dehm, "Can microscale fracture tests provide reliable fracture toughness values? A case study in silicon," *Journal of Materials Research*, vol. 30, no. 5, pp. 686-698, 2015/03/01 2015, doi: 10.1557/jmr.2015.2.

[318] H. Hirakata, Y. Takahashi, D. Van Truong, and T. Kitamura, "Role of plasticity on interface crack initiation from a free edge and propagation in a nano-component," *International Journal of Fracture*, vol. 145, no. 4, pp. 261-271, 2007/06/01 2007, doi: 10.1007/s10704-007-9079-0.

[319] E. Kawai, K. Sanada, T. Sumigawa, and T. Kitamura, "Delamination crack initiation from copper/silicon nitride interface edge with nanoscale singular stress field," *Engineering Fracture Mechanics*, vol. 120, pp. 60-66, 2014/04/01/ 2014, doi: https://doi.org/10.1016/j.engfracmech.2014.02.001.

[320] Y. Takahashi *et al.*, "Evaluation of Interfacial Fracture Strength in Micro-Scale Components Combined with High-Voltage Environmental Electron Microscopy," *Exp Mech*, vol. 55, no. 6, pp. 1047-1056, 2015/07/01 2015, doi: 10.1007/s11340-015-0008-2.

[321] Y. B. Gerbig, S. J. Stranick, and R. F. Cook, "Measurement of residual stress field anisotropy at indentations in silicon," *Scripta Materialia*, vol. 63, no. 5, pp. 512-515, 2010/09/01/ 2010, doi: https://doi.org/10.1016/j.scriptamat.2010.05.017.

[322] A. J. Gayle *et al.*, "Two-dimensional strain-mapping by electron backscatter diffraction and confocal Raman spectroscopy," *Journal of Applied Physics*, vol. 122, no. 20, 2017, doi: 10.1063/1.5001270.

[323] A. J. Wilkinson, "Modelling the effects of texture on the statistics of stage I fatigue crack growth," (in English), *Philos Mag A*, vol. 81, no. 4, pp. 841-855, Apr 2001. [Online]. Available: <Go to ISI>://WOS:000167998700004.

[324] H. J. Christ, C. P. Fritzen, and P. Köster, "Micromechanical modeling of short fatigue cracks," *Current Opinion in Solid State and Materials Science*, vol. 18, no. 4, pp. 205-211, 2014/08/01/ 2014, doi: https://doi.org/10.1016/j.cossms.2014.05.001.

[325] D. J. Chen, F. P. Chiang, Y. S. Tan, and H. S. Don, "Digital speckle-displacement measurement using a complex spectrum method," *Applied Optics*, vol. 32, no. 11, pp. 1839-1849, 1993/04/10 1993, doi: 10.1364/AO.32.001839.

[326] J. A. Duff and T. J. Marrow, "In situ observation of short fatigue crack propagation in oxygenated water at elevated temperature and pressure," *Corrosion Science*, vol. 68, pp. 34-43, 2013/03/01/ 2013, doi: https://doi.org/10.1016/j.corsci.2012.10.030.

[327] J. Newman, *Stress-intensity factor equations for cracks in three-dimensional finite bodies subjected to tension and bending loads*. Langley Research Center, National Aeronautics and Space Administration, 1984.

[328] J. Réthoré, N. Limodin, J.-Y. Buffière, F. Hild, W. Ludwig, and S. Roux, "Digital volume correlation analyses of synchrotron tomographic images," *The Journal of Strain Analysis for Engineering Design*, vol. 46, no. 7, pp. 683-695, 2011, doi: 10.1177/0309324711409999.

[329] J. Liu, J. Lyons, M. Sutton, and A. Reynolds, "Experimental Characterization of Crack Tip Deformation Fields in Alloy 718 at High Temperatures," *Journal of Engineering Materials and Technology*, vol. 120, no. 1, pp. 71-78, 1998, doi: 10.1115/1.2806840.

[330] J. Réthoré, N. Limodin, J.-Y. Buffière, S. Roux, and F. Hild, "Three-dimensional Analysis of Fatigue Crack Propagation using X-Ray Tomography, Digital Volume Correlation and Extended Finite Element Simulations," *Procedia IUTAM*, vol. 4, pp. 151-158, 2012/01/01/ 2012, doi: https://doi.org/10.1016/j.piutam.2012.05.017.

[331] R. Moutou Pitti, C. Badulescu, and M. Grédiac, "Characterization of a cracked specimen with full-field measurements: direct determination of the crack tip and energy release rate calculation," *International Journal of Fracture*, vol. 187, no. 1, pp. 109-121, 2014/05/01 2014, doi: 10.1007/s10704-013-9921-5.

[332] Y. Xu, W. Wan, and F. P. E. Dunne, "Microstructural fracture mechanics: Stored energy density at fatigue cracks," *J Mech Phys Solids*, vol. 146, p. 104209, 2021/01/01/ 2021, doi: https://doi.org/10.1016/j.jmps.2020.104209.

[333] J. Westerweel and F. Scarano, "Universal outlier detection for PIV data," *Experiments in Fluids*, vol. 39, no. 6, pp. 1096-1100, 2005/12/01 2005, doi: 10.1007/s00348-005-0016-6.

[334] C. F. Shih and R. J. Asaro, "Elastic-Plastic Analysis of Cracks on Bimaterial Interfaces: Part II—Structure of Small-Scale Yielding Fields," *Journal of Applied Mechanics*, vol. 56, no. 4, pp. 763-779, 1989, doi: 10.1115/1.3176170.

[335] W. F. Wan and F. P. E. Dunne, "Microstructure-interacting short crack growth in blocky alpha Zircaloy-4," (in English), *Int J Plasticity*, vol. 130, Jul 2020, doi: http://doi.org/10.1016/j.ijplas.2020.102711.

[336] W. Elber and M. Rosenfeld, "The Significance of Fatigue Crack Closure," in *Damage Tolerance in Aircraft Structures*, vol. STP486-EB: ASTM International, 1971, p. 0.

[337] D. Gan and J. Weertman, "Crack closure and crack propagation rates in 7050 aluminum," *Engineering Fracture Mechanics*, vol. 15, no. 1, pp. 87-106, 1981/01/01/ 1981, doi: https://doi.org/10.1016/0013-7944(81)90108-9.

[338] S. Suresh, "Crack growth retardation due to micro-roughness: A mechanism for overload effects in fatigue," *Scripta Metallurgica*, vol. 16, no. 8, pp. 995-999, 1982/08/01/ 1982, doi: https://doi.org/10.1016/0036-9748(82)90142-9.

[339] S. Suresh, "Micromechanisms of fatigue crack growth retardation following overloads," *Engineering Fracture Mechanics*, vol. 18, no. 3, pp. 577-593, 1983/01/01/ 1983, doi: https://doi.org/10.1016/0013-7944(83)90051-6.

[340] C. M. Ward-Close, A. F. Blom, and R. O. Ritchie, "Mechanisms associated with transient fatigue crack growth under variable-amplitude loading: An experimental and numerical study," *Engineering Fracture Mechanics*, vol. 32, no. 4, pp. 613-638, 1989/01/01/ 1989, doi: https://doi.org/10.1016/0013-7944(89)90195-1.

[341] J. D. Dougherty, T. S. Srivatsan, and J. Padovan, "Fatigue crack propagation and closure behavior of modified 1070 steel: Experimental results," *Engineering Fracture Mechanics*, vol. 56, no. 2, pp. 167-187, 1997/01/01/ 1997, doi: https://doi.org/10.1016/S0013-7944(96)00103-8.

[342] L. P. Borrego, J. M. Ferreira, J. M. Pinho da Cruz, and J. M. Costa, "Evaluation of overload effects on fatigue crack growth and closure," *Engineering Fracture Mechanics*, vol. 70, no. 11, pp. 1379-1397, 2003/07/01/ 2003, doi: https://doi.org/10.1016/S0013-7944(02)00119-4.

[343] C. Makabe, A. Purnowidodo, and A. J. McEvily, "Effects of surface deformation and crack closure on fatigue crack propagation after overloading and underloading," *Int J Fatigue*, vol. 26, no. 12, pp. 1341-1348, 2004/12/01/ 2004, doi: https://doi.org/10.1016/j.ijfatigue.2004.03.017.

[344] K. D. Singh, K. H. Khor, and I. Sinclair, "Roughness- and plasticity-induced fatigue crack closure under single overloads: Finite element modelling," *Acta Mater*, vol. 54, no. 17, pp. 4393-4403, 2006/10/01/ 2006, doi: https://doi.org/10.1016/j.actamat.2006.04.017.

[345] V. Tvergaard, "Effect of underloads or overloads in fatigue crack growth by crack-tip blunting," *Engineering Fracture Mechanics*, vol. 73, no. 7, pp. 869-879, 2006/05/01/ 2006, doi: https://doi.org/10.1016/j.engfracmech.2005.10.009.

[346] M. A. Meggiolaro, A. C. O. Miranda, J. T. P. Castro, and L. F. Martha, "Stress intensity factor equations for branched crack growth," *Engineering Fracture Mechanics*, vol. 72, no. 17, pp. 2647-2671, 2005/11/01/ 2005, doi: https://doi.org/10.1016/j.engfracmech.2005.05.004.

[347] A. T. Kermanidis and S. G. Pantelakis, "Prediction of crack growth following a single overload in aluminum alloy with sheet and plate microstructure," *Engineering Fracture*

Mechanics, vol. 78, no. 11, pp. 2325-2337, 2011/07/01/ 2011, doi: https://doi.org/10.1016/j.engfracmech.2011.05.005.

[348] E. Salvati, S. O'Connor, T. Sui, D. Nowell, and A. M. Korsunsky, "A study of overload effect on fatigue crack propagation using EBSD, FIB–DIC and FEM methods," *Engineering Fracture Mechanics*, vol. 167, pp. 210-223, 2016/11/01/ 2016, doi: https://doi.org/10.1016/j.engfracmech.2016.04.034.

[349] S. Y. Lee, P. K. Liaw, H. Choo, and R. B. Rogge, "A study on fatigue crack growth behavior subjected to a single tensile overload: Part I. An overload-induced transient crack growth micromechanism," *Acta Mater*, vol. 59, no. 2, pp. 485-494, 2011/01/01/ 2011, doi: https://doi.org/10.1016/j.actamat.2010.09.049.

[350] P. Lopez-Crespo *et al.*, "Measuring overload effects during fatigue crack growth in bainitic steel by synchrotron X-ray diffraction," *Int J Fatigue*, vol. 71, pp. 11-16, 2015/02/01/ 2015, doi: https://doi.org/10.1016/j.ijfatigue.2014.03.015.

[351] T. Wigger *et al.*, "In situ mapping of normal strains in the field of a growing fatigue crack in a steel weld using digital image correlation and energy dispersive synchrotron X-ray diffraction," *Int J Fatigue*, vol. 115, pp. 11-19, 2018/10/01/ 2018, doi: https://doi.org/10.1016/j.ijfatigue.2018.05.016.

[352] M. Croft *et al.*, "Strain profiling of fatigue crack overload effects using energy dispersive X-ray diffraction," *Int J Fatigue*, vol. 27, no. 10, pp. 1408-1419, 2005/10/01/ 2005, doi: https://doi.org/10.1016/j.ijfatigue.2005.06.022.

[353] J. P. Belnoue, T.-S. Jun, F. Hofmann, B. Abbey, and A. M. Korsunsky, "Evaluation of the overload effect on fatigue crack growth with the help of synchrotron XRD strain mapping," *Engineering Fracture Mechanics*, vol. 77, no. 16, pp. 3216-3226, 2010/11/01/ 2010, doi: https://doi.org/10.1016/j.engfracmech.2010.08.018.

[354] M. Thielen *et al.*, "In situ synchrotron stress mappings to characterize overload effects in fatigue crack growth," *Int J Fatigue*, vol. 121, pp. 155-162, 2019/04/01/ 2019, doi: https://doi.org/10.1016/j.ijfatigue.2018.12.013.

[355] M.-L. Zhu, Y.-W. Lu, C. Lupton, and J. Tong, "In situ near-tip normal strain evolution of a growing fatigue crack," *Fatigue Fract Eng M*, vol. 39, no. 8, pp. 950-955, 2016, doi: https://doi.org/10.1111/ffe.12391.

[356] J. M. Vasco-Olmo, B. Yang, M. N. James, and F. A. Díaz, "Investigation of effective stress intensity factors during overload fatigue cycles using photoelastic and DIC techniques," *Theoretical and Applied Fracture Mechanics*, vol. 97, pp. 73-86, 2018/10/01/ 2018, doi: https://doi.org/10.1016/j.tafmec.2018.07.011.

[357] A. Koko, E. Elmukashfi, T. H. Becker, P. S. Karamched, A. J. Wilkinson, and J. Marrow, "In situ characterisation of the strain fields of intragranular slip bands in ferrite by high-resolution electron backscatter diffraction," *Acta Mater*, vol. 239, Oct 15 2022, doi: 10.1016/j.actamat.2022.118284.

[358] R. Scales, "Environmental & Orientation Effects on the Ultrasonic Fatigue of a Single-crystal Nickel Superalloy," PhD Thesis, University of Oxford, Oxford, 2024.

[359] J. C. Gong and A. J. Wilkinson, "Anisotropy in the plastic flow properties of single-crystal α titanium determined from micro-cantilever beams," *Acta Mater*, vol. 57, no. 19, pp. 5693-5705, Nov 2009, doi: 10.1016/j.actamat.2009.07.064.

[360] J. W. Gong, A. J., "Ultra small scale high cycle fatigue testing by micro-cantilevers," in *Nanomechanical Testing in Materials Research and Development V*, Grande Real Santa Eulalia Hotel, Albufeira, Portugal, 2015.

[361] A. J. Wilkinson and T. B. Britton, "Strains, planes, and EBSD in materials science," (in English), *Mater Today*, vol. 15, no. 9, pp. 366-376, Sep 2012, doi: Doi 10.1016/S1369-7021(12)70163-3.

[362] T. B. Britton *et al.*, "Tutorial: Crystal orientations and EBSD - Or which way is up?," (in English), *Mater Charact*, vol. 117, pp. 113-126, Jul 2016, doi: 10.1016/j.matchar.2016.04.008.
[363] P. Earp, "Deformation and strain concentrations in coarse-grained alpha-uranium," PhD Thesis, University of Oxford, Oxford, 2019.
[364] A. Koko, "In situ full-field characterisation of strain concentrations (deformation twins, slip bands and cracks)," PhD Thesis, University of Oxford, Oxford, 2022.
[365] C. Zhu and M. De Graef, "EBSD pattern simulations for an interaction volume containing lattice defects," *Ultramicroscopy*, vol. 218, p. 113088, 2020/11/01/ 2020, doi: https://doi.org/10.1016/j.ultramic.2020.113088.
[366] T. C. Isabell and V. P. Dravid, "Resolution and sensitivity of electron backscattered diffraction in a cold field emission gun SEM," *Ultramicroscopy*, vol. 67, no. 1, pp. 59-68, 1997/06/01/ 1997, doi: https://doi.org/10.1016/S0304-3991(97)00003-X.
[367] C. J. Harland, P. Akhter, and J. A. Venables, "Accurate microcrystallography at high spatial resolution using electron back-scattering patterns in a field emission gun scanning electron microscope," *Journal of Physics E: Scientific Instruments*, vol. 14, no. 2, p. 175, 1981/02/01 1981, doi: 10.1088/0022-3735/14/2/011.
[368] D. J. Dingley and D. P. Field, "Electron backscatter diffraction and orientation imaging microscopy," *Mater Sci Tech-Lond*, vol. 13, no. 1, pp. 69-78, 1997, doi: 10.1179/mst.1997.13.1.69.
[369] O. Engler, Randle, V. , *Introduction to Texture Analysis: Macrotexture, Microtexture, and Orientation Mapping, Second Edition*, 2nd ed. CRC Press, 2009.
[370] R. A. Schwarzer, D. P. Field, B. L. Adams, M. Kumar, and A. J. Schwartz, "Present State of Electron Backscatter Diffraction and Prospective Developments," in *Electron Backscatter Diffraction in Materials Science*, A. J. Schwartz, M. Kumar, B. L. Adams, and D. P. Field Eds. Boston, MA: Springer US, 2009, pp. 1-20.
[371] E. Demir, A. Martinez-Pechero, C. Hardie, and E. Tarleton, "OXFORD-UMAT: An efficient and versatile crystal plasticity framework," *International Journal of Solids and Structures*, vol. 307, p. 113110, 2025/01/15/ 2025, doi: https://doi.org/10.1016/j.ijsolstr.2024.113110.
[372] S. Suresh and R. Ritchie, "Propagation of short fatigue cracks," *International metals reviews*, vol. 29, no. 1, pp. 445-475, 1984.
[373] T. B. Britton *et al.*, "Factors affecting the accuracy of high resolution electron backscatter diffraction when using simulated patterns," *Ultramicroscopy*, vol. 110, no. 12, pp. 1443-1453, 2010/11/01/ 2010, doi: https://doi.org/10.1016/j.ultramic.2010.08.001.
[374] N. P. Padture, M. Gell, and E. H. Jordan, "Thermal Barrier Coatings for Gas-Turbine Engine Applications," *Science*, vol. 296, no. 5566, pp. 280-284, 2002, doi: doi:10.1126/science.1068609.
[375] F. P. E. Dunne and D. Rugg, "On the mechanisms of fatigue facet nucleation in titanium alloys," *Fatigue Fract Eng M*, vol. 31, no. 11, pp. 949-958, 2008, doi: https://doi.org/10.1111/j.1460-2695.2008.01284.x.
[376] D. Chen, X.-F. Zhang, and R. O. Ritchie, "Effects of Grain-Boundary Structure on the Strength, Toughness, and Cyclic-Fatigue Properties of a Monolithic Silicon Carbide," *Journal of the American Ceramic Society*, vol. 83, no. 8, pp. 2079-2081, 2000, doi: https://doi.org/10.1111/j.1151-2916.2000.tb01515.x.
[377] N. Al Nasiri, N. Ni, E. Saiz, J. Chevalier, F. Giuliani, and L. J. Vandeperre, "Effect of microstructure and grain boundary chemistry on slow crack growth in silicon carbide at ambient conditions," *Journal of the European Ceramic Society*, vol. 35, no. 8, pp. 2253-2260, 2015/08/01/ 2015, doi: https://doi.org/10.1016/j.jeurceramsoc.2015.02.020.
[378] M. Z. Mughal, H.-Y. Amanieu, R. Moscatelli, and M. Sebastiani, "A Comparison of Microscale Techniques for Determining Fracture Toughness of LiMn2O4 Particles,"

Materials, vol. 10, no. 4, p. 403, 2017. [Online]. Available: https://www.mdpi.com/1996-1944/10/4/403.

[379] D. E. J. Armstrong, M. E. Rogers, and S. G. Roberts, "Micromechanical testing of stress corrosion cracking of individual grain boundaries," *Scripta Materialia*, vol. 61, no. 7, pp. 741-743, 2009/10/01/ 2009, doi: https://doi.org/10.1016/j.scriptamat.2009.06.017.

[380] H. Dugdale, D. E. J. Armstrong, E. Tarleton, S. G. Roberts, and S. Lozano-Perez, "How oxidized grain boundaries fail," *Acta Mater*, vol. 61, no. 13, pp. 4707-4713, 2013/08/01/ 2013, doi: https://doi.org/10.1016/j.actamat.2013.05.012.

[381] K. Matoy, T. Detzel, M. Müller, C. Motz, and G. Dehm, "Interface fracture properties of thin films studied by using the micro-cantilever deflection technique," *Surface and Coatings Technology*, vol. 204, no. 6, pp. 878-881, 2009/12/25/ 2009, doi: https://doi.org/10.1016/j.surfcoat.2009.09.013.

[382] J. P. Best, J. Wehrs, M. Polyakov, M. Morstein, and J. Michler, "High temperature fracture toughness of ceramic coatings evaluated using micro-pillar splitting," *Scripta Materialia*, vol. 162, pp. 190-194, 2019/03/15/ 2019, doi: https://doi.org/10.1016/j.scriptamat.2018.11.013.

[383] R. F. Cook, "Strength and sharp contact fracture of silicon," *Journal of Materials Science*, vol. 41, no. 3, pp. 841-872, 2006/02/01 2006, doi: 10.1007/s10853-006-6567-y.

[384] A. Masolin, P.-O. Bouchard, R. Martini, and M. Bernacki, "Thermo-mechanical and fracture properties in single-crystal silicon," *Journal of Materials Science*, vol. 48, no. 3, pp. 979-988, 2013/02/01 2013, doi: 10.1007/s10853-012-6713-7.

[385] W. C. Oliver and G. M. Pharr, "An improved technique for determining hardness and elastic modulus using load and displacement sensing indentation experiments," *Journal of Materials Research*, vol. 7, no. 6, pp. 1564-1583, 1992/06/01 1992, doi: 10.1557/JMR.1992.1564.

[386] M. A. Hussain, S. L. Pu, and J. Underwood, "Strain Energy Release Rate for a Crack Under Combined Mode I and Mode II," presented at the 1973 National Symposium on Fracture Mechanics, Part II, Washington, United States, 100 Barr Harbor Drive, PO Box C700, West Conshohocken, PA 19428-2959, 1973, 1973. [Online]. Available: https://hal.science/hal-04166069.

[387] R. J. Nuismer, "An energy release rate criterion for mixed mode fracture," *International Journal of Fracture*, vol. 11, no. 2, pp. 245-250, 1975/04/01 1975, doi: 10.1007/BF00038891.

[388] K. Palaniswamy and W. G. Knauss, "II - On the Problem of Crack Extension in Brittle Solids Under General Loading," in *Mechanics Today*, S. Nemat-Nasser Ed.: Pergamon, 1978, pp. 87-148.

[389] J. Chang, J.-q. Xu, and Y. Mutoh, "A general mixed-mode brittle fracture criterion for cracked materials," *Engineering Fracture Mechanics*, vol. 73, no. 9, pp. 1249-1263, 2006/06/01/ 2006, doi: https://doi.org/10.1016/j.engfracmech.2005.12.011.

[390] F. Erdogan and G. C. Sih, "On the Crack Extension in Plates Under Plane Loading and Transverse Shear," *Journal of Basic Engineering*, vol. 85, no. 4, pp. 519-525, 1963, doi: 10.1115/1.3656897.

[391] G. C. Sih, "Strain-energy-density factor applied to mixed mode crack problems," *International Journal of Fracture*, vol. 10, no. 3, pp. 305-321, 1974/09/01 1974, doi: 10.1007/BF00035493.

[392] G. C. Sih, *Mechanics of Fracture Initiation and Propagationn: surface and volume energy density applied as failure criterion*. Springer Science & Business Media, 1991, pp. XXII, 410.

[393] S. Maddali *et al.*, "Concurrent multi-peak Bragg coherent x-ray diffraction imaging of 3D nanocrystal lattice displacement via global optimization," *npj Computational Materials*, vol. 9, no. 1, p. 77, 2023/05/23 2023, doi: 10.1038/s41524-023-01022-7.

[394] P. S. Karamched, N. Saravanan, J. C. Haley, A. J. Wilkinson, and S. Lozano-Perez, "Effect of sample thinning on strains and lattice rotations measured from Transmission Kikuchi diffraction in the SEM," *Ultramicroscopy*, vol. 225, p. 113267, 2021/06/01/ 2021, doi: https://doi.org/10.1016/j.ultramic.2021.113267.

[395] H. Yu, J. Liu, P. Karamched, A. J. Wilkinson, and F. Hofmann, "Mapping the full lattice strain tensor of a single dislocation by high angular resolution transmission Kikuchi diffraction (HR-TKD)," *Scripta Materialia*, vol. 164, pp. 36-41, 2019/04/15/ 2019, doi: https://doi.org/10.1016/j.scriptamat.2018.12.039.

[396] M. J. Hÿtch and A. M. Minor, "Observing and measuring strain in nanostructures and devices with transmission electron microscopy," *MRS Bulletin*, vol. 39, no. 2, pp. 138-146, 2014, doi: 10.1557/mrs.2014.4.

[397] R. Daniel *et al.*, "Grain boundary design of thin films: Using tilted brittle interfaces for multiple crack deflection toughening," *Acta Mater*, vol. 122, pp. 130-137, 2017/01/01/ 2017, doi: https://doi.org/10.1016/j.actamat.2016.09.027.

[398] W. Kuang, M. Song, and G. S. Was, "Insights into the stress corrosion cracking of solution annealed alloy 690 in simulated pressurized water reactor primary water under dynamic straining," *Acta Mater*, vol. 151, pp. 321-333, 2018/06/01/ 2018, doi: https://doi.org/10.1016/j.actamat.2018.04.002.

[399] M.-R. He, D. C. Johnson, G. S. Was, and I. M. Robertson, "The role of grain boundary microchemistry in irradiation-assisted stress corrosion cracking of a Fe-13Cr-15Ni alloy," *Acta Mater*, vol. 138, pp. 61-71, 2017/10/01/ 2017, doi: https://doi.org/10.1016/j.actamat.2017.07.042.

[400] P. Hosemann, C. Shin, and D. Kiener, "Small scale mechanical testing of irradiated materials," *Journal of Materials Research*, vol. 30, no. 9, pp. 1231-1245, 2015, doi: 10.1557/jmr.2015.26.

[401] P. D. Edmondson, A. London, A. Xu, D. E. J. Armstrong, and S. G. Roberts, "Small-scale characterisation of irradiated nuclear materials: Part I – Microstructure," *J Nucl Mater*, vol. 462, pp. 369-373, 2015/07/01/ 2015, doi: https://doi.org/10.1016/j.jnucmat.2014.11.067.

[402] C. M. Hamel, K. N. Long, and S. L. B. Kramer, "Calibrating constitutive models with full-field data via physics informed neural networks," *Strain*, vol. 59, no. 2, p. e12431, 2023/04/01 2023, doi: https://doi.org/10.1111/str.12431.

[403] F. Pierron and M. Grédiac, "Towards Material Testing 2.0. A review of test design for identification of constitutive parameters from full-field measurements," *Strain*, vol. 57, no. 1, p. e12370, 2021/02/01 2021, doi: https://doi.org/10.1111/str.12370.

[404] D. J. Long, Y. Liu, W. Wan, and F. P. E. Dunne, "A microstructure-sensitive analytical solution for short fatigue crack growth rate in metallic materials," *International Journal of Mechanical Sciences*, vol. 253, p. 108365, 2023/09/01/ 2023, doi: https://doi.org/10.1016/j.ijmecsci.2023.108365.

[405] M. Alfano, G. Lubineau, and G. H. Paulino, "Global sensitivity analysis in the identification of cohesive models using full-field kinematic data," *International Journal of Solids and Structures*, vol. 55, pp. 66-78, 2015/03/01/ 2015, doi: https://doi.org/10.1016/j.ijsolstr.2014.06.006.

[406] H. Tran, Y. F. Gao, and H. B. Chew, "An inverse method to reconstruct crack-tip cohesive zone laws for fatigue by numerical field projection," *International Journal of Solids and Structures*, vol. 239-240, p. 111435, 2022/03/15/ 2022, doi: https://doi.org/10.1016/j.ijsolstr.2022.111435.

[407] M. D. Sangid, "Coupling in situ experiments and modeling – Opportunities for data fusion, machine learning, and discovery of emergent behavior," *Current Opinion in Solid State and Materials Science*, vol. 24, no. 1, p. 100797, 2020/02/01/ 2020, doi: https://doi.org/10.1016/j.cossms.2019.100797.

Appendix

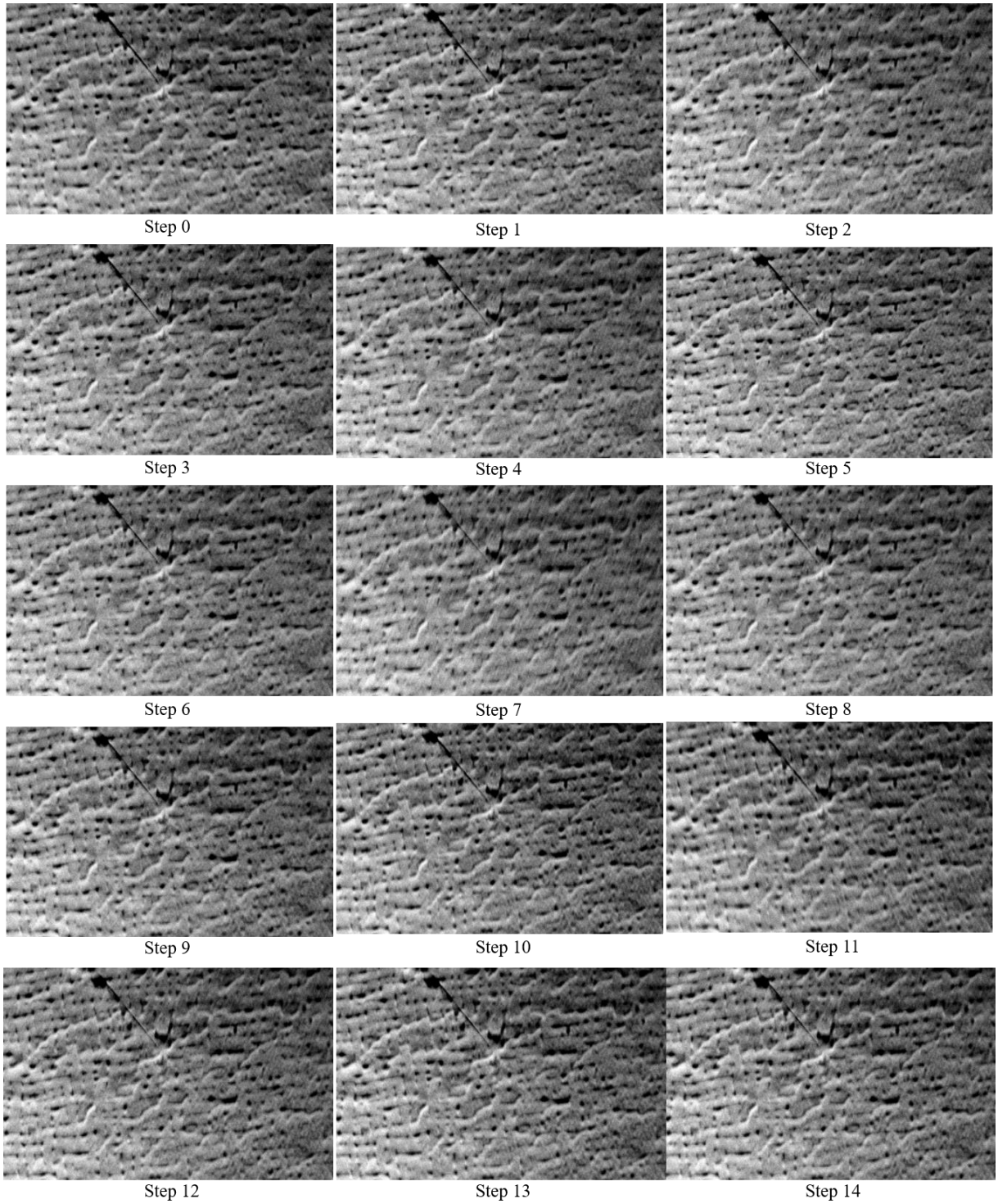

FIGURE.
FSE Images of Experiment 2.

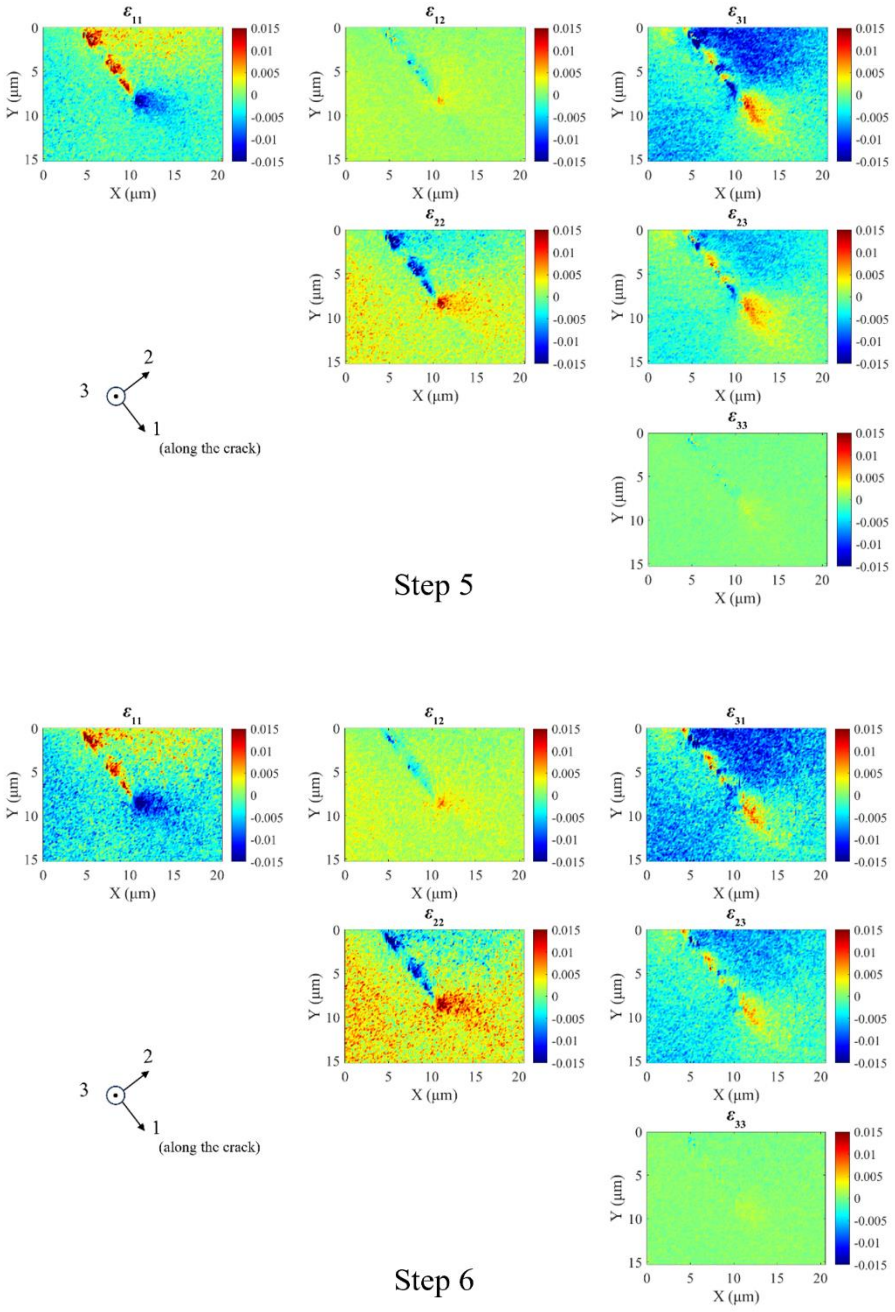

FIGURE.

Elastic strain tensor fields obtained by HR-EBSD for Cycle B and C at loading steps 5 to 14, Experiment 2. Reference points were selected from the unstressed wake region of the crack, assuming a strain-free condition near the free surface. The maps are distributed across multiple pages for clarity.

Appendix

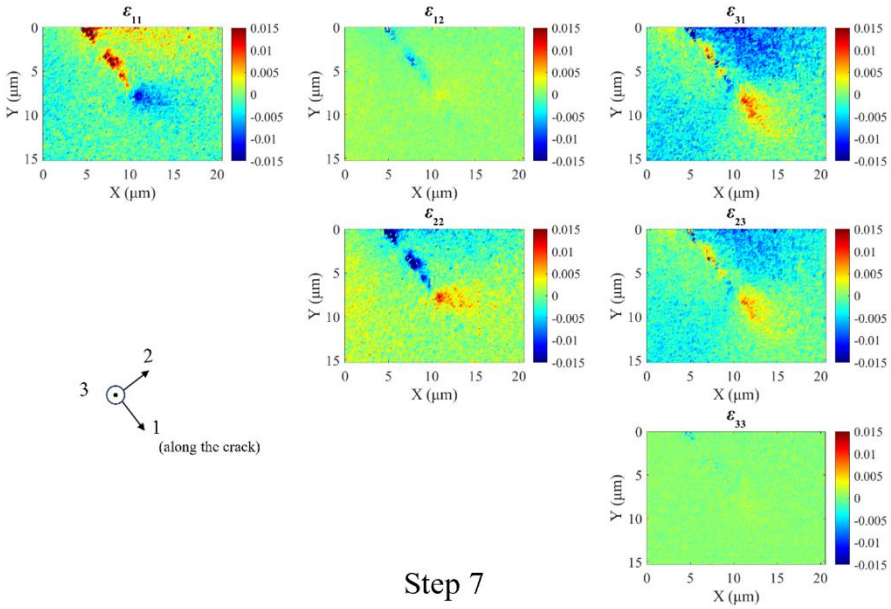

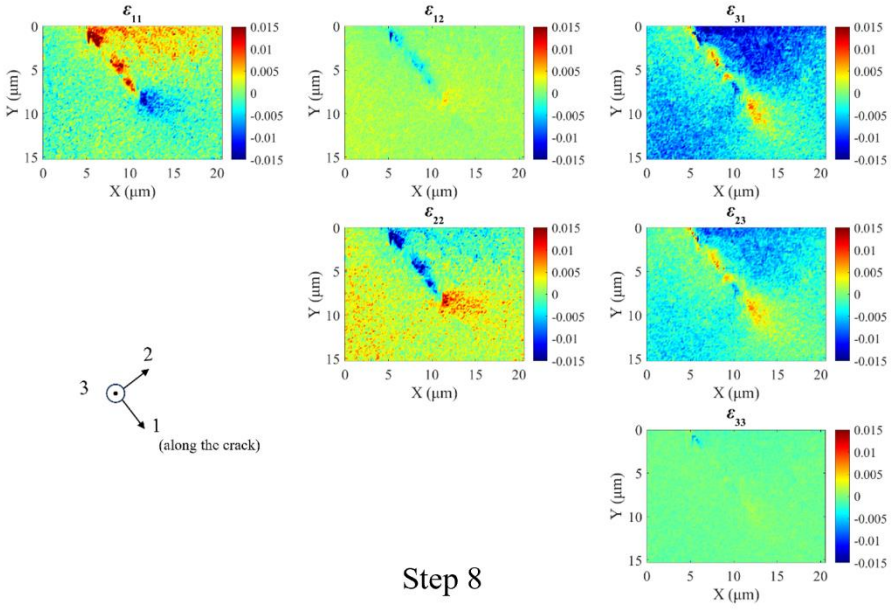

FIGURE.

Elastic strain tensor fields obtained by HR-EBSD for Cycle B and C at loading steps 5 to 14, Experiment 2. Reference points were selected from the unstressed wake region of the crack, assuming a strain-free condition near the free surface. The maps are distributed across multiple pages for clarity.

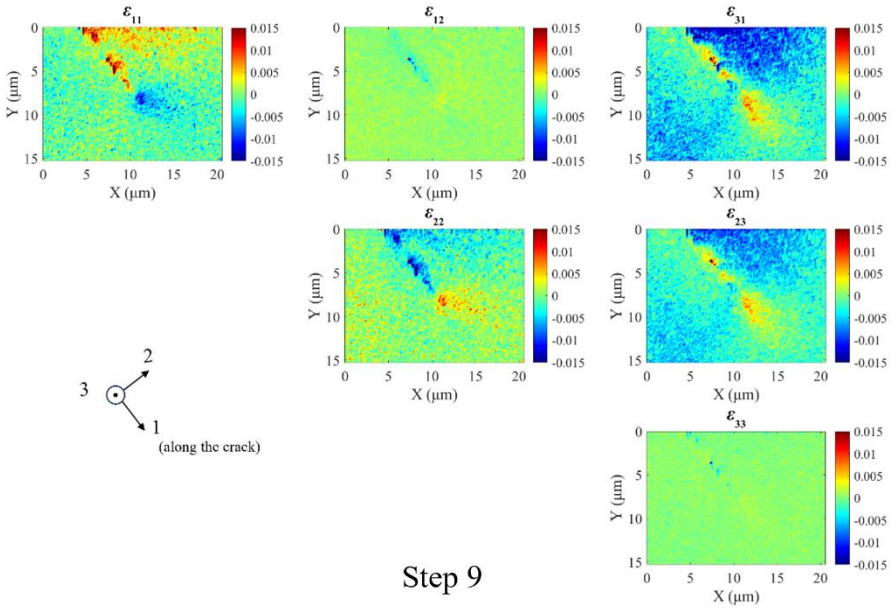

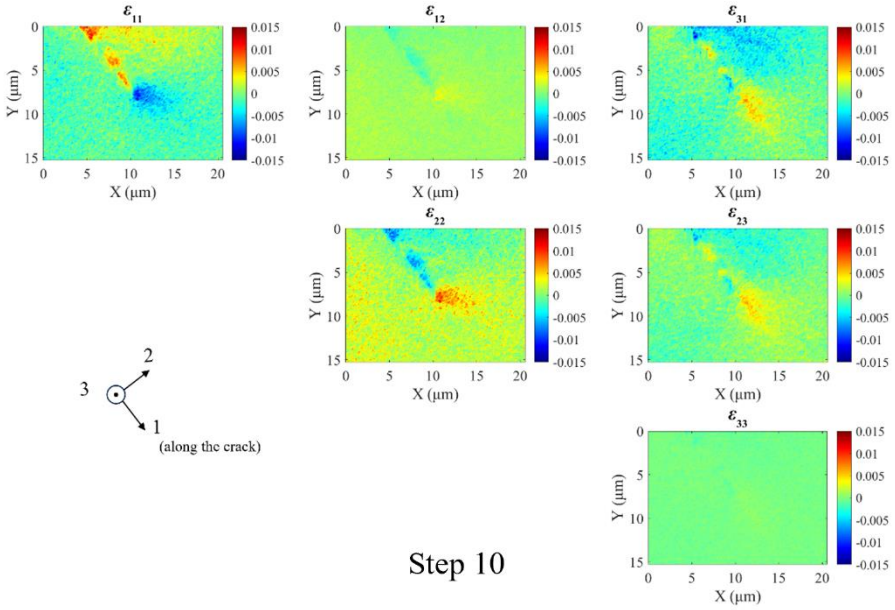

FIGURE.

Elastic strain tensor fields obtained by HR-EBSD for Cycle B and C at loading steps 5 to 14, Experiment 2. Reference points were selected from the unstressed wake region of the crack, assuming a strain-free condition near the free surface. The maps are distributed across multiple pages for clarity.

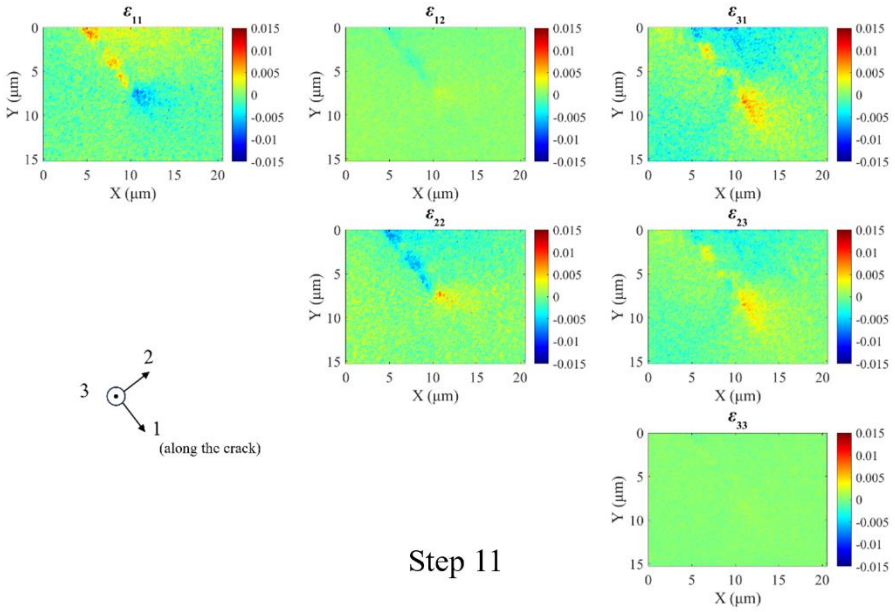

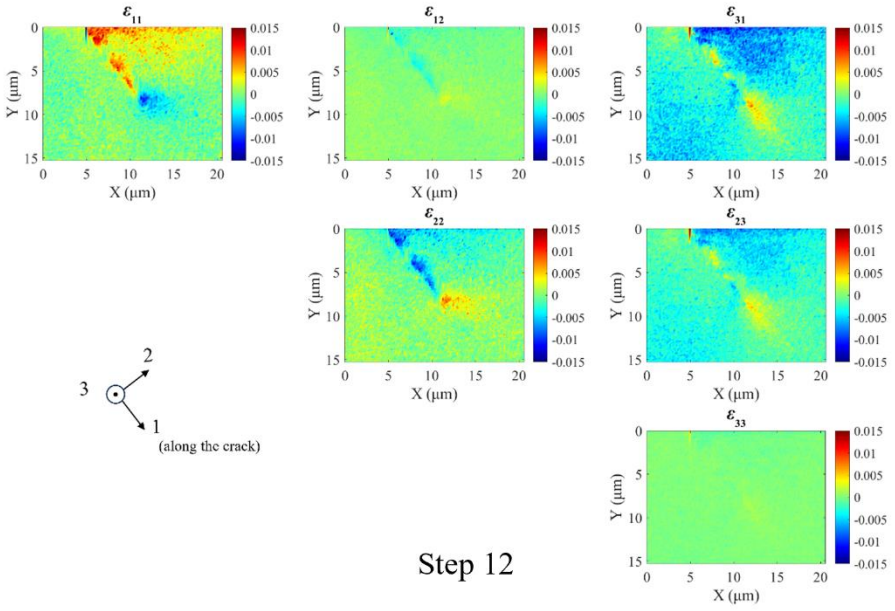

FIGURE.

Elastic strain tensor fields obtained by HR-EBSD for Cycle B and C at loading steps 5 to 14, Experiment 2. Reference points were selected from the unstressed wake region of the crack, assuming a strain-free condition near the free surface. The maps are distributed across multiple pages for clarity.

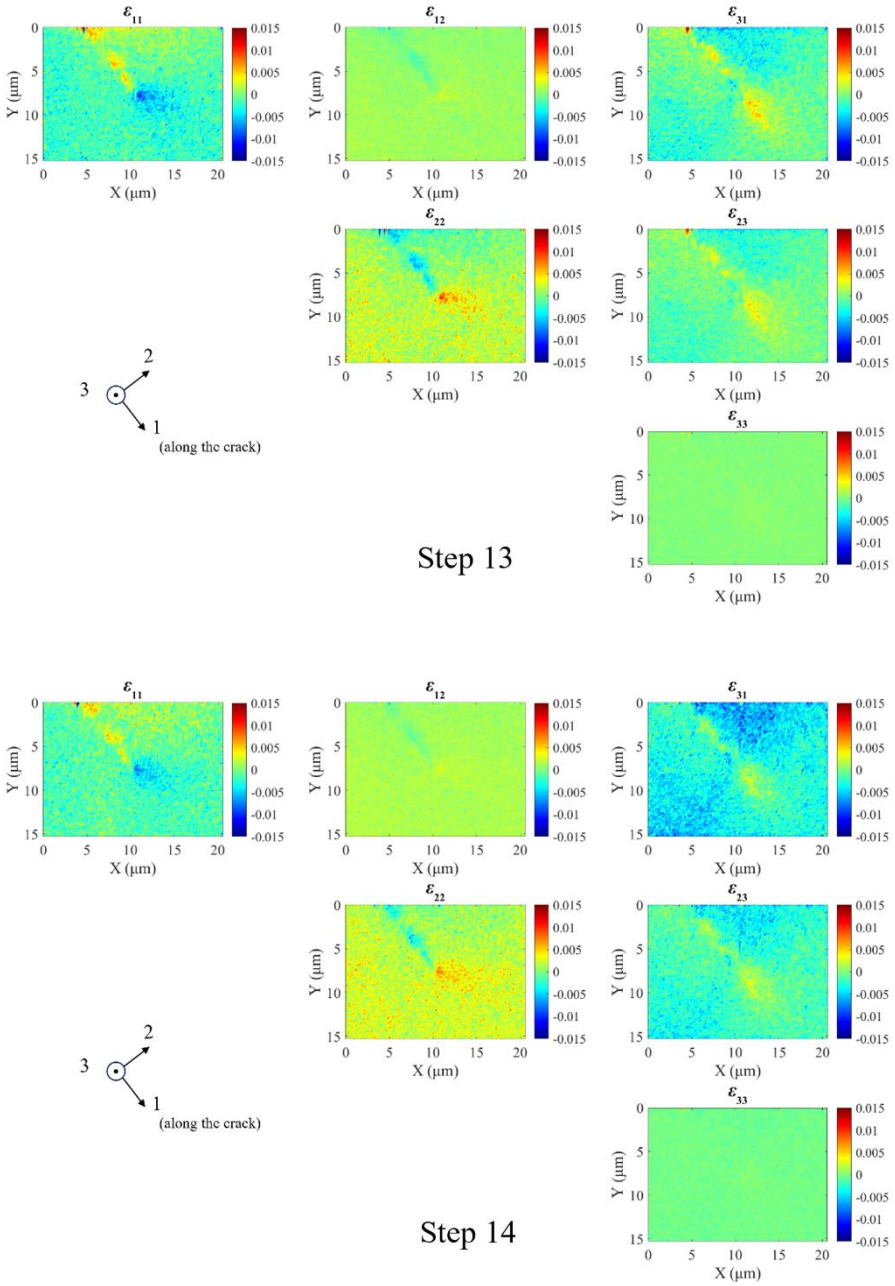

FIGURE.

Elastic strain tensor fields obtained by HR-EBSD for Cycle B and C at loading steps 5 to 14, Experiment 2. Reference points were selected from the unstressed wake region of the crack, assuming a strain-free condition near the free surface. The maps are distributed across multiple pages for clarity.

Appendix

TABLE

Summary of energy integral results from Experiment 2.

Load (N)	J-integral (remote BC)	J-integral (DIC)	J-integral (EBSD+Direct)
0	0	0	24.14 ± 15.07
0.25	30.03	13.18 ± 6.613	44.81 ± 13.98 ($\Delta J = 20.67$)
0.50	60.06	19.71 ± 11.538	72.62 ± 22.21 ($\Delta J = 48.48$)
0.75	90.10	7.98 ± 1.477	69.38 ± 19.59 ($\Delta J = 45.24$)
1.00	120.11	19.81 ± 11.642	88.83 ± 17.63 ($\Delta J = 64.69$)
0	0	0	35.63 ± 6.72
0.50	60.06	42.7 ± 3.739	101.60 ± 23.69 ($\Delta J = 65.97$)
1.00	120.11	38.64 ± 15.647	63.68 ± 14.79 ($\Delta J = 28.05$)
1.50	180.17	40.02 ± 3.903	83.96 ± 18.95 ($\Delta J = 48.33$)
2.00	240.22	41.15 ± 19.218	29.97 ± 8.02 ($\Delta J = -5.66$)
0	0	0	6.17 ± 3.03
0.25	30.03	26.74 ± 14.648	15.25 ± 2.03 ($\Delta J = 9.08$)
0.50	60.06	59.86 ± 2.016	19.22 ± 8.39 ($\Delta J = 13.05$)
0.75	90.10	60.79 ± 9.015	12.66 ± 3.18 ($\Delta J = 6.49$)
1.00	120.11	118.32 ± 13.023	24.01 ± 12.00 ($\Delta J = 5.18$)

TABLE

Summary of energy integral results from Experiment 2.

Load (N)	K_{I} (remote BC)	K_{I} (DIC)	K_{I} (EBSD+Direct)
0	0	0	1.17 ± 0.42
0.25	1.14	2.53 ± 0.316	$1.74 \pm .52$ ($\Delta K_{\mathrm{I}} = 0.57$)
0.50	2.28	3.16 ± 0.547	2.15 ± 0.58 ($\Delta K_{\mathrm{I}} = 0.98$)
0.75	3.42	4.37 ± 0.28	2.02 ± 0.72 ($\Delta K_{\mathrm{I}} = 0.85$)
1.00	4.57	5.1 ± 0.292	2.56 ± 0.64 ($\Delta K_{\mathrm{I}} = 1.39$)
0	0	0	1.50 ± 0.51
0.50	2.28	4.13 ± 0.996	3.51 ± 0.47 ($\Delta K_{\mathrm{I}} = 2.01$)
1.00	4.57	4.58 ± 0.407	1.92 ± 0.46 ($\Delta K_{\mathrm{I}} = 0.42$)
1.50	6.85	4.94 ± 0.026	2.80 ± 0.63 ($\Delta K_{\mathrm{I}} = 1.3$)
2.00	9.14	4.29 ± 1.323	1.33 ± 0.54 ($\Delta K_{\mathrm{I}} = -0.17$)
0	0	0	0.56 ± 0.24
0.25	1.14	3.25 ± 0.529	0.55 ± 0.19 ($\Delta K_{\mathrm{I}} = -0.01$)
0.50	2.28	3.37 ± 0.16	1.14 ± 0.30 ($\Delta K_{\mathrm{I}} = 0.58$)
0.75	3.42	4.25 ± 0.658	0.92 ± 0.20 ($\Delta K_{\mathrm{I}} = 0.36$)
1.00	4.57	4.81 ± 1.41	1.60 ± 0.38 ($\Delta K_{\mathrm{I}} = 1.04$)

Appendix

TABLE

Summary of energy integral results from Experiment 2.

Load (N)	K_{II} (remote BC)	K_{II} (DIC)	K_{II} (EBSD+Direct)
0	0	0	0.50 ± 0.25
0.25	0.32	0.96 ± 0.041	1.13 ± 0.20 ($\Delta K_{II} = 0.63$)
0.50	0.64	2.36 ± 0.390	0.79 ± 0.42 ($\Delta K_{II} = 0.29$)
0.75	0.96	1.92 ± 0.115	0.96 ± 0.29 ($\Delta K_{II} = 0.46$)
1.00	1.29	3.33 ± 0.278	0.97 ± 0.32 ($\Delta K_{II} = 0.47$)
0	0	0	0.73 ± 0.30
0.50	0.64	1.3 ± 0.323	1.02 ± 0.41 ($\Delta K_{II} = 0.29$)
1.00	1.29	2.89 ± 0.275	1.60 ± 0.74 ($\Delta K_{II} = 0.87$)
1.50	1.93	2.25 ± 0.175	0.66 ± 0.33 ($\Delta K_{II} = -0.07$)
2.00	2.58	0.46 ± 0.759	1.1 ± 0.37 ($\Delta K_{II} = 0.37$)
0	0	0	0.46 ± 0.18
0.25	0.32	1.47 ± 0.161	0.47 ± 0.14 ($\Delta K_{II} = 0.01$)
0.50	0.64	1.87 ± 0.512	0.90 ± 0.29 ($\Delta K_{II} = 0.44$)
0.75	0.96	0.66 ± 0.463	0.81 ± 0.10 ($\Delta K_{II} = 0.35$)
1.00	1.29	0.76 ± 1.036	0.89 ± 0.09 ($\Delta K_{II} = 0.43$)

TABLE

Summary of energy integral results from Experiment 2.

Load (N)	K_{III} (remote BC)	K_{III} (DIC)	K_{III} (EBSD+Direct)
0	0	–	1.33 ± 0.76
0.25	0.49	–	1.95 ± 0.47 ($\Delta K_{III} = 0.62$)
0.50	0.98	–	2.74 ± 0.54 ($\Delta K_{III} = 1.41$)
0.75	1.47	–	2.63 ± 0.68 ($\Delta K_{III} = 1.30$)
1.00	1.97	–	2.83 ± 0.92 ($\Delta K_{III} = 0.50$)
0	0	–	1.89 ± 0.21
0.50	0.98	–	2.49 ± 0.69 ($\Delta K_{III} = 0.60$)
1.00	1.97	–-	2.31 ± 0.31 ($\Delta K_{III} = 0.42$)
1.50	2.95	–	2.72 ± 0.23 ($\Delta K_{III} = 0.83$)
2.00	3.94	–	1.53 ± 0.38 ($\Delta K_{III} = -0.36$)
0	0	–	0.70 ± 0.30
0.25	0.49	–	1.47 ± 0.11 ($\Delta K_{III} = 0.77$)
0.50	0.98	–	1.17 ± 0.35 ($\Delta K_{III} = 0.47$)
0.75	1.47	–	0.94 ± 0.26 ($\Delta K_{III} = 0.24$)
1.00	1.97	–	1.08 ± 0.44 ($\Delta K_{III} = 0.38$)